University of Essex

NONLINEAR DYNAMICS OF SOLITARY AND OPTICALLY-INJECTED SPIN VERTICAL-CAVITY LASERS

SAMI S. ALHARTHI

A thesis submitted for the degree of Doctor of Philosophy (Ph.D.)

School of Computer Science and Electronic Engineering

University of Essex

MAY 2016

SUMMARY

This work investigates the nonlinear dynamics and polarisation properties of Spin-Vertical-(External)-Cavity Surface-Emitting Lasers (V(E)CSELs). The focus is on gaining a broad understanding of the various polarised resolved nonlinear dynamical effects in solitary and injected 1300 nm spin-V(E)CSELs.

We report a comprehensive study including theory, based on the Spin Flip Model, and experiments of the stability characteristics of solitary 1300 nm dilute nitride Quantum-Well (QW) spin-VCSELs. Various forms of oscillatory behaviour causing self-sustained oscillations in the polarisation of the spin-VCSEL subject to Continuous-Wave (CW) pumping are found. Additionally, this work is extended to study experimentally and theoretically the evolution of the output polarisation ellipticity, and experimentally the nonlinear dynamics of the light polarisation emitted by the QW spin VCSELs under polarised optical injection. Rich nonlinear dynamics of the optically injected QW spin-VCSEL are reported ranging from polarisation control, polarisation switching and bistability to periodic oscillations and chaos. Good agreement is found between measurements and calculations where theoretical results are available.

We also report the first 1300 nm Quantum-Dot (QD) Semiconductor Disk Laser (SDL) using a very simple and compact laser configuration involving a high reflection (HR)-coated fibre as the top mirror. Moreover, by applying spin injection to the 1300 nm SDL via CW polarised optical pumping we also demonstrate the first 1300 nm QD spin Vertical-External-Cavity Surface-Emitting Laser (Spin-VECSEL). This is also accompanied by an investigation of the dynamics of the solitary 1300 nm QD spin-VECSEL.

Finally, we present the first experimental study of the evolution of the output polarisation ellipticity and nonlinear dynamics of the 1300 nm QD spin-VECSEL under polarised optical injection. Our findings show nonlinear effects similar to the ones seen in optically injected QW spin-VCSELs.

ACKNOWLEDGEMENTS

All glories, praise and bundle of thanks be to Almighty God, the most gracious and the most merciful. It is indeed just due to his mercy, graces and bounties that I have accomplished this thesis.

The completion of this thesis would not have been possible without the generous help of many people whom I want to take this opportunity to thank and acknowledge. First of all, I would like to express my deepest gratitude to my supervisors Profs. M. J. Adams and I. D. Henning for their invaluable, constant advice, support, encouragement, patience, and expert guidance as well as their suggestions during my studies, including their comments and corrections on the manuscripts of the published papers and also this thesis. Their enthusiasm for research has always been a driving force for me to finish any task. In addition, their knowledge and unique way of handling the scientific challenges has been and will be a constant source of motivation and inspiration for all my endeavors. As I always say to my friends, working with them has been a blessing for me due to their vast understanding.

I would like to thank our previous research group members especially Drs. Antonio Hurtado and Nadir Khan as well as Dr. Rihab Al-Seyab for advice and support in the early experiments and simulations, respectively. Also, above all I am very thankful to Dr. Kevin Schires for introducing me to the real experimental work on the spin injection during the early part of my work. Most of the experimental data presented in this thesis was acquired using his smart toolbox software ‘’LabMate’’, so I am indebted to him.

A number of technical staff also deserves thanks particularly Nick Warren for his help with optical fibre splicing and fusion, Adrian Boland-Thoms and Paul Vincent for their technical assistance in handling the spin laser's samples and for advice and work on the custom laser mounts.

I am also grateful to Prof. Mircea Guina and Dr. Ville-Markus Korpijärvi, from the Tampere University of Technology, and also Dr. Edmund Clarke from the Engineering and Physical Sciences Research Council (EPSRC) National Centre for III-V Technologies for supply of the spin-V(E)CSEL wafers.

Great regards and blessings should go to my friends and colleagues who supported or prayed for me in any respect during the completion of the project. There are many other people who supported and encouraged me during my PhD studies. To list all of them here is, of course, not possible but I acknowledge all of them.

I have no words to express my heartiest gratitude to my parents for their unconditional support and encouragement whom continuous prayers brought me to this stage. I am also grateful for the support of my immediate and extended family.

Finally, the sincerest appreciation is to my wife and truly friend for her total moral support, passion and companionship. The sincere love of my beloved sons, Mohannad and Mohammed, has been a source of my inspiration and played a key role in the completion of this thesis.

Table of Contents

CHAPTER 1: INTRODUCTION

Abstract:

In this chapter the historical background of this study is presented. The characteristics of VCSELs are first described. These include the polarisation behaviour, the advantages and applications of VCSELs, the gain media and the importance of dilute nitride materials and the telecom wavelength of 1300 nm. Finally, the objectives and scope of this PhD are presented followed by the thesis outline.

1.1 Historical Context

The foundations of today's information and communication technology can be traced back to early developments in semiconductor electronics and ferromagnets since data is processed and computed using semiconductor transistors, whereas information is mostly stored magnetically on hard discs.

After the invention of the first transistor in 1947 [1] microelectronics technology has seen unprecedented advances in terms of both scale and functionality. This is often characterised by citing Moore's law. According to the famous Moore's Law, which was set up by Intel co-founder Gordon Moore in 1965 as an empirical rule of thumb, the number of transistors on a chip doubles roughly every eighteen months [2]. Thanks to technological developments [3, 4] this trend still holds true since the first publication. However, in spite of the tremendous advances in lithography and innovations in device engineering, the progressive reduction of the device dimensions in electronic components will soon be confronted with fundamental physical limits which will make continued progress more difficult as well as prohibitively expensive to commercialise. Therefore, new concepts and technology are required to keep on the track with this extraordinary rate of advance. One such new concept based on quantum mechanics makes use of electron spin, the so-called the magnetic angular momentum of electrons, with or without the charge of electrons. This technology is often termed 'spintronics'.

1.2 Spintronics

In the last two decades, a new rapidly growing research field of 'spintronics' has emerged. In this the electron spin can be used as an additional degree of freedom within semiconductor electronics and optoelectronics. This direction can be traced

back to the discovery of the giant magneto-resistive (GMR) effect in 1988 by Albert Fert and Peter Grunberg (Nobel Prize laureates in 2007) [5, 6]. It builds on the concept of using the electron spin in an electronic device as an information carrier in order to produce novel devices to revolutionise the field of information technology [7]. The information can be encoded via the spin orientation of the electron [8]. For instance, spin-up could represent a logic ’1’ while spin-down could represent a logic ’0’. The controlled manipulation of the spin orientation in semiconductors promises components with new or improved functionalities in comparison to their conventional counterparts [8]. Preliminary theoretical predictions reveal that optimised spintronic devices will lead to new multifunctional devices offering non-volatility, fast processing, low power consumption, and higher packaging and integration density than conventional electronic devices [9]. Generally speaking, the spintronics field includes the investigation of the basic fundamental physical processes such as spin injection [10, 11] which will be the focus of this thesis, spin transport [12, 13], spin manipulation, and spin detection. However, operationally spintronics faces the challenge that the electron spin orientation will be lost due to spin relaxation mechanisms [14, 15]; this will be discussed in the next chapter.

The first idea to use spin injection in semiconductors was the spin-controlled transistor which was proposed in 1990 by Datta and Das [16]. Since then there has been considerable research work to find ways of generating a spin polarised carrier population in a semiconductor system. One approach aims to utilise electrical spin injection by using ferromagnetic contacts with the aid of an external magnetic field to create an imbalance between population densities of the two spin subbands. Alternatively the absorption of circularly polarised light [17] can be used to create a spin polarised carrier population. This in fact forms the basis of an important subclass

of spintronics: spin optoelectronics. Spin optoelectronics deals with the components that relate the optical selection rules of the light polarisation to the carrier spin polarisation in semiconductor systems. This includes, for example, spin-LEDs [18, 19], spin detectors [20] and spin-lasers [21, 22]. However, despite extensive research on electrical spin injection into semiconductors few device demonstrations which use ferromagnet contacts have been produced. These prototypes currently work either at low temperatures with a relatively low efficiency or under large external magnetic field. The optical excitation (pumping) with circularly polarised light in particular is preferred since it delivers spin which is robust to environmental factors like temperature. In addition, the lower cost and complexity of the device and experiments required to investigate and achieve spin polarisation in semiconductor systems are attractive from a practical point of view. Therefore, throughout this thesis optical pumping is used to excite semiconductor spin-lasers, specifically Vertical-(External)-Cavity Surface-Emitting Lasers, V(E)CSELs and the associated behaviour is investigated as will be shown in chapters 3 and 7. Using this basic system, polarised coherent optical injection is introduced to the spin device as a means to generate further nonlinear dynamics which can be used in a variety of potential applications such as optical communications as will be discussed in chapters 4, 5 and 8.

1.3 Vertical-(External)-Cavity Surface-Emitting Lasers, V(E)CSELs

Semiconductor lasers in general consist of multilayers of semiconductor materials grown on top of each other on a substrate. This structure is usually made by different epitaxial growth techniques such as molecular beam epitaxy (MBE), metal organic

chemical vapour deposition (MOCVD) or chemical beam epitaxy (CBE). Then the wafer is processed to produce a laser device [23].

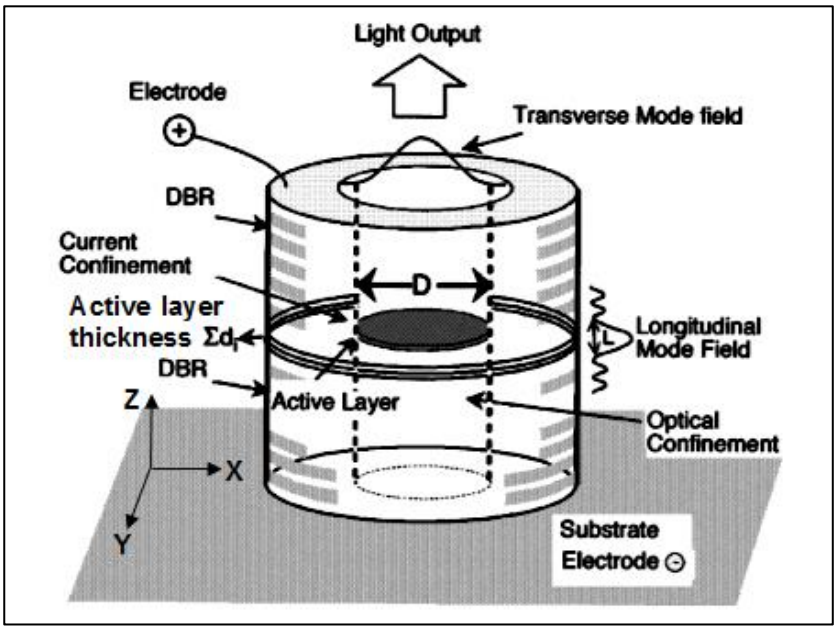

Fig. 1.1: Structure of VCSEL [24].

Our candidate for a spin laser is the Vertical-Cavity Surface-Emitting Laser (VCSELs) which was demonstrated first by Iga et al. in 1979 [25]. In VCSELs, the light emitting layer (active layer), its thickness denoted by $\sum d_i$ in Fig. 1.1, is sandwiched between two highly reflective mirrors (Distributed Bragg Reflectors, DBRs). Their reflectivity is typically higher than 99.9% in order to compensate for the short gain region which results in a low level of amplification achieved for a single round trip of the optical wave inside the cavity (see Fig. 1.1). The DBRs are constructed from alternate layers of semiconductors with high and low refractive indices. The majority of the VCSEL's structure is the DBRs with a short resonant cavity between them designed to support emission of one single-mode. The resonant cavity is perpendicular to the active layer. Therefore, the light is emitted perpendicularly to the layers and escapes through the surface of the DBR mirrors [26-28].

A particular type ‘close cousin’ of VCSEL is the vertical-external-cavity surface-emitting laser (VECSEL). The VECSELs originate from VCSELs and distinguish themselves from VCSELs by having an external cavity. In other words, a VECSEL utilises a half-VCSEL, consisting solely of the bottom DBR and active region. However, the top DBR of the VCSEL is removed and replaced by one or more additional external-cavity dielectric mirrors as an output coupler.

1.3.1 Polarisation behaviour of VCSELs

The polarisation of the VCSEL's emitted light is not well stabilised or predefined due to the geometry of a typical VCSEL. The fundamental transverse mode of the VCSEL can have two linear polarisations corresponding to the crystal axes due to the variation in the refractive index (propagation constant) of a VCSEL, resulting from the birefringence of the materials. The birefringence arises from strain and electro-optic effects in the material of the device [29-31]. Near threshold, one of the two linear polarisations corresponds to the lasing mode and the other to the subsidiary (non-lasing) mode. It is convenient to define the lasing mode positioned at the short wavelength side as the parallel mode, which is usually dominant, while the subsidiary mode at the long wavelength side is the orthogonal mode. Polarisation switching (PS) between these two linearly polarised (LP) modes takes place when the subsidiary mode becomes dominant. This switching is known as PS type I whereas the reverse action is known as PS type II. PS can occur due to the effect of different factors such as changing the pumping power, which causes changes in the phase anisotropy [32], and the application of external perturbation such as optical injection [33-37] or optical feedback [38]. Theoretically, the PS induced by these factors can be explained by the well-known Spin Flip Model (SFM) [39-41].

The control of the polarisation state of the VCSEL's emission has been extensively studied. Different techniques have been proposed to control the polarisation state either at the fabrication level [42-44] or by an external method such as optical injection from an external laser [33-37] or optical feedback [38]. However, the polarisation of the VCSEL can be controlled by manipulating the spin orientation of active region carriers, i.e. the angular momentum of the carriers involved in the optical transitions [45]. This in turn leads to an ability to manipulate the polarisation of the emission. Accordingly, spin injection into VCSELs via circularly polarised excitation is a promising means to modulate the laser polarisation without altering the carrier density or the output intensity. This property offers potential applications such as: reconfigurable optical interconnects, ultrafast all-optical switches, cryptography, and telecommunications with enhanced bandwidth.

1.3.2 Advantages and Applications of VCSELs

The structure of a VCSEL offers various features compared to a conventional Edge Emitting Laser (EEL) as follows:

1- A VCSEL supports single longitudinal mode emission due to the small cavity length (~1μm) [24].

2- The VCSEL device can be tested at wafer level before it is packaged which ensures low cost potential [46].

3- Circular and stable low-divergence output beams provide high fibre coupling efficiency and eliminate the need for corrective optics [28].

4- The VCSEL structure makes for easy fabrication and integration in two dimensional array configurations [46].

5- A VCSEL can have lower temperature sensitivity than an EEL [24].

6- The VCSEL normally emits light from the surface which gives easy alignment and packaging with other optical devices [46].
7- High-density arrays can be performed due to the low threshold currents in VCSELs [46].
8- VCSELs demonstrate good dynamic performance, such as low noise operation and high-speed digital modulation; they can be modulated in the GHz frequency range [25].

Therefore, conventional EELs are potentially going to be substituted by VCSELs in many applications, such as GHz Ethernet networks, fibre to the home links, local area networks (LANs), optical interconnects, and optical sensing as well as data storage and DVD reading [46, 47]. Since VCSELs will find more and more practical applications the use of spin injection to control their output polarisation could offer further potential enhancement of their functionality.

1.3.3 Quantum Confined Gain Media

Semiconductor structures can be classified based on the number of dimensions in which the charge carriers can freely move. There is no confinement in bulk material, where the carriers have a quasi-continuous energy spectrum and carriers are free to move in all three directions. Quantum confinement is realised when one or more dimensions become comparable with de Broglie wavelength. Quantum confinement decreases the available energy levels (density of states) and thus can increase the number of available carriers at a certain level. The density of states shows how many states that excited electrons of certain energies can occupy. To achieve confinement a narrow band-gap material is sandwiched between wider band-gap materials to produces potential barriers to spatially confine electrons and holes. The charge carriers

can be confined by the potential barriers in one, two and three dimensions, in the so-called quantum well (QW), quantum wire (QWR) and quantum dot (QD), respectively (see Fig. 1.2). Comparison between these types as well as the pros and cons of each one of them is beyond the scope of this thesis.

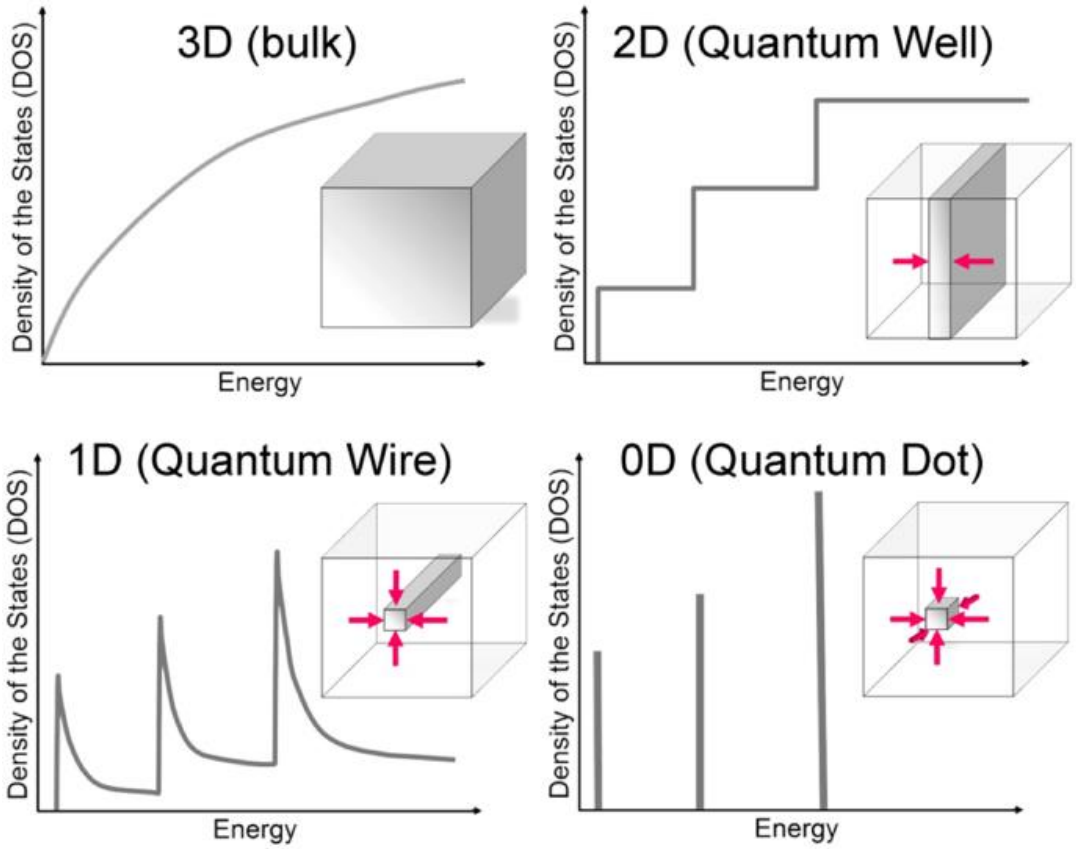

Fig. 1.2: Semiconductor structures with different quantum confinement and correspondent density of states, reprinted from [48].

Bulk structures are usually not preferred for spin devices due to the degeneracy between the light and heavy hole (hh) states in the valence band. Therefore, our main concentration is on the confined structures. Specifically, two types of quantum confinement structures will be used in this work and they will be briefly reviewed as follows:

1- Quantum Well (QW) active medium

A quantum well (QW) structure is fabricated by sandwiching a thin slab of semiconductor material between two layers of barrier material with a larger energy band-gap compared to the material in between. In this structure, one dimensional confinement is provided and the density of states becomes step-like. Carriers are free to move in the plane (2D) normal to the growth direction (z) but are quantized in the confined direction (along the growth direction). In the first part of this thesis, the nonlinear dynamics of solitary and optically injected 1300 nm dilute nitride QW spin-VCSELs will be studied and will be presented in Chapters 3, 4 and 5.

2- Quantum Dot (QD) active medium

Quantum Dots (QDs) are islands of nano-sized semiconductor material embedded in another semiconductor material possessing a larger band-gap. In a QD the charge carriers are confined in all 3D forming an atom-like energy spectrum consisting of separate levels. The motion of the carriers is restricted in 3D in the QDs which, in principle, prolongs their spin lifetime in comparison to bulk (three dimensional) and QW (two dimensional) structures. This is due to the strong quenching of spin relaxation via the D'yakonov-Perel (DP) spin scattering process [49-52]. Such an ability to preserve the spin states in the QDs enables the realisation of a QD spin-laser. Combining the potential of spin polarised injection with the advantages of a QD-based active region, such as low threshold, low chirp, reduced temperature sensitivity, and broad gain spectra [53], makes the QD spin-laser a very promising candidate device for a wide variety of applications. Therefore, the nonlinear dynamics of both solitary and optically injected 1300 nm QD spin-VECSELs will be investigated and presented in Chapters 7 and 8.

1.3.4 Dilute Nitride Materials

The dilute nitrides are a class of III-V semiconductors containing small amounts of nitrogen. GaInNAs is one such III-N-V compound, and was first proposed by Kondow et al in 1996 [54]. The first dilute nitride (GaInNAs) VCSEL operating at 1300 nm at room temperature (RT) was demonstrated in 2000 [55]. Incorporation of a small amount of Nitrogen (N) in conventional GaInAs semiconductors leads to decrease in both band-gap energy and lattice constant, which makes it possible to grow epitaxial layers emitting in the 1.3-1.55 m wavelength range [54]. Furthermore, introducing a small amount of N into GaInAs semiconductor results in attractive electronic and optical properties of the materials. These properties include temperature stability [54], which makes them good candidates for operation under optical pumping particularly if this is combined with undoped material since the latter simplifies the device growth processes [56]. Moreover, there is evidence to suggest that the spin relaxation time in these materials is long at RT due to the formation of defects slowing down the DP spin-relaxation mechanism [57, 58]. Therefore, this makes the dilute nitrides ideally suited for novel optically pumped spin-based devices.

1.3.5 The importance of 1300 nm Wavelength

The wavelength of 1300 nm is very attractive for use in communications since the attenuation of standard single mode optical fibre at 1300 nm is around 0.3 dB/km, while the attenuation at 850 nm is 2 dB/km [59]. The other attractive thing about 1300 nm is that the chromatic dispersion of the fibre is zero at this wavelength, so that signals of different wavelengths in this region travel at very similar velocities and there is minimum pulse spreading. Therefore, wavelengths in the 850-nm window are only useful for local-area networks (LANs), while the ones in the 1300 nm window are

suitable for metropolitan and wide-area networks (WANs) as their transmission distance extends up to 10 km [60]. Therefore, VCSELs emitting around 1300 nm are currently attracting much research interest.

1.4 The Objectives and Scope of This Project

In this work we aim to investigate the dynamical properties of both solitary and optically injected spin-V(E)CSELs. This is accomplished in several stages as follows:

1.4.1 Stability Study of Solitary Optically-Pumped QW Spin-VCSEL

The first aim was to investigate theoretically and experimentally the dynamics of 1300 nm QW spin-VCSELs as stand-alone lasers. Recent experimental investigations of these spin-VCSELs showed different stability behaviours. These include either stable behaviour [22] or regions of instability with polarisation oscillations in the range of 8.6 - 11 GHz under some conditions [61]. Thus, more experimental work and simulation to explore and predict the influence of a wider range of parameters around the observed behaviours is required.

1.4.2 Study of Optically-Injected QW Spin-VCSELs

The second aim of this project was to apply polarised optical injection to optically pumped 1300 nm QW spin-VCSELs and to gain a better understanding of the resulting dynamics and behaviour. Previous experimental works focused on the characteristics and dynamics of solitary spin-VCSELs. So the experimental dynamics of spin-VCSELs subject to polarised optical injection has not been received much attention. Furthermore, theoretical prediction conducted in previous work in our group revealed

that spin-VCSELs under polarised optical injection could exhibit rich nonlinear dynamics [62]. The goal of this work is thus to investigate the characteristics of the dynamics of telecom-wavelength spin-VCSELs at RT under different polarised optical injection conditions. This task will be divided into two sub-tasks as follows. The first one is to study the effect of the wavelength and power of optical injection on the output polarisation of the spin-VCSELs. The experimental results obtained from this work will be compared with theoretical ones using the SFM. The second sub-task will be to study the nonlinear dynamics induced by polarised optical injection into spin-VCSELs.

1.4.3 Demonstration of Telecom-Wavelength QD Semiconductor Disk Laser

The third goal of this thesis is concerned with the demonstration of a QD semiconductor disk laser (SDL) operating at RT and at the important telecom wavelength of 1300 nm. This will be accomplished by employing an innovative technique with a very simple and compact cavity using an HR-coated fibre as the top mirror. QD-SDLs operating in this wavelength range are few and most of them slightly below 1300 nm. In addition these lasers were realised using one or more external dielectric mirrors. Thus, by applying our simple cavity configuration including an HR-coated fibre and QD half-VCSEL sample, we aim to demonstrate a QD SDL operating above 1300 nm. This task basically was set to achieve the next goal.

1.4.4 Demonstration of Telecom-Wavelength QD Spin-VECSELs

The fourth goal of this study is to investigate the optical spin injection of a telecom-wavelength QD Vertical External Cavity Surface Emitting Laser. Most of the works on spin injection using circularly polarised photo-pumping reported in the literature were

performed on QW structures. Moreover, all these studies were applied to monolithic VCSELs at short wavelengths apart from those of our group on a 1300 nm spin-VCSEL [22]. However, one work reported spin injection in VECSELs at the wavelength of 980 nm with a QW active region [63]. Thus, our aim was to combine the potential of spin polarised injection with the advantages of a QD-based active region as already mentioned to demonstrate a QD spin-VECSEL at telecom-wavelength and at RT. Incorporating these two elements into a VECSEL, also brings benefits from the external cavity degree of freedom.

1.4.5 Study of Optically-Injected QD Spin-VECSELs

The final goal of this study is to investigate the dynamics of the optically injected 1300 nm QD spin-VECSEL. Reports of optical injection into VECSELs are extremely limited and the dynamics and behaviour of VECSELs under optical injection have not been explored. To the best of our knowledge, optical injection in VECSELs was only employed to achieve a single-frequency, Continuous-Wave (CW) and high output power optically pumped semiconductor laser [64]. Furthermore, this goal also included a comparison of the results for optical injection in a QD spin-VECSEL with those for a dilute nitride QW spin-VCSEL, with both devices operating near 1300 nm.

1.5 Thesis Outline

This thesis is organised as follows. Chapter 2 presents a literature review of optical spin injection in V(E)CSELs, the principles of operation for these elements, injection-locking phenomenon and QD-SDLs. The spin-dependent rate equation model, known as the SFM used to simulate and predict the behaviour of solitary and optically injected

spin-VCSELs is introduced. Following this chapter the thesis is divided into two parts based on the type of quantum confinement of the gain media used to achieve spin injection.

In the first part of the thesis we deal with the dynamics of solitary and optically injected 1300 nm QW dilute nitride spin-VCSELs as presented in Chapters 3, 4 and 5. In Chapter 3, the dynamics of the solitary spin-VCSEL are presented. The stability characteristics of solitary 1300 nm dilute nitride spin–VCSELs are theoretically and experimentally investigated.

Chapter 4 presents an experimental study of the evolution of the output polarisation ellipticity dynamics of the 1300 nm spin-VCSEL under polarised optical injection. This is achieved by means of a combination of polarised optical pumping and polarised optical injection. The extended SFM is used to simulate the measured dynamics showing a very high degree of agreement with the experimental findings.

Chapter 5 experimentally presents rich nonlinear dynamics of the optically injected 1310 nm dilute nitride spin VCSEL with different types of polarised injection. These dynamics are similar to the ones reported in the literature for optically injected conventional VCSELs.

The second part of this thesis looks into the dynamics of solitary and optically injected 1300 nm QD spin-VECSELs as presented in Chapter 6, 7 and 8. Chapter 6 focuses on the first RT QD-SDL operating at 1300 nm. The experimental setup used to demonstrate the 1300 nm QD-SDL using a very simple and compact laser configuration by employing a high reflection (HR)-coated fibre as the top mirror is presented.

Chapter 7 presents our investigation of the dynamics of a 1300 nm QD spin-VECSEL. The experimental setup of the optical pumping of the VECSEL sample is

first described. The measured results on the spin-injection are presented. Finally, the oscillatory dynamics of the solitary QD spin-VECSEL are presented.

Chapter 8 presents an experimental study of the evolution of the output polarisation ellipticity dynamics of the 1300 nm QD spin-VECSEL under polarised optical injection. In addition, this chapter presents experimental findings showing rich nonlinear dynamics of an optically injected 1310 nm QD spin-VECSEL with different types of polarised injection. These dynamics are similar to the ones reported in the Chapter 4 and 5 for optically injected QW spin-VCSELs.

Chapter 9 concludes this thesis. In this chapter the work that has been undertaken is summarised and notable results are restated. The direction of future research is also discussed.

CHAPTER 2: BACKGROUND AND LITERATURE REVIEW

Abstract:

In this chapter the background of this study is presented. The characteristics of spin-V(E)CSELs are first described as well as the state of the art of spin polarised V(E)CSELs. Recent experimental work on spin-injection is then reviewed and the model used for theoretical investigation of spin-VCSELs, the Spin Flip Model, is presented. The principles of optical injection are then discussed, along with a review of recent experimental investigations of the dynamics of optically-injected lasers. Finally, the operation principles of QD VECSELs are reviewed in addition to the recent achievements of QD VECSELs.

2.1 Introduction

This chapter will discuss the background of this study and the recent related works made so far in the spin injection phenomenon as well as injection locking (IL) in vertical cavity lasers. Firstly it describes the principles of spin injection into a V(E)CSEL with a review of recent experimental investigations of spin controlled V(E)CSELs. Recent experimental work on optical injection in V(E)CSELs is then reviewed. This will be followed by the basic rate equations model, known as the SFM used to predict and simulate the observed experimental results. The last section will briefly review the field of SDLs, also known as Vertical External Cavity Surface Emitting Lasers (VECSELs), with an emphasis on QD active media devices.

2.2 Spin Vertical Cavity Surface Emitting Lasers (Spin-VCSELs)

One important class of spintronic devices is spin-polarised light sources including both spin-polarised light-emitting diodes (spin-LEDs) and spin polarised lasers (spin-lasers). In conventional, electrically driven, vertical cavity semiconductor lasers the injected carriers are non-polarised so the numbers of spin-up and spin-down carriers are equal. Therefore, to realise spin polarised lasers, one has to create a population of spin polarised carriers. This can be done by injecting spin polarised carriers into the QD or QW active region of the laser as will be discussed below. However, while a general treatment of this situation requires consideration of both electron and hole spin relaxation processes, very dissimilar relaxation times can result in the effective dominance for one of these i.e. for electrons in spin lasers as argued in [14].

2.2.1 Spin Injection

In spin injection the spin polarised carriers are injected into the active region of the device to create an imbalance in spin-up and spin-down carrier populations that leads to circularly polarised emission [15]. In other words, the information carried by the spin polarised carriers is converted into circular polarisation information carried by the emitted photons [65, 66]. This occurs in accordance with the optical quantum selection rules, depicted in Fig. 2.1, where spin-up (spin-down) electrons recombine radiatively with spin-up (spin-down) hh generating light of left (right) circularly polarised photons [66]. Hence spin polarised electrons couple selectively to one of the two circularly polarised modes [67]. Consequently, the spin angular momentum of the carriers is converted into the angular momentum of the photons [68]. For this to be an efficient conversion process and in order to obtain a high output polarisation ellipticity (close to unity; net circular polarisation), spin-polarised carrier relaxation needs to be slow enough to ensure that they have not lost their spin orientation before radiative recombination occurs [15] as will be discussed later in this chapter. Thus, this makes the control of the output polarisation of the spin-based device possible and this makes spin-polarised light sources uniquely attractive for a number of applications from a practical point of view. However, these spin-devices are only attractive for applications if they operate at RT and without the need for large external magnetic field.

Fig. 2.1 shows the band structure for a quantum confined structures based on a direct band-gap semiconductor like GaAs which is reduced to a 4-level diagram around the Γ-point area according to Bloch states [15]. Each state is given by a quantum number m_j corresponding to the projection of the total angular momentum consisting of both orbital and spin momenta onto the positive z axis; perpendicular to the direction of confinement [14].

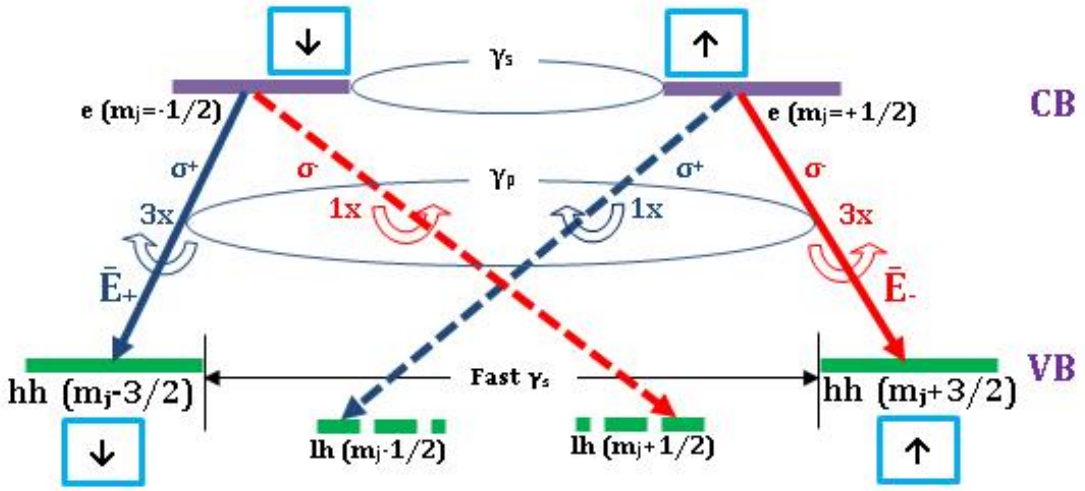

Fig. 2.1: Schematic band structure and optical selection rules of the transitions in a bulk and quantum confined based on a semiconductor like GaAs.

The two upper states consist of two electron states representing the s-like conduction band (CB), the lowest range of vacant electronic states, which includes two electron levels with opposite spins ($m_j = \pm 1/2$) [15]. The four lower states express the p-like valence band (VB), the highest range of electron energies in which electrons are normally present at absolute zero temperature, which are divided into two hh states with opposite spins ($m_j = \pm 3/2$) and two light hole (lh) states having also two opposite spins ($m_j = \pm 1/2$) [15]. The two distinct transitions for carriers with spin up and spin down are coupled by the spin flip relaxation process, denoted by γs. Hole spins usually relax much faster than electron spins. Therefore, spin-flip processes for holes in the VB are usually neglected. Also, the two orthogonally polarised fields of the VCSEL E_+ and E_- are coupled with the birefringence γ_p and the gain anisotropy γ_a. These parameters will be explained in more detail later in section 2.4. At the Γ-point in bulk direct band-gap semiconductor, the hh states are degenerate with the lh states while in the case of quantum confined structures, the hh and lh states in the valence band are non-degenerate with an energy difference between them, as represented in Fig. 2.1. The energy difference between lh and hh in quantum confined structure as shown in

Fig. 2.1 arises from quantum confinement and hence the spin degeneracy of the hh and lh states is lifted [15]. In either case the number of possible optical transitions is four. The allowed optical transitions between the conduction and valence bands must have $\Delta m_j = \pm 1$ (i.e. angular momentum is conserved) which is known as the first optical selection rule [15, 66]. Hence emission of right (RCP) and left circularly polarised (LCP) photons have a projection of their angular momentum on the direction of the wave vector, perpendicular to the QW or QD plane, equal, respectively, to Δm_j=-1 and +1 (in units of $\hbar$ which describes the quantization of angular momentum; where $\hbar$ is the reduced Planck's constant) [15]. A reduction of the quantum number (i.e. transition from m_j = -1/2 to m_j = -3/2) is linked to right circularly polarised light (σ+) while an increase (i.e. transition from m_j = 1/2 to m_j = 3/2) is linked to left circularly polarised emission (σ-) [69] as indicated in Fig. 2.1. For instance, assume that the electron (m_j =-1/2) state is fully occupied and has a spin polarisation of 100%. Then, the emitted light combines a part of right circularly polarised emission (σ+ = -1/2 to -3/2) and a part of left circularly polarised emission (σ- = -1/2 to +1/2). Transitions into the hh and lh states are determined by different probabilities due to the different geometries of the wave functions of the hh and lh states [14]. It turns out that the transition probabilities into the hh states are three times larger than into the lh states [14]. Hence in our example above it follows that the RCP part of the emission is three times higher than the left one [1,2,7]. The polarisation of the carriers can be defined as [7, 15]:

$$\varepsilon_n = \frac{n_+ - n_-}{n_+ + n_-} \qquad 2.1$$

where $n_\pm$ are the electron densities in the +1/2 and -1/2 electron state, respectively. The optical polarisation ellipticity is defined in terms of the intensities of the right $I(\sigma^+)$and left $I(\sigma^-)$ circularly polarised light fields as [7, 15]:

$$\varepsilon = \frac{I(\sigma^+) - I(\sigma^-)}{I(\sigma^+) + I(\sigma^-)} \qquad 2.2$$

Taking account of the ratio of 3 between transitions involving hh and lh states, it follows from equations 2.2 and 2.1 that [7, 14, 15, 70]:

$$\varepsilon = \frac{I(\sigma^+) - I(\sigma^-)}{I(\sigma^+) + I(\sigma^-)} = \frac{(n_+ + 3n_-) - (3n_+ + n_-)}{(n_+ + 3n_-) + (3n_+ + n_-)} = \frac{n_- - n_+}{2(n_+ + n_-)} = -\frac{\varepsilon_n}{2} \qquad 2.3$$

The minus sign indicates that the spin carriers are oriented in the opposite direction to the angular momentum of the incident photons. In the case of QW and QD active media when the spin degeneracy of hh and lh states is lifted it is a reasonable approximation to ignore transitions from the conduction band to the lh states because the latter will be much more likely to be vacant than the hh states in a light emitting device. With this approximation, degrees of circular polarisation (*DOCP*) of up to 100% can be achieved for a 100% injected spin polarisation [7, 14, 15, 70].

The second optical selection rule is that the energy difference between the initial and final states must equal the energy of the emitted or absorbed photon (i.e. energy is conserved) [14, 15, 69, 71].

According to the first optical selection rule, transitions leading to circularly polarised light are slightly complicated in the case of QW or QD and require a special geometry of the semiconductor [15]. In this special geometry, the carriers' spin orientation and the light emission have to be perpendicular to the QW or QD plane as shown in Fig. 2.2 [15]. Thus, V(E)CSELs seem to be the most appropriate concept for a spin-polarised laser at RT with respect to a conventional EEL because generally a V(E)CSEL is a laterally isotropic device with nearly circular symmetry which emits light perpendicularly to the active region [15, 69].

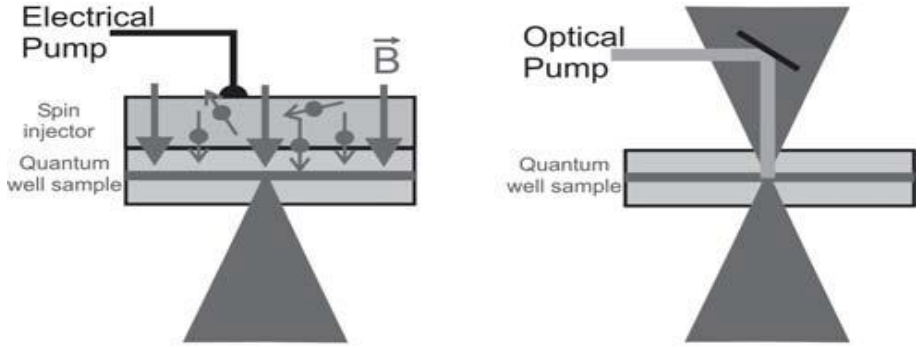

Fig. 2.2: Vertical geometry for the selection rules in case of quantum well structure for an electrically (left) and optically (right) pumping, reprinted from [69].

A spin-polarised V(E)CSEL can be achieved by optical pumping with circularly polarised light [67], by the electrical pump with spin-polarised current [21] or by a combination of both [72] in which each technique leads to production of spin-polarised carrier populations [14]. Schematics for the two main ways (electrical (left) and optical excitation (right)) are shown in Fig. 2.2. These two techniques will be discussed as follows.

2.2.2 Electrical pumping with spin polarised current

The spin polarised current can be generated by placing a ferromagnetic contact before the semiconductor, for example iron contacts, or injection of an unpolarised current through a spin-aligning layer somewhere in the vicinity of the contact of the spin-optoelectronic device in which a magnetic field is applied perpendicular to the active region plane of the device. However, this may produce a strong spin dephasing at the interface of the magnetic metal and the semiconductor due to conductivity mismatches which consequently leads to inefficient electrical spin injection. In addition these devices require high magnetic fields and low temperatures to achieve efficient circular polarisation degrees desirable and attractive for applications. Furthermore, efficient electrical spin injection is not a trivial task and different

techniques have been proposed to enhance the spin-injection efficiencies across ferromagnetic contact and semiconductor interfaces but are beyond the scope of this project and can be found elsewhere [14, 15, 69]. However, Table 2.1 summarises some of the electrically pumped spin-VCSELs demonstrated to date with their emission wavelengths (λ) and degrees of circular polarisation. The spin-VCSEL composition of the active region is shown as well as the structure orientation axis. The operation temperature and magnetic field (B) in tesla are also included. In addition, the spin relaxation rate γ_s which is defined as $\gamma_s = 1/\tau_s$, where τ_s is the spin relaxation time, is also given. In this table and the following one values with superscripted stars were either design dependant or found by fitting theory to experiment whereas values with superscripted dots were measured by polarisation-dependent time-resolved Photoluminescence (PL). It should be mentioned that all these lasers were electrically pumped with CW regim. Interestingly, all these electrically driven spin-VCSEL were demonstrated by the same group at the University of Michigan, USA.

Table 2.1: Summary of some of the electrically pumped spin-VCSELs demonstrated to date

Spin Injection	λ (nm)	Material	Confinement	Substrate Orientation axis	B (T)	T (K)	*DOCP* (%)	γ_s (ns^{-1})	Year	Reference
Electrical	945	InGaAs	QW	100	1	80	4.6	--	2005	[21]
	948	InGaAs	QW	100	2.2	50	23	3.3*	2007	[73]
	983	InAs/GaAs	QD	--	3	200	8	10*	2008	[74, 75]
	983	InAs/GaAs	QD	--	2	200	14	6.7*	2009	[76]

2.2.3 Optical pumping with circularly polarised light

The optical pumping with circularly polarised light is considered a very efficient way to achieve spin injection in V(E)CSELs since moderate optical pumping avoids the self-heating effect in the electrically-driven devices in addition to the complexity of the device design and growth. Spin injection via optical pumping can be done by illuminating the semiconductor with circularly polarised light either with pulsed (PW) or continuous (CW) wave excitation regime [67, 69, 77]. The CW pump maintains a constant population inversion leading to CW emission. However, the constant pumping may cause heating to the device which is undesirable in many applications. The pulsed pump enables the device to be pumped with a high power without significant heating. The latter may also be used for the VCSEL under hybrid electrical and optical excitation in case where the CW pump causes heating in the VCSEL which in turn leads to undesirable wavelength shift. After illuminating the semiconductor, the active region of the device then absorbs the circularly polarised photon and promotes electrons from the valence band to the conduction band with two requirements according to the optical selection rules. Spin-up and spin-down electrons produce greater gain for the left- and right-circularly polarised lasing modes, respectively. Therefore, if the gain of one lasing mode reached the laser threshold whereas the other did not, the emitted light polarisation degree would be expected to rise up to 100% even at very small spin polarisation in the active region [69]. Accordingly, the output polarisation is higher than the input polarisation and the output polarisation is controlled by the input polarisation [78]. This efficiently amplifies the spin information at RT due to the nonlinearity of the laser at threshold and without the need for an external magnetic field [15, 69, 77].

The first optically pumped spin-VCSELs have been reported by Hallstein et al [79] although the scope of that study did not include demonstrating spin controlled VCSELs, but rather focused on the feasibility of VCSEL modulation via spin manipulation. Subsequently Ando et al [80] reported optically pumped, circularly polarised lasing in a (100)-oriented sample of bulk GaAs VCSEL operating at 865 nm at RT; this is considered in most of the literature to be the first demonstration of a spin-controlled VCSEL. In the same year, Hendriks et al demonstrated the first CW optically pumped spin-controlled VCSEL, although the authors did not call it by that name [81]. Rudolph and co-workers demonstrated another important feature of a spin-VCSEL in which spin polarised pumping in AlGaAs/GaAs (100)-QW VCSELs reduced the laser threshold by up to 50% [67] and 33% [82] at 6 and 294 K, respectively, compared to conventional pumping with unpolarised electrons. In 2005, the wavelength of spin-VCSELs was extended from 830~865 nm, as in the previous studies, to 1000 nm when Hövel et al reported emission at 1000 nm with 100% degree of circular polarisation (*DOCP*) from a GaInAs QW spin VCSEL [78]. A CW pumping scheme was applied to the latter in 2007 by the same group and the DOCP was reduced to 75% due to the heating effect caused by the CW pump laser [77]. Furthermore, the same group has achieved a spin-VCSEL using a hybrid pumping technique where a commercial VCSEL was electrically driven up to 87% of its electrical threshold. Then, circularly polarised light from another PW laser was injected into the VCSEL to exceed the lasing threshold and to control its output polarisation ellipticity via spin injection [72]. Indeed, a *DOCP* of 100% was achieved under this hybrid pumping scheme [72]. High degrees of circular polarisation of the VCSELs' output which require a longer electron spin relaxation time in the active layers are essential to realise spin-VCSEL applications. However, the short electron

spin relaxation time (<100ps) at RT found in (100)-oriented QW limits these devices' performance. Nonetheless, (110) QW-VCSELs emerged as alternatives since longer electron spin relaxation time (τ_s) for devices with (110) substrate orientation has been demonstrated [83, 84]. The long τ_s offers major advantages for realising practical spin-controlled VCSELs. Optically pumped QW spin-VCSELs grown on a (110) substrate operating at 77K [85-87] and RT [86-88] have been reported. The spin relaxation time τ_s in the (110) QW spin-VCSEL was 2.8 ± 0.3 ns at 77 K which was almost 10 times longer than that in (100) QWs (230 ps at 70 K) whereas at RT, τ_s was 440 ± 50 ps for devices lasing at 865 nm and 917 nm, respectively [86]. No threshold reduction was found at 77 K whereas a slight reduction of ~10% was observed at RT [87]. The same group has also demonstrated circularly polarised lasing with a *DOCP* of 96% at RT that originated from a long electron spin relaxation time of 0.7 ns in a (110)-oriented GaAs QW spin-VCSEL [89]. Recently, our group successfully demonstrated CW optical pumping of a dilute nitride QW spin-VCSEL at long wavelength of 1300 nm [22]. A year after our group's report, the first demonstration of optical spin injection in a Vertical-External-Cavity-Surface-Emitting-Laser (spin-VECSEL) reaching a *DOCP* of 80% at RT was reported by Frougier et al [63]. In that work, a (100)-oriented InGaAs QW VECSEL sample (1/2-VCSEL) was pumped with a circularly polarised pump laser through a very complex cavity configuration to achieve spin polarised emission at a wavelength of 980 nm. During the first experimental stages of their work they encountered some challenges including the residual birefringence that locked the output polarisation of the VECSEL to a linear state even under 100% circularly polarised pumping. However, they managed to compensate this residual birefringence by employing a Faraday rotator inside the external cavity to overcome this issue and hence they proved the feasibility of their spin-VECSEL concept [63].

Finally, during this PhD we have reported the first demonstration of optical spin injection in a QD Vertical-External-Cavity-Surface-Emitting-Laser achieving a *DOCP* of 84% operating at the important telecom wavelength of 1300 nm at RT [90]. QD active media never have been reported previously in an optically pumped spin-V(E)CSEL although they have been used in electrically pumped spin-VCSELs.

Table 2.2: Summary of the optically pumped spin-V(E)CSELs demonstrated to date.

Spin Injection	λ (nm)	Pumping regime	Material	Confinement	Substrate orientation axis	T (K)	*DOCP* (%)	γ_s (ns^{-1})	Year	Reference
Optical	835	PW	InGaAs	QW	--	15	--	2•	1997	[79]
	865	PW	GaAs	Bulk	100	RT	82	25•	1998	[80]
	835	PW	InGaAs	QW	100	6	50	2•	2003	[67]
	850	PW	GaAs	QW	100	294	--	25•	2005	[82]
	1000	PW	InGaAs	QW	--	RT	100	25*	2005	[77, 78]
	865	PW	InGaAs	QW	110	77	94	0.4•	2009	[87]
	917	PW	InGaAs	QW	110	RT	42	2.3•	2009	[87]
	856	PW	GaAs	QW	110	RT	96	1.4•	2011	[89]
	853	PW	GaAs	QW	--	295	35	200*	2014	[91]
	857	CW	GaAs	QW	--	278	16	300*	1998	[81]
	1000	CW	InGaAs	QW	--	RT	75	25*	2006	[77]
	1300	**CW**	**GaInNAs**	**QW**	**100**	**293**	**73**	**105***	**2012**	**[22]**
	980	CW	InGaAs	QW	100	285	80	10*	2013	[63]
	1300	**CW**	**InAs/InGaAs**	**QD**	**100**	**293**	**84**	--	**2015**	**[90]**
Hybrid	853 / 830	PW	GaAs	QW	100	RT	100	200*	2008	[72, 91]

Table 2.2 summarises the state of the art of spin injection in V(E)CSELs through circularly-polarised optical pumping where the spin-V(E)CSELs presented in this thesis are shown in bold.

Optical pumping with circularly polarised light offers many advantages over its electrical pumping counterpart. One of these advantages is decreasing the cost of manufacturing the device. Thus, if the pump is incorporated with VCSEL, which is already a low-cost device, that would make it even more attractive for applications. Optical pumping also helps to avoid all the constraints arising from the electrical pumping requirements, such as the complexity of the device design and growth, focusing only on the optical properties of the device. Additionally, pumping a semiconductor laser with optical polarised light reduces its heating resulting in a good performance [14, 56].

Spin-VCSELs offer a number of merits over conventional VCSELs including improved light and polarisation stability and polarisation control [14], which leads to many potential applications including coherent detection systems, cryptography, magneto-optical recording, optical switches, reconfigurable optical interconnects and telecommunications with enhanced bandwidth [14, 15, 22, 69, 78, 89]. Spin- VCSELs also have been found to operate at a reduced threshold current [15, 67, 73, 82, 92, 93]. Moreover, they have the advantage of fast modulation dynamics [75, 94, 95]. Such devices will find applications in cryptography, reconfigurable optical interconnects and advanced optical switches and modulators [96, 97]. Therefore, different techniques have been experimentally used to achieve spin-VCSELs over a wide range of parameters and operating conditions [10].

2.2.4 Spin relaxation mechanisms

In order to realise spin-based V(E)CSELs with practical applications, spin polarised carriers must retain their orientation (e.g. imbalanced spin population) for a relatively long time sufficient to allow them to recombine radiatively and produce circularly

polarised emission. This needs to occur before the spin information is lost due to various spin relaxation mechanisms. In other words, a spin polarisation of the carriers corresponds to a non-equilibrium state, which is equilibrated by spin relaxation processes. There are four spin relaxation mechanisms for electrons in semiconductors which contribute to attain spin population equilibrium (e.g. lose spin population imbalance or more precisely the spin alignment). These spin relaxation processes are Elliot-Yafet (EY) [98], Dyakonov-Perel (DP) [99], Bir-Arhonov-Pikus (BAP) and hyperfine interactions. These mechanisms will be briefly reviewed below.

2.2.4.1 Elliot-Yafet (EY) Mechanism

The basis of the EY mechanism is the spin-orbit interaction. It leads to the coupling of electronic states with opposing spin system, so that the Bloch-states are not spin eigenstates, but a mixture of spin-up and spin-down states [98]. In the EY process, the spin relaxes by momentum scattering which is usually caused by boundaries, impurities at low temperatures or phonons at high temperatures. Boundaries, impurities, and phonons could all contribute to electrons transitions between spin up and spin down reservoirs via the spin-orbit interaction, resulting in spin equilibrium in the two electronic states. The spin flipping from up to down state or vice versa becomes probable each time the electron experiences momentum scattering leading to spin relaxation. Therefore, the spin relaxation rate through EY process for electrons in the conduction band is proportional to the electron momentum scattering. The EY is dominant in materials with narrower bandgap and larger spin orbit coupling and high electron momentum scattering rate [52, 100].

2.2.4.2 Dyakonov-Perel (DP) Mechanism

A very efficient spin relaxation mechanism was established in 1971 by Dyakonov and Perel [99]. It is based on the spin-orbit interaction in systems lacking inversion symmetry in which the spin up and spin down degeneracy of the conduction band is lifted. The absence of an inversion centre in semiconductors with zinc-blende (e.g. GaAs) structure and a possible structural asymmetry in a semiconductor heterostructure induce an effective magnetic field in the semiconductor due to spin-orbit interaction. Once the moving electron experiences this effective magnetic field, the electron spin precesses at a particular angle, thereby leading to spin relaxation. The spin relaxation time depends on the time between two scattering events whereas the magnitude and direction of the effective magnetic field depend on the electron momentum, where they change randomly after each scattering process. So, contrary to the EY process, the spin relaxes in between the scattering events. Thus, the more the scattering events, the less is the spin relaxation since the spin will have enough time to precess to cause a spin flipping between two scattering events. Thus, a change in momentum of the spin electron leads to changes the direction and magnitude of the effective magnetic field, and consequently to a change in precession angle. In addition, the faster the electron momentum scattering, the slower the spin relaxation rate which is opposite to the case of the EY process. The DP mechanism dominates in III-V and II-VI zinc-blende semiconductors as well as in middle to large bandgap semiconductors and at high temperatures for structures with adequately low hole densities. Furthermore, the DP mechanism provides a source of spin relaxation in many semiconductor heterostructures where asymmetric confining potentials are present, even for materials that may not have inversion asymmetry in their bulk form [52].

2.2.4.3 Bir-Aronov-Pikus (BAP) Mechanism

Bir, Aronov and Pikus BAP mechanism [101] is induced by the electron-hole exchange interaction, and it is present in semiconductors with a high concentration of holes. In these materials there will be exchange coupling with holes where a spin electron exchanges its spin with a hole and ultimately the total spin is preserved in the process. However, due to strong overlap between the electron and the hole in the valence band, holes lose their spin very fast due to strong spin-orbit interaction. In this case, holes act as a sink for the electron spin polarisation. As soon as the spin carriers get into this sink, the spin polarisation is lost almost instantaneously [7, 101]. In general, the BAP-mechanism increases at lower temperature because the electron-hole exchange interaction is reduced and it also increases for larger confining potentials in the case of QWs and QDs [52].

2.2.4.4 Hyperfine interaction with nuclear spins

The interaction between a nucleus and its surrounding environment is known as a hyperfine interaction. From the spin carrier point of view, the hyperfine interaction originates from exchange interaction between the angular momenta of electrons and nuclei in the lattice. The spin relaxation is affected by random fluctuations of the magnetic field of the atomic nuclei generated by the hyperfine interaction [7]. It is very weak for free electrons in metals and bulk semiconductors, and cannot cause effective spin relaxation. However, for free electrons in confined structures, such as QDs or donor bound electrons the spin dephasing is due to hyperfine interaction [102] since the electron wave function is spread over a region containing many nuclear spins. The hyperfine interaction can therefore flip electron spin causing spin relaxation. Furthermore, the hyperfine interaction increases in case of optical pumping [103-105].

2.3 Injection Locking

Injection locking (IL) of an oscillator (often known as the slave) to a stabilised one (known as the master oscillator) has been a subject of great interest for centuries. IL is the state when the frequency and phase of the slave, are locked via injection by another oscillator. This phenomenon applies to all kinds of oscillators ranging from mechanical oscillators to electronic oscillators and optical oscillators. It was first studied through the forced electrical oscillation by Poincare and Van der Pol [106]. The technique was later applied to electronic circuits by Adler [107] and upon Adler's successful demonstration a new era in communication was opened up. IL was demonstrated for the first time for lasers (optical oscillators) in 1966 with the HeNe gas laser [108], then in 1971 for dye lasers [109], and later extended to semiconductor lasers in 1980 when well engineered semiconductor lasers became available [110].

IL in lasers is the process when the Slave Laser (SL) oscillates with the same frequency, phase and polarisation as the Master Laser (ML). Optical injection generally is a technique which uses an external second laser (ML) to inject photons into the SL at a certain frequency close to the lasing frequency of the SL so that the injection is referred to as coherent (as opposed to, e.g., optical pumping where the injected frequency just has to be high enough to ensure that carriers are generated in the laser). The back reflection constituting bidirectional injection is usually prevented by an optical isolator which is included in the path between the two lasers. As a result, the SL is locked to the ML due to the coherent nonlinear interaction inside the cavity [111]. This technique is also used to synchronise a free running (slave) laser to a more stable (master) laser whose frequency purity is usually higher than the slave. The advantage of IL is that the SL characteristics can be modified drastically resulting in a better device performance. Furthermore, under optical injection, a semiconductor laser

is able to exhibit variety of nonlinear dynamics such as chaotic and bistable behaviours as well as stable locking phenomena which can be utilised in different applications such as receiver design in optical coherent communication [112].

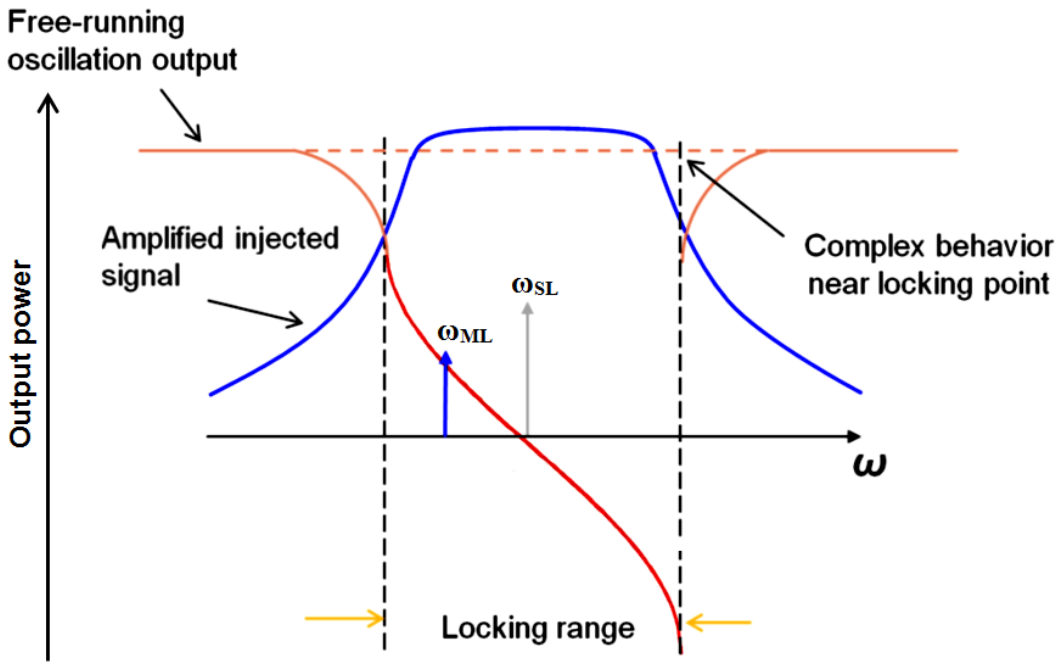

Fig. 2.3: Injection locking mechanism in a laser with the locking range on either side of the free-running frequency, reprinted from [113].

The IL of a laser is accomplished by injecting photons from an unperturbed signal with angular frequency ω_{ML} from the ML into the resonance of an SL having free running frequency of ω_{SL}. The detuning $\Delta\omega$ is defined as the difference between ω_{ML} and ω_{SL}. Consider the case when the ML is tuned over a range of frequency across the free running frequency of ω_{SL}, starting from a lower frequency away from ω_{SL} and ending at a higher frequency also far from ω_{SL} or vice versa. Initially, the output of the laser comprises both the injected ω_{ML} and the free running ω_{SL} signals. However, as ω_{ML} approaches ω_{SL} the ML signal will be amplified and its intensity will increase dramatically saturating the laser gain, switching off the free-running oscillation and leaving only one signal at ω_{ML}. At this point the ML reached the boundary of the locking range from one side as can be seen in Fig. 2.3. For further tuning, the SL will

follow the ML where the injection signal ML will be locking the SL in phase and frequency and the system will be controlled by the ML until the other side of the locking range. For any tuning beyond this boundary the ML will unlock the SL and they will operate simultaneously in two different frequencies.

Depending on the values of the pump power of the SL [114], the power of the ML and the frequency detuning $\Delta\omega$ between the ML and the solitary SL, the SL can operate as it would without the injection, exhibit stable or unstable locking to the ML, or produce various type of nonlinear dynamics [111, 115-117].

Using a VCSEL as the SL, optical injection was investigated for the first time by Pan et al. using an orthogonal optical injection scheme [33]. Following that pioneering work, optical injection in VCSELs has been extensively investigated and demonstrated in the short [118-123] and long wavelength [35, 36, 124-126] regions, in recent years. Moreover, when polarisation of the injected optical field is taken into account VCSELs' behaviours have been widely studied under polarised optical injection (parallel, orthogonal, [125, 127, 128] and elliptical [126, 129, 130]). However, reports of circularly polarised injection in conventional VCSELs are very limited. Experimentally, we are only aware of one recent work [131] reporting circularly-polarised injection into an 850 nm conventional VCSEL. In complementary studies, theoretical investigations on the effects of different polarised optical injection (elliptical, circular or linear) in conventional VCSELs have been reported by our group [129, 130]. Our recent demonstration of the first circularly polarised optical injection in a long wavelength (1300 nm) spin-VCSEL [132, 133] will be discussed later in this thesis.

Injection-locking of VECSELs, or SDLs, has not received much attention. To the best of our knowledge, optical injection in VECSELs was only employed to achieve a

single-frequency, CW and high output power optically pumped semiconductor laser [64]. However, in this thesis we will present the first study of circularly polarised optical injection into a QD spin-VECSEL.

The IL phenomenon of VCSELs has demonstrated enhanced frequency response [134], and an enhancement to the modulation bandwidth, when modulating either the SL [135] or the ML output [136-139] as well as an improvement in the performance in both analogue and digital communications applications, and high modulation rates [140]. Reduction in various laser properties such as spectral linewidth, noise [136], chirp and nonlinearities has also been reported for injection-locked VCSELs. An improvement of the performance of a directly modulated laser in the stable locking region has been reported in [141, 142]. Under a strong IL, optical injection helps greatly to increase the relaxation oscillation frequency (ROF) of the VCSEL without modifying the laser design. An enhancement in the ROF to > 50GHz by optical injection in 1.55μm VCSELs has been achieved in [135]. Most of the works in the literature show that the ROF enhancement increases by increasing the frequency detuning or the injection power [140, 141, 143]. Using the IL method, a combined configuration of a low-noise ML with poor high-frequency characteristics together with another laser, the SL, which is noisier with better high-frequency characteristics, leads to low noise and high speed operation [144]. This technique can be used in many applications ranging from very simple to highly sophisticated. For instance, from secure optical communications systems to all-optical logical gates [145], all-optical digital signal processing and wavelength conversion between telecom wavelength bands [146], in most optical network elements, parameter characterisation and for radio-over-fibre applications [147].

2.3.1 Nonlinear phenomena accompanying optical injection in VCSELs

The IL is a very important result of optical injection in which the VCSEL (SL) is synchronised (in phase and wavelength) to a stabilised laser (ML). The ability of a VCSEL to show periodic behaviour can be demonstrated under optical injection with the right injection power and frequency detuning. Depending on the values of these parameters, the VCSEL shows a rich variety of nonlinear responses and dynamics ranging from (PS), polarisation bistability (PB), limit cycle oscillation (P1), period doubling (P2), chaotic oscillation (C), frequency pulling and pushing effects, and four-wave mixing (FWM). These dynamics have been experimentally and theoretically found and analysed for short wavelength of 850 nm [119, 120, 123, 148-153] and for long wavelength of 1550 nm [125-127, 154] devices under orthogonal optical injection. Period one (P1) dynamics correspond to the beating between the ML and injected SL frequencies and appear as a periodic oscillation of the laser output at a single frequency and its harmonics. P2 dynamics appear as additional peaks on each side of the optical spectrum of the SL's lasing mode correspond to the first subharmonic of the P1 oscillation. Wave mixing which is characterised by the presence of additional weak side band peaks on one or both sides of the SL. The frequency splitting between the SL (ML) and the upper side band USB (lower side band, LSB) is equal to that one between the SL and ML and half that one between the SL and LSB (USB). Also, chaotic oscillations (C) correspond to a complex behaviour, with strong aperiodic oscillation of the SL output. Finally, PS and PB also have been reported in short and long wavelength conventional VCSELs subject to parallel [37] and orthogonal [33, 126, 151, 152, 155-158] optical injection. Optical injection of arbitrary polarisation was also reported theoretically by Al-Seyab et al. [130] and

experimentally by Hurtado et al [155] to produce PS in a 1550-nm VCSEL. Nevertheless, there has only been one experimental report of PS induced by circularly-polarised injection into two 850 nm VCSELs [131]. In this work, we will study these nonlinear dynamics, for the first time to the best of our knowledge, in a spin-V(E)CSEL subject to circularly polarised optical injection and compare it with the dynamics reported in the literature on conventional VCSELs [133].

2.4 Spin Flip Model (SFM)

Lasers in general are described and modelled theoretically based on a phenomenological gain model which utilises first-order rate equations to describe the carrier and photon densities within the cavity medium. Solving this type of equation determines the output intensity of the laser. These models have provided a very good description of EELs because they only emit a single LP mode. However, their functionality in describing VCSELs is not sufficient, particularly for explaining the PS behaviour. This arises because VCSELs emit two perpendicular LP optical modes due to the weak cavity birefringence, which leads to more complicated behaviour. Therefore, the necessity for a new model had arisen to understand the nonlinear dynamics of VCSELs [39].

San Miguel et al in 1994 proposed a new improved model to describe the PS behaviour in VCSELs which is now known as the SFM. Since then, The SFM has been extensively used to explain polarisation properties in solitary conventional VCSELs [40, 41], dynamics of optically injected conventional VCSELs [152, 159-161], dynamics of solitary spin-polarised VCSELs [77, 78, 162, 163] and recently dynamics of optically injected spin-polarised VCSELs [132]. In these studies, with appropriate modification of the pumping term, the SFM was used to model electrically or optically

driven conventional or spin VCSELs. In addition, when an additional external signal from an ML is injected into the cavity, the system retains the general form of the original equations, but with extra terms describing the effects of the optical injection as will be discussed below.

The SFM was simplified by neglecting the anisotropy and the birefringence leading to analytical results for threshold reduction and performance improvements [78, 164]. These approximations method also can be used to simulate QD spin-VCSELs by including transitions from the wetting layer to the dot levels [15, 73, 76]. More recently, our group modified the SFM to simulate optically pumped QD-VCSELs by incorporating rate equations which describe the carrier dynamics and field by ignoring the spin effects [165], into the key aspects of the SFM which itself includes the carriers' spin state, birefringence and the gain anisotropy (dichroism) [166, 167]. J.Rudolph and co-workers have applied a slightly complicated version of the SFM to model optically pumped VCSELs by allowing transitions from the barrier to the QWs [67, 82]. The SFM also has been used to model VCSELs with electrical spin injection by modifying the pumping term as presented in [15, 73, 76]. It has also demonstrated a good agreement with experimental results to model PW or CW optical pumping of spin-VCSELs [77, 168]. Assuming that the right and left circular polarised components have the same frequency and maintain a constant phase is a simple approach to numerically solve the rate equations in the steady state. This permits an investigation of the effect of the relevant parameters, the spin relaxation rate, the decay rate of the total carriers, the birefringence, the linewidth enhancement factor, the photon life time as well as the ellipticity and magnitude of the pumping on the VCSEL output [162]. This approach has explored the influence of the laser parameters on the dependence of output polarisation on the pump polarisation as well as the reduction in threshold

[162]. In the last few years, the SFM has been extended to include the injection terms in the rate equations which enables modelling solitary VCSELs subject to optical injection [159, 160, 169]. Moreover, the type of the polarised optical injection in addition to the influence of spontaneous emission noise have been taken into consideration to accurately explain the PS behaviour and the model also has been formulated to flexibly simulate any type of optically polarised injection [126]. In this project, the SFM rate equations describing the solitary optically pumped spin-VCSEL presented in [170] will be used to simulate and predict the observed experimental behaviours of our 1300 nm dilute nitride spin-VCSEL in its solitary state. In addition, the equations for the solitary spin-VCSEL as in [170] are combined in an extended version of the SFM with the terms for arbitrary polarisation of an optical injected signal in [75], to include polarised terms; to simulate the behaviour of optically injected spin-VCSELs as will be discussed below. The case of circularly polarised optical injection into a spin-VCSEL was explored first in [62], chapter 8, and this has never been published in a journal or a conference presentation.

2.4.1 SFM rate equations for solitary spin-VCSELs

The SFM has been derived from Maxwell-Bloch equations based on combining the classical electrodynamics that occurs within the laser with the quantum mechanics associated with the active material [39]. In the SFM the Maxwell-Bloch equations are reduced, after the material dipole polarisation is eliminated by considering that the VCSEL operates in single longitudinal mode with the fundamental transverse mode, to a set of rate equations describing the electron-hole transitions between conduction and valence bands for carrier densities associated with spin up and spin down as shown in Fig. 2.1. The transitions between the conduction and valence bands are governed by

the optical selection rules. First, the energy difference between the initial and final states must equal the energy of the absorbed photon (i.e. energy is conserved) [7]. Second, the total spin of the electron and hole must equal the angular momentum of the absorbed photon (i.e. angular momentum is conserved) [7]. These selection rules link the spin polarisation of the carriers and the polarisation of the emitted or absorbed light. In QWs, the heavy-hole band is energetically higher than the light-hole band and the transition probabilities into them are three times higher than those into the lh (see Fig. 2.1); hence, the transitions from the conduction bands to lh bands are neglected [69]. Therefore, different RCP and LCP emissions rise from the spin-up and spin-down lasing transitions between the conduction and valence bands.

In VCSELs, the total angular momentum (m_j) for electrons in conduction bands (CB) and hh in valence bands (VB) is respectively ±1/2 and ±3/2 as shown in Fig. 2.1. In a QW for circularly right (left) polarised light emission, E_+ (E_-), with transverse electric field in xy-plane, the transition between CB and VB must be $m_{jzVB} - m_{jzCB} = -1(+1)$, in other words from -1/2(1/2) to -3/2(3/2).

The schematic in Fig. 2.1 shows the spin flip relaxation process, denoted by γ_s couples the two distinct transitions for carriers with spin up and spin down. Also, the two orthogonally polarised fields of the VCSEL E_+ and E_- are coupled with the birefringence γ_p and the gain anisotropy γ_a which take different refractive indices along the two orthogonally crystallographic axes into account. The birefringence is strongly dependent on VCSEL structure [39-41, 171]. Based on this, the SFM equations are conventionally written in terms of the right- and left-circularly polarised complex fields, denoted, respectively by $\bar{E}_+$ and $\bar{E}_-$ as well as the their corresponding normalised carrier densities n_+ and n_-, associated respectively with spin-down and spin-up electron populations. The model takes into account the spin relaxation rate (γ_s) that couples

spin-up and spin-down carriers, the rates of birefringence (γ_p) and gain anisotropy (γ_a) which take into account the different (complex) refractive indices along the two orthogonal crystallographic axes and which couple the two orthogonally polarised fields. The spin relaxation of holes in the valence band is assumed to be instantaneous. The model also includes the conventional parameters used to describe semiconductor lasers when polarisation is ignored, namely the carrier recombination rate γ, the photon decay rate κ, and the linewidth enhancement factor α. In addition, normalised right- (RCP) and left-circularly polarised (LCP) pump components (η_+, η_-) are included to allow for polarised optical pumping. Writing the complex fields in terms of real and imaginary parts as $\bar{E}_\pm = E_{\pm R} + iE_{\pm I}$, the six rate equations for the optically pumped spin-VCSEL can be written as [170]:

$$\frac{dE_{+_R}}{dt} = \kappa(N + m - 1)(E_{+_R} - \alpha E_{+_I}) - \gamma_a E_{-_R} + \gamma_p E_{-_I} \quad 2.4$$

$$\frac{dE_{+_I}}{dt} = \kappa(N + m - 1)(E_{+_I} + \alpha E_{+_R}) - \gamma_a E_{-_I} - \gamma_p E_{-_R} \quad 2.5$$

$$\frac{dE_{-_R}}{dt} = \kappa(N - m - 1)(E_{-_R} - \alpha E_{-_I}) - \gamma_a E_{+_R} + \gamma_p E_{+_I} \quad 2.6$$

$$\frac{dE_{-_I}}{dt} = \kappa(N - m - 1)(E_{-_I} + \alpha E_{-_R}) - \gamma_a E_{+_I} - \gamma_p E_{+_R} \quad 2.7$$

$$\frac{dN}{dt} = \gamma[\eta_+ + \eta_- - (1 + |\bar{E}_+|^2 + |\bar{E}_-|^2)N - (1 + |\bar{E}_+|^2 - |\bar{E}_-|^2)m] \quad 2.8$$

$$\frac{dm}{dt} = \gamma(\eta_+ - \eta_-) - [\gamma_s + \gamma(|\bar{E}_+|^2 + |\bar{E}_-|^2)m] - \gamma(|\bar{E}_+|^2 - |\bar{E}_-|^2)N \quad 2.9$$

where the photon τ_p and electron τ_n lifetimes are embedded in the equations as $2\kappa = \tau_p^{-1}$ and $\gamma = \tau_n^{-1}$, respectively. The carrier densities are expressed in terms of normalised carrier variables as [163]:

$$N = \frac{n_+ + n_-}{2} \ , \ m = \frac{n_+ - n_-}{2} \qquad 2.10$$

$$\eta = \eta_+ + \eta_- \qquad 2.11$$

The polarisation pump ellipticity (P) is defined as [163]:

$$P = \frac{\eta_+ - \eta_-}{\eta_+ + \eta_-} \qquad 2.12$$

It should be mentioned that when $\eta_+ = \eta_-$ the SFM is equivalent to the model describing electrically driven conventional VCSELs (non-spin injecting contacts). The polarisation output ellipticity (ε) is given by:

$$\varepsilon = \frac{|\bar{E}_+|^2 - |\bar{E}_-|^2}{|\bar{E}_+|^2 + |\bar{E}_-|^2} \qquad 2.13$$

where the corresponding optical intensities are denoted by $I_+ = |\bar{E}_+|^2$ and $I_- = |\bar{E}_-|^2$.

2.4.2 SFM rate equations for optically injected spin-VCSELs

To simulate the behaviour of the spin-VCSEL under optical injection the extended version of the spin-flip model (SFM) reported in [130] with the inclusion of polarised optical pumping and the spontaneous noise terms is used. The six rate equations (2.4–2.9) presented in the previous subsection can be written in terms of the amplitude and phases of the polarised electric field components denoted respectively by $E_{x(y)}$ and $\phi_{x(y)}$.

$$\bar{E}_x = \frac{\bar{E}_+ + \bar{E}_-}{\sqrt{2}} \ ; \ \bar{E}_y = -i\frac{\bar{E}_+ - \bar{E}_-}{\sqrt{2}} \qquad 2.14$$

where

$$\bar{E}_x = E_x \, e^{i\theta_x} \ ; \ \bar{E}_y = E_y \, e^{i\theta_y} \qquad 2.15$$

E_x, and E_y represent the magnitude values of the LP x-LP and y-LP fields, respectively, while $ø_x$, and $ø_y$ represent their phases. The phases of the linear field in the last equation are given in an explicit form and include two terms as:

$$\theta_x = \omega_x t + \phi_x \;\; ; \;\; \theta_y = \omega_y t + \phi_y \qquad 2.16$$

Using the equations 2.14 – 2.16 the SFM rate equations 2.4 – 2.9 are converted to six ordinary differential equations (ODEs). The optical injection is modelled by adding the effect of the external field with amplitude E_{inj} , angular frequency ω_{inj} , and coupling coefficient $K_{inj} = \sqrt{\zeta f_d}$, where $\zeta$is the efficiency at which power from the injecting beam is coupled into the active region of the SL, and f_d is the longitudinal-mode spacing [111]. Additionally, ω_{inj} is used as the reference frequency, and the injection frequency detuning $\Delta\omega$ is defined as the difference between ω_{inj} and the frequency intermediate between those of the x-polarised (ω_x), and y-polarised (ω_y) modes of the solitary SL as shown in Fig. 2.4. Full derivation and conversion between the two sets of rate equations and the inclusion of ML effect can be found in [62]. The final SFM set of rate equations can be cast as:

$$\frac{dE_x}{dt} = \kappa\left[(N-1)E_x - mE_y(\sin\Delta\phi + \alpha\cos\Delta\phi)\right] - \gamma_a E_x + K_{inj}E_{injx}\cos\Delta_x + \sqrt{\beta_{sp}(N+m)}\xi_x(t) \qquad 2.17$$

$$\frac{dE_y}{dt} = \kappa\left[(N-1)E_y + mE_x(\alpha\cos\Delta\phi - \sin\Delta\phi)\right] + \gamma_a E_y + K_{inj}E_{injy}\cos\Delta_y + \sqrt{\beta_{sp}(N-m)}\xi_y(t) \qquad 2.18$$

$$\frac{d\phi_x}{dt} = \kappa\left[\alpha(N-1) + m\frac{E_y}{E_x}(\cos\Delta\phi + \alpha\sin\Delta\phi)\right] - \Delta\omega - \alpha\gamma_a + K_{inj}\frac{E_{injx}}{E_x}\sin\Delta_x \qquad 2.19$$

$$\frac{d\phi_y}{dt} = \kappa\left[\alpha(N-1) - m\frac{E_x}{E_y}(\alpha\sin\Delta\phi - \cos\Delta\phi)\right] - \Delta\omega + \alpha\gamma_a + K_{inj}\frac{E_{injy}}{E_y}\sin\Delta_y \qquad 2.20$$

$$\frac{dN}{dt} = -\gamma\left[N\left(1 + E_x^2 + E_y^2\right) - (\eta_+ + \eta_-) - 2mE_yE_x \sin\Delta\phi\right] \quad 2.21$$

$$\frac{dm}{dt} = -\gamma_s m + \gamma(\eta_+ - \eta_-) - \gamma\left[m\left(E_x^2 + E_y^2\right)\right] + 2\gamma NE_yE_x \sin\Delta\phi \quad 2.22$$

E_{injx} and E_{injy} are the field amplitudes for the injection signal whereas δ_x , δ_y correspond to their phases respectively. The two fields are related by the auxiliary angle θ_{p} given by:

$$E_{injx} = E_{injy} \tan\theta_p \quad 2.23$$

$$E_{injx} = E_{inj} \sin\theta_p \quad ; \quad E_{injy} = E_{inj} \cos\theta_p \quad 2.24$$

To simplify the equations without loss of generality, when the dominant mode of the VCSEL is parallel to the y-direction, we set the phase $\delta_y = 0$ and write $\delta_x = \delta$ which is included in the definition:

$$\Delta_x = \omega_y t - \phi_x + \delta \quad 2.25$$

The injection level (P_{inj}) is normalised to the linearly-polarised (LP) output of the solitary-VCSEL and can be calculated from the following equation:

$$P_{inj} = 10\log\left(\frac{|E_{inj}|^2}{|E_{sol}|^2}\right) \quad 2.26$$

where E_{sol} defined as [62]:

$$|E_{sol}|^2 = \frac{\eta}{1-\frac{\gamma_a}{\kappa}} - 1 \quad 2.27$$

The incident polarisation of the injection is completely described by two variables: the auxiliary angle θ_p and the phase difference δ between x- and y-components of the injected field. Thus, the state for right (left) circularly-polarised injection is achieved by setting the injection angle and the phase difference between x- and y- coordinates as θ_{p}= 45 and δ= 90˚ (-90˚) respectively.

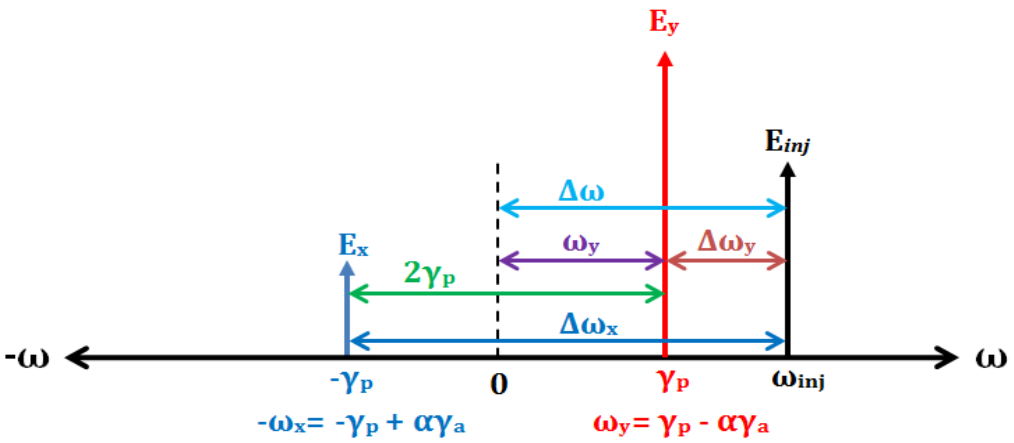

Fig. 2.4: Frequency diagram for the SFM with optical injection.

The angular frequency of the x-LP (y-LP) mode is denoted by ω_x (ω_y), respectively as shown in Fig. 2.4. The detuning between the master and slave can be calculated using the following relationship:

$$\Delta\omega = \omega_{inj} - \omega_{SL} \qquad 2.28$$

Based on which mode the injection takes place.

$$\Delta\omega = \omega_y + \Delta\omega_y \quad ; \quad \Delta\omega = \omega_x + \Delta\omega_x \qquad 2.29$$

$$\omega_x = \alpha\gamma_a - \gamma_p \quad ; \quad \omega_y = \gamma_p - \alpha\gamma_a \qquad 2.30$$

$$\Delta\phi = 2\omega_y t + \phi_y - \phi_x \qquad 2.31$$

$$\Delta_y = \omega_x t - \phi_y \qquad 2.32$$

In order to get PS in VCSELs we need a preponderant source of noise in the system and the source of noise in this system is the spontaneous emission and this is why it is needed in the model. The randomness of the spontaneous emission generates amplitude and phase fluctuations of the total optical field. Consequently spontaneous emission noise leads to the selection of the initial polarisation state. The effect of spontaneous emission noise has also been included by introducing a zero mean Gaussian noise source as in [128]. β_{sp} is the spontaneous emission factor ($\beta_{sp} \sim 10^{-5}$) [128] and $\xi_{x,y}$ are

Gaussian white noises of zero mean value. The rest of terms in the model are defined as:

$$\Delta = (\alpha\gamma_a - \gamma_p)t - \phi_y \quad 2.33$$

Equation (2.12) defines the polarisation of the pump. For example, setting P = 1 results in a right circular polarisation where η_+ is equal to the total pump η while η_- is zero. The reverse holds true when P = -1 which results in a left circular polarisation. Another example is that of zero spin polarisation (P = 0), as in a conventional VCSEL, which equates to two simultaneous right and left circular polarisation pumps corresponding to linear polarisation.

2.5 Quantum Dot Vertical External Cavity Surface Emitting Lasers (VECSELs)

Vertical External Cavity Surface Emitting Lasers (VECSELs) have been attracting attention from laser communities since their first report by Basov et al in 1965 [172]. These lasers are also known as SDLs. However, due to the poor external optical pumping capability only a few reports by the same group considered this type of laser for more than twenty years [173]. It was not until 1991 that Le et al [174] demonstrated an external-cavity n-type GaAs 135μm thick disk laser with 500 W peak-power output and 40% slope efficiency. The SDL was pumped by a Ti: Sapphire laser for pulsed operation [174]. Some years later, in 1997, Kuznetsov and his co-workers made the first demonstration of a practical SDL that was diode-pumped and operated at high power with high beam quality and operating wavelength near 980 nm [175]. This report was a changing point in the development of SDL's and since then they have received great interest, improvements and modifications.

Since the gain region of the SDL is thin, (typically a few microns), SDLs require high gain materials. Most of the SDL devices demonstrated had gain regions based on QWs but recently (QD)-based SDLs have also been developed in order to exploit their broad gain bandwidth in tunable sources. The first demonstration of a QD based SDL was reported in 2005 [176]. The authors claimed that the peak output powers exceeded 5 mW for emission near 1300 nm but no further details were disclosed. Three years later, more powerful QD SDLs were reported with output powers of 1.4 W at 1040 nm and 0.5 W at 950 nm for InAs/GaAs QDs and 300 mW at 1040 nm and 1210 nm for InGaAs QDs [177, 178]. In 2009, Schlosser et al achieved laser emission with peak wavelengths at 716, 729, and 739 nm, respectively, from three samples. They also reported a wavelength tuning from 729 to 755 nm of the third sample in addition to a maximum CW output power of 52 mW at 739 nm with threshold and slope efficiency of 220 mW and 5.7% respectively [179]. A high-power InP QD-based SDL with output exceeding 1.3W and operating at 655 nm has been demonstrated [180]. Albrecht et al have reported a QD-VECSEL with a continually variable emission wavelength from 1220 to 1280 nm [181]. Butkus et al have explored wavelength tunable regions centred on 1040, 1180 and 1260 nm [182]. All the active regions reported in the literature for wavelengths below 2 μm were based on InGaAs or InGaP QDs. However, emission wavelengths at 3.5, 4.3 and 5.6 μm from SDLs based on PbTe, PbSe and PbS, respectively, were demonstrated [183-185]. Table 2.3 summaries the state of the art of QD V(E)CSELs along with the emission wavelength and output power as well as the tuning range if presented.

Table 2.3: Some of QD-VECSELs reported to date with their wavelength tuning ranges and output power.

λ (nm)	Material	Tuning (nm)	P (W)	Year	Reference
655	InP	--	1.39	2013	[180]
655	InP	--	0.001	2014	[186]
716	InP	--	0.030	2009	[179]
729	InP	26	0.045	2009	[179]
739	InP	--	0.052	2009	[179]
950	GaAs	--	0.5	2008	[177]
960	InAs	--	0.143	2011	[187]
960	InAs	--	5.2	2011	[188]
970	InAs	--	1.05	2011	[187]
1003	InGaAs	60	6	2011	[182]
1040	InAs	--	1.4	2008	[177]
1040	InGaAs	--	0.300	2008	[177]
1040	InGaAs		0.280	2008	[189]
1040	InGaAs	45	8.41	2014	[190]
1059	InGaAs	--	0.027	2008	[191]
1180	InGaAs	69	6	2011	[182]
1180	InGaAs	37	7	2015	[192]
1200	InGaAs	--	2	2012	[193]
1210	InGaAs	--	300	2008	[177]
1250	InAs	--	4.65	2011	[194]
1250	InAs	--	3.25	2010	[195]
1260	InGaAs	25	1.6	2011	[182]
1280	InAs	--	0.400	2011	[181]
1300	**InGaAs**	**14**	**0.001**	**2015**	**[196]**
1300	InGaAs	--	0.225	2015	[197]
4300	PbTe	--	0.05	2014	[184]
5600	PbTe	--	0.100	2010	[183]

As it can be seen, there are relatively few reports on QD SDLs at the important telecom wavelength of 1300 nm and there is a need for further work in order to gain a deeper understanding of the potential of such devices. Thus in this work we have demonstrated the first observation, to the best of our knowledge, of an optically-pumped 1305 nm QD-SDL [196, 198] operating at RT with a very simple and compact cavity using an HR-coated fibre as the top mirror, as reported in [199, 200] for QW

active regions. The cavity design and arrangement can be seen in Fig. 2.5(b). In addition, our work has been followed by a report on a QD-based SDL emitting at 1.3 μm with an output power over 200 mW [197].

QD based SDLs within the long wavelength of 1-1.3 μm offer a number of novel features over other semiconductor lasers. These features are summarised in the following points [201]:

- 1-1.3 μm spectral range can be used in biophotonic applications
- Broad wavelength tuneability is a great feature that could be incorporated in compact and cheap tuneable laser sources like SDLs.
- (QD-SDLs) may provide important advantages such as low thresholds, high temperature stability, power scalability and broad gain bandwidths which could be exploited to improve the performance efficiency of some devices by making them cheaper, battery powered, more integrated and handheld. However, QD-SDLs can offer either lower threshold and high temperature sensitivity if very uniform dot is used or broadband gain if the dots are not uniform.
- QD-SDLs are successfully used as gain material for mode-locked VECSELs as well as absorber material in semiconductor saturable absorber mirrors (SESAMs) [191, 202].

The SDL usually combines a gain medium and a fully reflecting DBR and is optically pumped by a laser. An external cavity is formed by one or more dielectric mirrors and they control the fundamental mode operation. This cavity design is the most reported and common configuration to achieve an SDL. The simplest design is the straight cavity comprising a gain medium and bottom DBRs and an additional external mirror as the top mirror as shown in Fig. 2.5(a).

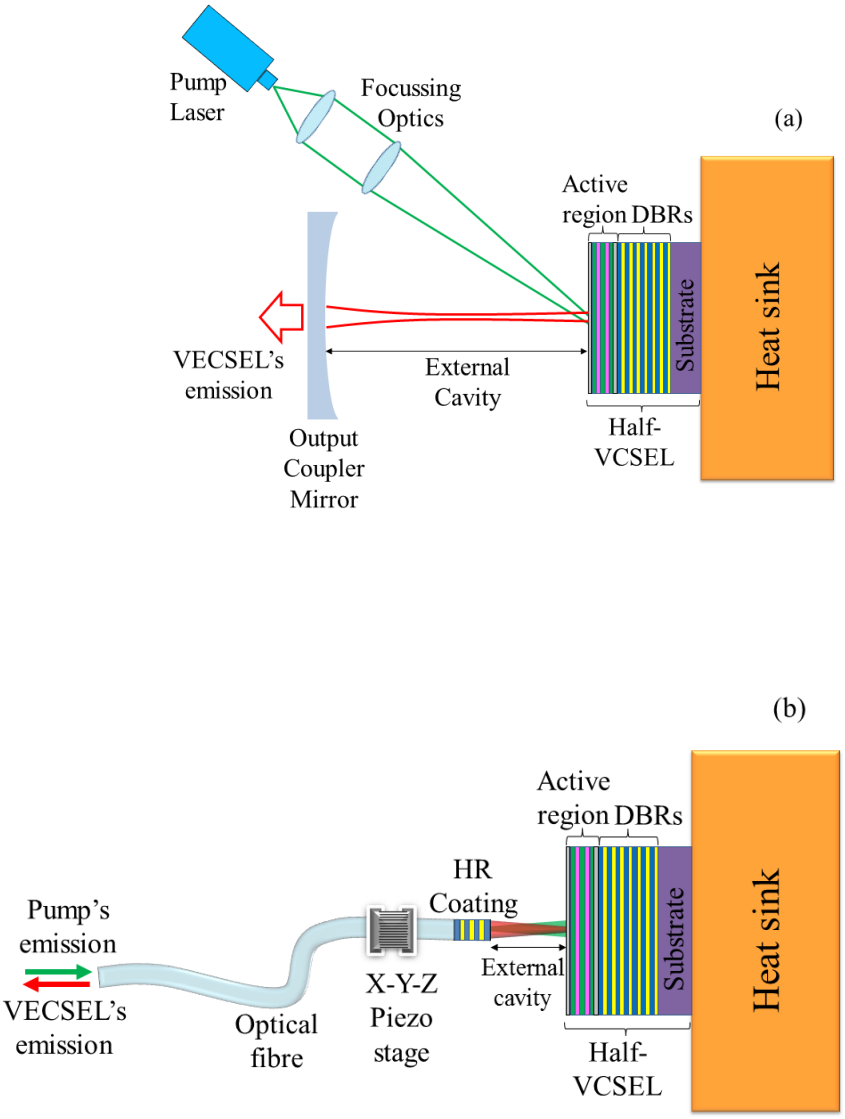

Fig. 2.5: Schematic drawing of the semiconductor disk laser with its main components in (a) a straight cavity configuration, (b) with an HR-coated fibre as the top mirror.

There are also more complex cavity configurations which involve multiple external mirrors or other components such as saturable absorbers, second harmonic generation crystals, birefringent filters or multiple gain elements. However, very few reports have employed a compact HR-coated fibre as the top mirror as shown in Fig. 2.5(b) [199, 200] instead of the dielectric mirror commonly used. In this work, we will use this configuration to achieve a QD-SDL at 1300 nm.

2.6 Summary

In this chapter, a detailed survey about spin injection, spin-V(E)CSELs, and optical injection phenomena in VCSELs and QD VECSELs was presented. The SFM and rate equations were given which describe the physics behind each characteristic and polarisation behaviour of solitary and optically injected spin VCSELs. The principles of operation for spin-polarised V(E)CSELs and QD VECSELs were discussed. An understanding of the physical mechanisms governing spin polarised V(E)CSELs operation is essential to the proper design and characterisation of these devices. The state of the art of spin-V(E)CSELs and, the achievements to date in QD VECSEL output power, wavelength coverage, tuneability were reviewed. Further chapters will concentrate on studying the nonlinear dynamics of solitary and optically injected QW and QD spin polarised VCSELs and VECSELs, respectively.

Part I

QW Spin-VCSEL

CHAPTER 3: INSTABILITIES OF QW SPIN-VCSEL[i]

Abstract:

In this Chapter the stability characteristics of solitary 1300 nm dilute nitride spin–VCSELs are theoretically and experimentally investigated. Rich dynamics and various forms of oscillatory behaviour causing self-sustained oscillations in the polarisation of the spin VCSEL subject to CW pumping have been found due to the competition of spin-flip processes and birefringence. Theoretical and experimental results in this chapter are in good agreement.

[i] This chapter is based on the papers:

1- Sami S. Alharthi, Rihab K. Al Seyab, Ian D. Henning and Michael J. Adams, ''Simulated dynamics of optically pumped dilute nitride 1300nm spin-VCSELs'', IET Optoelectronics, vol. 8, no. 2, pp. 117–121 (2014). [319]

2- S.S. Alharthi, I.D. Henning and M.J. Adams, ''Simulated dynamics of dilute nitride1300nm spin Vertical Cavity Surface Emitting Laser (VCSEL)'', Semiconductor and Integrated Optoelectronics (SIOE), Cardiff, UK, April 2013.

3.1 Introduction

In this chapter the stability characteristics of solitary 1300 nm dilute nitride spin–VCSELs are experimentally and theoretically investigated. The investigation has been done and presented for two different samples. Before presenting the general measured characteristics of the spin-VCSEL, the basic model used in the theoretical calculations is briefly explained. These calculations were done by numerically solving the ODEs of the SFM. Then the measured instability dynamics of the solitary spin-VCSEL are presented first and followed by the theoretical calculations. The experimental and theoretical dependence of the output polarisation ellipticity and oscillations on the pumping power and polarisation ellipticity is discussed and compared. Theoretical results are presented in 2D contour maps of pump polarisation versus magnitude of the optical pump. Rich dynamics and various forms of oscillatory behaviour causing self-sustained oscillations in the polarisation of the spin-VCSEL subject to CW pumping have been found due to the competition of spin-flip processes and birefringence. The measured results in this chapter are in good agreement with the theoretical calculations.

This study was motivated by the recent demonstration of the first CW (CW) optically-pumped dilute nitride spin-VCSEL operating at 1300 nm with output polarisation determined by that of the pump [22, 61], since the experimental investigations of these spin-VCSELs showed different stability behaviours. For stable behaviour, it has been demonstrated that the output polarisation ellipticity (ε) follows that of the pump (P) as reported in [22]. Moreover, polarisation oscillations have been observed in the range of 8.6 - 11 GHz under some conditions as reported in [61]. Thus, more experimental work and simulation to explore and predict the influence of a wider range of parameters around the observed behaviours is required.

3.2 Theoretical Model

The four-level (SFM) derived first by San Miguel et al in 1995 [39] and developed further in [41, 163] was used to theoretically investigate the characteristics and stability of optically pumped 1300 nm dilute nitride GaInNAs spin-VCSELs. The SFM rate equations are written in terms of right- and left-circularly polarised complex fields denoted by $\bar{E}_+$ and $\bar{E}_-$, respectively, with the corresponding normalised carrier densities n_+ and n_- associated with spin-down and spin-up electron populations, respectively. In this chapter, we follow the same approach reported in [126, 163, 170], to treat and solve the SFM rate equations. By writing the complex fields in terms of real and imaginary parts as $\bar{E}\pm = E_{\pm,R} + iE_{\pm,I}$, the SFM rate equations become;

$$\frac{dE_{\pm_R}}{dt} = \kappa(N \pm m - 1)(E_{\pm_R} - \alpha E_{\pm_I}) - \gamma_a E_{\mp_R} + \gamma_p E_{\mp_I} \quad 3.1$$

$$\frac{dE_{\pm_I}}{dt} = \kappa(N \pm m - 1)(E_{\pm_I} + \alpha E_{+_R}) - \gamma_a E_{\mp_I} - \gamma_p E_{\mp_R} \quad 3.2$$

$$\frac{dN}{dt} = \gamma[\eta_+ + \eta_- - (1 + |\bar{E}_+|^2 + |\bar{E}_-|^2)N - (1 + |\bar{E}_+|^2 - |\bar{E}_-|^2)m] \quad 3.3$$

$$\frac{dm}{dt} = \gamma(\eta_+ - \eta_-) - [\gamma_s + \gamma(|\bar{E}_+|^2 + |\bar{E}_-|^2)m] - \gamma(|\bar{E}_+|^2 - |\bar{E}_-|^2)N \quad 3.4$$

Full derivation of the above equations can be found in [62]. Numerical solutions for the full set of the SFM rate equations provide time series for the output power of circularly-polarised intensities $I_+ = |\bar{E}_+|^2$ and $I_- = |\bar{E}_-|^2$ in addition to the corresponding normalised carrier densities $N = (n_+ + n_-)/2$ and $m = (n_+ - n_-)/2$. These solutions can be presented as 2D contour maps in the plane of the normalised pump power $\eta = \eta_+ + \eta_-$ where η_+ and η_- are the right and left circularly-polarised normalised pump components and pump polarisation ellipticity P. The relationship between the normalised η and the measured pump power S is given by [203, 204]:

$$\eta = \frac{\frac{S}{S_{th}} - \frac{S_{tr}}{S_{th}}}{1 - \frac{S_{tr}}{S_{th}}} \quad 3.5$$

where S is the measured pump power and S_{tr}, S_{th} are its values at transparency and threshold, respectively whilst the pump polarisation ellipticity P is defined as:

$$P = \frac{\eta_+ - \eta_-}{\eta_+ + \eta_-} \quad 3.6$$

These maps represent the output in terms of circularly polarised intensities I_+, I_-, $I_{total} = (I_+ + I_-)$, and polarisation ellipticity (ε) as defined:

$$\varepsilon = \frac{|E_+|^2 - |E_-|^2}{|E_+|^2 + |E_-|^2} \quad 3.7$$

These maps have been used to predict and simulate the more general characteristics and stability behaviours for two samples of optically pumped 1300 nm dilute nitride GaInNAs spin-VCSELs used recently at RT under CW pumping by our group [22, 61] as will be discussed in the following sections.

3.3 Structure and design of the dilute nitride Spin-VCSEL samples

The design of the QW spin-VCSEL used in this thesis was based on that of the first 1300 nm optically pumped dilute nitride spin-VCSEL [22]. The dilute nitride (GaInNAs/GaAs) spin-VCSEL sample was grown by solid source MBE, equipped with a radio frequency plasma source for nitrogen incorporation. The 3-λ cavity of the device as shown in Fig. 3.1 consisted of five stacks of three QWs placed approximately at the antinodes of the standing wave pattern of the optical field. Each 7nm $Ga_{1-x}In_xN_yAs_{1-y}$ QW was located between 2 nm $Ga_{1-x}In_xN_yAs_{1-y}$ strain mediating layers (SMLs) shown in white lines in between the QWs in Fig. 3.1. The active region is then

enclosed between 16 and 20.5 GaAs/AlAs pairs forming respectively the top and bottom Bragg stacks (with reflectivities estimated as 99.2% and 99.8%).

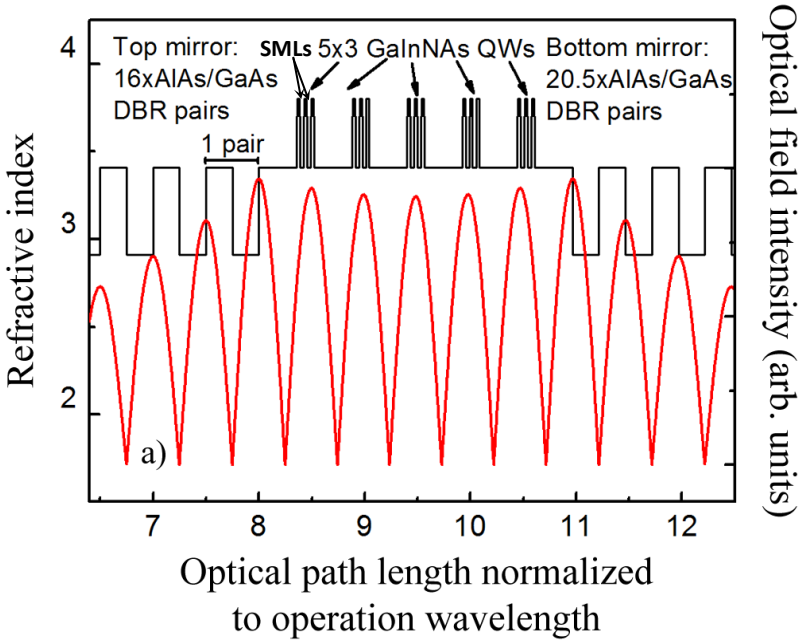

Fig. 3.1: Optical design of the dilute nitride spin-VCSEL structure [22].

The two samples used in this work come with different Nitrogen concentrations as illustrated below in Table 3.1.

Table 3.1: Material compositions of the QW and SML of Spin-VCSEL samples.

Sample	$GaIn_xN_yAs$ QW		$GaIn_xN_yAs$ SML	
	x	y	x	y
1	0.33	0.016	0.25	0.017
2	0.29	0.02	0.2	0.022

The demonstrated optically-pumped dilute nitride VCSEL [56] is a promising candidate for an optically pumped spin-VCSEL. The combination of GaInNAs/GaAs active regions with GaAs/AlAs DBRs is an attractive system for 1.3 μm VCSEL

devices [56]. In devices designed to operate under optical pumping, it has been shown experimentally that even small concentrations of Nitrogen in the active material lead to a significant increase of the spin relaxation time due to the formation of defects which slow down the dominant DP room temperature spin-relaxation mechanism [57, 205].

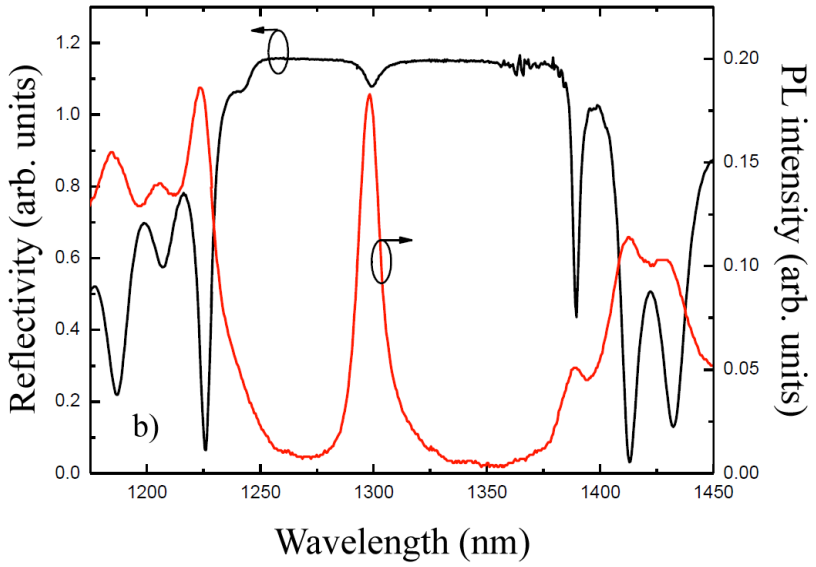

Fig. 3.2: Dilute nitride spin-VCSEL reflectivity and photoluminescence spectra [22].

Fig. 3.2 shows the RT PL and normalised reflectivity signal obtained at the Tampere University of Technology. The very strong PL peak at the cavity resonance gives rise to lasing at the expected wavelength around 1300 nm.

3.4 Experimental Setup

The experimental setup used to investigate the instability of the 1300 nm dilute nitride spin-VCSEL is shown in Fig. 3.3. The spin-VCSEL sample was pasted on a silicon wafer and held on a customised temperature-controlled copper mount. The spin-VCSEL sample was optically pumped by a commercial 980 nm pump laser via an isolator (IS) to prevent back reflections to the pump.

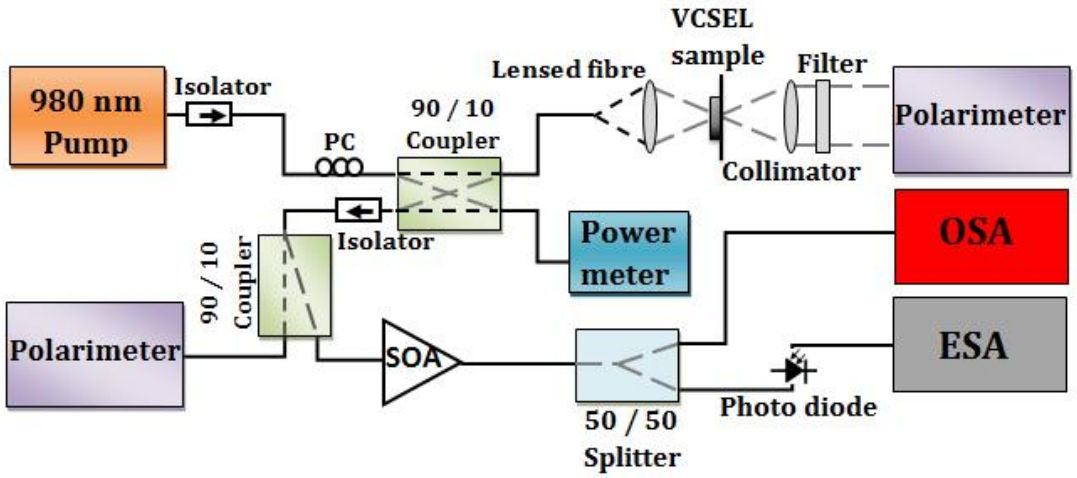

Fig. 3.3: Setup used for investigating the 1300 nm spin-VCSE instability. OSA: Optical Spectrum Analyser; SP: Splitter; IS: Isolator; SOA: Semiconductor Optical Amplifier; PC: Polarisation Controller; PD: Photodiode; ESA: Electrical Spectrum Analyser

The polarisation of the pump was controlled with a polarisation controller (PC). A 90/10 optical coupler was connected to the PC to direct 10% of the optical pump to a power meter to monitor the CW pumping power. In the meantime, the remaining 90% of the optical pump was focused onto the sample using a long focal-distance lens-ended fibre which was also used to collect the spin-VCSEL's output. A free-space polarimeter located behind the copper mount was used to measure the polarisation of the pump and that of the spin-VCSEL via an interchangeable filter (IF) placed before the polarimeter. This filter was used to block either the 980 nm pump or the 1300 nm spin-VCSEL emission as required. All the outputs were sent via the fourth port of the coupler to another 90/10 optical coupler which in turn sends 10% to an in-line polarimeter for polarisation analysis. However, the pump emission was blocked from travelling further in the setup by a 1300 nm IS placed between the 90/10 couplers. The 90% of the spin-VCSEL emission is amplified using a semiconductor optical amplifier (SOA) and then sent to a 50/50 splitter (SP). Finally, the SP equally splits the spin-VCSEL output between an optical spectrum analyser (OSA) and an Electrical

Spectrum Analyser (ESA), also known as radio frequency RF analyser, with a fast photodiode (PD). More details about all instruments can be found in Appendix B.

3.5 Results

Initial results showed that the optical spectrum of the spin-VCSEL wafers was relatively broad (~ 1nm) [22], hindering clear identification, directly from the OSA, of the polarisation dynamics of the solitary or optically-injected spin-VCSEL (see later in Chapters 4 and 5). This was thought to arise due to the large spot size from the lensed fibre which produced a large pumped area of the spin-VCSEL sample leading to multimode/filamentary behaviour. Thus lateral patterns were made on top of the spin-VCSEL samples in order to better confine and control the lasing area and in turn reduce the width of the optical spectrum of the device. More details about the patterns and how they have been done can be found in Appendix D. The patterns should only allow very small regions of the sample to be optically pumped. This may help to shrink the width of the optical spectrum which in turn enables us to identify any oscillatory behaviours occurring in the device directly by looking at its spectrum on the OSA.

Unfortunately, after these patterns have been applied on the samples, the resultant optical spectrum (see Fig. 3.4 (a)) of the patterned devices looks not much different from their bare counterparts (see Fig. 3 of [22]). However, the input-output characteristics have been considerably improved with a new threshold of 90 mW (see Fig. 3.4 (b)) instead of 158 mW (see Fig. 1 (c) of [132]) as will be discussed in the next sections. The threshold reduction is attributed to the focus of the optical pump on very small regions of the sample hence much more power coupled into the active region than before. Nevertheless, it should be noted that this reduction in the threshold is not entirely caused by the patterns, since a remarkable improvement and optimisation was

made to the experimental setup which led to a reduction in the threshold of the samples without patterns as will be shown in the next chapters. We believe that the threshold reduction improvement caused by the patterning was between 20 to 25% and the rest was due to improvement in equipment and alignment.

3.5.1 Experimental results

Using the experimental setup described in the previous section, the input-output curve has been studied and the stability of the 1300 nm dilute nitride spin-VCSEL at RT under CW optical pumping has been investigated. It should be noted that sample 1 always shows stable behaviour under the polarised pumping as reported in [22] for all the possible pumping powers at our lab. However, sample 2 on the other hand shows polarisation oscillations between the two circularly polarised modes [61]. These polarisation oscillations can be controlled by either the pump ellipticity (P) or the pump power (η) as will be discussed in the following sections. Hence, all the experimental results presented in this chapter have been conducted on sample 2, the 1300 nm dilute nitride ($Ga_{0.71}In_{0.29}N_{0.020}As_{0.980}$ QWs and $Ga_{0.80}In_{0.20}N_{0.022}As_{0.978}$ strain mediating layers) spin-VCSEL.

3.5.1.1 Input-output characteristics

Fig. 3.4(a) shows the optical spectrum of the dilute nitride spin-VCSEL emitting at 1297.5 nm. The input-output characteristic of the solitary spin-VCSEL is also illustrated in Fig. 3.4(b) with a pumping threshold of 90 mW when the sample was subject to right circular polarised (RCP) optical pumping.

It should be noted that the pumping power in this figure does not accurately reflect the optical pumping power delivered and coupled into the active region of the sample

since this pumping power has been measured and calibrated right after the lensed fibre by the head of the power meter while the sample was removed from its mount. Also, the optical power on the y-axis of the same figure reveals the normalised output power of the spin-VCSEL which is coupled back to the lensed fibre then sent to the rest of the setup. So, it has been definitely experiencing some losses but the general shape of the input-output curve is preserved. It should be mentioned that the actual output power of the spin-VCSEL in Fig. 3.4 before the normalisation was within 1 mW range.

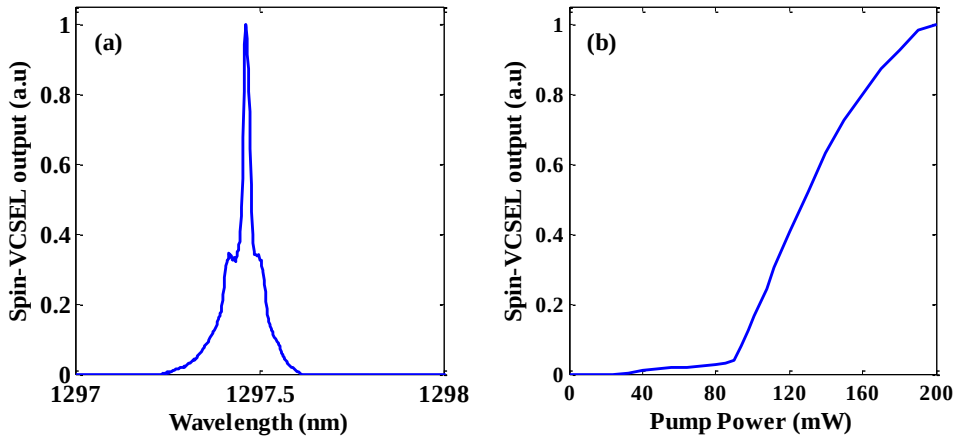

Fig. 3.4: (a) Optical spectrum of the spin-VCSEL. (b) The output power versus the pump power under RCP pumping for the solitary spin-VCSEL.

3.5.1.2 The impact of the pumping power on the polarisation oscillations of the spin-VCSEL

Fig. 3.5 presents different measurements of the RF spectrum of the intensity of the solitary spin-VCSEL for different pump powers at a constant pump ellipticity of 0.70. These spectra show peaks with frequencies between 8 and 15 GHz as the pump power was increased from 160 mW to 200 mW which reveals periodic oscillations in the output of the spin-VCSEL under polarised pumping. The RF power also becomes stronger with a well-defined peak as the pump increases for the same ellipticity. It should be mentioned that the RF spectra contain a pedestal of the noise within the first 5 GHz. These features are most likely attributed to the Relative Intensity Noise (RIN)

of the spin-VCSEL; this describes the instability and fluctuations in the optical power level of the laser and is defined as the noise power normalised to the average power level.

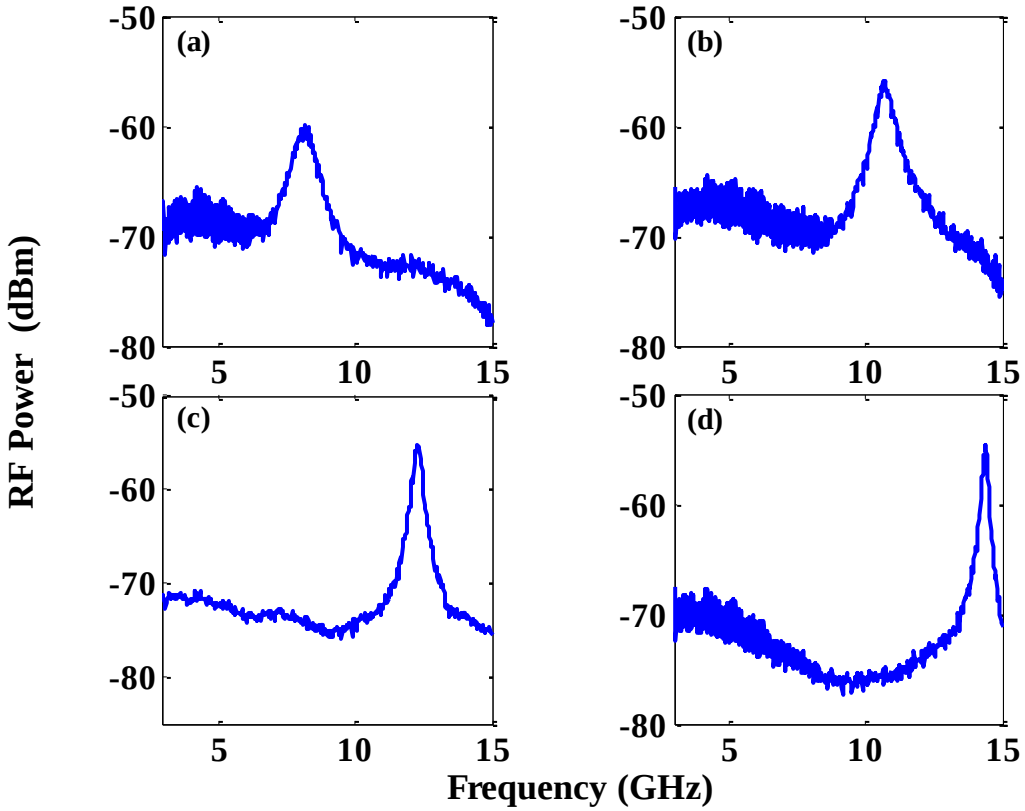

Fig. 3.5: RF spectrum of the output of the spin-VCSEL with pump ellipticity of 0.70 for increasing pumping power from (a)160, (b)170, (c)190 and (d)200 mW.

3.5.1.3 The impact of the pump ellipticity (P) on the polarisation oscillations of the spin-VCSEL

To see how the polarisation pump ellipticity (P) affects the polarisation oscillations, RF spectra have been taken for different pump ellipticity values ranging from left circular polarisation LCP (P=-1) to right circular polarisation RCP (P=1) at a constant pumping power . In addition, this step has been repeated for different pumping powers to investigate how the combination of the pump ellipticity and the pump power will influence the polarisation oscillations of the spin-VCSEL.

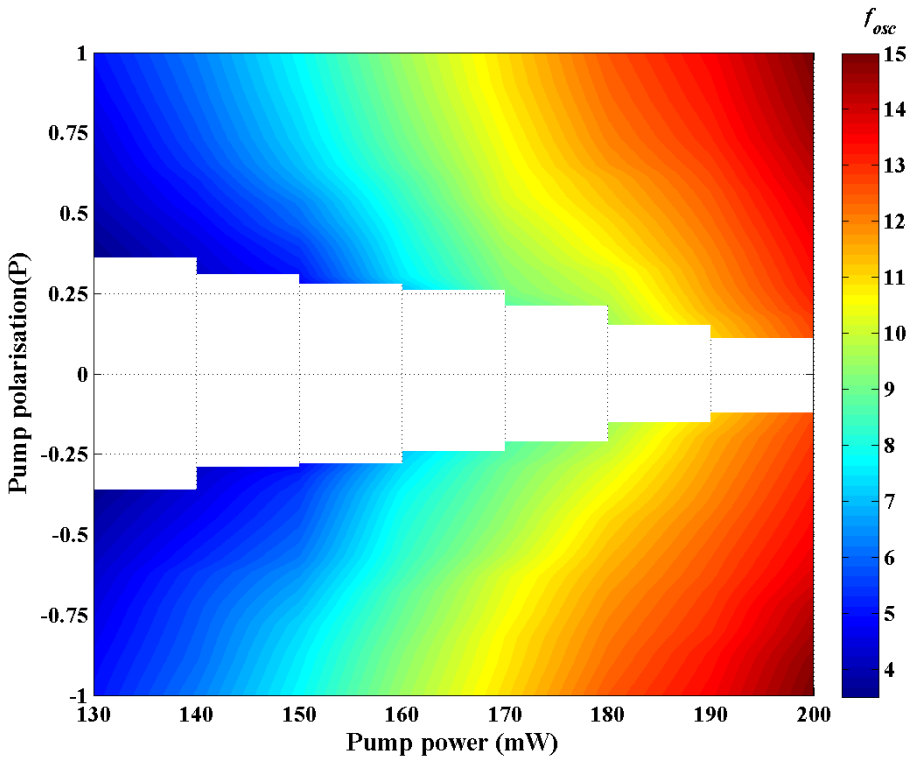

Fig. 3.6: Experimentally measured contours of frequency of oscillation in the plane of pump polarisation versus pump power.

Fig. 3.6 presents a contour map of the RF oscillation frequency of the spin-VCSEL in the plane of pump ellipticity versus pumping power. This figure shows that the polarisation oscillation can be controlled by changing either the pump ellipticity or pumping power. It should be mentioned that some points were interpolated for clarity. Periodic oscillations start appearing under pumping power of 130 mW for pump ellipticities greater or lower than +0.35 and -0.35 respectively. Under this level of pump the frequency of oscillation (f_{osc}) increases from 3.5 GHz to 5 GHz as the pump ellipticity increases from $|P|$ = 0.35 to 1 giving a range of frequencies of 1.5 GHz. This range of frequencies grows up until 2.6 GHz as the pumping power increases to 200 mW. The output ellipticity (ε) of the spin-VCSEL for pump ellipticities between -0.35 and +0.35 is stable. It is convenient to define this region where no polarisation oscillations were observed, as the stable region. The stable region shrinks gradually as the power of the pump increases from 130 mW to 200 mW until being only stable

between ellipticities of -0.08 and +0.08. As can be seen from Fig. 3.6 the frequency of oscillation f_{osc} can be tuned by choosing the proper pumping power and ellipticity values.

Since the appearance of such oscillations could be a result of optical feedback within the free space optical system of our setup, any changes in the alignments between the sample and the lensed fibre would impact on these oscillations. In contrast, our experimental observations reveal no effect on the existence of these oscillations related to any changes in the alignment which confirms that the system was not experiencing any optical feedback. However, the RF power of the oscillations slightly changes due to changes in the alignment as will be shown below.

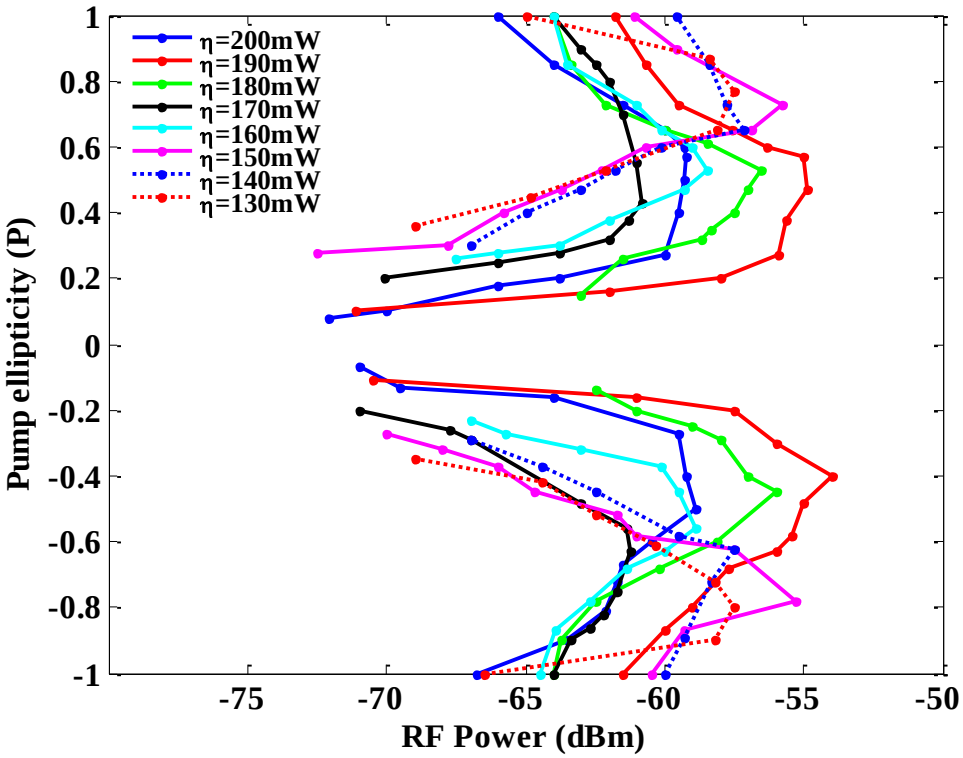

Fig. 3.7: Experimentally measured evolution of RF power with pump ellipticity.

Fig. 3.7 shows the measured RF power as a function of the pumping ellipticity curves for the oscillations reported in Fig. 3.6 at different pumping powers. It reveals that under a constant pumping power the RF power increases until reaches its maximum, which is found approximately around $|P| = 0.6\sim0.8$, and then decreases as

the pump ellipticity is changed. The RF power also increases for the increasing pump at constant ellipticity but, as mentioned above, there are slight changes when the alignment between the sample and the lensed fibre changed. This is most likely caused by changes in the coupling between the sample and the lensed fibre since each two successive measurements taken at the same session under the same condition, e.g. alignment; show the increase in RF power as the pump increases.

3.5.1.4 The impact of the polarisation and the power of the pump on the output polarisation ellipticity

The output polarisation ellipticity (ε) as a function of that of the pump (P) for sample 2 is shown in Fig. 3.8(a-b) under 130 mW and 150 mW pumping power, respectively.

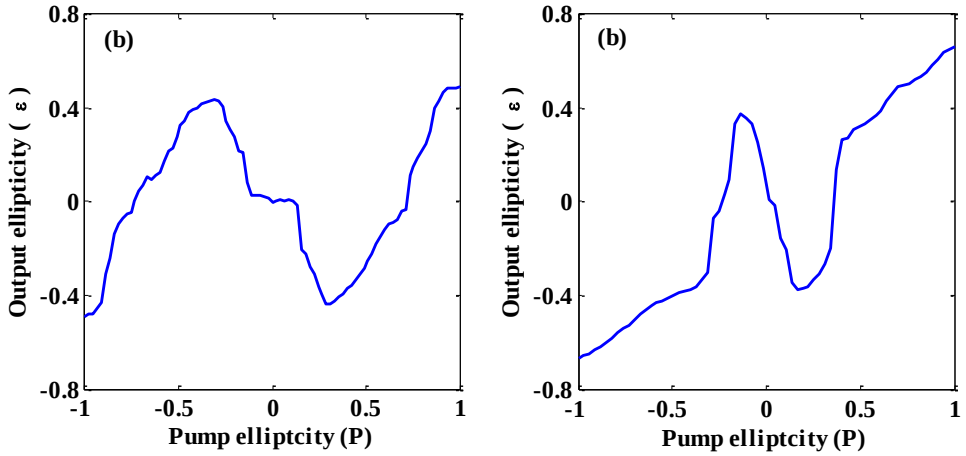

Fig. 3.8: Spin-VCSEL ellipticity as a function of the pump ellipticity for pump powers of : a) 130mW, b) 150mW.

This figure demonstrates that the output polarisation ellipticity (ε) follows that of the pump at the beginning and then at $|P|$=0.40 in Fig. 3.8(a) and $|P|$=0.25 in Fig. 3.8(b) it switches to the reversed sign. It is interesting to note that the region of negative slope at some points has relatively high output polarisation degrees for lesser degrees of the pump polarisation which is an indication of polarisation and spin

amplification. This region also shrinks and becomes steeper as the pumping power approaches higher values. It should be noted that the output ellipticity (ε) experiences polarisation oscillations from the beginning before switching to the reversed polarisation state where it is stable within that region. But due to the fact that the polarimeter was averaging the ellipticity values within this region, it appears in the normal shape.

3.5.2 Theoretical results

In order to see the whole picture of the dynamic behaviour of the spin-VCSELs, 2D contour maps in the plane of pump power η and pump polarisation P have been calculated for the 2 spin-VCSEL samples using SFM parameters as reported in [22, 61]. These parameters have been found by fitting experimental data and from this the model parameters have been chosen as can be seen in Table 3.2. The value of γ used here is consistent with the high quality of the active material and with the recombination rates reported from pressure and temperature measurements in 1300 nm GaInNas VCSELs [206]. A relatively fast spin relaxation rate was used here in comparison with other studies where values of γ_s usually range from 1 to 100 ns^{-1} [15, 89, 162]. Measured values of the spin relaxation rate for as-grown GaInNAs QWs in the literature are typically in the range from 0.5 ns^{-1} [57] to 13 ns^{-1} [207]. However, a large increase in relaxation rate has been reported after annealing [57]. Since the active region of a VCSEL is effectively annealed during the growth of the top Bragg stack, this may result in an increased spin relaxation rate of the order of that used in the simulation here. Stable operation with a fast spin relaxation rate requires a slow birefringence rate as dictated by the conditions for linear polarisation stability derived in [41]. While a closer agreement between the experimental and theoretical ellipticities

was found with lower values of γ_s and a large γ_p, in such a case PS was predicted with linear pump polarisation which was in disagreement with the experimental data. Hence, this justifies the use of lower value for γ_p for sample 1.

Table 3.2: SFM parameters for 2 samples of GaInNAs spin-VCSELs.

Parameter	Description	Sample 1 [22]	Sample 2 [61]
α	Linewidth enhancement factor	2	5
γ_p	Birefringence rate	5 rad/ns	34.5 rad/ns
γ_s	Spin relaxation rate	105 rad/ns	105 rad/ns
γ_a	Gain anisotropy (dichroism)	0 GHz	0 GHz
γ	Electron density decay rate	1 GHz	1 GHz
κ	Photon decay rate	250 GHz	250 GHz

It has been found that the values of α and p have a strong effect on the stability of the output ellipticity of the spin-VCSEL [62]. This effect specifically can be seen in the appearance of periodic oscillations in terms of the dynamic type and frequency of such oscillation [62]. Therefore, α was selected equal to 5 to get an oscillation for $0.2 < |P| < 1$ as in the experiment. When $\alpha < 5$ the oscillation occurred over a different range of P, as when $P = \pm 1$ only stable behaviour was found. While, γ_p has an effect on the dynamics and frequency of the oscillation. Using $\gamma_p = 11\pi$ rad/ns, leads to P1 oscillation when $0.2 < |P| < 1$ (as found in the experiment) with oscillation frequency f_{osc} decreasing from 16 GHz to 13.6 GHz as the pump ellipticity was reduced from $|P| = 1$ to 0.2 (see Figs. 1(d-e) of [61]). The theoretical value of f_{osc} is higher than the experimental by 5 GHz, however the frequency reduction range with P in both results was exactly the same (=2.4 GHz) as shown in Figs. 1(d-e) of [61]. In fact, using $\gamma_p < 11\pi$ rad/ns, can reduce f_{osc} further, however this will change the dynamics of the

oscillation from just P1, to P1, P2, and C dependent on the value of *P*. This was not observed in the experiment [62].

3.5.2.1 Influence of the SFM parameters on 1300nm GaInNAs spin-VCSEL sample (1)

The steady state values and polarisation properties of the first sample of 1300 nm dilute nitride ($Ga_{0.67}In_{0.33}N_{0.016}As_{0.984}$ QWs and $Ga_{0.75}In_{0.25}N_{0.017}As_{0.983}$ strain mediating layers) spin-VCSEL have been calculated and presented as 2D contour maps in the plane of (η-*P*) for the normalised circularly polarised output intensities I_+, I_-, $I_{total} = (I_+ + I_-)$, and polarisation ellipticity (ε) in Fig. 3.9 (a-d) using the same parameter set as summarised in Table 3.2 under sample 1 and reported in [22].

The simulated results demonstrate that the polarisation of the output of the optically pumped spin-VCSEL can be controlled by the polarisation of the optical pump as can be seen in the contours in Fig. 3.9. This is in good agreement with the predicted results reported in [163] and with the experimental results demonstrated under pulsed pumping in [72, 77, 82]. Colours in the map indicate the steady-state values of the normalised output intensities and the output polarisation ellipticity (ε) when the spin-VCSEL is stable (see the colour bars for the values). It is clear from Fig. 3.9(a) and Fig. 3.9(b) that when the spin-VCSEL is fed with right $P = +1$ (left $P = -1$) circularly polarised pump, the right I_+ (left, I_-) circularly polarised mode of spin-VCSEL appears as the dominant mode while the other mode I_- (I_+) is off. These 2 maps show that at a certain pump power when I_+ (I_-) is the dominant mode, its intensity decreases by reducing (increasing) the pump ellipticity from $P = +1$ to $P = -1$ ($P = -1$ to $P = +1$) and the reverse holds true for the nonlasing mode I_- (I_+). It is also noted from Fig. 3.9(b) (Fig. 3.9(a)) that the threshold of the nonlasing mode I_- under RCP pump *P*

= +1 (I_+ under LCP pump P = -1) is delayed until about twice the threshold (η = 2) of the lasing mode.

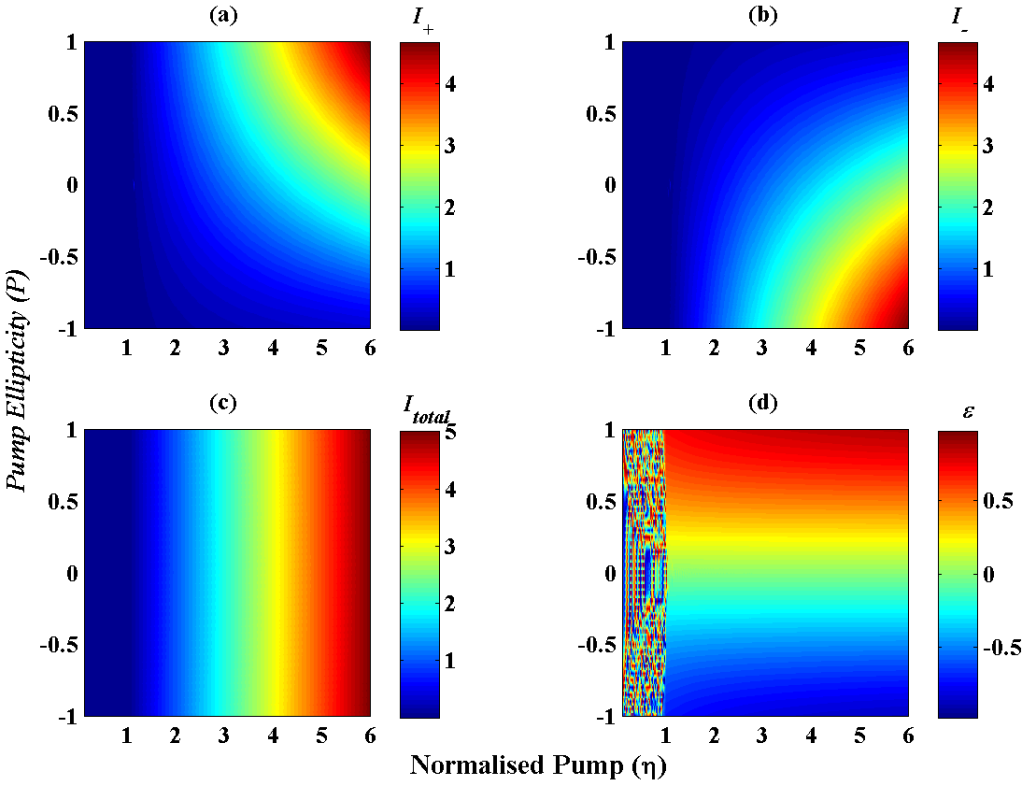

Fig. 3.9: Calculated 2D contour maps for 1300nm dilute nitride spin-VCSELs (sample 1) normalised output intensities I+ (a), I- (b), Itotal (c) and output polarisation ellipticity ε (d) using SFM parameters as in [22].

Fig. 3.9(c) indicates that the laser is stable and the total output intensity appears approximately independent of the pump ellipticity P with linear proportionality to the pump intensity η. In fact, the total intensity I_{total} is slightly affected by the pump polarisation when $|P| > 0.7$ but this effect is not noticeable on the scale of this map and would be much clearer in the output polarisation ellipticity (ε) map. The output polarisation ellipticity is presented in Fig. 3.9(d). This contour demonstrates that the output polarisation ellipticity follows that of the pump. The randomly-coloured area in this map refers to the spontaneous emission below threshold where the VCSEL is not lasing. It can be seen from this map that by increasing the pump power, the value of the

output polarisation ellipticity (ε) increases then saturates and a high degree of output circular polarisation is achievable on this spin-VCSEL at high pump powers when $|P| = 1$. These simulated results show very good agreement with the experimental results presented in [22].

3.5.2.2 Influence of the SFM parameters on 1300nm GaInNAs spin-VCSEL sample (2)

In this subsection, we present the same contour maps for the 1300 nm dilute nitride ($Ga_{0.71}In_{0.29}N_{0.020}As_{0.980}$ QWs and $Ga_{0.80}In_{0.20}N_{0.022}As_{0.978}$ strain mediating layers) spin-VCSEL where polarisation oscillations have been observed in the experimental work. Fig. 3.10(a-d) shows the calculated contour maps for the variables I_+, I_-, I_{total} and the output polarisation ellipticity (ε) using SFM parameters as summarised in Table 2.1 under sample 2 and reported in [61]. The coloured regions in the maps indicate the steady-state values of the normalised intensity and the output polarisation when the spin-VCSEL is stable while the white region indicates the region of instability where the spin-VCSEL is unstable and shows polarisation oscillations caused by the competition between spin relaxation processes and birefringence as first predicted theoretically in [163] and studied further in [170]. Contours in Fig. 3.10 show completely different shapes and behaviours from those simulated for sample 1. These differences arise from slight changes in the parameter values of the birefringence (γ_p) and linewidth enhancement factor (α). Changes in the birefringence lead to changes in the frequency of the oscillations where the frequency f_{osc} increases linearly with γ_p for a certain value of α hile changes in the linewidth enhancement factor influence the peak- to-peak amplitude of the RCP oscillatory components [62]. These changes depend on the values of γ_p and the other parameters of the SFM and more information about this influence can be found in [62]. Variations in birefringence and α-factor

values are attributed to strain and the fundamental physical processes at work in the device [163].

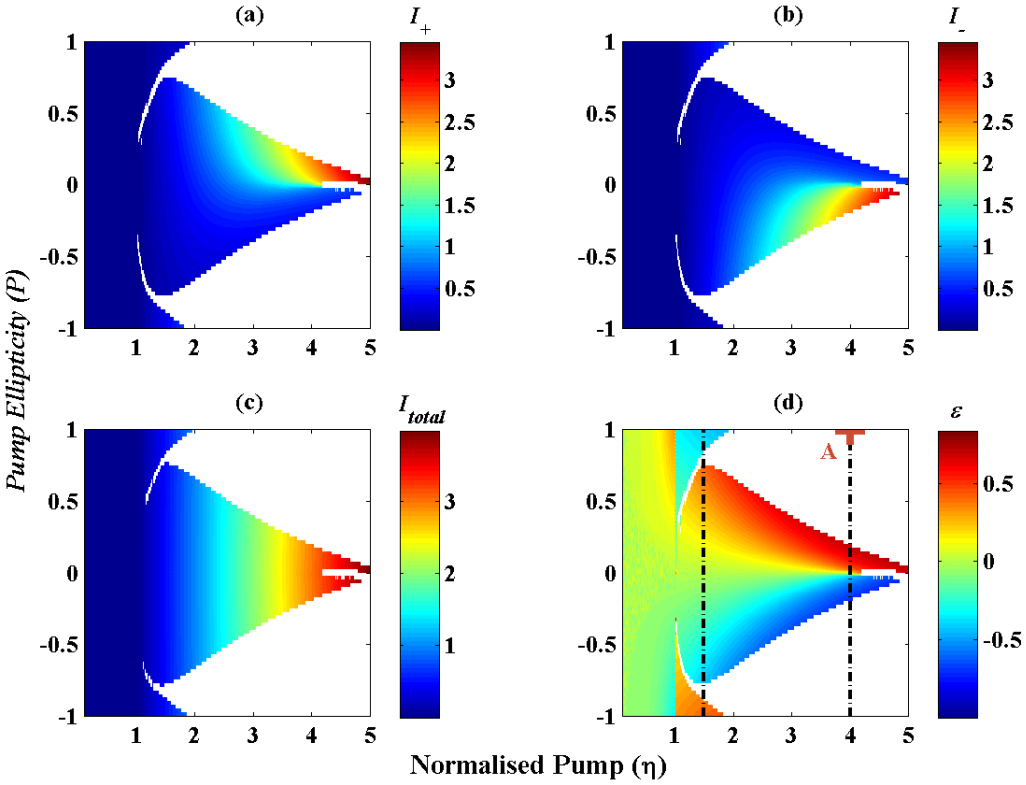

Fig. 3.10:Calculated 2D contour maps for 1300nm dilute nitride spin-VCSELs (sample 2) normalised output intensities I+ (a), I- (b), Itotal (c) and output polarisation ellipticity ε (d) using SFM parameters as in [61].

It can be seen from Fig. 3.10(a-b) that the instability region widens with increasing optical pump power until it becomes dominant beyond five times the threshold ($\eta > 5$) at all polarisation values (P). It is also clear that the right (left) circularly polarised component I_+ (I_-) gives the highest intensity under left (right) circularly polarised pump which is an indication of PS as will be discussed later. Fig. 3.10(c) presents the total output intensity contour map and illustrates that the total output intensity increases with increasing optical pump whereas it seems to be independent of the pump polarisation within the stable region. In Fig. 3.10(d), the output polarisation ellipticity (ε) has been mapped in the plane of (η-P). This map shows that the output polarisation

ellipticity (ε) of the dilute nitride spin-VCSEL is controlled by that of the pump within the stability region (the almost triangular golden yellow and indigo areas within the range $1< \eta < 2$ and $0.25 < |P| < 1$). Outside this range and within the stability region, the spin-VCSEL switches to the opposite polarisation state (e.g. from right- to left-circular polarisation or the reverse) showing PS. To see the PS clearly, the output polarisation ellipticity (ε) has been plotted versus the pump ellipticity P at two pump powers, (η = 1.5 and η = 4 as indicated by the dashed lines in Fig. 3.10(d), in Fig. 3.11(a - b), respectively. To identify the polarisation selection mechanisms it is necessary to determine regions of stability and of PS by carrying out a Routh-Hurwitz stability analysis. This is beyond the scope of the present project but a recent stability analysis has been reported [208].

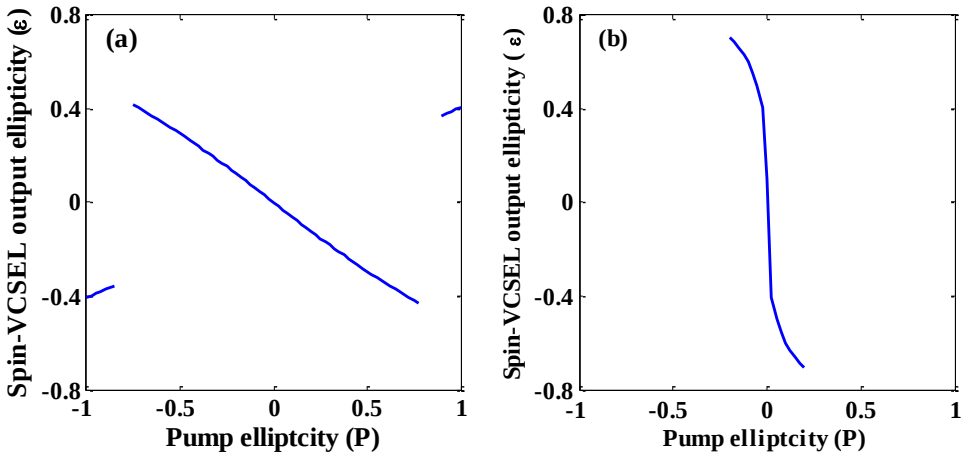

Fig. 3.11: Spin-VCSEL (sample 2) output ellipticity as a function of the pump ellipticity at η = 1.5 and η =4.

Fig. 3.11(a) demonstrates that the calculated output polarisation ellipticity (ε) follows that of the pump at the beginning and then it switches to the opposite state after passing through an unstable region. Furthermore, Fig. 3.11(b) shows that a relatively high output polarisation degree (about 0.75) is achievable with lesser degree of the pump polarisation (about 0.25). These theoretical results are in good agreement with the experimental results presented in Fig. 3.8(a & b) where the output polarisation

ellipticity experiences instability for higher values of $|P|$ then becomes stable with reversed sign for lower values of $|P|$, thus showing PS. This also can be seen clearly when the output polarisation ellipticity is studied as a function of that of the pump for certain values within the region of instability in order to determine the direction and values of the ellipticity of the spin-VCSEL. Now, we would like to investigate the instability region in more detail. For this task, the time series of the output polarisation ellipticity has been generated as in Fig. 3.12 for this sample at point A which represents the parameters (η = 4, P = +1).

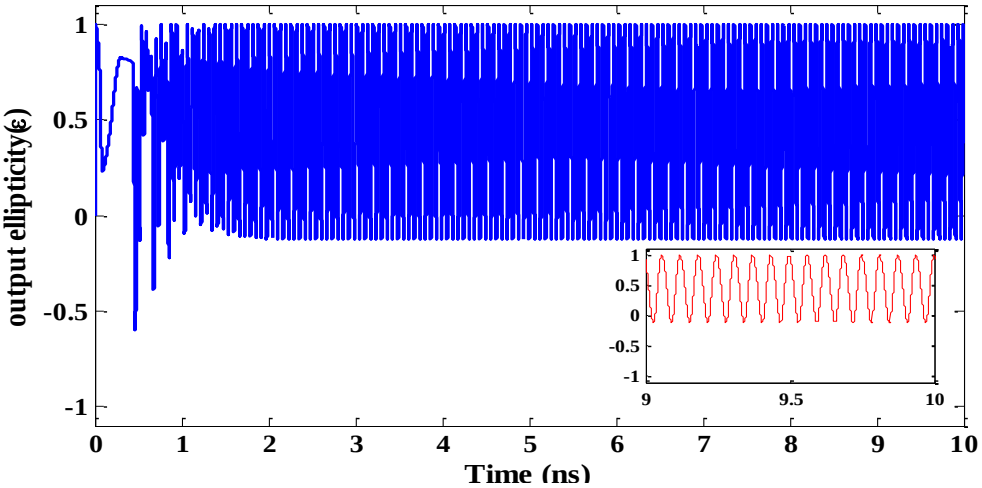

Fig. 3.12: Calculated time series of the output polarisation ellipticity for sample 2 at (η = 4, P = +1).

This figure demonstrates oscillations of the polarisation of the emitted light. Moreover, if we zoom in the last nanosecond of the time series we can see that these polarisation oscillations form self-sustained periodic oscillations as illustrated in red in the inset.

In order to see the influence of the SFM parameters of sample 2 on the polarisation oscillation frequency, the Fast Fourier Transform (FFT) has been used to transform the time series to the frequency domain. The frequency of oscillation (f_{osc}) for the instability region is presented in a 2D contour map in Fig. 3.13.

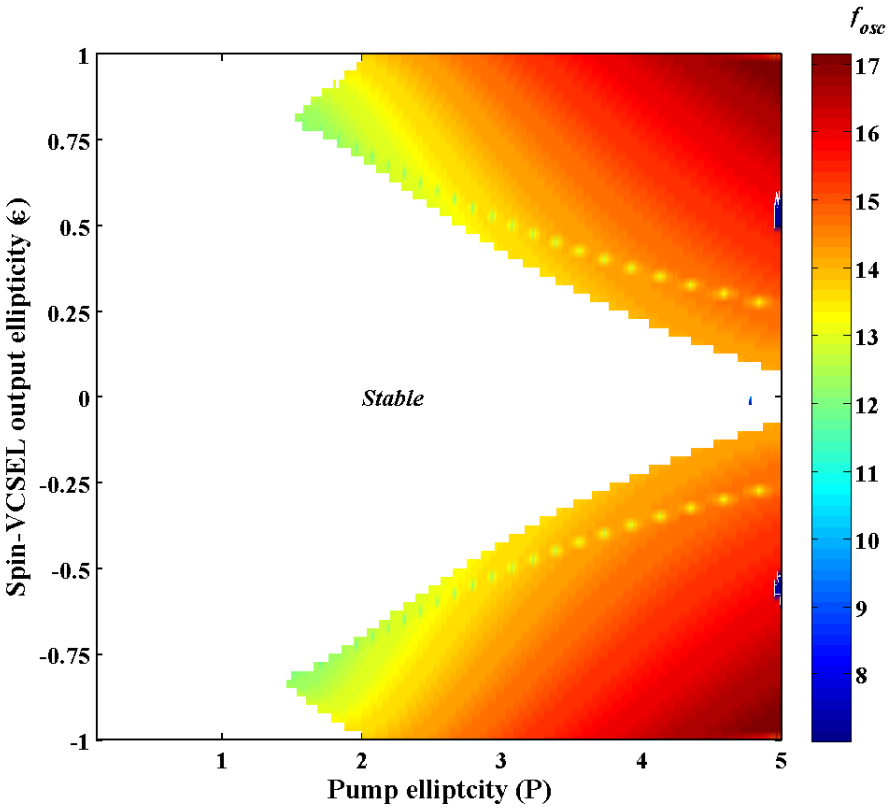

Fig. 3.13: Calculated 2D contour map for frequency of oscillation fosc (in GHz) of the spin-VCSEL instabilities.

Fig. 3.13 illustrates that the frequency of oscillations is influenced by variations in the pump power η and pump ellipticity P (see the colour bar for values in Gigahertz). The frequency of oscillations increases as the pump power increases. It is also sensitive to the pump ellipticity where it increases as the pump polarisation ellipticity P goes to a high DOCP. The range of frequencies that could be attained by changing pump ellipticity P varies from 1.5 to 2.6 GHz. The SFM predictions show that the frequency of oscillations dominated by the birefringence of the micro-cavity in combination with the dichroism and spin relaxation rate, as originally predicted by Gahl et al [163]. These results show very good agreement with the experimental results presented in [61] where polarisation oscillations have been observed in the range 8.6 - 11 GHz. Fig. 3.13 is also in good agreement with the experimental results presented in Fig. 3.6 in terms of stability and instability regions as well as the range of frequencies obtained

by changing pump ellipticity *P* for a specific pumping power. However, the experimental results show frequencies down to 3.5 GHz which was not found in the calculations. However, even at these lower frequencies the range of frequencies for pump ellipticity P variations under a constant pumping power was still comparable to the theoretical simulations for higher frequencies.

3.6 Discussion

The results presented reveal that the two samples of spin-VCSEL under polarised pumping (circular or elliptical) exhibit two different stability behaviours based on their design and structure and material compositions as follows. The difference between sample 1 and 2 lies in the material composition and Nitrogen concentration as shown in Table 3.1. The differences in the Nitrogen concentration in the active material of an optically pumped sample could result in the formation of defects which slow down the dominant DP room temperature spin-relaxation mechanism which in turn increases the spin relaxation time [57, 205].

For sample 1 ($Ga_{0.67}In_{0.33}N_{0.016}As_{0.984}$ QWs and $Ga_{0.75}In_{0.25}N_{0.017}As_{0.983}$ SML) experimental measurements and theoretical calculations shows a stable behaviour under different values of the power (η) and ellipticity of the pump (P). The measurements and theoretical predictions confirm what has been demonstrated in [22] for the same sample in which that the output polarisation ellipticity (ε) is controlled by that of the pump (P). Controlling the output polarisation by that of the input is experimentally demonstrated in [72, 77, 82].

On the other hand, for sample 2 ($Ga_{0.71}In_{0.29}N_{0.020}As_{0.980}$ QWs and $Ga_{0.80}In_{0.20}N_{0.022}As_{0.978}$ SML) an oscillatory behaviour has been theoretically and

experimentally found. This sample produces PS in addition to tunable self-sustained periodic oscillations. It has been found from measured and calculated results that oscillations can be tuned by changing the power or the polarisation ellipticity of the pump. The experimental measurements show that the frequency of oscillation can be tuned from 3.5 up to 15 GHz while simulations predict frequency of oscillation between 12 and 16 GHz by proper adjusting of η and P. Moreover, calculations predict the possibility of obtaining frequencies down to 8 GHz in the blue islands of Fig. 3.13 under (η = 5, P = ±0.6). The experimental and theoretical ranges of frequencies obtained by only tuning the ellipticity of the pump (P) are (1.5~2.6) and (1.5~2.6) GHz, respectively. Both measured and calculated results reveal the dependence of the polarisation oscillations of the spin-VCSEL on the pumping power and ellipticity, in addition to the symmetry in the dynamics and stability behaviours between the negative and positive ellipticities.

The first observations of self-sustained oscillation have been reported for the same sample but with a range of frequency of 8.6-11 GHz in [61, 61]. Apart from this, no similar dynamics have been reported on spin-VCSEL since the previous slow measurements of the output polarisation ellipticity and power [69, 78] or the use of streak cameras to record real-time series of the left- and right-circularly polarised components with a slow time frame of about 0.1 ns [89, 89] conducted on most of the demonstrated spin-VCSELs were not sufficient to measure such dynamics. However, transient and damped oscillations of the output ellipticity in the vicinity of the PS point in response to pulsed optically spin-polarised pumping were predicted and observed in [95, 209, 210] and were reported for conventional electrical pumping in [211-213]. Such self-sustained polarisation oscillations are of interest for optical clock generation, especially since the frequency can be tuned with the pump polarisation and power.

The PS and polarisation oscillations denoted by the white regions in Fig. 3.10 are caused by the competition between fundamental physical processes at work in the device, namely the spin-flip processes that tend to equalize the gain for right- and left-circularly polarised fields, dichroism which tries to equalize the field amplitudes, and birefringence which couples power back and forth between the polarised fields [163]. These polarisation oscillations are related to PS and the development of the ellipticity in the case of $P = 0$ [41, 211, 214].

Tuning the birefringence by structurally engineering the spin-VCSEL or by applying additional stain to the spin-VCSEL could lead to fast polarisation oscillations. The latter could be exploited for optical communication and high performance interconnects such as optical oscillators for radio-over-fibre applications. Indeed, Hendriks et al were able to change the birefringence in a conventional VCSEL by applying strain to the VCSEL [81, 81]. Birefringence values of 19 ns^{-1} and 6.6 ns^{-1} were reported therein (see Figs. 2 and 5, respectively, in [81]) by fitting theory to experiment. Furthermore, a high-birefringence rate of $\gamma_p/\pi \sim 80$ GHz has been experimentally obtained using mechanical strain along first the [1,-1,0] axis and then the [1,1,0] axis of a conventional VCSEL [215] where a VCSEL was bent in a direction coinciding with one of the two preferred polarisation directions. Such uniaxial bending causes tensile strain which results in an anisotropic change of the refractive index leading to wavelength difference between the two orthogonally polarised modes. For the [1,1,0] axis the frequency splitting between the two polarisation modes increases from 1.3 GHz up to 79 GHz [215]. Very recently high-frequency birefringence were theoretically predicted with possibility of attaining oscillating frequency of >200 GHz [216]. This work was followed by an experimental demonstration of revealing birefringence values of > 250 GHz [217, 218], in QW

VCSELs via mechanically induced stress along [0,1,-1] and [0,-1,-1] crystal directions. Therefore special care should be taken when engineering a device for high frequency applications.

Polarisation amplification and amplification of spin information have been demonstrated experimentally and theoretically where results show that a relatively high output polarisation degree can be obtained under lesser degree of the pump polarisation. This feature is considered as great advantages of spin-VCSELs [14, 69].

Finally, simulations using the SFM yielded good agreement with the experimental results, confirming the dependence of oscillation frequency on the pumping power and ellipticity.

3.7 Summary

In this chapter we presented measured and simulated dynamics for 1300 nm dilute nitride spin-VCSELs under CW pump at RT. Simulated results were shown for two samples of 1300 nm GaInNAs/GaAs spin-VCSEL whilst measurements of dynamics were only conducted on sample 2, since sample 1 shows no instabilities. For sample 1, theoretical results demonstrate the dependence of output polarisation ellipticity on that of the pump and that a large DOCP can be achieved for circular pump polarisation which has been already demonstrated experimentally for the same sample. Sample 2 exhibits experimentally and theoretically polarisation instabilities with self-sustained periodic oscillations. Periodic oscillation frequencies up to 16 GHz were observed with the device subject to circularly-polarised optical pumping. These oscillations can be finely tuned by varying the pump polarisation and power. The highest RF oscillation power was found with elliptically-polarised pumping with P = ±0.6~0.8. Simulated results have been done using the SFM. Two sets of parameters have been used for the

two samples of spin-VCSEL. The instability of 1300 nm spin-VCSEL has been investigated and presented in 2D contour maps. Very good agreement was found between experimental and theoretical data in different aspects such as the output polarisation ellipticity, the shape of the instable region, the frequency of oscillation and RF oscillation power.

CHAPTER 4: POLARISATION ELLIPTICITY-RESOLVED DYNAMICS OF OPTICALLY INJECTED SPIN-VCSEL[i]

Abstract:

This chapter reports the experimental control of the light polarisation emitted by a 1310 nm dilute nitride spin-VCSEL at room temperature. This is achieved by means of a combination of polarised optical pumping and polarised optical injection. A numerical model has been developed showing a very high degree of agreement with the experimental findings. In addition to this the experimental observations of circular polarisation switching (PS) and polarisation bistability (PB) in the spin-VCSEL are described.

---

[i] This chapter is based on the papers:

1- S.S. Alharthi, A. Hurtado, R.K. Al Seyab, V.-M. Korpijarvi, M. Guina, I.D. Henning and M.J. Adams, "Control of emitted light polarisation in a 1310nm dilute nitride spin-vertical cavity surface emitting laser subject to circularly polarised optical injection", Appl. Phys. Lett., vol. 105(18), p. 181106 (2014) [132]

2- S.S. Alharthi, A. Hurtado, V.-M. Korpijarvi, M. Guina, I.D. Henning and M.J. Adams, " Control of the Emitted Polarisation in a 1310 nm spin-VCSEL Subject to Circularly Polarised Optical Injection", presented at CLEO 2014, San Jose, USA, 8-13 June 2014 [230]

3- S.S. Alharthi, A. Hurtado, V.-M. Korpijarvi, M. Guina, I.D. Henning and M.J. Adams, "Polarisation switching and bistability in a 1300 nm spin-VCSEL Subject to Circularly Polarised Optical Injection", presented at IPC 2014, IEEE Photonics Conference, San Diego, California, USA, 12-16 October 2014 [324]

4- S.S. Alharthi, A. Hurtado, R.K. Al Seyab, V.-M. Korpijarvi, M. Guina, I.D. Henning and M.J. Adams, "Circular polarisation switching and bistability in an optically injected 1300 nm spin-VCSEL", Applied Physics Letters, vol. 106(2), p. 021117 (2015). [133]

4.1 Introduction

Optical injection using a LP coherent external signal into conventional (electrically driven) VCSELs induces novel nonlinear responses which offer additional unique functionality, and performance enhancements leading to a wider range of potential applications [219]. Examples include IL [140], [220],[221] and a wide range of associated nonlinear dynamics, enhanced modulation bandwidth [221] and new applications such as all-optical memory [222-225], all-optical logic [226-228], signal regeneration [229], microwave and chaotic signal generation [161].

Locking and nonlinear dynamics have been extensively studied under polarised optical injection in conventional VCSELs (parallel, orthogonal, [125, 127, 128] and elliptical [126, 129, 130]). However, reports of circularly polarised injection in conventional VCSELs are very limited. Experimentally, we are only aware of one previous work [131] reporting circularly-polarised injection into an 850 nm conventional VCSEL. In complementary studies, theoretical investigations on the effects of different polarised optical injection (elliptical, circular or linear) in conventional VCSELs have been reported by our group [129, 130].

Whilst most work has concentrated on the characteristics and dynamics of solitary spin-VCSELs, the dynamics of spin-VCSELs subject to optical injection has not received much attention. In solitary spin-VCSELs the polarisation of the optical pump shows full controllability over the polarisation of the spin-VCSEL [22] in addition to the possibility of creating polarisation oscillations as presented in Chapter 3. On top of these merits, optical injection could be used to enhance the performance of the spin-VCSELs without modifying their design. Hence, in the present chapter, the spin-VCSEL is combined with coherent circularly polarised optical injection. Theoretical and experimental investigations of the dynamic behaviour and circular polarisation

properties of a 1300 nm dilute nitride spin-VCSEL operating at RT and subject to circularly polarised optical injection are presented.

First the well-known SFM which forms the base of the theoretical calculations in this chapter is explained with additional extensions to include optical injection terms. Then, control of the emitted polarisation by the optically injected signal is experimentally demonstrated, in good agreement with numerical studies based on the (SFM). The polarisation state of the optical pump and that of the external signal is interchanged and results are presented accordingly. This is followed by a report on the experimental observation of different forms of PS and PB induced by circularly polarised optical injection into the1300 nm dilute nitride spin-VCSEL. Wavelength- and power-induced circular PS and PB for interchanged pump and output polarisation ellipticities states are discussed.

4.2 Theoretical Model

The spin-flip model (SFM) used in the theoretical calculations in this work is the extended version reported in [130] with the inclusion of polarised optical pumping and the spontaneous noise terms. This model includes six rate equations written in terms of the amplitude and phases of the LP electric field components denoted respectively by $E_{x(y)}$ and $\phi_{x(y)}$. The corresponding normalised carrier densities n_+ and n_-, associated respectively with spin-down and spin-up electron populations, are expressed in terms of normalised carrier variables $N = (n_+ + n_-)/2$ and $m = (n_+ - n_-)/2$. The model takes into account the spin relaxation rate (γ_s) that couples spin-up and spin-down carriers, the rates of birefringence (γ_p) and gain anisotropy (γ_a) which influence the different (complex) refractive indices along the two orthogonal crystallographic axes and which couple the two orthogonally polarised fields. The model also includes the conventional

parameters used to describe semiconductor lasers when polarisation is ignored, namely the carrier recombination rate γ, the photon decay rate κ, and the linewidth enhancement factor α. In addition, normalised right- (RCP) and left-circularly polarised (LCP) pump components (η_+, η_-) are included to allow for polarised optical pumping. The six rate equations for the optically injected VCSEL can be written as [62]:

$$\frac{dE_x}{dt} = \kappa\left[(N-1)E_x - mE_y(\sin\Delta\phi + \alpha\cos\Delta\phi)\right] - \gamma_a E_x + K_{inj}E_{injx}\cos\Delta_x + \sqrt{\beta_{sp}(N+m)}\xi_x(t) \quad 4.1$$

$$\frac{dE_y}{dt} = \kappa\left[(N-1)E_y + mE_x(\alpha\cos\Delta\phi - \sin\Delta\phi)\right] + \gamma_a E_y + K_{inj}E_{injy}\cos\Delta_y + \sqrt{\beta_{sp}(N-m)}\xi_y(t) \quad 4.2$$

$$\frac{d\phi_x}{dt} = \kappa\left[\alpha(N-1) + m\frac{E_y}{E_x}(\cos\Delta\phi + \alpha\sin\Delta\phi)\right] - \Delta\omega - \alpha\gamma_a + K_{inj}\frac{E_{injx}}{E_x}\sin\Delta_x \quad 4.3$$

$$\frac{d\phi_y}{dt} = \kappa\left[\alpha(N-1) - m\frac{E_x}{E_y}(\alpha\sin\Delta\phi - \cos\Delta\phi)\right] - \Delta\omega + \alpha\gamma_a + K_{inj}\frac{E_{injy}}{E_y}\sin\Delta_y \quad 4.4$$

$$\frac{dN}{dt} = -\gamma\left[N\left(1+E_x^2+E_y^2\right) - (\eta_+ + \eta_-) - 2mE_yE_x\sin\Delta\phi\right] \quad 4.5$$

$$\frac{dm}{dt} = -\gamma_s m + \gamma(\eta_+ - \eta_-) - \gamma\left[m\left(E_x^2+E_y^2\right)\right] + 2\gamma NE_yE_x\sin\Delta\phi \quad 4.6$$

where K_{inj} is the coupling rate. Δω is the frequency detuning defined as the difference between angular frequency of the injected signal ω_{inj} and the frequency intermediate between those of the x-polarised ($\omega_x = \alpha\gamma_a - \gamma_p$) and y-polarised ($\omega_y = \gamma_p - \alpha\gamma_a$) modes of the solitary VCSEL. The total normalised pumping rate is defined by $\eta = \eta_+ + \eta_-$; where η_+ (η_-) is the normalised rate for right- (left-) circularly polarised pumping and the pump ellipticity is defined as:

$$P = \frac{\eta_+ - \eta_-}{\eta_+ + \eta_-} \quad 4.7$$

E_{injx} and E_{injy} are the field amplitudes for the injection signal whereas δ_x , δ_y correspond to their phases respectively. The two fields are related by the auxiliary angle θ_{p} given by:

$$E_{injx} = E_{injy} \tan\theta_p \quad 4.8$$

To simplify the equations without loss of generality, when the dominant mode of the VCSEL is parallel to the y-direction, we set the phase $\delta_y = 0$ and write $\delta_x = \delta$ which is included in the definition:

$$\Delta_x = \omega_y t - \phi_x + \delta \quad 4.9$$

The injection level (P_{inj}) is normalised to the linearly-polarised (LP) output of the solitary-VCSEL and can be calculated from the following equation:

$$P_{inj} = 10\log\left(\frac{|E_{inj}|^2}{|E_{sol}|^2}\right) \quad 4.10$$

where E_{sol} is defined as [160]:

$$|E_{sol}|^2 = \frac{\eta}{1-\frac{\gamma a}{\kappa}} - 1 \quad 4.11$$

The importance of the spontaneous emission noise was explained in 2.4.1. Therefore its effect has been included by introducing a zero mean Gaussian noise source as in [128]. β_{sp} is the spontaneous emission factor ($\beta_{\text{sp}} = 10^{-5}$) [128] and $\zeta_{\text{x,y}}$ are Gaussian white noises of zero mean value. The rest of the terms in the model are defined as:

$$\Delta\phi = 2\omega_y t + \phi_y - \phi_x \quad 4.12$$

$$\Delta_y = \omega_x t - \phi_y \quad 4.13$$

The incident polarisation of the injection is completely described by two variables: the auxiliary angle θ_p and the phase difference δ between x- and y-components of the

injected field. Thus, the state for right (left) circularly-polarised injection is achieved by setting the injection angle and the phase difference between x- and y- coordinates as $\theta_p = 45$ and $\delta = 90^\circ$ (-90˚) respectively.

In this work, the following Eqs. 4.14 have been used to convert from the Cartesian field into the corresponding circularly polarised components as follows [41]:

$$\bar{E}_+ = \frac{\bar{E}_x + \bar{E}_y}{\sqrt{2}} \quad , \quad \bar{E}_- = -i\frac{\bar{E}_x - \bar{E}_y}{\sqrt{2}} \tag{4.14}$$

where, $\bar{E}_+(\bar{E}_-)$ correspond to the RCP (LCP) fields of the VCSEL. The polarisation ellipticity (DOCP) of the VCSEL is defined as [163]:

$$\varepsilon = \frac{|\bar{E}_+|^2 - |\bar{E}_-|^2}{|\bar{E}_+|^2 + |\bar{E}_-|^2} \tag{4.15}$$

4.3 Experimental Setup

Sample 1 which is a GaInNAs/GaAs VCSEL (described in chapter 3) was used in the experiments reported in this chapter. Fig. 4.1 presents the experimental setup used in this work to investigate the effects of optical injection on the ellipticity (ε) of the spin-VCSEL's emission (defined as in Eq.4.15). The sample was pasted on a silicon carrier wafer clamped to a temperature-controlled copper mount. The mount has an aperture to allow part of the spin-VCSEL's back-side emission (transmitted through the VCSEL and silicon wafers) to be directed towards a free-space polarimeter. A 980 nm pump laser driven by a 1 A CW current source was used to optically pump the spin-VCSEL sample. The pump is connected to an IS to avoid backward reflections and its output polarisation was controlled with an in-line fibre PC. 10% of the optical pump was directed to a power meter using a 90/10 coupler to monitor the CW pumping power. The other 90% was focused onto the sample using a long focal-distance lensed fibre (HI1060) which was also used to collect the spin-VCSEL sample's emission. An

interchangeable optical filter is used between the free-space polarimeter and the copper mount to allow either the 980 nm pumping light or the 1310 nm spin-VCSEL emission as required. The polarisation of the pump and that of the spin-VCSEL are both analysed using the aforementioned free-space polarimeter. Under these conditions an external optical signal, from a 1300 nm external cavity tunable laser ML is amplified using an SOA, and injected into the spin-VCSEL sample via an optical circulator. The ML's output power was set to 2 mW and the SOA current was 300 mA, thus delivering 7.3 mW to the sample. A second PC is used to control the ML's polarisation. The third port of the circulator is followed by a 1300 nm IS and another 90/10 coupler to direct part of the spin-VCSEL sample's light to an OSA and part to an in-line polarimeter for further analysis.

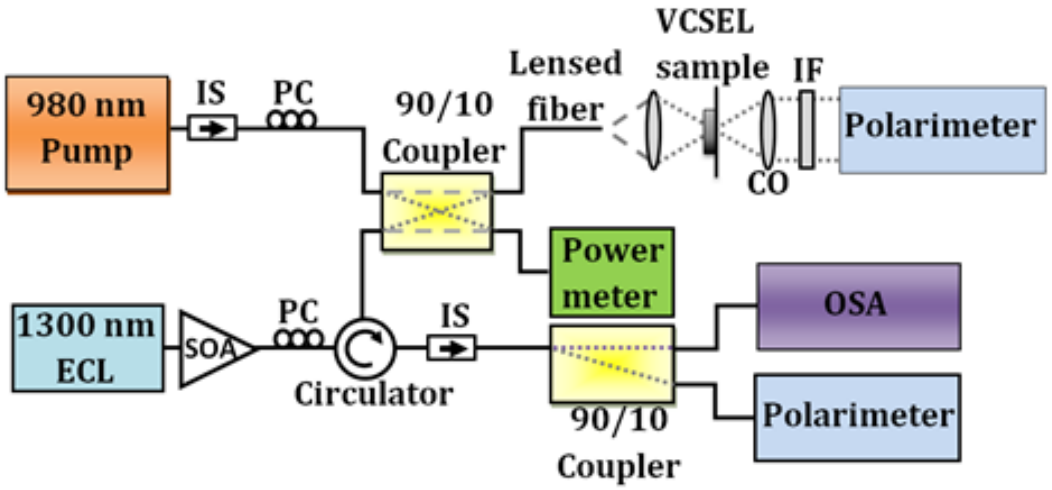

Fig. 4.1: Setup used in this work to study the effect of polarised optical injection in an optically-pumped 1300 nm spin-VCSEL sample. OSA: Optical Spectrum Analyser, SOA: Semiconductor Optical Amplifier; ECL: External Cavity Laser, IS: isolator; PC: polarisation controller; IF: Interchangeable Filter, CO: collimator.

4.4 Results

4.4.1 Optical spectrum and input versus output curve

Fig. 4.2(a) shows the optical spectrum of the 1300 nm dilute nitride spin-VCSEL emitting at 1297.5 nm while (b) shows the corresponding input-output characteristics of the solitary spin-VCSEL when the sample was subject to right circular polarised (RCP) optical pumping. It should be mentioned that the actual output power of the spin-VCSEL in Fig. 4.2 before the normalisation was within 1 mW range.

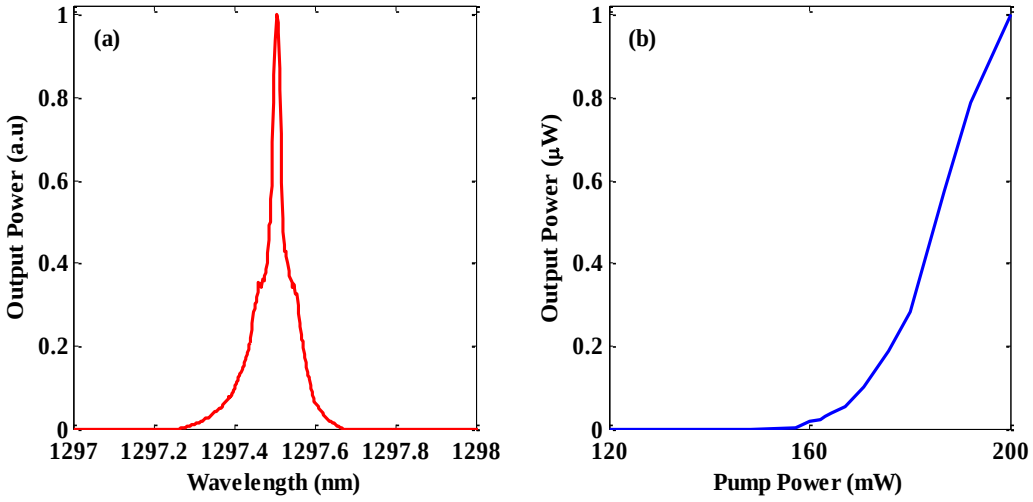

Fig. 4.2: (a) Optical spectrum of the spin-VCSEL. (b) The input-output curve under LCP pumping for the solitary spin-VCSEL with LCP output as the pump.

The input-output curve shows that the pumping threshold is 158 mW. As can be seen from Fig. 4.2(b) the input-output characteristics and optical spectrum shape have been improved in terms of pumping threshold and spectrum linewidth, respectively, compared to results reported in [22]. This improvement is due to improvements and optimisation of the experimental setup as mentioned in chapter 3.

4.4.2 Control of polarisation in a Spin-VCSEL subject to circularly polarised optical injection

In this section we have investigated the effects of the injection strength, polarisation and initial detuning of the externally injected optical signal on the ellipticity (ε) of the spin-VCSEL's emission. Previous work had experimentally demonstrated that the solitary spin-VCSEL's polarisation follows that of the optical pump [22]. However, under optical injection with either RCP or LCP, the spin-VCSEL shows a different behaviour as shown in Fig. 4.3. Specifically, Fig. 4.3(a) and Fig. 4.3(b) show, respectively, the experimentally measured polarisation ellipticity of the spin-VCSEL's light emission as a function of the initial detuning when the device is subject simultaneously to LCP optical pumping with 180 mW and optical injection with 7 mW of either RCP (Fig. 4.3(a)) or LCP (Fig. 4.3(b)).

4.4.2.1 Output polarisation behaviour of spin-VCSEL under LCP pumping and RCP injection

Fig. 4.3(a) shows that initially the spin-VCSEL's output polarisation follows that of the pump; then as the ML's frequency approaches the locking bandwidth of the solitary spin-VCSEL (the emission peak is located at 1297.51 nm as shown in Fig. 4.2(a)), the ML increasingly controls the polarisation of the spin-VCSEL, switching it gradually from almost LCP (ε = -0.85) to RCP (ε = +1). As the detuning is increased to higher values, the polarisation of the spin-VCSEL returns abruptly to LCP (ε = -0.85) being again controlled by that of the pump.

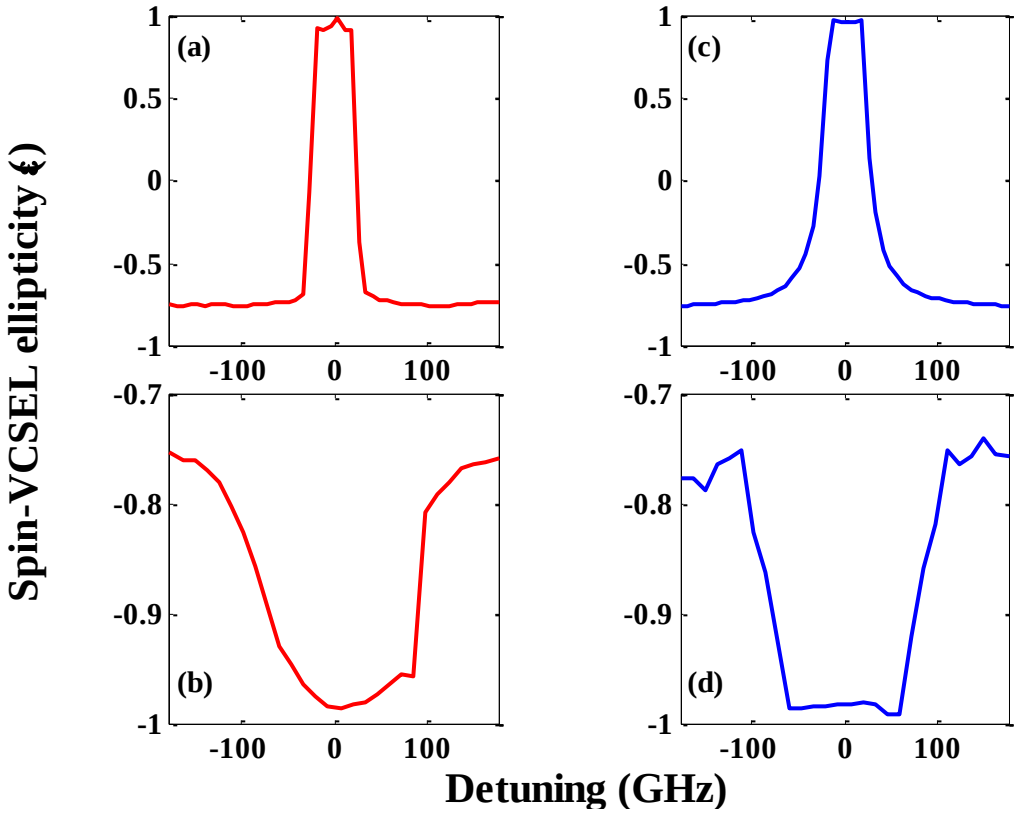

Fig. 4.3: Measured (a & b, in red) and calculated (c & d, in blue) output polarisation of the spin VCSEL versus detuning. The spin VCSEL is optically-pumped with LCP light. The optically-injected signal from the ML had RCP (a & c) and LCP (b & d).

Fig. 4.3(b) presents the case where the polarisations of the pump and the ML's injected signal are both set to LCP. It can be seen here that the optically injected signal controls the polarisation of the spin-VCSEL within its locking bandwidth, achieving a high degree of LCP ($\varepsilon \approx -0.98$). Fig. 4.3(c) and Fig. 4.3(d) plot the theoretically calculated results for the same conditions as in Fig. 4.3(a) and Fig. 4.3(b). Good agreement is found between the experimental findings and the numerical calculations. The SFM parameter values used in Fig. 4.3(c) were (α =2, γ_p = 4.2 ns^{-1} , γ_s =105 ns^{-1}, η = 1.1, γ_a = 0, κ = 250 ns^{-1}, γ = 1 ns^{-1}, P_{inj} = 7 mW , K_{inj} = 43 ns^{-1}, δ = +90^o and θ_p = 42˚), while in Fig. 4.3(d) they are the same except γ_p = 4.5 ns^{-1} , K_{inj} = 148 ns^{-1} and δ = -90^o. These parameters were found by best fit to the experimental data. Initially, the main SFM parameters values were chosen as discussed in section 3.5.2. The linear

anisotropies, birefringence and dichroism, have not been experimentally determined due to the relatively broad spectrum of the device which does not permit the high-resolution measurements required to find these parameters. The birefringence and linewidth enhancement factor were changed by small values to fit the theoretical output polarisation ellipticity for the solitary spin-VCSEL to its experimental counterpart. It is believed that the different values of birefringence arise from the strain in the sample, which changes at different positions, and hence they depend on the pumped and injected position. In fact, this also has been reported by Hendriks et al who were able to change the birefringence by applying strain to the VCSEL [81]. They fitted theory to experiment with values of 19 ns^{-1} and 6.6 ns^{-1} therein (see Figs. 2 and 5, respectively in [81]). For modelling the polarised optical injection effect on the spin-VCSEL the experimental value for the injection strength P_{inj} was used in the SFM after normalising it to the output of the SL. At first high degrees of the coupling efficiency *K*inj were considered unless proven wrong where it was then slightly reduced until the best fit was obtained. It is also worth noting that the difference in the injection strength values refers to the coupling efficiency of the injected signal into the active region of the sample. The coupling efficiency between the sample and the lensed fibre changes each time the setup experiences modifications such as changing the sample, the polarisation state of the ML and the lensed fibre etc. Therefore, the more the injection power coupled into the sample the higher the DOCP to be achieved and the lower the coupling rate value would be used in the SFM. Thus, one would expect to use the same coupling rate value in the SFM under the same experimental circumstances. This justifies the difference of values for some parameters such as the birefringence and the coupling rate.

In addition to analysing the effect of the initial detuning we have also investigated the effect of the ML's injection strength on the polarisation properties of the spin-VCSEL.

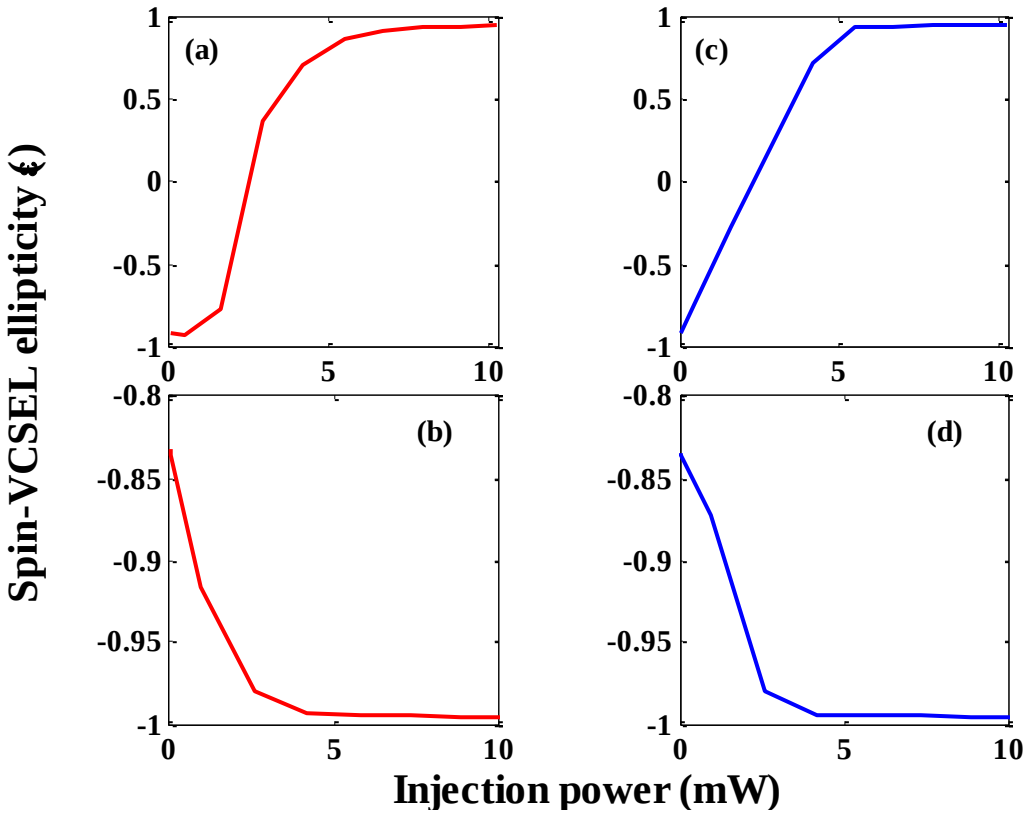

Fig. 4.4: Measured (a & b, in red) and calculated (c & d, in blue) output polarisation of the spin VCSEL versus optical injection strength. The spin VCSEL is optically-pumped with LCP light. The ML's injection had RCP (a & c) and LCP (b & d).

It is found that when the injection strength is low, the polarisation of the pump controls that of the spin-VCSEL. However, under high injection strength it is the polarisation of the ML's injected signal which controls that of the spin-VCSEL. We have found that as the injection strength is increased gradual PS as well as high degrees of circular polarisation are achieved when the spin-VCSEL is subject to either LCP or RCP optical injection. This is illustrated graphically in the experimental plots of Fig. 4.4(a) and Fig. 4.4(b) for the case of optical injection at a constant wavelength of 1297.3 nm when the solitary spin-VCSEL was pumped up to about 1.5 times the

threshold (~240 mW) in both cases. The spin-VCSEL in both cases was optically-pumped with LCP light. Fig. 4.4(a)/ (Fig. 4.4(c)) shows gradual PS towards very high degrees of RCP/ (LCP) as the injection strength is increased. The behaviours experimentally measured in Fig. 4.4(a) and Fig. 4.4(b) are in good agreement with numerical calculations using the SFM depicted in Fig. 4.4(c) and Fig. 4.4(d). The SFM parameter values used in Fig. 4.4(c) were (α =2, γ_p = 3.6 ns^{-1} , γ_s =105 ns^{-1}, η = 1.5, γ_a = 0, κ = 250 ns^{-1}, γ = 1 ns^{-1}, $\Delta\omega$ = 24.8 rad/ns, K_{inj} = 95 ns^{-1}, δ = -90 and θ_p = 43˚), while in Fig. 4.4(d) the difference was in the following values: (α =2.9, γ_p = 4.5 ns^{-1} , η = 1.1, K_{inj} = 70 ns^{-1}, δ = -90˚ and θ_p = 38˚). These parameters were chosen through the same steps summarised in the previous subsection. The difference in injection strength is related to the coupling efficiency of the injected signal into the device, while the difference in the injection angle is related to the accuracy of the PC since it needs more effort to maintain the injection angle at θ_p = 45˚all the time.

4.4.2.2 Output polarisation behaviour of spin-VCSEL under RCP pumping and LCP injection

We have also investigated the effects of the injected power, polarisation and detuning on the ellipticity (ε) of the spin-VCSEL's emission. As already demonstrated, when the spin-VCSEL is pumped with right circular polarisation (RCP), it produces LCP emission [22]. However, under LCP and RCP optical injection, the spin-VCSEL shows different behaviours as shown Fig. 4.5(a) and Fig. 4.5(b), respectively. Specifically, Fig. 4.5a(b) shows the output polarisation ellipticity of the spin-VCSEL under RCP pumping versus the detuning of the LCP (RCP) ML's injection. Fig. 4.5(a) shows that the spin-VCSEL polarisation follows that of the pump at first; then as the ML's wavelength approaches the solitary spin-VCSEL's locking bandwidth (the peak is at 1297.5 nm as shown in Fig. 4.2(a)), the ML controls the polarisation of the

spin-VCSEL and switches it gradually from almost RCP (ε = 0.75) to LCP (ε = -1). As the ML's wavelength approaches higher detunings, the polarisation of the spin-VCSEL returns gradually to RCP (ε = 0.75) where it is now controlled again by that of the pump. This PS from RCP to LCP (and vice-versa) is caused by competition between the pump and the ML to control the spin-VCSEL's emission. Fig. 4.5(b) presents the case where the polarisations of the pump and the ML are both set to RCP.

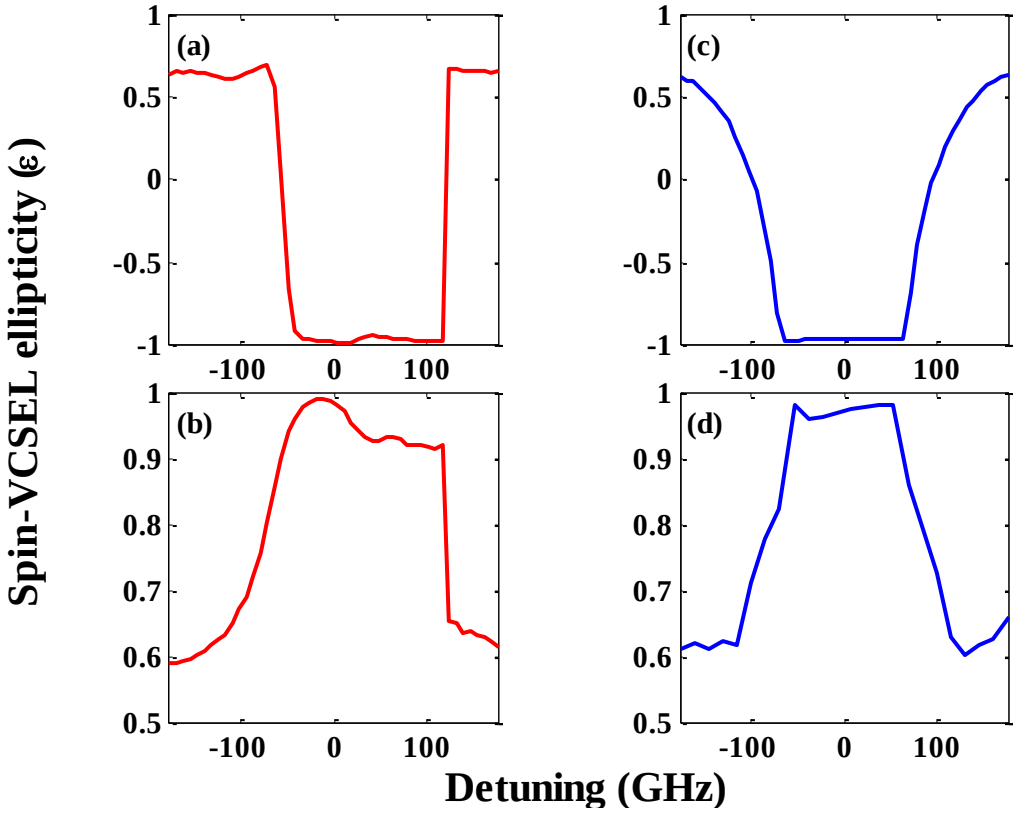

Fig. 4.5: Measured (a & b, in red) and calculated (c & d, in blue) output polarisation of the spin VCSEL versus initial detuning. The spin VCSEL is optically-pumped with RCP light. The optically-injected signal from the ML had LCP (a&c) and RCP (b&d).

It can be seen here that the ML controls the polarisation of the spin-VCSEL within its locking bandwidth and helps to achieve a high degree of RCP. Good agreement is found between the experimental (Fig. 4.5(a) and Fig. 4.5(b)) and the theoretically predicted results (Fig. 4.5(c) and Fig. 4.5(d)) using some of the SFM parameter values as used in [22] but with different values for γ_p in Fig. 4.5(d). The SFM parameter

values used in Fig. 4.5(c) were (γ_p = 2 ns^{-1} , γ_s =105 ns^{-1}, η = 1.1, γ_a = 0, κ = 250 ns^{-1}, γ = 1 ns^{-1}, P_{inj} = 7 mW , K_{inj} = 170 ns^{-1}, δ = -90^o and θ_p = 39°), while in Fig. 4.5(d) they are the same except γ_p = 6.2 ns^{-1} , θ_p = 44° and δ = +90^o.

As in the previous subsection, it is also found that when the injection strength is low, the polarisation of the pump controls that of the spin-VCSEL. However, under high injection strength it is the polarisation of the ML which controls that of the spin-VCSEL, and gradual PS under LCP injection is achieved as well as high degrees of circular polarisation with RCP or LCP injection.

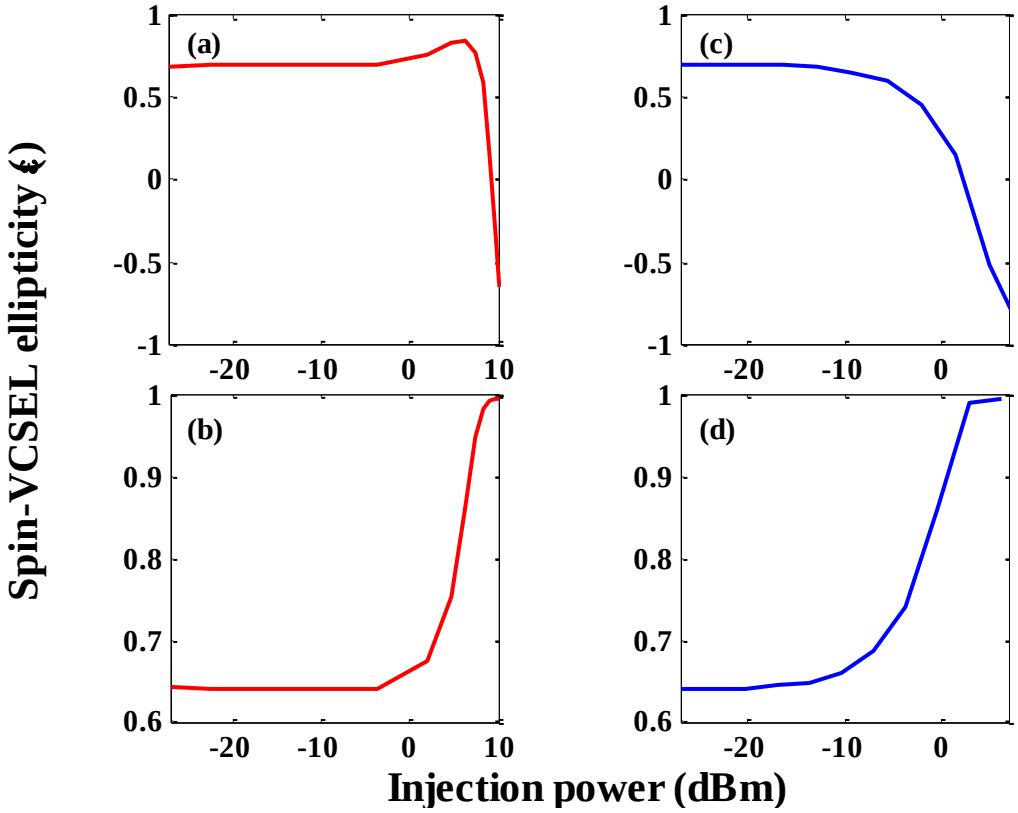

Fig. 4.6: Measured (a & b, in red) and calculated (c & d, in blue) output polarisation of the spin VCSEL versus optical injection strength. The spin VCSEL is optically-pumped with RCP light. The ML's injection had LCP (a & c) and RCP (b & d).

This is illustrated in Fig. 4.6(a) and Fig. 4.6(b) showing the effect of the LCP (RCP) ML's injection strength at a detuning of 35 GHz when the spin-VCSEL is optically-pumped with RCP. The behaviours in Fig. 4.6(a) and Fig. 4.6(b) are in good agreement

with numerical calculations using the SFM (Fig. 4.6(c) and (d)). The SFM parameter values used in Fig. 4.6(c) were (γ_p = 5.2 ns^{-1} , γ_s =105 ns^{-1}, η = 1.1, γ_a = 0, κ = 250 ns^{-1}, γ = 1 ns^{-1}, $\Delta\omega$= 75.4 rad/ns , K_{inj} = 170 ns^{-1}, δ = -90^o and θ_p = 43°), while in Fig. 4.6(d) they are the same except K_{inj} = 60 ns$^{-1,}$, θ_p = 45° and δ = +90^o. The difference between the experimental and predicted detuning scales can be accounted for by the width of the spin-VCSEL's spectrum. The theory assumes a perfectly monochromatic line, so the detuning range to see these effects is small. By contrast, the experimental spectrum is quite broad (see Fig. 4.2(a)), extending the tuning range needed to see the effects.

4.4.3 Circular polarisation switching and bistability

The investigation of the nonlinear dynamics of optically injected dilute nitride spin-VCSEL is further extended in this section. Experimental observation of circular PS and PB in the 1300 nm dilute nitride spin-VCSEL has been studied. The device was optically pumped with CW light at 980 nm and operated at RT. We demonstrate that the injection of an external optical signal at 1300 nm, which is polarised either with left- or right-circular polarisation can switch the polarisation at the output of the spin-VCSEL from right-to-left circular polarisation and vice versa. Moreover, different forms of PS and PB between right- and left-circular polarisations are observed by controlling the injection strength and the initial wavelength detuning.

Two experimental scenarios were used to study PS and PB in the 1300 nm dilute nitride spin-VCSEL. In the first scenario the ML injection power was kept constant while the output polarisation ellipticity (ε) of the spin-VCSEL's emission (defined as the ratio between the *DOCP* and the total degree of polarisation *DOP*) was measured as a function of increasing and decreasing initial wavelength detuning ($\Delta\lambda$) between the ML and SL. In the second scenario the initial wavelength detuning ($\Delta\lambda$) was fixed

and the influence of injection power on the output polarisation ellipticity (ε) of the spin-VCSEL was examined. In both scenarios the spin-VCSEL sample was optically pumped above threshold (>200 mW) and injected with a circularly polarised optical signal from the ML. In each scenario, there were two cases depending on the polarisation state of the optical pumping as discussed below.

4.4.3.1 Wavelength induced circular polarisation switching and bistability

In this scenario the output polarisation ellipticity (ε) of the spin VCSEL's emission was measured as a function of increasing and decreasing initial wavelength detuning (Δλ) between the ML and SL under constant power of the ML injection. Two cases of wavelength induced PS and PB depending on the polarisation state of the optical pumping with respect to that of the optical injection were observed and analysed as in the following subsections.

4.4.3.1.1 Wavelength induced PS and PB behaviour of spin-VCSEL under RCP pumping and LCP injection

Fig. 4.7 illustrates the first case of the first scenario showing the relationship between the output polarisation ellipticity (ε) of the spin-VCSEL and the initial wavelength detuning (Δλ). In this case, the spin-VCSEL was simultaneously pumped with RCP light and optically-injected with a left circular polarisation (LCP) signal from the ML. The amplified injection power was fixed at 7 mW. The blue-solid and red-dashed lines plot the measured value of ε of the SL's emission for increasing and decreasing values of Δλ, respectively. Initially, Fig. 4.7 shows a well-known feature of the spin-VCSEL where its output polarisation (ε) is determined by that of the optical pump [22]; then as the ML wavelength approaches the solitary spin-VCSEL's locking bandwidth (zero detuning), the ML pulls the SL's polarisation changing it gradually

from almost RCP (ε = 0.88) to LCP (ε = -1), a behaviour that has been recently theoretically [62, 132] and experimentally reported [132, 230]. With increasing ML wavelength to detunings beyond the spin-VCSEL's emission peak, an abrupt PS from LCP to RCP occurs and the SL's output polarisation is now controlled again by that of the optical pump. With decreasing detuning the observed PS does not occur at the same point but at a slightly lower value of Δλ. Thus circular PB with an associated anticlockwise hysteresis cycle (with a total width of 9 GHz) is experimentally observed.

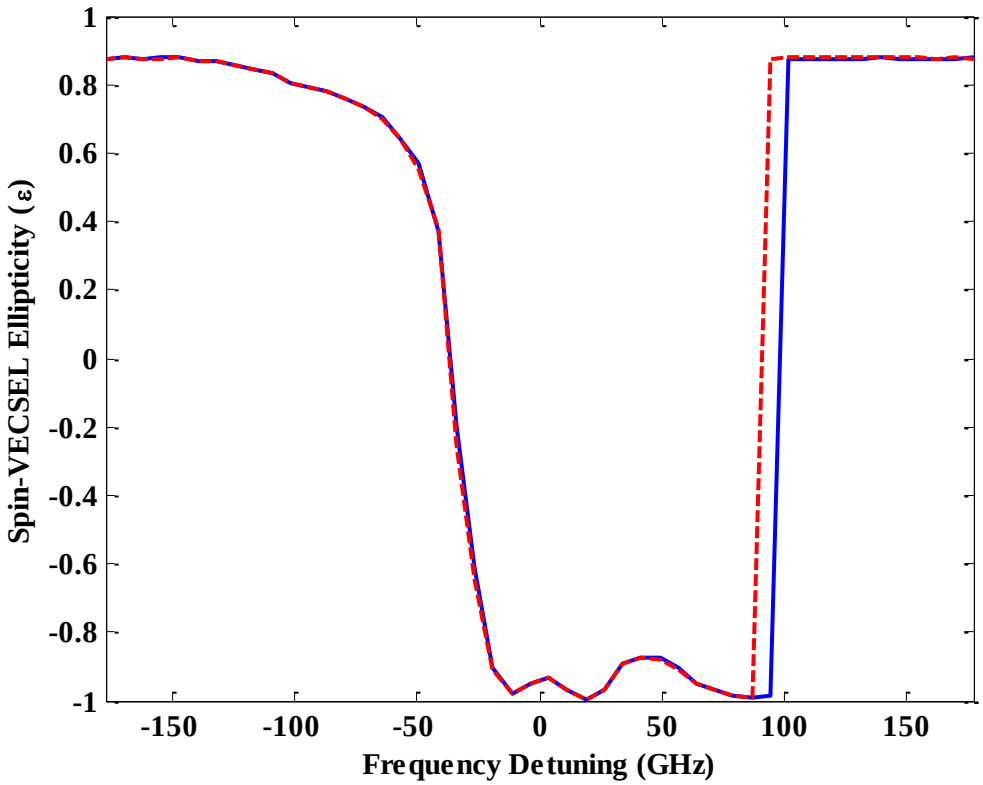

Fig. 4.7: Output polarisation ellipticity (ε) as a function of wavelength detuning (Δλ) under RCP pumping and LCP optical injection. Results are plotted for increasing (Blue solid lines) and decreasing (Red dashed lines) initial wavelength detuning.

4.4.3.1.2 Wavelength induced PS and PB behaviour of spin-VCSEL under LCP pumping and RCP injection

This scenario was then extended to include the opposite case of LCP optical pumping and RCP optical injection. Once again the SL's output ellipticity (ε) was

studied as a function of the wavelength detuning Δλ revealing similar overall behaviour as illustrated in Fig. 4.8.

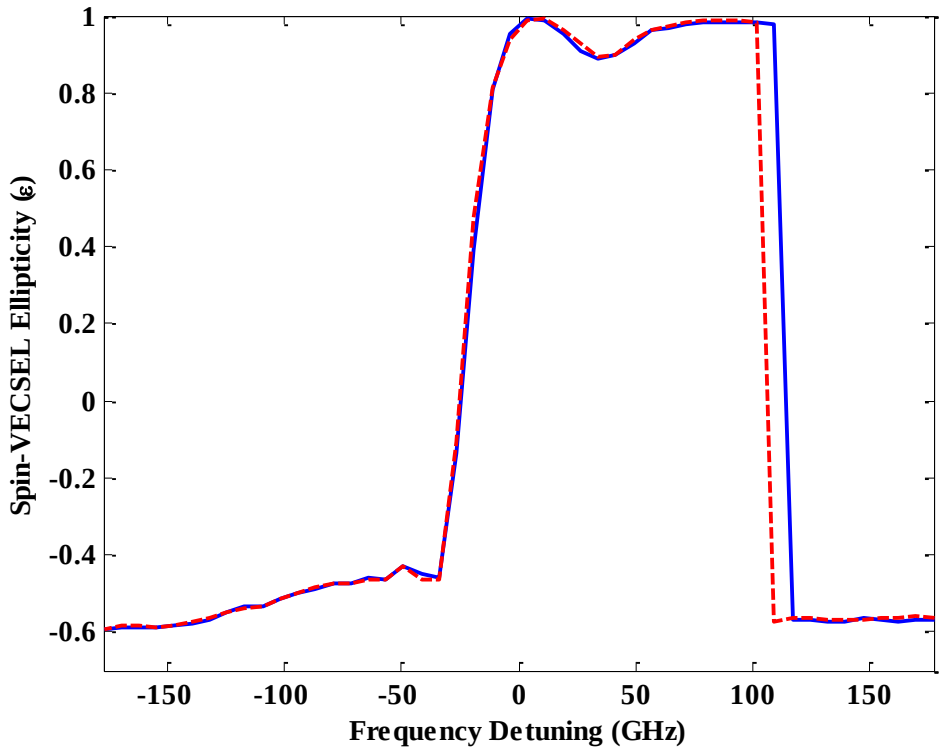

Fig. 4.8: Output polarisation ellipticity (ε) as a function of wavelength detuning (Δλ) under LCP pumping and RCP optical injection. Results are plotted for increasing (Blue solid lines) and decreasing (Red dashed lines) initial wavelength detuning.

This figure shows that when increasing Δλ (blue-solid line in Fig. 4.8) the polarisation controllability occurred within the locking bandwidth of the SL from LCP (ε = -0.60) to RCP (ε = +1) followed by an abrupt PS at the higher detuning side. While for decreasing Δλ (red-dashed line in Fig. 4.8), the PS from LCP to RCP takes place at a slightly lower value of Δλ than the one previously observed. This is an indication of circular PB with an associated clockwise hysteresis cycle. The total width of the hysteresis cycle in this case is 7.5 GHz.

4.4.3.2 Power induced circular polarisation switching and bistability

Now we will discuss the second scenario where the initial wavelength detuning (Δλ) between the ML and SL was kept constant while the output polarisation ellipticity (ε) of the spin-VCSEL's emission (defined as the ratio between the DOCP and the total DOP) was measured as a function of increasing and decreasing ML injection power. All the measurements have been conducted when the spin-VCSEL sample was optically pumped to 1.1 times the threshold and injected with a circularly polarised optical signal from the ML. Also, the measurements have been taken for different initial wavelength detunings as will be discussed below. Moreover, two different cases have been analysed for this scenario based on interchanging the polarisation states of the pump and that of the ML between right- (RCP) and left-circularly polarised (LCP) states (i.e. when the polarisation of the pump is RCP the ML's one is LCP and vice-versa) as will be discussed later.

4.4.3.2.1 Power induced PS and PB behaviour of spin-VCSEL under RCP pumping and LCP injection

Fig. 4.9 illustrates the relationship between the output polarisation ellipticity (ε) of the spin-VCSEL and the ML's injection power for different values of initial wavelength detuning. The injection power was measured as the amount of ML's optical power incident on the surface of sample. Results are shown for different negative initial wavelength detunings, -0.50, -0.40, -0.30, -0.20, -0.10, and 0 nm as indicated. Here, the spin-VCSEL was simultaneously pumped with RCP light and optically-injected with an LCP signal from the ML. Initially, Fig. 4.9 shows a well-known feature of spin-VCSELs whereby its output polarisation (ε) is determined by that of the optical pump [22]; then, as the injected optical power is continuously increased the ML switches the SL's light polarisation gradually from almost RCP (ε =

0.75) to almost LCP (ε = -0.95), a behaviour that has been recently theoretically [62, 132] and experimentally reported [132, 230]. Fig. 4.9 shows that by changing the wavelength detuning from zero to -0.50 nm the lower the negative wavelength detuning, the more injection power is needed to achieve the nonlinear gradual PS transition. It should also be mentioned that there was no abrupt PS or PB observed in all the measurements reported in this work for the negative wavelength detuning.

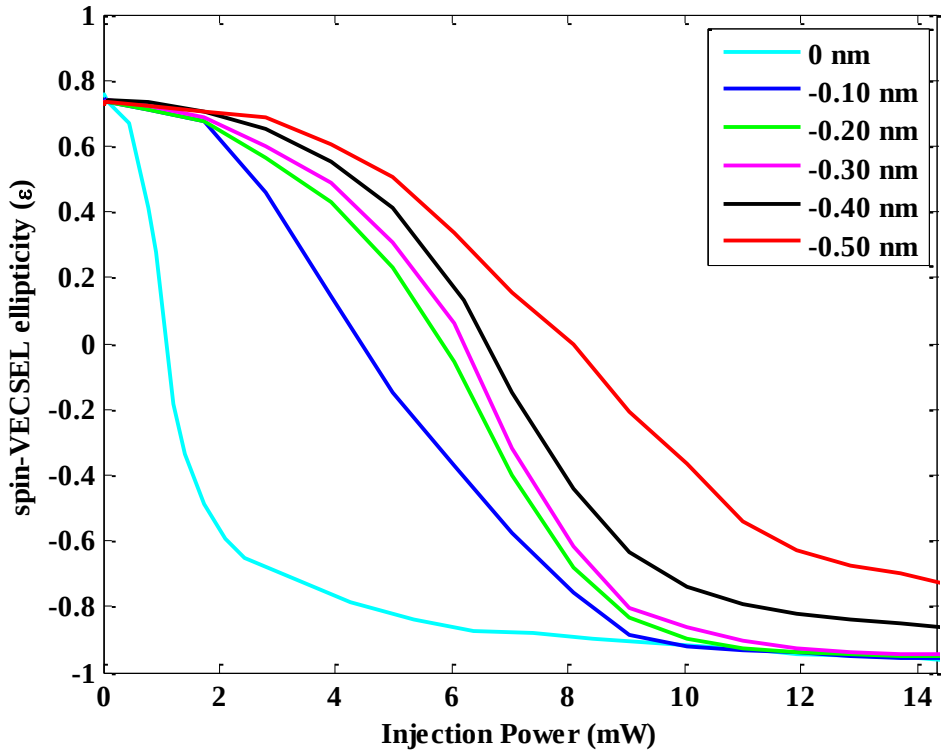

Fig. 4.9: Output polarisation ellipticity (ε) vs injected optical power when the spin VCSEL is subject to RCP optical pumping and LCP optical injection for negative initial wavelength detunings. Results are plotted for increasing injection strength.

Now we will study the effect of increasing and decreasing the injection power of the ML on the output polarisation ellipticity of the spin-VCSEL (ε) under the same conditions but for positive initial wavelength detunings (Δλ). Fig. 4.10 shows the output polarisation ellipticity (ε) as a function of increasing and decreasing values of the injection power for different initial wavelength detunings (Δλ), +0.10, +0.20, +0.30, +0.40 and +0.50 nm. Solid and dashed lines in Fig. 4.10 plot respectively the

measured values of ε for increasing and decreasing values of injection strength. In this case, when the initial wavelength was set to a positive value (i.e. 0.10 nm) initially the SL's output ellipticity follows that of the pump and exhibits a value close to RCP emission (ε = 0.75). However, under sufficient injection power (exceeding 700 μW) the LCP ML switches abruptly the SL's polarisation from almost RCP (ε = 0.75) to almost LCP (ε = -0.95).

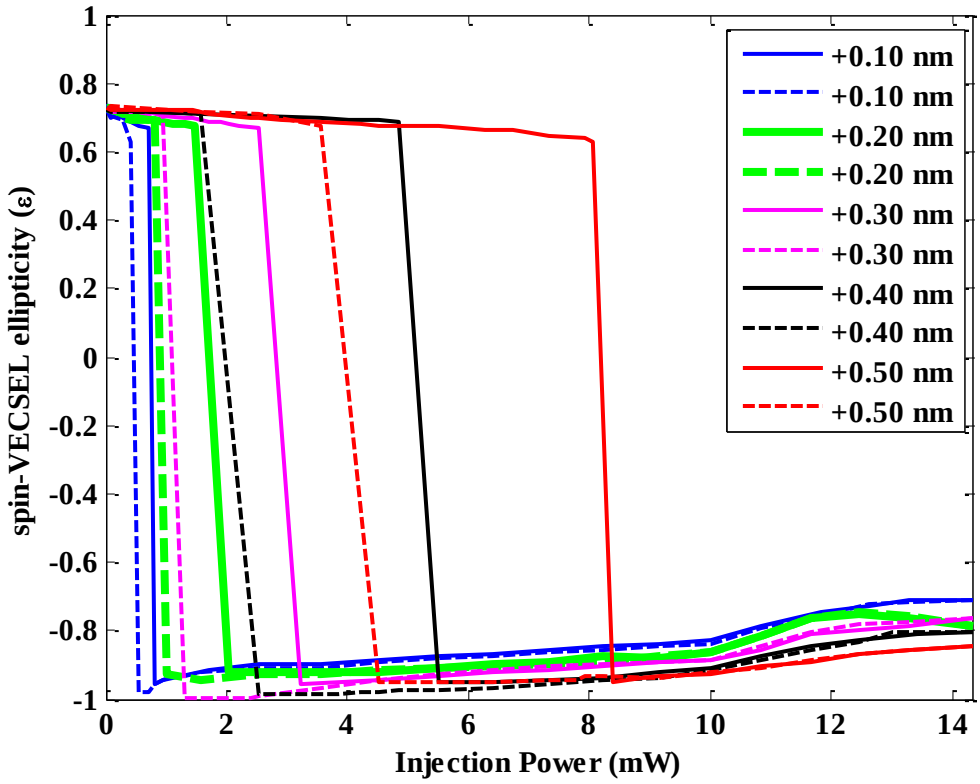

Fig. 4.10: Output polarisation ellipticity (ε) as a function of injection power under RCP optical pump and LCP optical injection for positive values of initial wavelength detuning as indicated. Results are plotted for increasing (solid lines) and decreasing (dash lines) injection strength values.

On the other hand, when the injection power was decreased back to zero, PS from almost LCP to RCP was observed at a different and lower switching point (560 μW) revealing therefore the existence of circular PB with a clockwise hysteresis cycle in the plane of ε vs. injection power depicted in Fig. 4.10. For higher positive initial wavelength detunings, it has been found that the PS requires more injection power to

occur as can be seen for the cases of +0.20, +0.30, +0.40 and +0.50 nm detunings. It is also clear that the width of the hysteresis cycle is dependent on the initial wavelength detuning and injection power. In other words, the higher the initial positive wavelength detuning, the wider is the hysteresis cycle and the more power is required to achieve PS. It is also worth mentioning that for detuning values below +0.10 nm, only gradual PS was observed (as in Fig. 4.9) and no abrupt PS or PB were obtained.

4.4.3.2.2 Power induced PS and PB behaviour of spin-VCSEL under LCP pumping and RCP injection

In the second case of the second scenario, the polarisation of the pump and that of the ML have been interchanged so the spin-VCSEL was subject to LCP optical pumping and RCP optical injection. Fig. 4.11 plots the relation between the spin-VCSEL output ellipticity (ε) and the injection power for different negative initial wavelength detunings (Δλ), -0.50, -0.40, -0.30, -0.20, -0.10, and 0 nm. As previously mentioned in connection with Fig. 4.9, this figure also shows that, initially, the polarisation of the spin-VCSEL is controlled by that of the optical pump (ε = 0.80) when the ML is off and then with increasing power of the ML to higher values, the SL's polarisation ellipticity is gradually switched from almost RCP (ε = 0.80) to LCP (ε = -1). Similarly, it can be also seen in Fig. 4.11 that for higher negative wavelength detunings, the spin-VCSEL output ellipticity requires more injection power to switch it gradually to the opposite polarisation state. However, the power required to achieve gradual PS in this case (under LCP pumping and RCP injection) is slightly lower than its counterpart in the case of Fig. 4.9 (under RCP pumping and LCP injection).

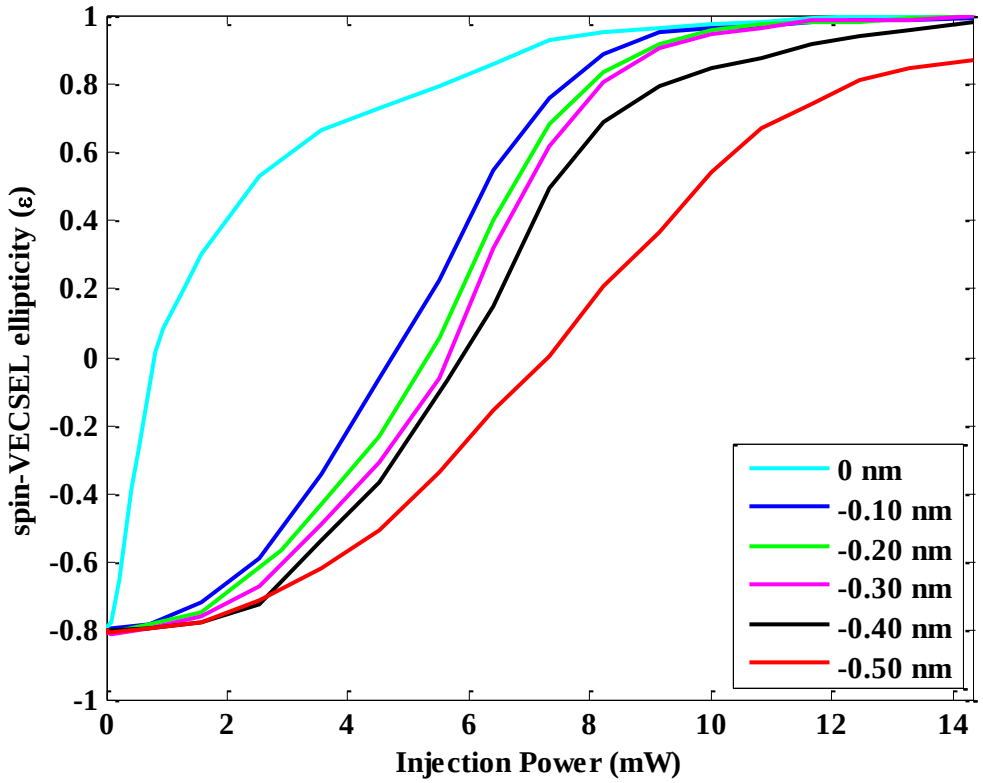

Fig. 4.11: Output polarisation ellipticity (ε) as a function of injection power under LCP optical pump and RCP optical injection for negative initial wavelength detunings. Results are plotted for increasing injection strength values.

The other part of this second case of analysis is shown in Fig. 4.12. This figure illustrates the variation of ε vs. injection power for positive initial wavelength detunings when the spin-VCSEL was subject to LCP optical pumping and RCP optical injection. Under the same conditions, the measurements were performed at different ML wavelength detuning (Δλ) of, +0.10, +0.20, +0.30, +0.40 and +0.50 nm. The SL's behaviour in this case is almost identical to the one shown in Fig. 4.10. For example when (Δλ) was set to +0.10 nm, starting with the injection strength at zero, the polarisation of the pump controls that of the SL for low enough injection power whereas for higher values of injection (above 1.7 mW) the control of the SL's polarisation passed from the pump to the ML. This was also accompanied by abrupt PS from almost LCP (ε = -0.80) to RCP (ε = +1). Moreover, decreasing the injection

power back to zero caused PS from RCP to LCP at a lower and different injection value (1.29 mW). This demonstrates the existence of PB with anticlockwise hysteresis cycle as illustrated in Fig. 4.12.

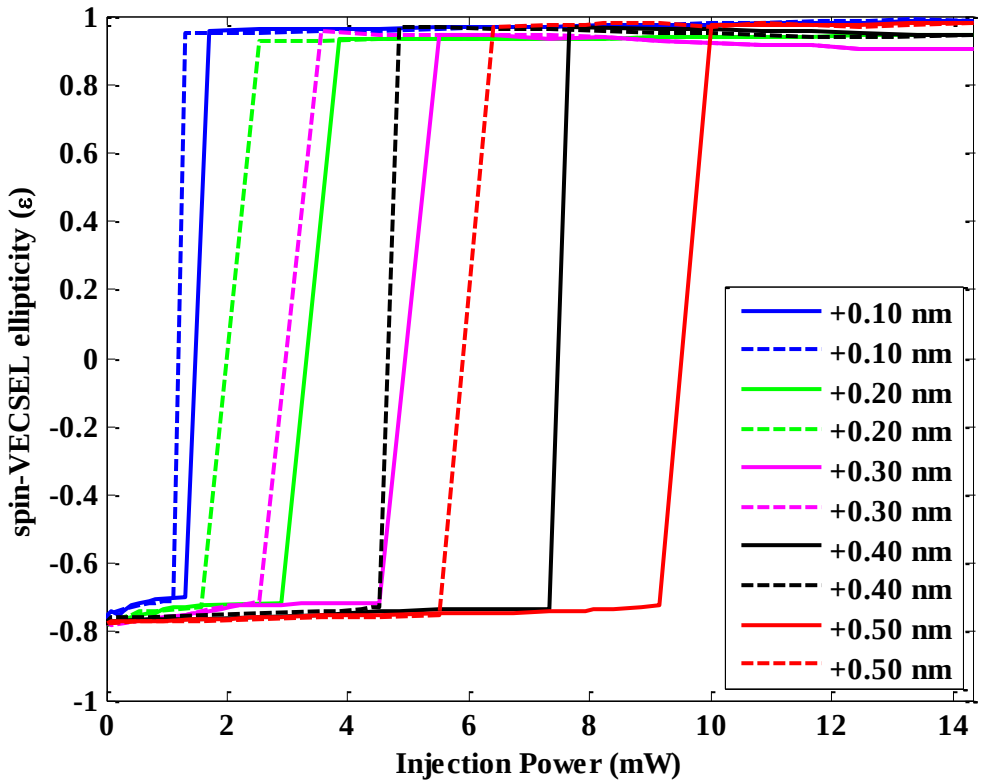

Fig. 4.12: Output polarisation ellipticity (ε) as a function of injection power under LCP optical pump and RCP optical injection for positive initial wavelength detunings. Results are plotted for increasing (solid lines) and decreasing (dashed lines) injection strength values.

This figure shows that the width of the nonlinear hysteresis cycle and PB transition changes as the initial wavelength detuning is increased for higher positive values. It can be also noted that the required injection power to achieve abrupt PS for positive wavelength detuning increases with increased initial detuning. However, the minimum injection power to achieve abrupt PS in this case (1.7 mW) is slightly higher than in the case of Fig. 4.10 (700 μW, under RCP pumping and LCP injection). Moreover, PS below +0.10 nm initial wavelength detuning takes place gradually,

similar to the PS in the negative detuning side, and neither abrupt PS nor PB were observed.

4.5 Discussion

The results presented in this chapter show that an optically pumped spin-VCSEL subject to polarised optical injection exhibits rich polarisation dynamics ranging from polarisation control [132] to circular PS and circular PB [133]. The results here started by presenting the input-output curve and optical spectrum of the solitary spin-VCSEL. Then, the effects of the injection strength, polarisation and initial detuning of the externally injected optical signal on the ellipticity (ε) of the spin-VCSEL's emission were investigated. It had previously been experimentally and theoretically demonstrated that the solitary 1300 nm dilute nitride spin-VCSEL polarisation follows that of the optical pump [22]. However, when the spin-VCSEL is optically injected with either RCP or LCP from an external ML, the spin-VCSEL shows a different behaviour. It has been found that the polarisation of the spin-VCSEL follows that of the optical pump under low injection power whereas under high injection power the polarisation of the spin-VCSEL was effectively controlled by the polarisation of the ML's optically injected signal [132] within the locking region of the SL. Moreover, optical injection with circularly polarised light (RCP or LCP) produced a high degree of ellipticity in the spin-VCSEL. It has also been experimentally and theoretically found that under the same circumstances it is much easier to lock the same helicity than the opposite one.

The experimental results were in good agreement with the theoretical calculations. However, there are some slight variations in some parameters such as birefringence, dichroism, coupling rate, injection strength and angle. These variations emerge when

one or more of the experiment's conditions changes such as changing the pump and injection spot position, changing the polarisation of the pump or that of the ML and changing the lens-ended fibre position with respect to the sample.

The different values of birefringence arise from the strain in the sample, which changes at different positions, and hence they depend on the pumped and injected position. As already mentioned, the birefringence was changed between 19 ns^{-1} and 6.6 ns^{-1} by applying strain to the VCSEL as shown in Figs. 2 and 5 of [81], respectively, for theoretical values fitted to experiment. Furthermore, mechanical strain along first the [1,-1,0] axis and then the [1,1,0] axis was experimentally used to achieve a high-birefringence rate of γ_p/π~80 GHz in conventional VCSEL [231] where a VCSEL was bent in a direction coinciding with one of the two preferred polarisation directions. Such uniaxial bending causes tensile strain which results in an anisotropic change of the refractive index leading to wavelength difference between the two orthogonally polarised modes. For the [1,1,0] axis, the mechanical strain-induced birefringence frequency splitting between the two polarisation modes increases from 1.3 GHz up to 79 GHz [231]. Theoretical predictions also reveal the possibility of obtaining high-frequency birefringence leading to an oscillation frequency of >200 GHz in spin-VCSELs [216]. Very recently, Pusch et al. have demonstrated a record-high birefringence splitting of more than 250 GHz in a QW 850 nm VCSEL via mechanically induced strain along [0,1,-1] and [0,-1,-1] crystal directions [218]. One last factor is that the birefringence could be induced by tightly focusing a beam on the surface of the spin-VCSEL. Jansen van Doorn et al have introduced intentional birefringence by creating a small hot spot at the surface of the VCSEL [29]. This was done by tightly focusing a Ti-sapphire beam on the surface of the VCSEL with the aid of a lens. Thermal expansion around this hot spot produces strain in the VCSEL

leading to birefringence in the VCSEL [29]. Therefore, since a very small lensed optical fibre was used in the pump/injection system in this work and since its position and distance with respect to the sample were frequently changed, it would be expected to get slightly different birefringence values of the spin-VCSEL each time the position of the fibre changes.

The difference in the injection strength and coupling rate values refer to the coupling efficiency of the injected signal into the active region of the sample since not all the optical injection power actually couples into the SL due to the optical alignment coupling losses. It is also difficult to maintain the same coupling efficiency level at every run of the experimental measurement when the experimental setup experiences any changes due to replacing the sample or moving the pump/injection spot position over the surface of the sample as well as the position of the tip of the lensed fibre with respect to the sample. Thus, the more the injection power coupled into the sample the higher the DOCP to be achieved. It should be noted that the injection power (strength) in the first two sections of the results was measured as the amount of ML's optical power incident on the surface of sample. The difference in the injection angle is related to the accuracy of the PC since experimentally it needs more effort to maintain the injection angle at ($\theta_p = 45^\circ$) all the time with a paddle-base PC.

In the third section of the results, circular PS and PB in the optically injected 1300 nm dilute nitride spin-VCSEL were studied. These are the first experimental observations of circularly polarised injection-induced circular PS and PB into a spin-VCSEL. However, PS and PB were reported for the first time in a short-wavelength conventional VCSEL subject to orthogonal optical injection by Pan et al [33]. Since then, parallel [127] and orthogonal [151, 155] optical injection has become a common method to obtain PS and PB in short or long conventional VCSELs [126, 152, 156-

158]. Optical injection of arbitrary polarisation was also reported theoretically by Al-Seyab et al. [130] and experimentally by Hurtado [155] to produce PS in a 1550-nm VCSEL. Nevertheless, there has only been one experimental report of PS induced by circularly-polarised injection into two 850 nm VCSELs [131].

Different forms of circular PS, gradual and abrupt, in addition to different forms of PB, anticlockwise and clockwise, have been experimentally observed. The gradual and abrupt PS depends on the injection power and initial wavelength detuning. The same dependence applies to the width of the hysteresis cycle of the PB. The dependence of the PS and PB on the injection power and initial wavelength has been already reported for conventional VCSELs and VCSOAs, among others in [145, 232-235].

The control of the polarisation is crucial for VCSELs in polarisation sensitive applications such as optical switching [236], external modulated systems, polarisation coherent transmission and magneto-optic disks as well as applications for information processing or storage [237, 238].

The PS and PB results are of great interest for the development of reduced manufacturing, low power consumption, high-speed all-optical bistable flip-flops [239, 240], all-optical inverter [241], logic gates [242, 243], as well as all optical bistable buffer memory [223-229] for all-optical signal processing applications in optical communication networks and novel photonic neurons [244, 245]. These functions are easily achievable with large hysteresis widths for PB, as has been reported in VCSELs.

4.6 Summary

In summary, this chapter reported the first experimental demonstration of optical injection into the dilute nitride 1300 nm spin-VCSEL. It has been found that the polarisation of the spin-VCSEL follows that of the optical pump under low injection

power whereas under high injection power the polarisation of the spin-VCSEL was effectively controlled by the polarisation of the ML's optically-injected signal. Moreover optical injection with circularly polarised light (RCP or LCP) produced a high degree of ellipticity in the spin-VCSEL. This behaviour is in good agreement with theoretical predictions from the SFM.

Moreover, the experimental observations of optical power circular PS and PB in a 1300 nm spin-VCSEL subject to circularly polarised external optical injection were presented. The relationships between output polarisation ellipticity and optical power variations have been experimentally analysed using different polarisation states for pump and injection. Different forms of circular PS, gradual and abrupt, in addition to different forms of PB, anticlockwise and clockwise, have been experimentally observed.

The effective and accurate control of the polarisation of the spin-VCSEL via the pump or the optical injection offers prospects for applications such as optical networks and spintronics for data encoding or for other applications where stabilised VCSEL polarisation is required. Moreover, the diversity of behaviour in a spin-VCSEL at the important telecom wavelength of 1300 nm and operated at RT offers promise for novel uses of spin lasers in optical signal processing, optical switching and optical interconnection applications, such as all-optical inversion and all-optical signal regeneration, in long-haul optical networks.

CHAPTER 5: NONLINEAR DYNAMICS OF OPTICALLY-INJECTED SPIN-VCSEL[i]

Abstract:

This *chapter experimentally presents rich nonlinear dynamics of an optically injected 1310 nm dilute nitride spin-VCSEL with different types of polarised injection. These dynamics are similar to the ones reported in the literature for optically injected conventional VCSELs. The nonlinear dynamics include limit cycle, period doubling, chaotic oscillations and four-wave mixing. In addition to this the findings reveal more dynamics such as light amplification, frequency pulling and pushing effect and wavelength conversion.*

---

[i] This chapter is based on the papers:

1- S.S. Alharthi, V.-M. Korpijarvi, M. Guina, I.D. Henning and M.J. Adams, "Nonlinear dynamics of a 1300 nm spin-VCSEL Subject to Circularly Polarised Optical Injection", in preparation.

5.1 Introduction

Over recent years the dynamics of optically injected conventional VCSELs have attracted great attention within the research community due to their nonlinear properties. Rich varieties of nonlinear responses were found in short and long wavelength VCSEL devices subject to optical injection. These nonlinear dynamics include IL [119, 127, 140, 148, 154, 220], periodic dynamics (P1, P2) [120, 127, 148, 154], irregular behaviour [126, 154], PS and PB [127, 155-157], quasiperiodic oscillations [246], periodic pulsations and C [119, 120, 126, 127, 154]. In addition to this optical injection in conventional VCSELs leads to different kind of wave mixing [118, 120, 121, 148, 169], subharmonic resonance [118, 120, 247] and frequency pulling and pushing effects [118, 154, 169, 248, 249]. Furthermore, the dynamic behaviour and circular polarisation properties of a spin-VCSEL subject to different forms of polarised optical injection (linear, circular, and elliptical) have been theoretically investigated in our group [62]. These include the effect of the external polarised optical injection on the lasing characteristics of spin-VCSELs and the effects of some parameters of the SFM such as the spin relaxation rate, birefringence decay rate, the pumping power and ellipticity on the stability and polarisation properties of optically injected spin-VCSELs. New regions of IL and nonlinear dynamics ranging from periodic dynamics to C were found [62].

In this chapter, we report an experimental study of the nonlinear dynamics induced by different types of polarised optical injection in a 1300 nm dilute nitride spin-VCSEL. The spin-VCSEL was always pumped with circular (either right or left) polarisation while the polarisation of the ML was interchanged between linear (horizontal and vertical) and circular (right and left) polarisations. Different cases are investigated including the situation when the pump and the ML have the same circular

polarisation state, when the pump is circular polarisation while the ML is linear vertical polarisation and the last case when the pump is circular polarisation and the ML has linear horizontal polarisation state. For the first time to the best of our knowledge we report experimentally measured evolution of optical spectra maps of that system identifying nonlinear dynamics via scanning the ML wavelength across the IL region of the spin-VCSEL for different injection strengths. A variety of nonlinear behaviours, including periodic (P1, P2), wave mixing and chaotic dynamics have been experimentally found. Special attention is paid to the influence of the frequency detuning and in some occasions on the type of the dynamics. Possible potential applications arising from optical injection-induced dynamics in spin-VCSELs are discussed in addition to those that have been already mentioned in the previous chapter.

5.2 Results

The experimental setup described in chapter 4 was used to conduct all the measurements and results presented in this chapter. All these measurements and results were obtained from sample 1 (described in chapter 3). This sample as reported in [22] and also mentioned in chapter 3 always shows stable behaviour under the polarised pumping for all the possible pumping powers at our lab. All the results in this chapter were obtained while the spin-VCSEL was pumped at 1.1 times its threshold.

5.2.1 Nonlinear dynamics of optically injected spin-VCSEL

This section is devoted to study the dynamic behaviour of spin-VCSELs subject to polarised optical injection. Different maps have been plotted to display the evolution of the optical spectrum of the spin-VCSEL with the ML wavelength at constant injection

strength (K). It is worth pointing out that, due to the coupling losses, not all the optical injection power actually couples into the SL. While it is difficult to directly measure the actual injection power ratio, the injection strength (K) is defined, from now until the end of this chapter, as the ratio of the ML power over the solitary SL power as it appears on the optical spectrum of the OSA. In addition, the frequency detuning is defined as $\Delta f = f_{ML} - f_{SL}$, where f_{ML} is the frequency of the (ML) and f_{SL} is the free-running frequency of the solitary spin-VCSEL SL. In this section four cases will be presented in accordance to the polarisation of the ML with respect to that of the pump. In all the cases the spin-VCSEL was optically pumped with either right or left circular polarisation and simultaneously injected with either linear or circular polarisation. One map of each case has been chosen as an example to show various behaviours and phenomena as will be shown later in following subsections.

5.2.1.1 Optical spectra maps and dynamics for the optically injected spin-VCSEL

The optical spectra of the optically injected spin-VCSEL will be presented in this subsection in the form of evolution maps in the plane of spin-VCSEL wavelength and the frequency detuning (Δf) between the ML and SL. The results presented in each case were obtained at a constant optical injection (K), while the frequency detuning was scanned, (decreased from positive, short wavelength, to negative, long wavelength, values), across the IL region of the solitary spin-VCSEL. For each case one example will be studied and its associated dynamics will be discussed.

First case: the SL was pumped and injected with the same circular polarisation state.

The example for this case is shown here when the SL was pumped and injected with LCP. Fig. 5.1 presents the evolution of the optical spectrum of the SL subject to LCP

pumping and LCP injection. The injection ratio (K) in this case was K = 0.85 while the wavelength of the solitary spin-VCSEL was 1296.65 nm and pumped at 1.1 times its threshold. The colour map is graded from black, representing the noise level of the measurement, to white, corresponding to the maximum peak power, through red and yellow.

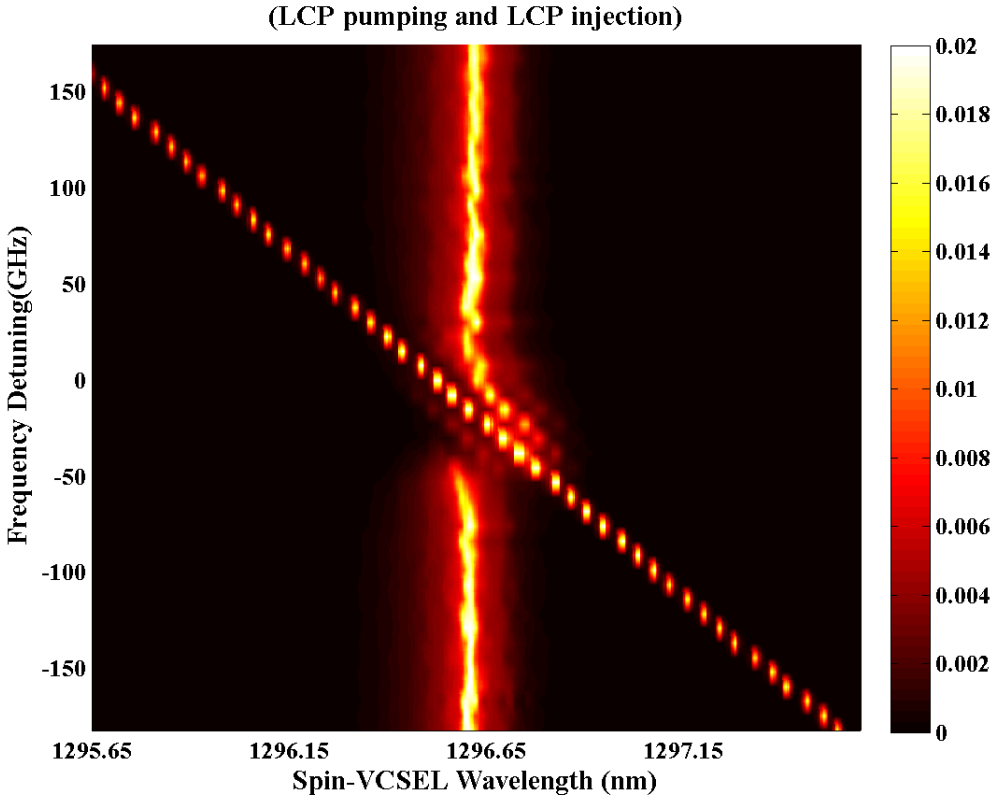

Fig. 5.1: Evolution of the optical spectrum of spin-VCSEL under LCP pumping and optical injection.

It can be seen that as the ML approached the SL's locking bandwidth, it started pushing its wavelength to higher values. The frequency pushing effect is already known in semiconductor lasers under optical injection and will be discussed in a section 5.2.2.2 of this chapter.

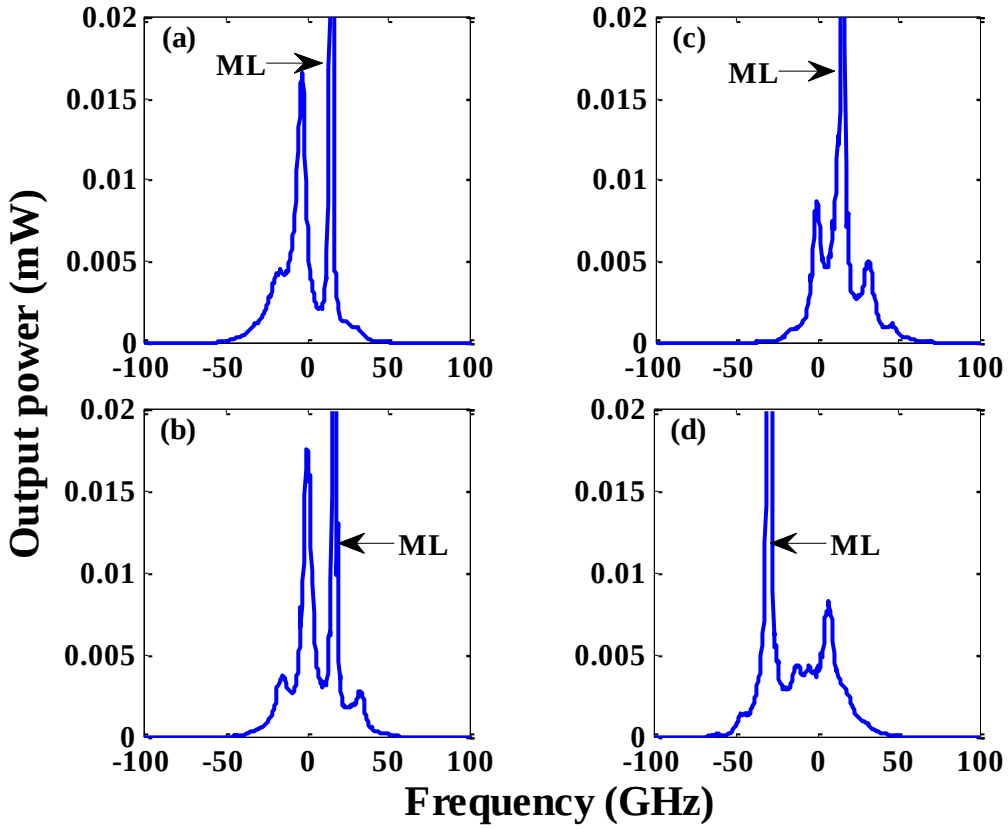

Fig. 5.2: Optical spectra of the spin-VCSEL subject to optical injection with LCP. The arrow marks the ML frequency position. (a) Period one. (b) Four-wave mixing FWM. (c) Degenerate four-wave mixing DFWM. (c) Chaotic behaviour.

As the frequency detuning between the ML and SL was varied in the range between 15 and -7 GHz, small peaks developed on both sides of the SL's spectrum revealing P1 oscillations as shown in the optical spectrum of Fig. 5.2(a). The zero of X-axes of the plots in Fig. 5.2 coincides with the SL frequency under injection while the arrow marks the ML frequency position and the spin-VCSEL output powers measured in few tens of μW. For a further frequency detuning decrease, two weak sideband peaks appeared outside the ML and the SL peaks, indicating Four Wave Mixing (FWM) dynamics as shown in Fig. 5.2(b). The two sideband peaks appeared for a frequency detuning range between -6 and -30 GHz. The lower and upper sideband peaks (LSB and USB) were positioned at the same frequency offset on either side of the ML and SL peaks. The weak sideband peaks of Fig. 5.2(b) correspond to the amplified signal and conjugate

beam from the four-wave mixing between the injection signal beam and the SL main peak. The frequency offset between the SL (ML) and the USB (LSB) is equal to that between the SL and ML and half that between the SL and LSB (USB). The power of these sideband peaks grew slightly while the SL power decreased when the frequency detuning decreased to lower values within this range until some features of the FWM disappeared. For a further decrease of the frequency detuning, the power of the SL peak decreased and the sideband peaks stretched and disappeared until the spectrum was dominated only by three peaks, which is a sign of degenerate wave mixing (DFWM) as shown in Fig. 5.2(c) within the detuning range of -29 to -46 GHz. Next the spectrum became dominated by a broad pedestal and small features as in Fig. 5.2(d), indicative of chaotic dynamics for detunings between -45 and -53 GHz, after which the SL returned to its free-running wavelength at a detuning of -52 GHz.

It should be noted that there was no clear injection IL observed whilst scanning the ML wavelength across the SL locking bandwidth. This might be due to the very broad optical spectrum of the spin-VCSEL or insufficient injection power. However, the broad spectrum of the spin-VCSEL could be treated as a two-mode spin-VCSEL with a very small separation in which case it will produce, in this case, very complex dynamical routes similar to those reported in [121] for VCSELs and in [250] for EELs. In this case the ML should lock one of the two modes whilst the other mode behaves independently. Resolving such dynamics is beyond the capabilities of our lab.

Second case: the SL was pumped and injected with opposite circular polarisation states.

Fig. 5.3 shows the evolution of the optical spectrum of the spin-VCSEL under LCP pumping and RCP optical injection. The injection ratio was K = 155 and the wavelength of the solitary spin-VCSEL was 1297.48 nm.

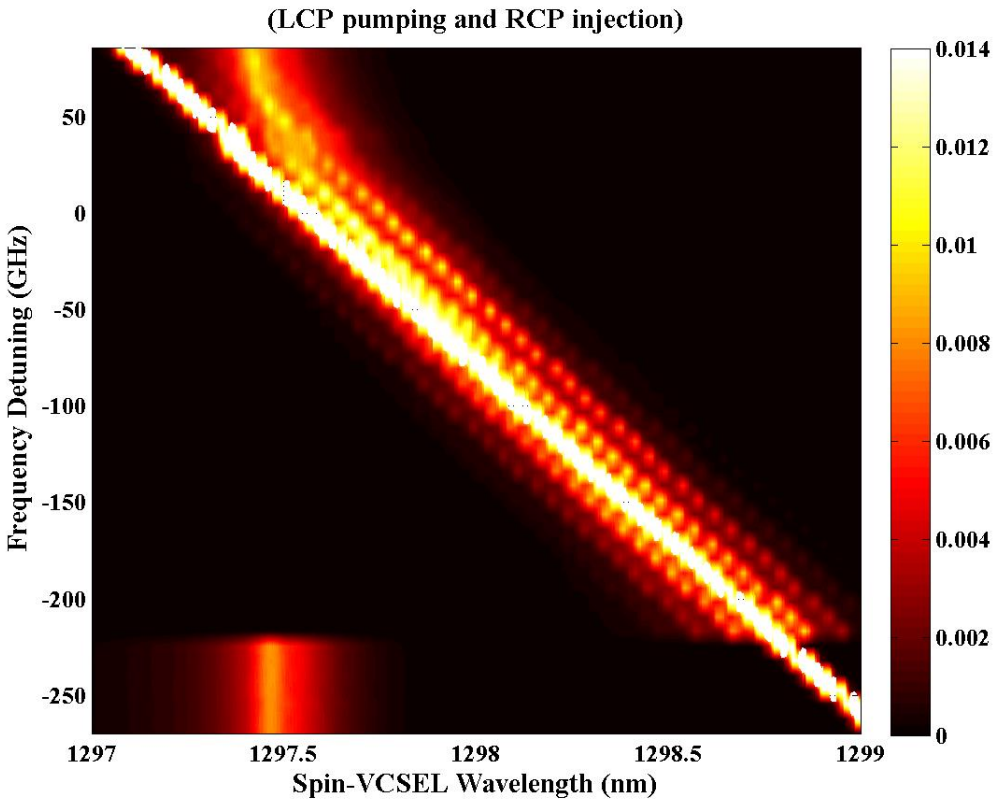

Fig. 5.3: Evolution of the optical spectrum of spin-VCSEL under LCP pumping and RCP optical injection.

Similar behaviour can be also seen where the ML pushed the SL to higher wavelength values as it entered its locking region, but in this case the pushing bandwidth is bigger than in the previous case. This is due to the high injection strength compared to the previous case as a strong optical injection power yields a wider range of wavelength detuning and hence a wider bandwidth of the frequency pushing effect. The coupling rate and efficiency also plays an important role in determining the bandwidth of the frequency pushing effect before the SL returns (is unlocked or released) to its solitary frequency position as already found in section 4.2.2.1 of chapter 4.

Dynamics appeared at the spin-VCSEL output, in the form of P1 oscillation, for frequency detuning between 64 and 41 GHz as shown in Fig. 5.4(a). For a further decrease of the frequency detuning between 40 and 25 GHz Fig. 5.4(b), the SL's

spectrum became dominated by a broad pedestal; such a spectrum is an indicative of chaotic dynamics. Then as the frequency detuning decreased the spectrum went again into a P1 dynamics region between 24 and -5 GHz characterised by two peaks around the SL peak. Decreasing the frequency detuning between -4 and -27 GHz, two other smaller side peaks appeared in the spectrum of the SL and between the sharp peaks, smaller features were observed, which indicates P2 dynamics as shown in Fig. 5.4(c). The frequency offset between the smaller peaks and the SL is double the one between the SL and the two sharp peaks. Then the spin-VCSEL went again into a chaotic region as the frequency detuning reduced within the range of -26 and -43 GHz. For a decrease of the frequency detuning, more peaks started growing up Fig. 5.4(d) on both sides of the ML and SL peaks of Fig. 5.4(c) forming cascade four-wave mixing. When frequency detuning is decreased into the region between -42 and -163 GHz, multiple peaks of FWM and Multi-Wave mixing (MWM) were observed in this region as shown in Fig. 5.4(e). Then at the frequency detuning of -164 GHz the power of the SL was transferred to a peak with shorter wavelength (positive detuning side) which is indicative of wavelength conversion as shown in Fig. 5.4(f). This phenomenon will be discussed further in section 5.2.2.3. For a further decrease of frequency detuning to -202 GHz, the SL power transferred back to its main peak until the SL was released at -224 GHz and returned back to the solitary frequency. It is worth mentioning that the signature of the peaks in the all the spectra shown in this chapter have been worked out by positioning the peaks of the SL at zero frequency and then measure the offset between it and the other appearing peaks via the OSA and Matlab during the data processing. This was done after converting the wavelength to into its corresponding frequency.

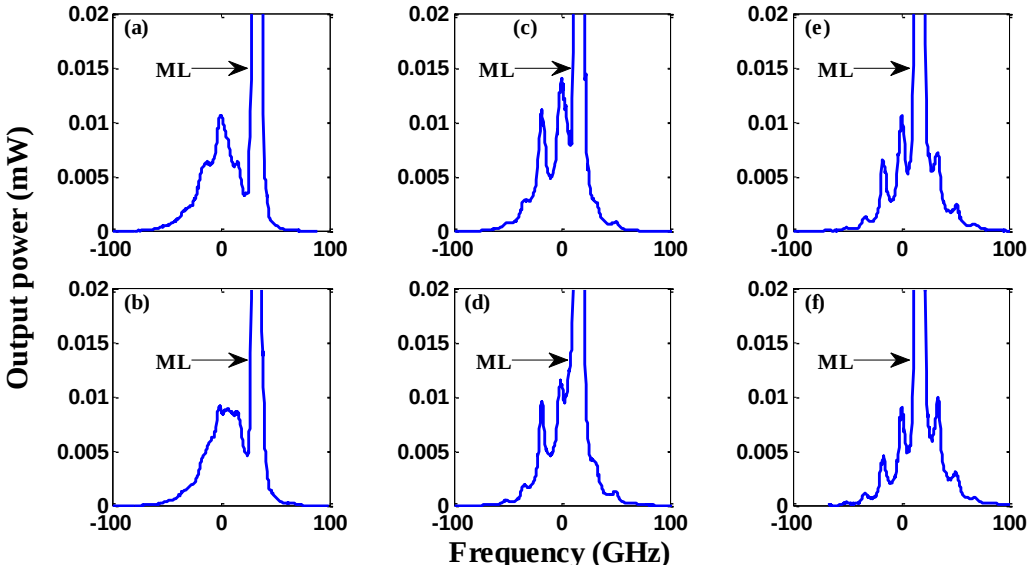

Fig. 5.4: Optical spectra of the spin-VCSEL pumped with LCP and subject to optical injection with RCP. The arrow marks the ML frequency position. (a) Period one oscillation P1. (b) Chaotic oscillation. (c) Period two P2. (d) More peaks appearance. (e) Four-wave mixing. (f) Wavelength conversion.

Third case: the SL was pumped with circular polarisation and injected with linear vertical polarisation.

The evolution of the optical spectrum of spin-VCSEL under LCP pumping and linear vertical polarised (LVP) optical injection is presented in Fig. 5.5. In this case the injection ratio was K = 53 and the wavelength of the solitary spin-VCSEL was 1298.03 nm. It can be seen that as the ML got closer to the SL, it started pulling its wavelength towards lower values. The SL was pulled towards the ML for a bandwidth of about 12 GHz. The pulling frequency is a well-known phenomenon in semiconductor lasers and will be discussed in more details later in section 5.2.2.2 of this chapter. For a further decrease of the frequency detuning the ML started pushing the SL towards higher wavelength values.

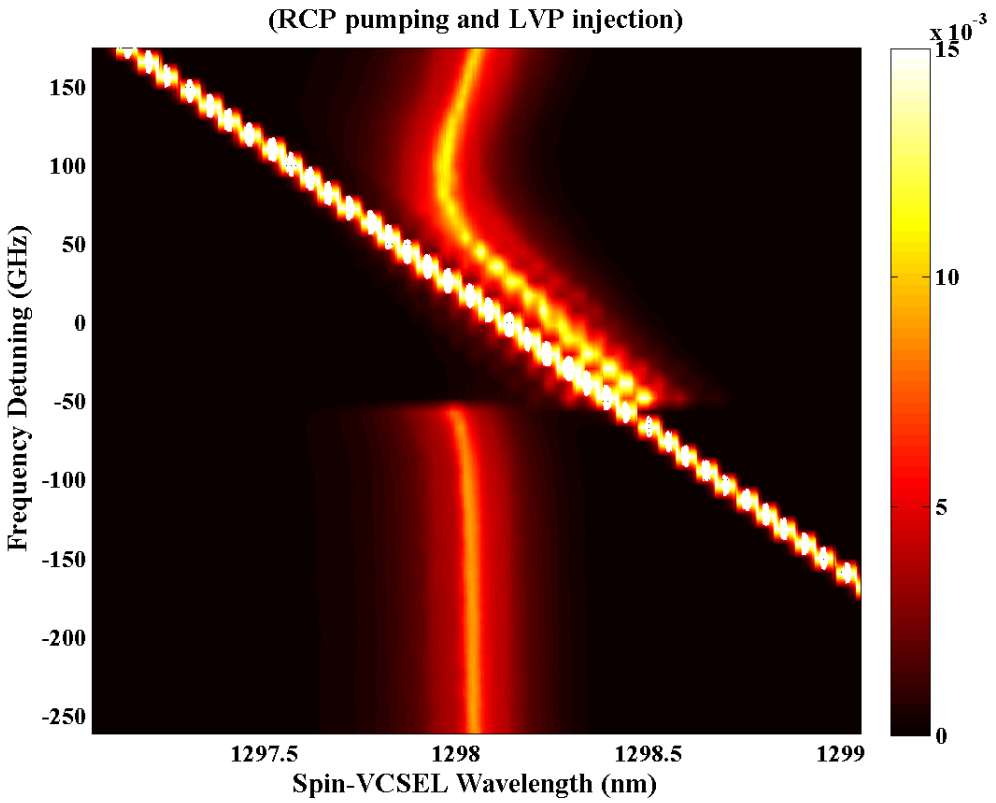

Fig. 5.5: Evolution of the optical spectrum of spin-VCSEL under RCP pumping and LVP optical injection.

The first observation of dynamics was at a frequency detuning between 72 and 17 GHz in the form of P1 oscillation as shown in Fig. 5.6(a). Then the SL went into P2 as the frequency detuning decreased from 16 to -10 GHz as Fig. 5.6(b) depicts. As the frequency detuning decreased to the range of -9 to -29 GHz the SL experienced broadening in its optical spectrum which might be a sign of chaotic oscillations as shown in Fig. 5.6(c). FWM and MWM were observed for frequency detuning between -28 and -38 GHz as shown in Fig. 5.6(d). For any detuning decrease after this range, the SL goes back to its solitary wavelength position. Moreover, the change in SL wavelength once the SL left the injection region indicates the possibility of PS occurring.

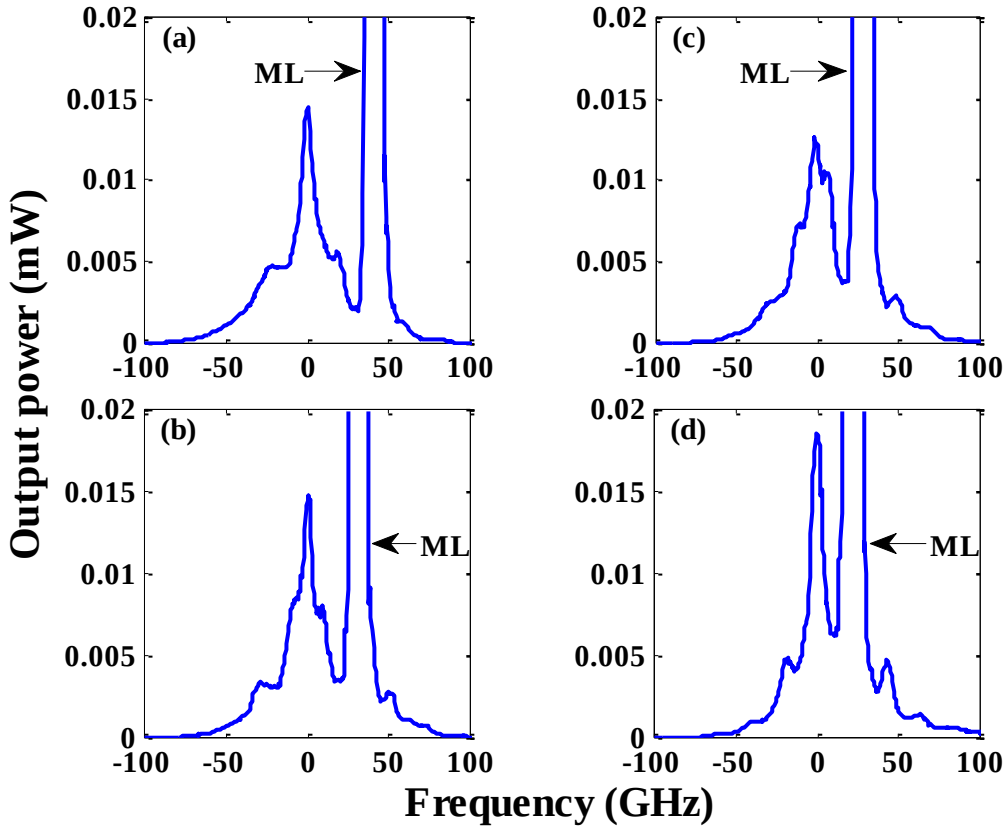

Fig. 5.6: Optical spectra of the spin-VCSEL pumped with LCP and subject to optical injection with LVP. The arrow marks the ML frequency position. (a) Period one P1. (b) Period doubling P2. (c) Chaotic oscillation C. (d) Four-wave mixing FWM.

Fourth case: the SL was pumped with circular polarisation and injected with linear horizontal polarisation.

The evolution of the optical spectrum of the spin-VCSEL under LCP pumping and linear horizontal polarised (LHP) optical injection is presented in Fig. 5.7. In this case the injection ratio was K = 66 and the wavelength of the solitary spin-VCSEL is 1298.04 nm. This figure shows that as the ML approached the SL, it started pulling its wavelength towards lower values. The SL was pulled towards the ML for a bandwidth of about 9 GHz. The pulling effect is slightly less than in the previous case due to the difference in the injection strength as will be presented in section 5.2.2.2 later in this chapter. Dynamics are illustrated and explained in Fig. 5.8.

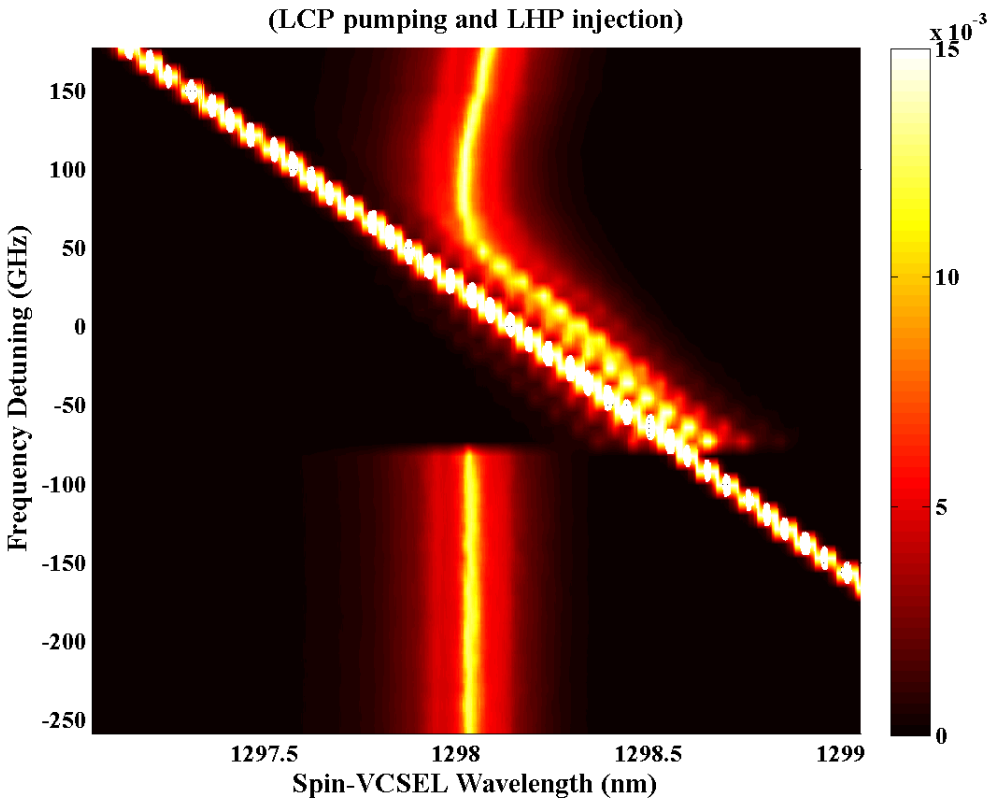

Fig. 5.7: Evolution of the optical spectrum of spin-VCSEL under LCP pumping and LHP optical injection.

When the detuning frequency decreases to 50 GHz, the ML started pushing the SL towards higher wavelength values. For a further decrease of the detuning frequency P1 oscillations were found in a detuning frequency range between 38 and 10 GHz as shown in Fig. 5.8(a). Fig. 5.8(b) presents the SL in a P2 region for the detuning frequency range between 9 and -8 GHz. For lower frequencies detuning within the range from -7 to -36 GHz the SL spectrum became broader without well-defined peaks which is a sign of chaotic oscillations as show in Fig. 5.8(c). For further decrease of the frequency detuning, the SL exhibited cascade FWM and MWM for detuning frequencies between -36 and -82 GHz as shown in Fig. 5.8(d). For a further decrease all the peaks stretched and disappeared except for those of the ML and SL (which was released back to the solitary wavelength).

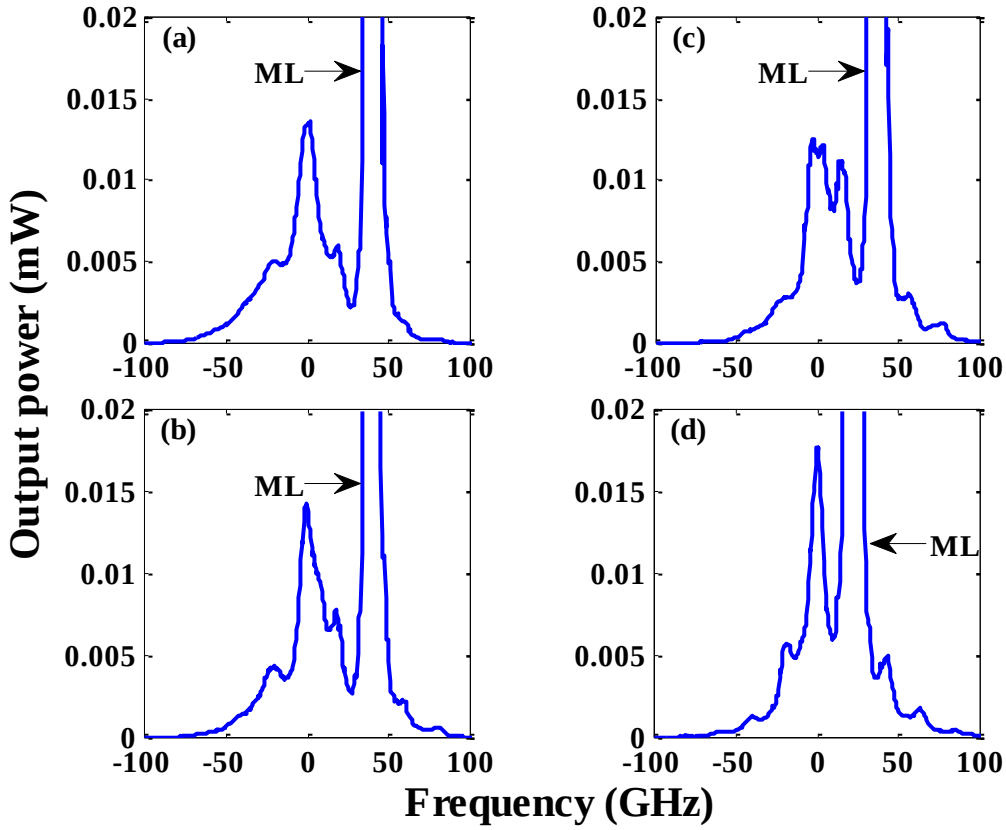

Fig. 5.8: Optical spectra of the spin-VCSEL pumped with LCP and subject to optical injection with LHP. The arrow marks the ML frequency position. (a) Period one P1. (b) Period doubling P2. (c) Chaotic oscillation C. (c) Four-wave mixing FWM.

As can be seen this case is to some extent similar to the previous case and the differences arose from the different values of injection strength. Once the SL left the IL region it set its wavelength to a value different from the solitary one which might be a sign of the occurrence of PS.

5.2.2 Other nonlinear dynamics accompanying optical injection into the spin-VCSEL

In this section the dynamics observed in all the cases presented in the previous section will be presented. These dynamics frequently occur in the spin-VCSEL subject to optical injection no matter what the polarisation state of the ML with respect to that of the pump is.

5.2.2.1 Characteristics of the ML's reflected output power

The behaviour of the output of the ML reflected from the sample of the SL and measured by the OSA is studied in this subsection.

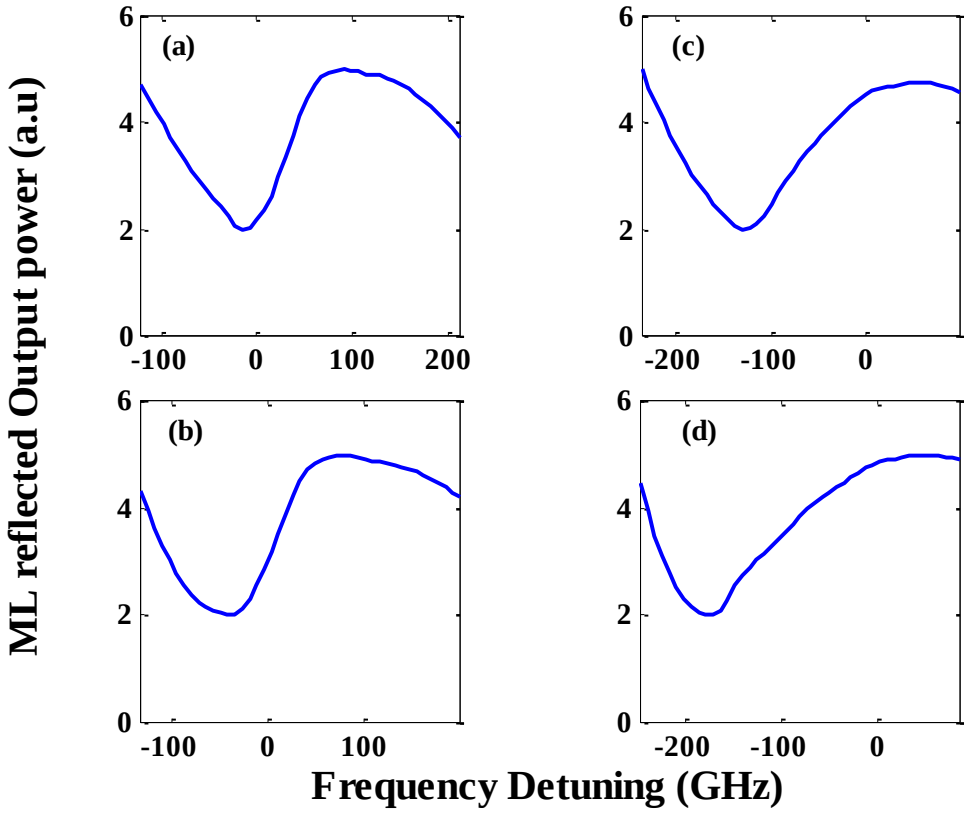

Fig. 5.9: ML's reflected output power as a function of the frequency detuning (Smoothed by 5%) for injection strength of: (a) 4. (b) 21. (c) 135. (d) 156.

Fig. 5.9 shows the ML's reflected output power as a function of the frequency detuning for different injection strength values as follows: (a) 4, (b) 21, (c) 135 and (d) 156. The lines in Fig. 5.9 were smoothed by 5% for clarity. It is worth mentioning that the SL was pumped to 1.1 times its threshold with LCP and injected with LCP in this case. The vertical axis of Fig. 5.9 reflects the magnitude of the output power of the ML measured from the ML's peak of the optical spectrum when the SL is subject to injection at constant injection strength and varying frequency detuning. The level of the output power in Fig. 5.9 was within 1 mW range. Under all the injection power

values of Fig. 5.9, it can be seen that as the detuning decreased, the reflected ML's output increased until it got closer to the IL region of the SL. This increase of the magnitude of the ML peaks corresponds to the occurrence of amplification in the ML signal. Then as the detuning further decreased, the ML's output power started decreasing until it reached a deepest point of the valley where it recovered again and increased for negative detuning values. The recovery point of the ML's output power coincides with the point where the SL returned to its free running frequency position. This point is supposed to be the unlocking point where the ML leaves the locking region of the SL. Fig. 5.9(a)-(d) shows that as the injection power increases from 4 to 156 the valleys in the spectra become shallower and shift away from zero detuning towards lower detuning frequency.

5.2.2.2 Injection-induced frequency pulling and pushing

Other phenomena resulting from optical injection into the spin-VCSEL are the frequency pulling and pushing effects. The injection-induced frequency pulling effect takes place at low injection levels when the ML approaches the IL bandwidth of the SL from shorter wavelengths; the injected signal pulls the SL away from the cavity resonance towards the injected frequency at higher detuning values. Hence, the pulling effect tends to reduce the frequency separation. By contrast the injection-induced frequency pushing occurs at high injection levels when the ML enters the IL region of the SL; the injected signal pushes the SL away from its resonance frequency towards lower detuning values.

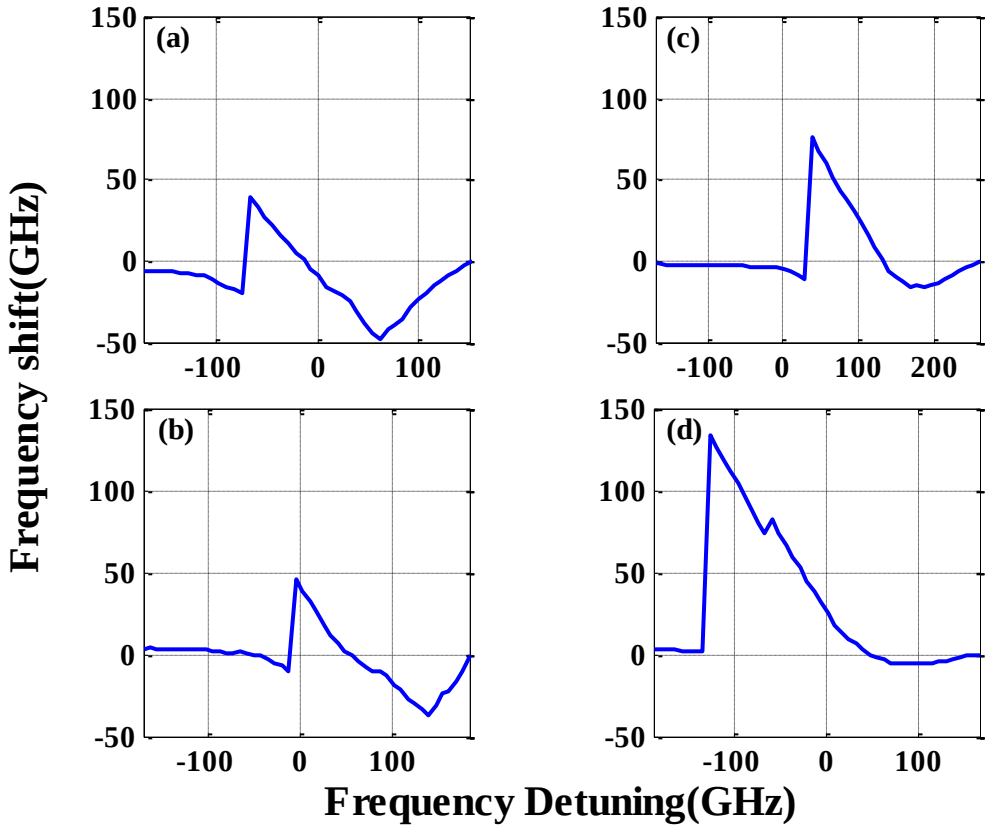

Fig. 5.10: Spin-VCSEL free running frequency shift as a function of the frequency detuning.

The example shown here is when the spin-VCSEL is pumped with RCP and optically injected also with RCP. Fig. 5.10 presents the frequency detuning as a function of the frequency shift from the free running resonance frequency under different injection ratios as follows: (a) 6, (b) 11, (c) 29 and (d) 90. The plots in Fig. 5.10 show that as the frequency detuning decreased the SL shifted its oscillation frequency from the free running resonance frequency towards the optical injection signal at positive detunings until it reached a minimum value. At this value the SL was pulled to a maximum value from its free running cavity resonance. Next as the detuning decreased, the SL went back towards its free running resonance. For a further decrease of the detuning, the SL frequency was pulled away towards lower detuning values until reaching a maximum point where any detuning decrease leads to returning the SL back to its solitary frequency. At this point the frequency pushing reached its

maximum effect. In addition, it can be also seen from Fig. 5.10(a)-(d) that as the injection ratio increases the frequency pulling effect decreases until it disappears at higher injection levels. However, it should be noted that at low injection levels when the injection ratio between the ML and SL powers is < 3, no pulling effect is found. The kink in Fig. 5.10(d) corresponds to wavelength conversion and power transfer similar to the one reported in Fig. 5.4(f) and it will be discussed in more detail in the following subsection.

The aforementioned frequency pulling and pushing maximum values are dependent on the injection strength as shown in Fig. 5.11.

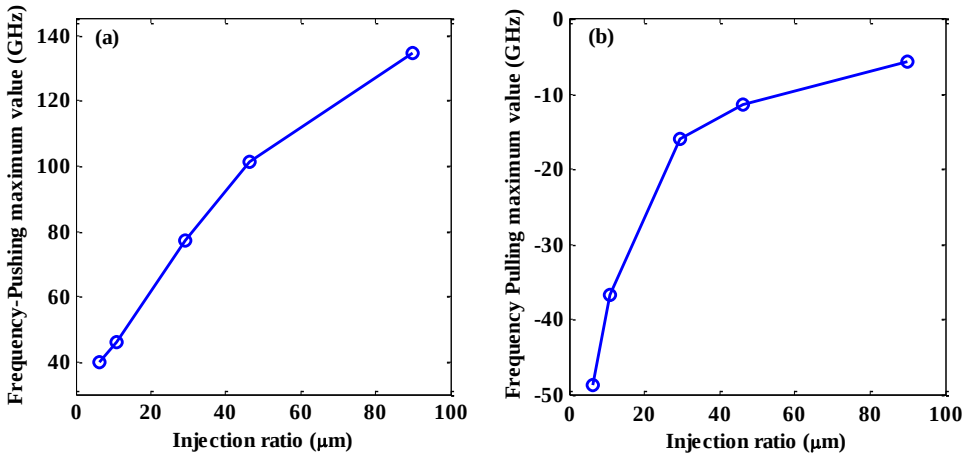

Fig. 5.11: Frequency-pulling and pushing maximum value as a function of the injection strength.

Fig. 5.11(a) presents the maximum values of the pushing effect as a function of the injection ratio. It can be seen from this figure that as the injection strength increases from 6 to 90 the pushing effect exponentially increases from 40 to 135 GHz. On the other hand, the relationship between the maximum values of the pulling effect and the frequency detuning is depicted in Fig. 5.11(b). It is clear from this figure that as the injection strength increases from 6 to 90, the pulling effect exponentially decreases

from -48 to -6 GHz. This might be due to heating effects caused by the strong injection as well as the competition between the pushing and pulling effect in the SL. We believe that pulling and pushing effects are sufficient enough to impede any locking in the negative and positive detuning sides, respectively. Furthermore, for injection strengths below 3 as already mentioned the pulling effect is not found.

5.2.2.3 Wavelength conversion and power transfer

The last phenomenon in this section is the wavelength conversion and power transfer that was shown in Fig. 5.4(f).

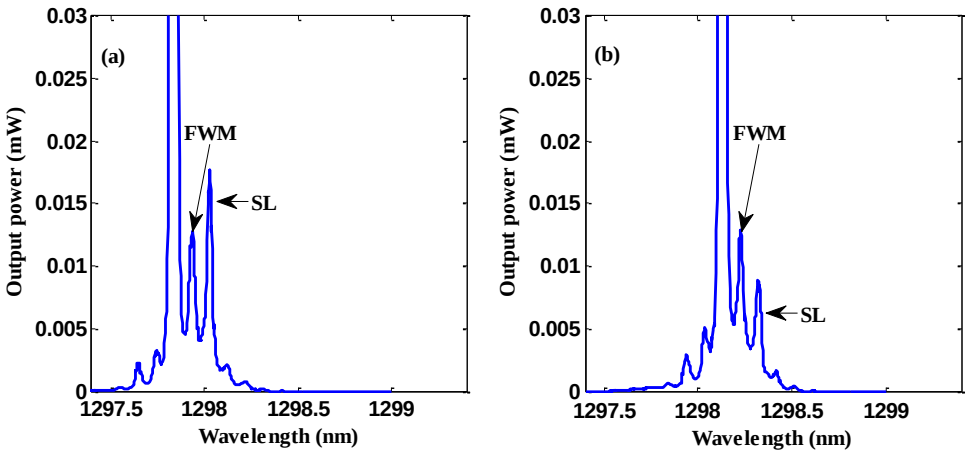

Fig. 5.12: Optical spectra of the optically injected spin-VCSEL showing wavelength switching.

This dynamic occurs only when the FWM and MWM exists within the negative detuning side. While scanning the frequency detuning across the locking region of the SL, two or more peaks appear on both sides of the ML spectrum forming FWM or MWM. Usually, the SL has the highest power apart from the ML. However, if the injection power is strong enough, the SL power decreases and the power of one of the other peaks with lower power value at a different wavelength grows accordingly.

Fig. 5.12 illustrates the optical spectra of the spin-VCSEL subject to LCP pumping and LCP injection. At a certain detuning the power of the SL is transferred to one of the FWM products with lower output which in turn becomes dominant forming wavelength conversion as shown in Fig. 5.12. The detuning frequency in Fig. 5.12(a) is Δf = -44 GHz and the injection strength K = 168. MWM appeared in the spectrum as a result of the injection. Apart from the ML's peaks, the SL presents the highest output power among the other wave-mixing peaks at this stage. As the detuning decreased to 67 GHz, Fig. 5.12(b), the power of the SL was transferred to the second highest peak forming wavelength conversion. The wavelength conversion and power transfer lasts for a certain detuning range then the SL switches back either to its previous peak position or to the free running wavelength position.

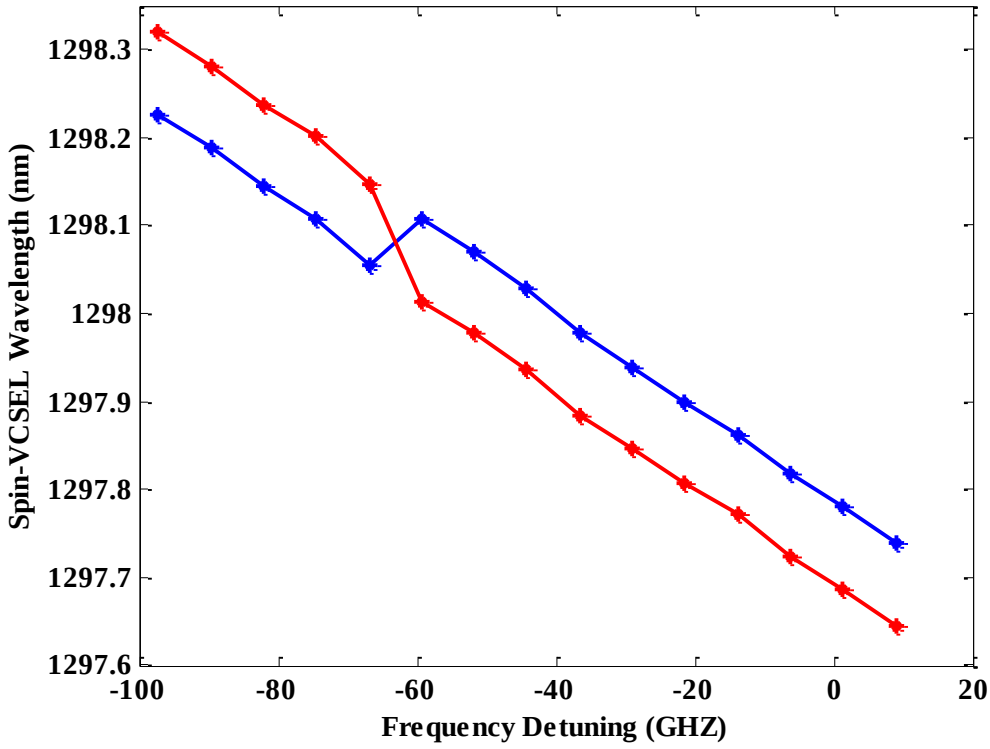

Fig. 5.13: Spin-VCSEL wavelength (blue line) as a function of the frequency detuning.

The wavelength conversion is clearly illustrated in Fig. 5.13 where the spin-VCSEL (blue) and the second highest peak of the FWM (red) are plotted as a function of the

frequency detuning within the FWM dynamics range. It can be seen that as the detuning decreased towards higher values, the SL's wavelength (blue line) exchanged its position with the wave-mixing product (red line), at detunings above 59.37 GHz, with the second highest peak of the FWM. In this case the latter peak became dominant until the SL returned to its solitary wavelength. However, it is worth noting that the output ellipticity of the SL was not changing with this switch where it was governed in this situation by the ML polarisation as discussed in chapter 4.

5.3 Discussion

The results presented in this chapter show that the optically pumped spin-VCSEL subject to polarised optical injection exhibits nonlinear dynamics similar to those found in conventional VCSELs. The nonlinear dynamics found in optically injected spin-VCSELs include P1, P2 and C [251-253]. Additionally, more complex dynamics such as wave mixing and frequency pulling and pushing phenomena were observed in the optically injected spin-VCSEL. All these nonlinear effects in this chapter were observed for the first time to the best of our knowledge for a spin-VCSEL subject to polarised optical injection.

In the first section of the results, a rich variety of nonlinear responses and dynamics of optically injected spin-VCSEL was presented. These included from P1, P2, C, and four-wave mixing (FWM). Similar nonlinear dynamics, including P1, P2, quasi-periodicity, IL, nearly-degenerate four-wave mixing (NDFWM) and C, of conventional VCSELs under orthogonal optical injection has been experimentally and theoretically found and analysed for short wavelength of 850 nm [119, 120, 123, 148-153] and for long wavelength of 1550 nm [125-127, 154, 254] devices.

Four types of nonlinear dynamics were studied in this work. P1 dynamics correspond to the beating between the ML and injected SL frequencies and appear as a periodic oscillation of the laser output at a single frequency and its harmonics. P2 dynamics appear as additional peaks on each side of the optical spectrum of the SL's lasing mode correspond to the first subharmonic of the P1 oscillation. Wave mixing is characterised by the presence of additional weak side band peaks on one or both sides of the SL. The frequency splitting between the SL (ML) and the USB (Lower side band, LSB) is equal to that between the SL and ML and half that between the SL and LSB (USB). Finally, chaotic oscillations (C) correspond to a complex behaviour, and a strong aperiodic oscillation of the SL output. These dynamics were identified based on the optical spectra of the optically injected SL (measured by the OSA) since there was not sufficient output power to allow it to be split between the OSA and ESA. An SOA might be required for further analysis. It should be noted that there were no clear features in the spectra which distinguish locked and unlocked regimes. Within the normal IL region, the different behaviours of the optical spectra clearly show rich nonlinear dynamics in response to the injection frequency detuning and injection ratio variations and, therefore, the SL might not be locked to the injection signal. For decrease of the detuning, the progressive unlocking might be associated with the frequency pushing effect. The nonlinear dynamics observed in this work are in good agreement with the theoretical predictions generated using the SFM in [62]. However, no locking was experimentally found as mentioned earlier due to the quite broad spectrum of the spin-VCSEL where theoretical predictions [62] revealed new locking regions in spin-VCSELs under circularly polarised optical injection in addition to the locking region found in conventional VCSELs under polarised optical injection. The broad spectrum of the spin-VCSEL could be treated as a multi transverse mode with

very short separations and hence under optical injection each mode behaves independently.

Nonlinear dynamics of optically injected semiconductor lasers are interesting for practical applications. P1 oscillation has already proven its potential candidacy to achieve frequency conversion in radio over-fibre (RoF) applications [147] and microwave generation [255, 256]. Optical injection can be used also for laser linewidth and frequency chirp reduction [257], mode partition noise suppression [258] and in enhancing of the bandwidth of chaotic dynamics solely by optical injection [138, 139] or in combination with optical feedback [259, 260] in addition to enhancing the modulation bandwidth without modifying the laser design [261]. Chaotic dynamics, specifically, are of great interest due their possible applications for the use in chaos-based communications [262-264] and efficient cryptography [265], random number generation [266-268] and chaotic lidar [269].

The second section of the results presented other nonlinear dynamics that have been found in the optically injected 1300 nm dilute nitride spin-VCSEL. Studying the ML's reflected power, it has been found that as the detuning decreases, the ML's power was amplified within the negative detuning regime until reaching close to the free-running SL frequency. Then as the detuning further decreases the ML's output power starts decreasing until it reaches a minimum point of the valley. Any further detuning decrease after this point leads to the recovery of the ML output within the negative detuning regime. The recovery point of the ML's output power coincides with the point where the SL returns to its free running frequency position. It has been found that the point of recovery is dependent on the injection ratio and frequency detuning. This behaviour indicates that the spin-VCSEL under optical injection might work as an amplifier. In this case the 1.3 μm input signal will be provided, as required, by the ML.

Amplified signal light will be detected using either the OSA or the optical power meter. The ML, along with the OSA in detection, allows the measurement of the evolution of the amplifier spectrum and peak gain under small input power, i.e. when the amplifier is not saturated.

When the frequency of the ML is outside the locking range and as the ML is detuned towards the SL resonance frequency, it experiences some regenerative amplification while the power of the SL is reduced. The amplification of the ML signal occurs at the cost of the SL output power since the injected signal continues competing with the SL signal by getting enough cavity gain from the SL active region [113]. As the ML is further detuned to inside the locking region, the ML causes a decrease in the carrier density in the active region of the SL due to stimulated emission processes; this, in turn, increases the refractive index in the active region causing the resonance of the SL to shift towards higher detuning [270]. The regenerative amplified signal within the IL range will not increase because the carrier density is reduced (as stated above), and hence the gain is too low [113]. Moreover, the reduced SL gain causes a reduction of the reflected ML output sent to the OSA.

Under normal conditions a further red-shifted cavity resonance leads to a regenerative amplification of the ML while the cavity resonance mode is suppressed. This also results in the SL gain being smaller than its threshold value and hence leads to a reduction of the reflected ML output. Therefore, the SL will be lasing at the master wavelength when it is injection locked [271]. However, since no clear IL was observed and due to the frequency pushing effect in our case, the ML signal will not be increased or amplified within the locking region. Instead, part of the ML output power will be used to compensate the gain reduction of the SL which in turn reduces the ML power reflected from the SL and collected by the OSA. For a further decrease of the

frequency detuning, the ML will leave the IL region and the SL will return to its free-running frequency. In the meantime, the ML's reflected power will recover to its level at the positive frequency detuning before experiencing any amplification. The higher the optical injection power, the wider the wavelength detuning range would be and consequently the more red-shifted the recovery point (defined in section 5.2.2.1) would be.

Furthermore, one of the well-known phenomena of optical injection in semiconductor lasers is the frequency pulling effect [272]. As previously mentioned outside the IL region the external injected light causes changes in the carrier density inside the SL medium. Subsequently, it leads to changes in the effective refractive index of the SL medium which in turn shifts the laser resonance frequency towards blue or red-side frequencies (i.e., SL is pulled towards ML) in accordance to the sign and magnitude of the carrier density difference. In the negative detuning regime, the carrier density will be reduced resulting in negative frequency shifts for the SL resonance frequency. On the contrary, injection in the positive detuning regime leads to increased carrier density which in turn causes positive frequency shift [273]. Inside the IL region, the SL is locked to the ML and the SL resonance frequency is determined by the emission frequency of the ML [270]. However, since no clear locking was found in our case the frequency shift would be expected to appear over all the locking range. The decrease in maximum value of the pulling effect as the injection strength is increased is believed to be due the heating effect caused by the strong injection in addition to the competition between the pulling and pushing effect as the ML was tuned towards higher detuning frequencies.

Under strong optical injection at positive detuning frequencies the pushing effect clearly takes place. This behaviour is already reported in semiconductor lasers subject

to optical injection [272]. Simpson et al [272] found that for optical injection at positive offset frequencies, the degree of frequency pushing effect increases as the detuning frequency is decreased or the injection power is increased. However, in our case for high injection strengths the SL frequency is progressively pushed away from the ML frequency without IL. The frequency pushing effect arises from the dependence of the refractive index of the SL on the carrier concentration in the active region, since the external optical signal causes a decrease of the carrier concentration and thus the increase of the refractive index of the SL, which in turn shifts the cavity resonance wavelength to the longer side [271]. As the optical injection is scanned from positive to negative frequency detuning the cavity resonance is pulled towards the injected light as explained above. As the frequency detuning between the SL and ML is decreased, at a critical point it will no longer be pulled towards the SL [271]. After this critical point, the ML is supposed to lock the SL. However, since no confirmed locking was found after the critical point in the positive detuning regime, the injection light pulls the cavity resonance towards higher detuning values by a small amount; hence the ML will obtain more cavity gain, which results in a further drop off of the carrier concentration and a more red-shifted cavity resonance. The red-shifted cavity resonance leads to the ML experiencing even more cavity gain. The red-shift will continue as the ML is further scanned towards lower detuning values until a specific point in which any further detuning decrease returns the SL to the free-running frequency.

The last interesting dynamic is the wavelength conversion and power transfer. This phenomenon takes place through the FWM dynamics when the wavelength and power of the SL are converted and transferred, respectively, to one of the FWM products as a result of changes in the injection power or frequency detuning. When the converted

signal has a wavelength that is higher (lower) than the SL's wavelength, this is referred to as up- (down-) conversion. Both situations were found under optical injection into the spin-VCSEL. This could be explained when the assumption of treating the broad spectrum of the spin-VCSEL as a multi-mode VCSEL with very short mode separations is taken into account. According to this assumption the converted signal is enhanced by the cavity resonance, since the converted signal might coincide with one of the resonance frequency peaks in the spin-VCSEL cavity [274].

The results in this section reveal that under optical injection a spin-VCSEL can act like an amplifier. Full understanding of the frequency-pulling and pushing effects is required for applications of the frequency convertors in optical communication systems. Wavelength conversion via FWM can be used in wavelength division multiplexed systems [275], wavelength switched optical networks [276] and for generation of self-pulsation in DFB lasers through passive mode locking [277].

5.4 Summary

In summary, this chapter reported the first experimental demonstration of optical injection into the dilute nitride 1300 nm spin-VCSEL. The results in this chapter presented studies of important characteristics of the dynamics of the optically injected spin-VCSEL. Evolution maps of the optical spectra of spin-VCSEL under optical injection with different polarisation states were shown. The investigation of the dynamics of the spin-VCSEL under different types of polarised injection (linearly - circularly) revealed the evolution of the nonlinear dynamics as the frequency detuning or optical injection ratio changed. Various types of instabilities and rich nonlinear dynamics were found including, P1, P2, C and four-wave mixing. These nonlinear dynamics were analysed based on the optical spectra of the spin-VCSEL subject to

optical injection. Finally, further processing of the experimental data revealed more dynamics such as power amplification, frequency-pulling and pushing effects in addition to wavelength conversion and power transfer. The physical mechanisms behind these dynamics were interpreted.

Part II

QD Spin-VECSEL

CHAPTER 6: 1300 NM QUANTUM DOT-SEMICONDUCTOR DISK LASER (QD-SDL)[i]

Abstract:

The first room temperature (RT) Quantum Dot Semiconductor Disk Laser (QD-SDL) operating at 1300 nm is presented in this chapter. The gain structure is composed of 5x3 QD layers; each threefold group was positioned at an antinode of the standing wave of the optical field. Continuous-wave (CW) optical output power above 0.8 mW with threshold pump power of 11 mW is demonstrated using a very simple and compact laser configuration by employing a high reflection (HR)-coated fibre as the top mirror. Using a piezo-electric translation stage the emission wavelength could be tuned over a 14 nm spectral range.

[i] This chapter is based on the papers:

1- S.S. Alharthi, E. Clarke, I.D. Henning and M.J. Adams, "1300 nm Quantum Dot Semiconductor Disk Laser (QD-SDL)", IEEE International Semiconductor Laser Conference (ISLC), Palma de Mallorca, Spain, 7-10 September 2014. [198]

2- S.S. Alharthi, E. Clarke, I.D. Henning and M.J. Adams, "1305 nm quantum dot vertical external cavity surface emitting laser", IEEE Photonics Technology Letters, vol. 27, no. 99 (2015). [196]

6.1 Introduction

In the last two decades, optically pumped SDLs, also known as VECSELs, have received growing interest [201]. These lasers combine distinctive characteristics as already reported in chapter 2. The most attractive properties of SDLs from a practical point of view are briefly summarised as follows:

1- **Beam quality**:

Beam quality is a great advantage of SDLs. Due to their cavity design and thin gain region these lasers can offer high-brightness, low divergence, diffraction limited circular beams, fundamental transverse mode TEM_{00}, and low-noise operation. Furthermore, the cavity mode size can be controlled by the pump spot size where larger pump spot size leads to excitation of a higher gain area which in turn allows higher order modes lasing and vice-versa [201].

2- **Power scaling:**

Power scaling is considered as one of the key important features of SDLs. SDL design provides for efficient power scaling with excellent beam quality. Power scaling levels up to 60W have been reported from optically pumped devices [201]. This feature is mainly advantageous in optically-pumped SDLs where the optical pumping permits a uniform and larger pumped area enabling power to be extracted from larger gain area. However, at some point there is a limit that the size of the pump spot cannot be increased anymore without reducing the performance of SDL or damaging it due to the heat dissipation from the active region. Thus, thermal management is crucial in this case.

3- **Wavelength tuning**

Wavelength tuning is a very important property of SDLs and is evidently of great practical interest. The wavelength of SDLs can be tuned by several techniques such as changing the cavity length via adjusting the position of a cavity mirror [278] or by the incorporation of optical element like an etalon filter inside the external cavity configuration [182]. Another way to achieve wavelength tuneability and selectivity is by band-gap engineering and intracavity frequency conversion [175, 279-281].

4- Laser versatility via incorporation of intracavity optical elements

Owing to their external cavity configuration, SDLs enable the incorporation of intracavity nonlinear optical elements such as nonlinear crystals and SESAMs to allow for a wide range of functionalities. In addition to this a SESAM can be integrated into the SDL structure to create mode locked sources generating ultra-short pulses [282-284].

These versatile features are the key factors that have made the VECSEL an attractive candidate for numerous commercial, medical, and scientific applications such as optical clocking, telecommunications, high-speed laser printing, high-density optical storage, photodynamic therapy, biophotonics, laser radar, materials processing, displays, and remote sensing [201].

Most SDLs demonstrated to date have gain regions based on different QW materials operating in the CW regime with spectral coverage from the ultraviolet to the mid-infrared [285]. Recently QD-based SDLs have been developed in order to exploit their low temperature sensitivity and broad gain bandwidth [286]. However, reports of QD-SDLs operating in the 1300 nm wavelength range are few. The first demonstration of a QD based SDL operating at long wavelength was reported in 2005 [176]. The authors claimed that the peak output powers exceeded 5 mW for emission at 1290-1305 nm but

no further details were disclosed. QD-SDLs with output powers of 1.4W, 0.5W and 300 mW at 1040 nm, 950 nm and 1040 and 1210 nm, respectively, have also been reported [177, 178]. Albrecht and co-authors have reported a QD-SDL with a continually variable emission wavelength from 1220 to 1280 nm [181]. Also, wavelength tunable regions centred on 1040, 1180 and 1260 nm have been explored by Butkus et al [182]. However, reports of studies of QD SDLs at long wavelengths around 1300 nm which is the focus of this work are relatively new.

An SDL usually combines a gain medium with two DBR mirrors. Commonly one DBR mirror and the active layer are grown epitaxially on the same substrate to form a monolithic half cavity. The overall cavity is then realised using one or more external dielectric mirrors. This simple cavity design is the most reported and common configuration to achieve a SDL. More complex cavity configurations involving various nonlinear optical components have been also reported. All the previous reports [176-178, 181, 182] have employed relatively long cavities to achieve the lasing action. A very few reports have employed an HR-coated fibre as the top mirror [199, 200] instead of the dielectric mirror commonly used. Recently, we have demonstrated the first observation, to the best of our knowledge, of optically-pumped 1300 nm QD-SDL [196, 198] operating at RT with a very simple and compact cavity using an HR-coated fibre as the top mirror as reported in [199, 200], for QW active regions. Our work has been followed by a report on a QD-based SDL emitting at 1.3 μm with an output power over 200 mW [197].

This chapter will discuss the first observation of CW lasing in QD-SDLs at RT. First, the sample design and structure will be presented followed by its optical characterisation. Then, the experimental setup will be described. Afterwards, the CW input-output power characteristics and optical spectrum of the 1300 nm QD-SDLs will

be presented. It will be followed by the results achieved for wavelength tuning. Finally, dual-wavelength emission results will be presented.

6.2 SDL wafer design and structure

The QD-SDL wafer used in this work was grown by Dr. Edmund Clarke at the Engineering and Physical Sciences Research Council (EPSRC) National Centre for III-V Technologies. The results in this chapter are based on four samples (5mm x 5mm) taken from the wafer (VN2596) illustrated in Table 6.1.

Table 6.1: Designed structures of QD SDL wafer (VN2596).

Repeats	Thickness	Material	Doping type	Comments
1	232.0 nm	GaAs	Undoped	
5	92.0 nm	GaAs	Undoped	
5	4.0 nm	GaAs	Undoped	
5	6.0 nm	$In_{(0.12)}Ga_{(0.88)}As$	Undoped	
5	0.7 nm	InAs	Undoped	
5	1.0 nm	$In_{(0.12)}Ga_{(0.88)}As$	Undoped	
5	29.0 nm	GaAs	Undoped	
5	4.0 nm	GaAs	Undoped	
5	6.0 nm	$In_{(0.12)}Ga_{(0.88)}As$	Undoped	
5	0.7 nm	InAs	Undoped	
5	1.0 nm	$In_{(0.12)}Ga_{(0.88)}As$	Undoped	
5	29.0 nm	GaAs	Undoped	
5	4.0 nm	GaAs	Undoped	
5	6.0 nm	$In_{(0.12)}Ga_{(0.88)}As$	Undoped	
5	0.7 nm	InAs	Undoped	
5	1.0 nm	$In_{(0.12)}Ga_{(0.88)}As$	Undoped	
1	50.5 nm	GaAs	Undoped	
25	94.5 nm	GaAs	Undoped	1290 nm DBR
25	110.8 nm	AlAs	Undoped	
1	200.0 nm	GaAs	Undoped	Buffer layer
Substrate Type		2” semi-insulating GaAs		

The semiconductor (half-cavity VCSEL) structure of the device used in this work comprises of a monolithic QD active region on top of a DBR grown on a GaAs substrate by MBE. Initially an InAs layer of atoms, also referred as a wetting layer, that was epitaxially grown on the surface upon which self-assembled QDs were created. The majority of the active region is GaAs, and it consists of 15 quantum dot-in-a-well (DWELL) capped InAs/$In_{0.12}Ga_{0.88}As$ layers arranged in five groups if three. These are centred at the antinodes of the cavity standing-wave of the optical field for increased optical gain and to achieve the maximum relative confinement factor. Each InGaAs capping layer is only 6 nm thick. The dot density, measured by atomic force microscopy, for an uncapped QD layer grown under similar conditions as the layers in the SDL sample was 4.0 $x10^{10}cm^{-2}$. The bottom DBR consists of 25 pairs of quarter-wavelength-thick GaAs/AlAs with a reflectivity above 99.9 % near 1300 nm. This structure is similar to the one reported in [284] but with 2 extra groups of DWELL layers.

6.2.1 Optical wafer characterisation

Optical characteristics measurements are standard and preliminary tests for most of the wafers to verify its properties. The most common techniques for wafer characterisation are measurements of the PL and reflectivity spectra as will be shown below.

Although these preliminary measurements were conducted at the University of Sheffield by Dr. Edmund Clarke, we include them here since they help in understanding the performance of the device, and can also be used to improve the device designs in the future if required.

6.2.2 Photoluminescence (PL) measurements

PL measurements are used to inspect the material quality and properties such as the characteristic of spontaneous emission, spectral width and estimation of the material gain peak wavelength of the device. Fig. 6.1(a) shows the RT, normal incidence PL spectrum obtained from the half-cavity VCSEL using an Accent PL mapping system. The peak wavelength of the PL spectrum was measured to be around 1290 nm which is the design laser operating wavelength. The PL peak wavelength and lineshape is determined by the cavity resonance but reference samples with QDs grown under the same conditions without an underlying DBR also show a ground state PL peak at 1290 nm. Therefore, the peak in the PL spectrum might be a function of the cavity resonance and the maximum of the QD spontaneous emission spectrum.

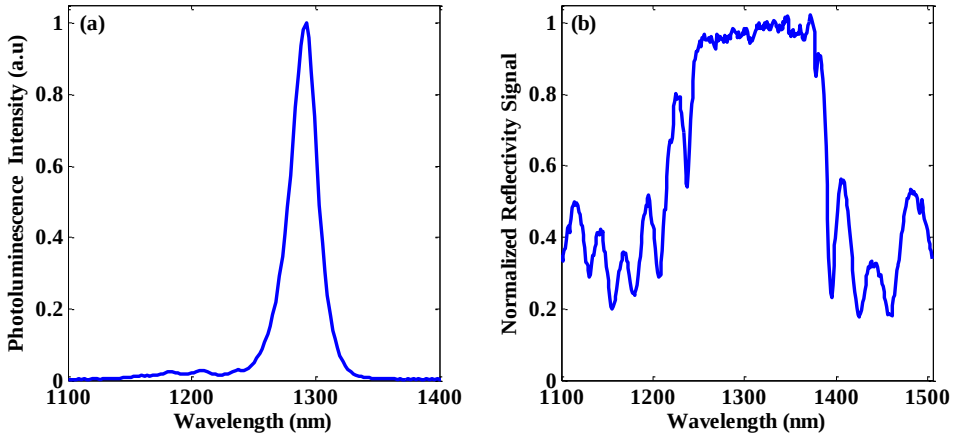

Fig. 6.1: Room temperature (a) PL measurements, and (b) reflectivity spectra of QD SDL wafer.

6.2.3 Reflectivity

Surface reflectivity is utilised to find out and assess the optical properties of the device such as the position of the cavity and Bragg reflectance band. The measured reflectivity spectrum for the SDL wafer is shown in Fig. 6.1(b) obtained using the same technique as the PL measurements. It can be seen that the width of the

reflectivity stopband is about 150 nm and the DBRs have their stopband at the design wavelength. There is a reflectivity dip that is due to absorption at the cavity resonance wavelength.

6.3 Experimental Setup

The QD-SDL configuration combines the aforementioned half-cavity VCSEL and an HR-coated single-mode optical fibre acting as the top mirror (see the inset in Fig. 6.3).

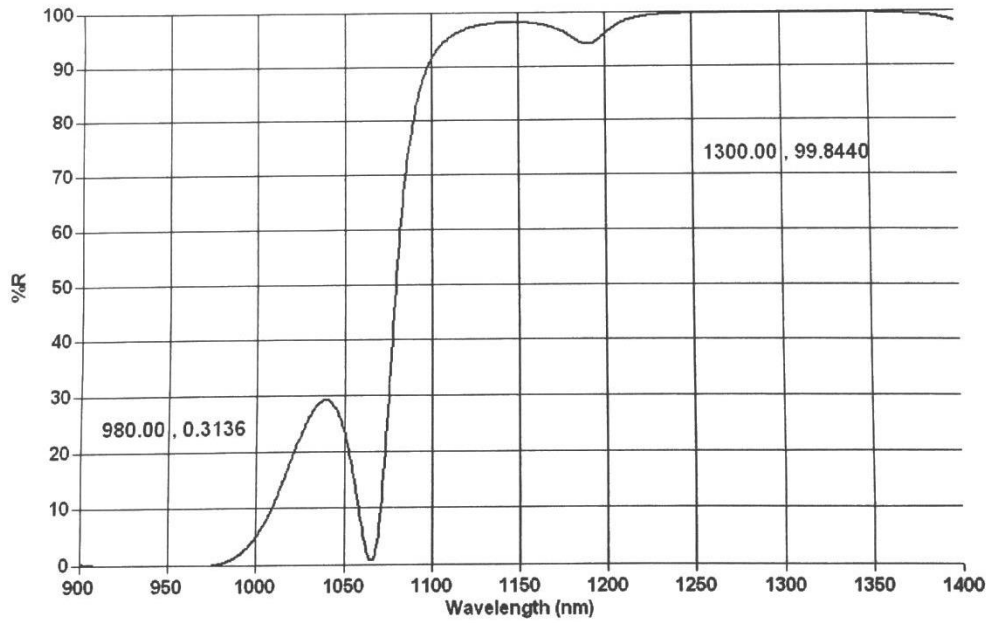

Fig. 6.2: Reflectivity spectrum of the HR-coated fibre. Courtesy of Laser 2000 [287].

The HR coated fibre has a reflectivity of 99.8% at 1300 nm, is nominally anti-reflective 0.3% at the pump wavelength of 980 nm (Fig. 6.2) and has a mode field diameter of typically ~6 μm. The HR coatings are either metal coatings or narrowband and broadband dielectric high reflecting coatings applied to the tip of H1060 fibres by OptoSigma. The coating was customised for our specifications above by the supplier and no information about the material used and how the coating was done were

enclosed. Such coating is commercially available upon request with the required specifications. The distance between the facet of the optical HR-coated fibre and the sample surface is then the length of the external cavity. The microcavity of the device was formed by bringing the HR-coated fibre in close proximity (~μm) to the sample using a piezo-electric translation stage.

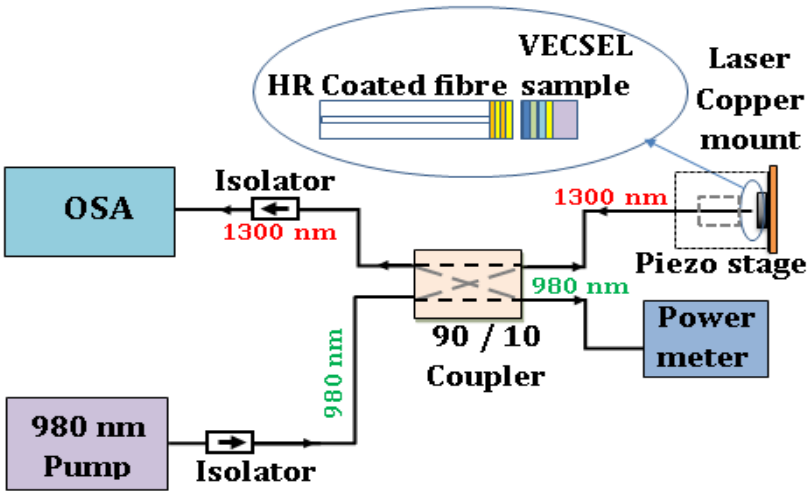

Fig. 6.3: Schematic of the experimental setup. The inset is a zoom of the QD-SDL design. OSA: Optical spectrum analyser.

Fig. 6.3 presents a schematic of the experimental setup used to achieve the 1300 nm QD-SDL. The half-VCSEL sample was pasted on a silicon wafer which then was clamped to a temperature-controlled copper mount which was maintained at RT (293 K). The half-VCSEL was mounted on the temperature-controlled copper mount with a Peltier element underneath to control the heat sink temperature. The Peltier element and the customised copper mount were supported on a mounting bracket mount which was attached to one side of a 3-axes piezoelectric translation stage. A photograph of this part of the experiment is shown in Fig. 6.4. The sample was optically pumped with a commercial 980 nm pump laser connected via an IS to prevent back reflections. The pump laser is a Fibre Bragg Grating (FBG) stabilised laser (FBG pump laser) because this both fixed the pump wavelength and offers narrow spectral width. A 90/10 optical

coupler was used to direct 90% of the optical pump to the sample through its cross port using the HR coated fibre and at the same time to couple 10% of the sample's output at 1300 nm through its bar port to the OSA.

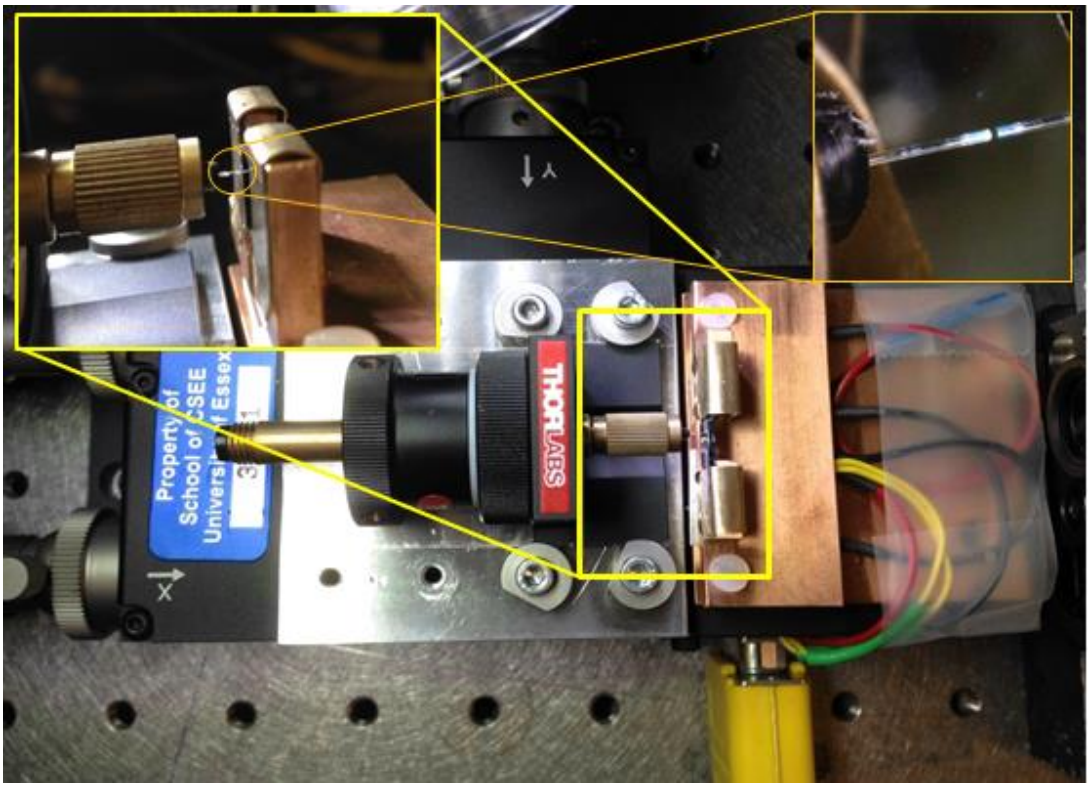

Fig. 6.4: Photograph of the QD-SDL experiment setup.

The majority of the sample's output at 1300 nm passes in the reverse direction through the cross port of the coupler towards the pump laser. A 1300 nm IS was used between the coupler and the OSA to prevent back reflections from the OSA to the sample. The other 10% of the optical pump was directed to a power meter through the 90/10 coupler to monitor the CW pumping power. The HR-coated fibre was held close to the sample by a 3-axes open-loop piezo-electric translation stage for fine movement.

6.3.1 Challenges and limitations

This experimental setup has undergone many improvements to enhance stability during operation since the tiny external cavity dimensions and light weight of the HR-coated fibre tip were sometimes problematic. These features of the HR-coated fibre made it sensitive to environmental vibrations around the setup. An improvement was made by mounting the fibre holder and the sample copper mount on the same translation stage by supporting the latter on a mounting bracket and attaching it to one side of a 3-axes piezoelectric translation stage as described above. Previously, mounting these on different stages meant that more parameters and angles had to be controlled and adjusted which required more effort and took a very long time. Moreover, the perpendicularity of the HR-coated fibre at the surface of the sample must be maintained to easily achieve stimulated emission from the SDL device. Using a side-loading fibre chuck sometimes made the fibre slightly tilted with respect to the sample and hence misaligned. However, this issue was solved by using a rear-loading fibre chuck to prevent any tilting. This fibre chuck type also plays an important role in maintaining stability of operation and facilitating the attainment of lasing action. It is also worth noting that the parallelism between the interface of the HR-coated fibre and the surface of the sample is a must to obtain the lasing action and collect detectable amounts of the SDL output power. This sometimes can be challenging when taking into account the fact that the area of the core of the HR-coated fibre is very small and the corresponding area of the surface of the sample is not completely and evenly flat due to surface roughness. Additionally, during the alignment and actuation of the piezo translating stage, the distance between the sample and the interface of the HR-coated fibre was monitored by a microscope camera to avoid damaging the fibre and to make the alignment easier. These improvements were reflected in the results presented in this

chapter. Specifically, the threshold power was reduced by almost a factor of two from 21 mW as reported in [196, 198] to 11 mW as a result of these improvements as well as replacement of the pump laser.

One obvious limitation of this cavity configuration is that the incorporation of intracavity nonlinear optical elements such as nonlinear crystals, SESAMs and etalon filters is not possible.

6.4 Experimental Results

Here we report the first observation of lasing in a QD SDL at 1300 nm operating at RT under CW optical pumping. The lasing action was obtained at different wavelengths between 1285-1325 nm depending on the air-gap length between the sample and the interface of the coated fibre and also on the pump beam spot position on the sample. These wavelengths were observed on different occasions by adjusting the three axes of the piezo-electric stage. The spatial non-uniformity as the pump beam spot was moved across the sample may result from small changes in cavity dimensions, variation in the DBR peak wavelength, or a change in gain with variation in the overlap of cavity resonance and QD emission peak. This is under investigation.

6.4.1 Optical spectrum and output versus input curve

The output power as a function of incident pump power for the QD-SDL is illustrated in Fig. 6.5. The lasing threshold occurs at a pumping power of 11 mW. This figure shows that CW output power of > 0.8 mW has been achieved at RT of 20˚C. It should be noted that a significant amount of the pump power is reflected and scattered from the surface of the sample so the achievable output power is limited by the

absorbed pump power. Moreover, observations show that the threshold and efficiency of the QD-SDL decrease when the fibre is moved away from the sample. This might be attributed to changes in the HR-coated fibre effective reflectivity in addition to the coupling losses associated with alignment changes. Therefore, we believe that by carefully adjusting the setup at least up to 10 mW can be achieved by changing the 90/10 coupler to a Wavelength Division Multiplexer (WDM) coupler and/or increasing the number of QDs since this sample was not optimised for high output power.

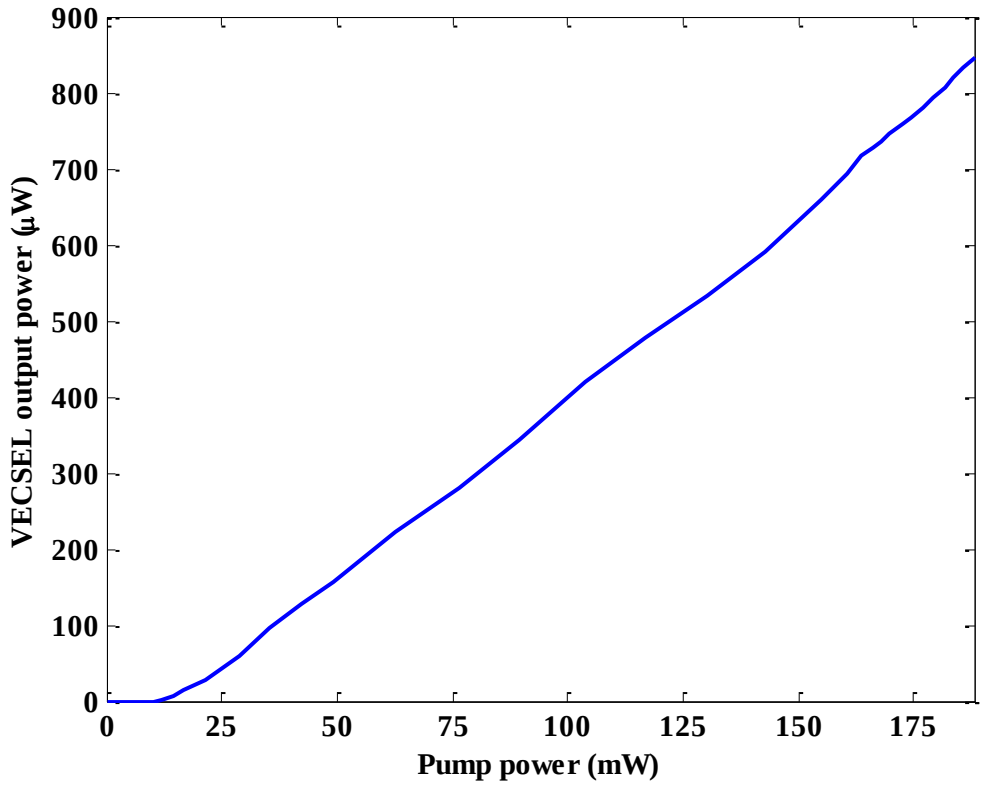

Fig. 6.5: Output versus pump power for the QD-SDL.

Fig. 6.6(a) shows the optical spectrum in linear scale for the QD-SDL under 90 mW pumping. This shows a very clear and narrow peak centred at 1301 nm due to the very compact configuration of the QD-SDL in addition to the small pump spot diameter.

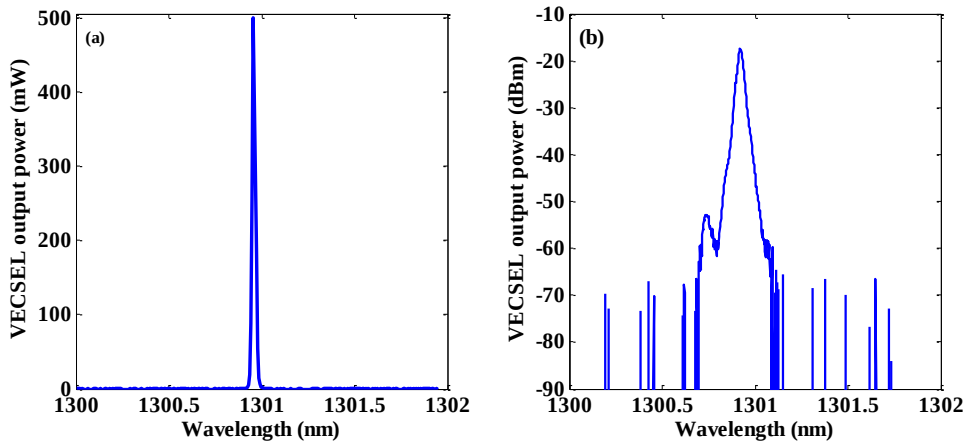

Fig. 6.6: Optical output spectra of the QD SDL (a) in mW, (b) in dBm.

Interestingly, it was observed that the QD-SDL emits in orthogonal polarisation, (the mode at the long wavelength side as defined in section 1.3.1), as shown in the log-scaled optical spectrum of Fig. 6.6(b). We attribute this to the combined effects of the birefringence and dichroism parameters of the device material. This figure reveals that the side-mode suppression ratio was more than 33 dB.

6.4.2 Temperature Dependent Properties

The dependence of SDL performance on heat sink temperature is of great importance from a practical point of view. The input-output power characteristics were measured as a function of different heatsink temperature and the results obtained are shown in Fig. 6.7. Output powers up to 900 μW and 680 μW were achieved for heatsink temperatures of 15 °C and 30°C respectively. It can be seen that the input-output curve slope efficiency decreased at higher temperatures. The threshold slightly increased with temperature while the maximum output power decreased. This is due to the temperature dependence of the gain, the cavity resonance and the energy band gap of the active material. It is worth noting that the maximum observed output power was

limited by the available pump power, and no sign of thermal rollover was observed and hence much more power could be achieved with a more powerful pump laser.

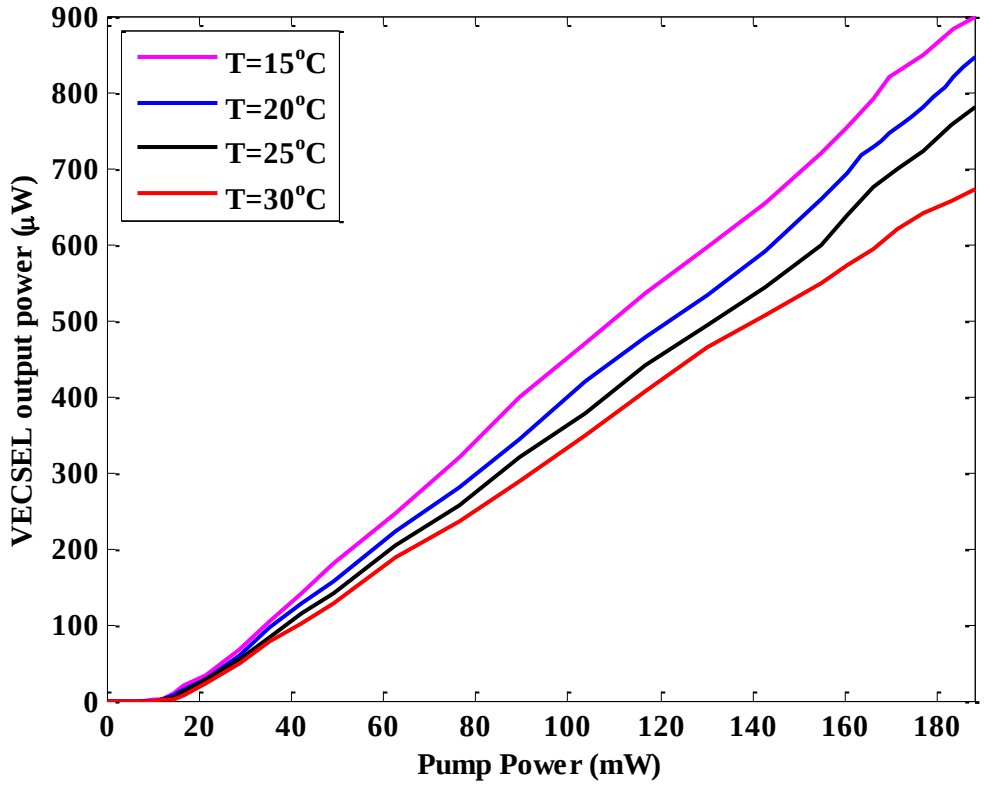

Fig. 6.7: Pump power vs. output power characteristics for the QD SDL sample for different heatsink temperatures.

6.4.3 Wavelength tuneability

As previously mentioned, the wavelength of the emitted beam from the QD-SDL depends on the air-gap length between the sample and the interface of the coated fibre. It is not possible to accurately measure the physical external cavity (air-gap) length; however, we estimate it to be ~ 6 μm based on measurements taken by the controller of the piezo-electric stage. Moving the HR-coated fibre with respect to the half-VCSEL, thus changing the air-gap length, results in a change of the resonant wavelength which, in turn, leads to wavelength tuning of the laser emission peak. Fine variation of the air-gap length could be achieved by translating the HR-coated fibre position via the piezo-

electric stage, and hence tuning the device wavelength. The precise control of the distance between the sample and the interface of the coated fibre using the piezo translation stage allows very fine tuning of the laser output wavelength.

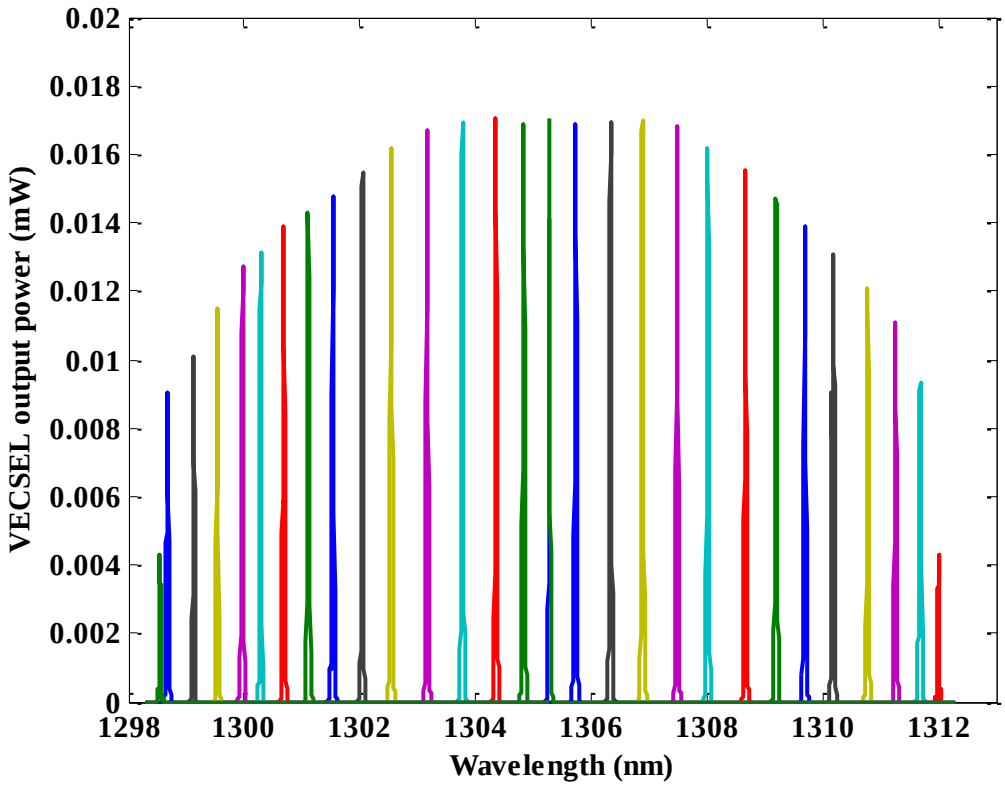

Fig. 6.8: Wavelength tuning characteristics and optical spectra for the QD-SDL sample.

Fig. 6.8 shows the tuning characteristics and several superimposed lasing optical spectra taken at different external cavity lengths (at different piezo voltages). By actuating a single axis (optical cavity axis, Z) of the piezo-translation stage we were able to tune the emission wavelength of the QD-SDL over 14 nm as shown in Fig. 6.8 with resolution down to 0.01 nm via tuning voltages of the piezo-translation stage between 21 and 40.5 volts. However, the tuning range is strictly limited by reflections, scattering and absorption, as well as coupling losses between the interface of the HR-fibre and the surface of the sample. Furthermore, it should be mentioned that this device was not optimised to act as a tunable source. Thus, for broader tuneability, the

large gain bandwidth feature of the QDs should be exploited by manipulating the density and size dispersion of QDs at the growth stage [288]. This feature, in addition to the design of a short anti-resonant sub-cavity structure can widen the emission spectral bandwidth [289].

6.4.4 Dual-wavelength semiconductor disk laser

Under some conditions when the interface of the HR-coated fibre was moved via the piezo stage towards the surface of the SDL sample, dual-wavelength lasing was observed as shown in Fig. 6.9.

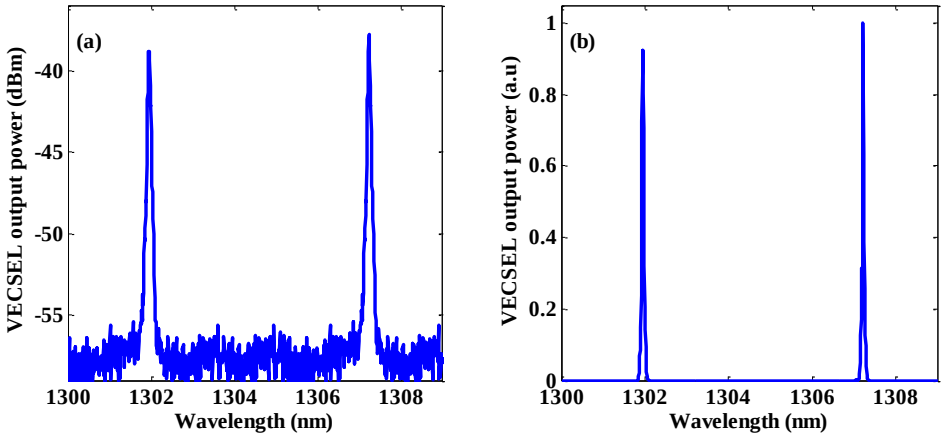

Fig. 6.9: Optical lasing spectra of the dual-wavelength QD SDL sample.

This behaviour might be attributed to a formation of two optical cavities with slightly different lengths. This was created when the pump spot was laid on uneven position of the sample or when the HR-coated fibre was tilted by few degrees with respect to the surface of the sample, hence creating different air-gap lengths between the sample and the interface of the fibre. This initiated lasing action with different wavelengths according to the cavity lengths. In other words, the two-wavelength splitting depends on the ratio between the lengths of the two cavities. It should be noted that any changes in the external cavity length via the piezo translating stage leads

to a reduction of the mode splitting and the output power of one mode until it diminishes. The output of the SDL in Fig. 6.9 measured within the range of 10 μW.

6.5 Discussion

This chapter presented the first demonstration of a 1300 nm optically pumped QD based semiconductor laser (QD-SDL) operating at RT with a very simple and compact cavity where a single-mode fibre was used simultaneously to pump the device and also to couple the output from the device. In this configuration, the interface of the optical fibre is coated with an HR-coating (R = 99.98%) at the device wavelength, and hence acts as the top mirror of the QD-SDL, while it is nominally anti-reflective (R = 0.3%) at the pump wavelength of 980 nm. The external cavity was formed using the air-gap length between the tip of the fibre and the sample surface. This cavity arrangement was already reported in [199, 200] for QW active regions. Lasing action was observed on several occasions at different wavelengths between 1285-1325 nm depending on the air-gap length with relatively low pump threshold of 11 mW compared to the QW spin-VCSEL discussed in the previous chapters. The use of QD gain materials in SDLs already demonstrated their ability to provide high gain and low operating threshold [290]. Moreover, up to 1 mW output power from the QD-SDL was recorded with no thermal rollover in the input-output curve.

The output power of the SDL was limited by several factors including the capabilities of the pumping system in our lab; these included the way the output power couples into the system via the 90/10 coupler, the reflected and scattered pump power from the surface of the sample and the coupling and alignment efficiencies between the HR-coated fibre and the sample. Therefore, further improvement could be done to increase the output power of the SDL to high levels by using a more powerful pump

laser or by optimising both the setup and the device for high output power delivery which can be done by several techniques. However, in order to obtain high output power levels, it is crucial to optimise the thermal management [282], since using a powerful laser may lead to rapid thermal rollover in the input-output characteristics of the device. Nevertheless, this could be avoided by introducing a wavelength-offset between the QD gain peak and the cavity resonance at the growth level to compensate the thermal shift at higher temperatures and powers at the cost of a slight increase in the threshold pump power [291]. One approach to increase the output power is that an anti-reflective (AR) coating can be applied on the surface of the sample to reduce the reflection and scattering of the pump power from the surface and to ensure that more of the pump is absorbed in the QDs [200]. Another option is changing the 90/10 coupler to a WDM coupler, as already mentioned, which makes the detection of the actual output power out of the SDL possible. Finally, since this sample was not optimised for high output power; hence increasing the number of QDs will lead to significant improvement in the output power of the device.

QD-SDLs feature a broadband gain due to their inhomogeneously broadened density of states. Thus, they are desirable sources for tunable lasers. The demonstrated QD-SDL in this work showed wavelength tuneability over a range of 14 nm. Up to date, the widest wavelength tuneability range demonstrated in the long wavelength window of 1-1.3μm from a QD-SDL was 63 nm where the laser was tuned from 1147 to 1210 nm via employing a birefringent filter inside the external cavity [182]. In the same work wavelength tuneability of 60 and 25 nm from 1003 to 1063 nm and from 1237 to 1262 nm were achieved, respectively, using different structures [182]. While other work by Albrecht et al. has demonstrated a 60 nm tunable QD-SDL by using

epitaxial variation across the wafer enabling tuneability between 1220-1280 nm as the pump spot's position was changed on the SDL surface [181].

It should be noted that the QD wafer investigated throughout this thesis was not optimised for wide tunable range operation. In addition the tuning range is strictly limited by reflections, scattering and absorption, as well as coupling losses between the interface of the HR-coated fibre and the surface of the sample. However, the tuning range could be improved by following different approaches. One option is to use an AR-coating on the surface of the sample in order to reduce the reflection and scattering from the sample-air interfaces as reported in [200] where the use of a $\lambda/4$ dielectric AR-coating extended the tuning range from 14.5 nm up to 18.5 nm. Moreover, a notably wide tuning range in QD lasers was achieved by growing multiple non-identical QD-layers with various thickness of their capping layers [288]; this allows different energy transitions which, in combination with the wide range of QD sizes, leads to a very wide continuous tuning. This strategy was used to achieve a record high tuning range of 207.7 nm from a QD external cavity semiconductor laser [292]. Moreover, the design of a short anti-resonant sub-cavity structure can widen the emission spectral bandwidth and hence the tuneability range [289].

Another feature observed in the demonstrated QD-SDL was the dual-wavelength emission. It was believed that this was due to the formation of two different cavities with slightly different lengths. This in turn leads to lasing with different wavelengths as observed with wavelength splitting dependent on the ratio between the lengths of the two cavities. An assumption was made to explain the mechanism behind this action: if the pump spot was incident on an uneven position of the sample or when the HR-coated fibre was tilted by few degrees with respect to surface of the sample, this created different air-gap lengths between the sample and the interface of the HR-fibre.

Tunable sources are of intense interest for potential applications such as medical treatment [293] and swept-laser sources [294] for optical coherence tomography [295, 296]. Specifically the long wavelength spectral region 1100-1300 nm is useful for biomedical imaging due to the minimal absorption and scattering in human tissue [295]. In addition, lasers with wide tuning ranges are attractive for spectroscopy [297, 298], environment monitoring [299], interferometry [300, 301], and optical fibre communications [302] in switching scenarios and for improving network resilience based on dense wavelength-division multiplexing [303-305], and as pump sources for other lasers [306]. Moreover, dual-wavelength light sources are very attractive candidates for potential application where one wavelength could be used as a reference and other as a probe. They have proven their capability in two-wavelength interferometry for optical path-length [307] and slope testing as well as surface profile measurements [308]. Furthermore, these light sources have been already utilised in interferometers [309], high-resolution cross-sectional imaging in optical coherence tomography [296, 310], absorption spectrophotometry [311-313], generation of microwave and terahertz radiation [282] and detection of microscopic biological particles [314].

6.6 Summary

In this chapter, the operation of the first, to the best of our knowledge, CW 1300 nm optically pumped QD-SDL lasing at RT was explored. The external cavity of the device was formed using an HR-coated fibre as the top mirror. Firstly, the design and structure of the QD-SDL's wafer grown at the EPSRC National Centre for III-V Technologies, University of Sheffield, was presented and characterised. Then a pumping threshold of 11 mW was reported and a CW output power greater than 0.8

mW at RT was achieved. Additionally wavelength tuning over 14 nm was reported showing the feasibility of this cavity configuration. This cavity arrangement can be utilised in any material structure, and thus the same configuration is applicable to other wavelengths.

However, it should be noted that the sample investigated in this work was neither optimised for high power nor for wide tuning range operations. It was designed to operate as a spin vertical-external-cavity surface emitting laser as will be discussed in the next chapter. Therefore, the output power and the tuning range could be improved via different techniques such as optimisation of setup and the QD layer distribution.

The results reported in this work open up the way to a range of novel potential applications in the physics of light-matter interaction, sensing, optical communications and metrology.

CHAPTER 7: 1300 NM OPTICALLY PUMPED QD SPIN VERTICAL EXTERNAL-CAVITY SURFACE-EMITTING LASER (SPIN-VECSEL)[i]

Abstract:

This chapter reports the first room temperature optically pumped Quantum Dot-based Spin-Vertical-External-Cavity Surface-Emitting laser (QD Spin-VECSEL) operating at the telecom wavelength of 1.3 μm. The spin-VECSEL is based on the QD-SDL reported in the previous chapter. The output polarisation ellipticity characteristics of the spin-VECSEL under circular-polarised pumping are shown. Investigations of the dynamics and behaviour of the spin-VECSEL such as polarisation switching and polarisation instability under circularly-polarised pumping at different pumping positions are presented.

[i] This chapter is based on the papers:

1- S.S. Alharthi, J. Orchard, E. Clarke, I.D. Henning and M.J. Adams, "1300 nm Optically Pumped Quantum Dot Spin Vertical External-Cavity Surface-Emitting Laser'', Applied Physics Letters, vol. 107, no.15, p. 151109 (2015). [90]

7.1 Introduction

In this work we present the first demonstration a QD-based spin-VECSEL emitting at 1300 nm and operating at RT under CW optical pumping [90]. An optically pumped QW spin-VECSEL has been demonstrated very recently at the shorter wavelength of 980 nm using a very complicated external cavity configuration in order to compensate for the residual linear birefringence in the structure [63]. Herein, we apply a polarised optical pumping scheme in the QD-SDL reported in the previous chapter to realise a spin-VECSEL. The use of an external cavity configuration introduces distinctive characteristics, as detailed in [201], and with the inclusion of QD gain materials which contribute their own attractive merits such as high gain, low operating threshold and broad gain bandwidth [71, 290], this promises to offer further enhancements in performance and functionality.

This chapter will discuss the first observation of CW lasing in QD spin-VECSEL at RT [90]. First, the Photoluminescence Excitation (PLE) characteristics of the wafer will be presented followed by a description of the experimental setup used to achieve the spin injection. The input-output curves and threshold characterisation under different polarised pumping states will be shown after this. Then, the output power and polarisation ellipticity evolutions come next. Afterwards, output polarisation ellipticity characteristics will be studied at different positions of the wafer. It will be followed by the results achieved with PS. Finally, observation of self-sustained polarisation oscillation will be presented.

7.2 Photoluminescence Excitation (PLE)

PLE is useful in studying the optical transitions in a material since it can have experimental advantages over absorption measurements. PLE is performed by scanning the excitation wavelength of the pump while the detection wavelength is set at the wavelength of interest which is in our case the peak of PL emission. Peaks in the PLE spectra correspond to absorption of light due to the increased density of states when the excitation energy corresponds to the energy of a certain transition. PLE is a useful technique to investigate the excitation, optical processes and electronic structure of a specific layer of semiconductor materials.

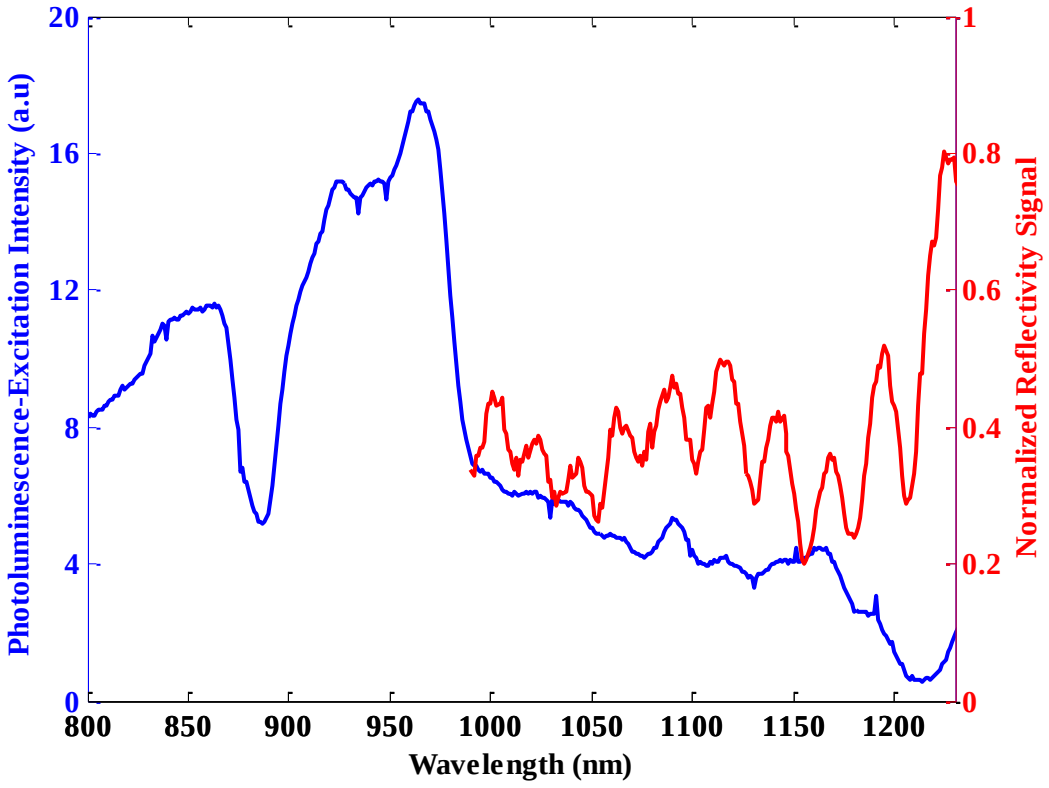

Fig. 7.1: Room temperature PLE (in blue) and reflectivity (in red) spectra obtained from the half-cavity VCSEL.

The RT PLE and reflectivity spectra shown in this section were supplied by Dr. Jon Orchard at the Department of Physics and Astronomy, University of Sheffield. Fig. 7.1

shows the RT PLE spectrum (in blue) obtained from the half-cavity sample. The spectrum was obtained using quasi-monochromatic excitation from a 150 W tungsten halogen lamp dispersed by a monochromator with the detection wavelength set to the peak of the QD ground state PL emission at 1290 nm. Peaks at 900-1000 nm are attributed to absorption in the InAs wetting layer and the InGaAs cap; however, since the InAs layer is very thin so most of the absorption signal will be in the InGaAs. Most of the features >1000 nm correspond to peaks in the reflectivity of the DBR, as also shown in Fig. 7.1 (in red). The increased intensity from wetting layer/InGaAs cap peaks compared to dot peaks is due to the increased absorption in the 2D states. The peak due to GaAs absorption at the short wavelength side has a lower energy and this might be due to cavity effects or reduced excitation power at these wavelengths. The PLE spectrum demonstrates that optical pumping of the half-cavity VCSEL structure at 980 nm is likely to be resonant with the wetting layer/ InGaAs cap states. It should be noted that the measured PLE is spin-independent since it was measured on a different experimental setup without polarisation optics in order to determine what part of the structure would be pumped by the 980 nm pump laser in the spin laser setup.

7.3 Experimental Setup

The experimental setup used to achieve the 1300 nm optically pumped QD spin-VECSEL is shown in Fig. 7.2. The QD half-VCSEL sample was pasted on a silicon wafer and held on a customised temperature-controlled copper mount which was maintained at RT (293K). The mounting bracket was attached to one side of a 3-axes piezo-electric translation stage. The external microcavity of the QD spin-VECSEL was formed, as already mentioned in the previous chapter, by bringing the HR-coated

optical fibre, acting as the top mirror (see the inset in Fig. 7.2), in close proximity (~μm) to the sample using a piezo-electric translation stage.

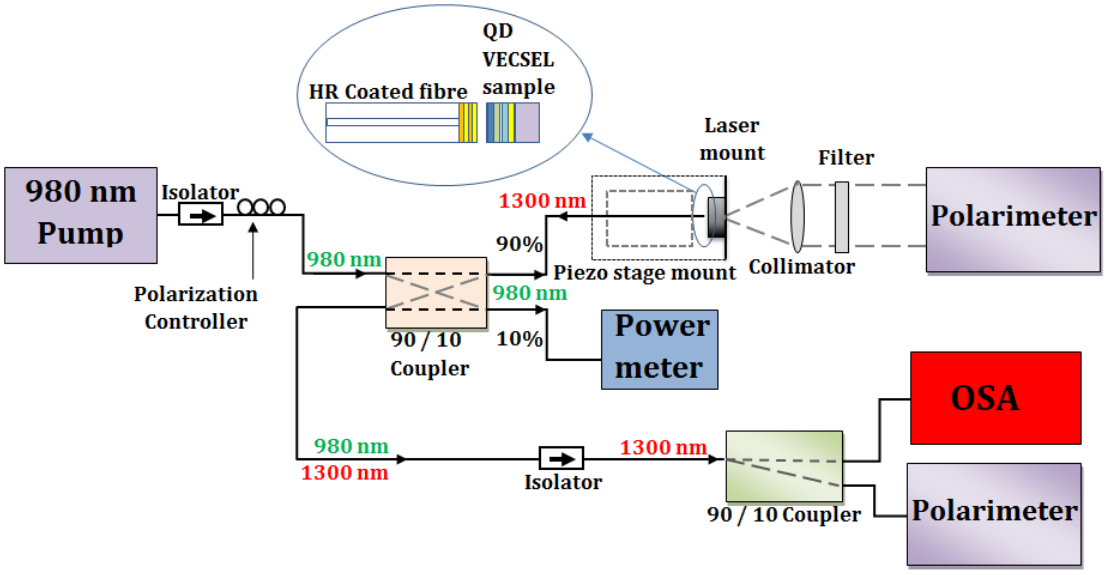

Fig. 7.2: Schematic diagram of the 1300 nm QD microcavity spin-VECSEL. The inset is a zoom of the QD spin-VECSEL design arrangement. OSA: Optical spectrum analyser.

The sample was optically pumped at the long-wavelength side of the peak of Fig. 7.1 (which is attributed to the absorption in the InGaAs cap) by a commercial 980 nm pump laser. The latter was connected to an IS to prevent back reflections. A PC was connected after the IS to set the polarisation of the pump. A 90/10 optical coupler directed 10% of the optical pump to a power meter to monitor the CW pump power while the remaining 90% of the pump was focused onto the sample using the HR coated fibre. The latter was held close to the sample by a fibre holder also attached to the 3-axes piezo-electric translation stage. The fibre served to both form the external cavity of the spin-VECSEL and to collect the sample's output at 1300 nm. By adjusting the external cavity length via the 3-axis translation stage wavelength matching between the optical gain and the cavity modes could be achieved.

In operation, a proportion of the pump and the spin-VECSEL output propagate through the half-cavity substrate, the silicon wafer and a window contained in the copper mount to be sampled at the head of a free-space polarimeter. A collimator lens and an IF were placed between the copper mount and the polarimeter. The filter was utilised to block either the 980 nm pump or the 1300 nm spin-VCSEL emission as required for the free space measurement. Both fibre collected outputs, the 1300 nm spin-VECSEL's emission plus the 980 nm reflected pump from the sample, pass through the fourth port of the 90/10 coupler to an OSA and an in-line polarimeter via another 90/10 coupler to permit a relative measurement of the VECSEL polarisation. In addition, another 1300 nm IS was used between the two 90/10 couplers to prevent both back reflection from the OSA to the sample and the 980 nm pump light from reaching the in-line polarimeter. The measurements taken via the single mode fibre path in the experimental configuration are subject to polarisation change arising from birefringence induced in the fibre through a combination of stress and thermal effects. The stress-induced birefringence is in general temperature dependant and any change in the fibre ambient is likely to modify the polarisation characteristics. This effect rotates the polarisation along the fibre by a certain angle. Thus, if the polarisation was measured before launching the light into the fibre and then at the end of the fibre the rotation angle could be derived and the system would be calibrated and corrected on the base. The effect might be suppressed by using polarisation maintaining fibres and this needs further investigations. This effect was eliminated from our measurements by injecting a reference 1300 nm light source of known polarisation into the setup (travelling over the same optical path as the VECSEL light), and measuring its polarisation at different points. Checks were made at the beginning and end of each measurement.

7.4 Experimental Results

7.4.1 Input-output characteristics and threshold reduction

Fig. 7.3 shows experimental output characteristic curves for pumping with circularly (in blue) and linearly (in red), (equivalent to electrical current biasing), polarised lights. The threshold is determined to be at a LP pump power of 13 mW. However, under the same conditions but with circularly polarised pumping, the threshold of the spin-VECSEL was reduced to about 12 mW. This shows a slight threshold reduction of few percent (~8%) when pumping circularly compare to the LP pumping (inset of Fig. 7.3).

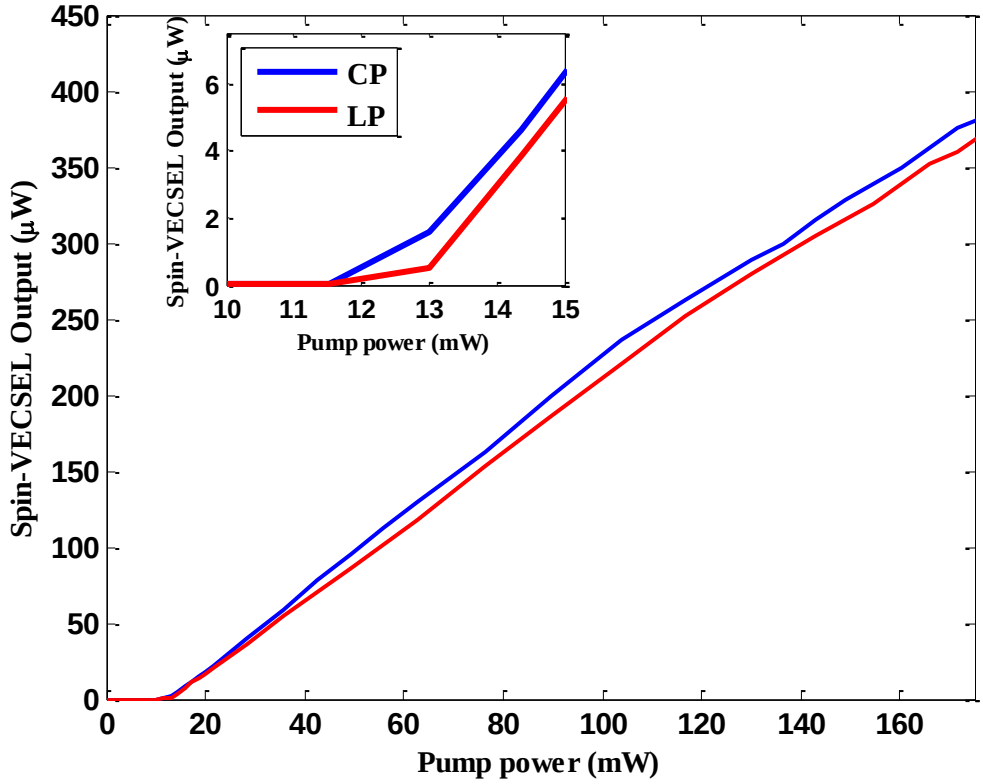

Fig. 7.3: Output versus CP (Blue) and LP (Red) polarised pump power for the spin-polarised VECSEL.

This figure also reveals an emission intensity enhancement of 4% at the maximum output power under CP pumping in comparison to its LP counterpart.

7.4.2 Evolution of the spin-VECSEL power with time

The first observations of lasing emission of the 1300 nm QD VECSEL lacked stability in the output power and experienced a reduction in the output power until eventually the laser ceased to operate. This power instability is attributed to the mechanical instability in the setup and in the lab in general.

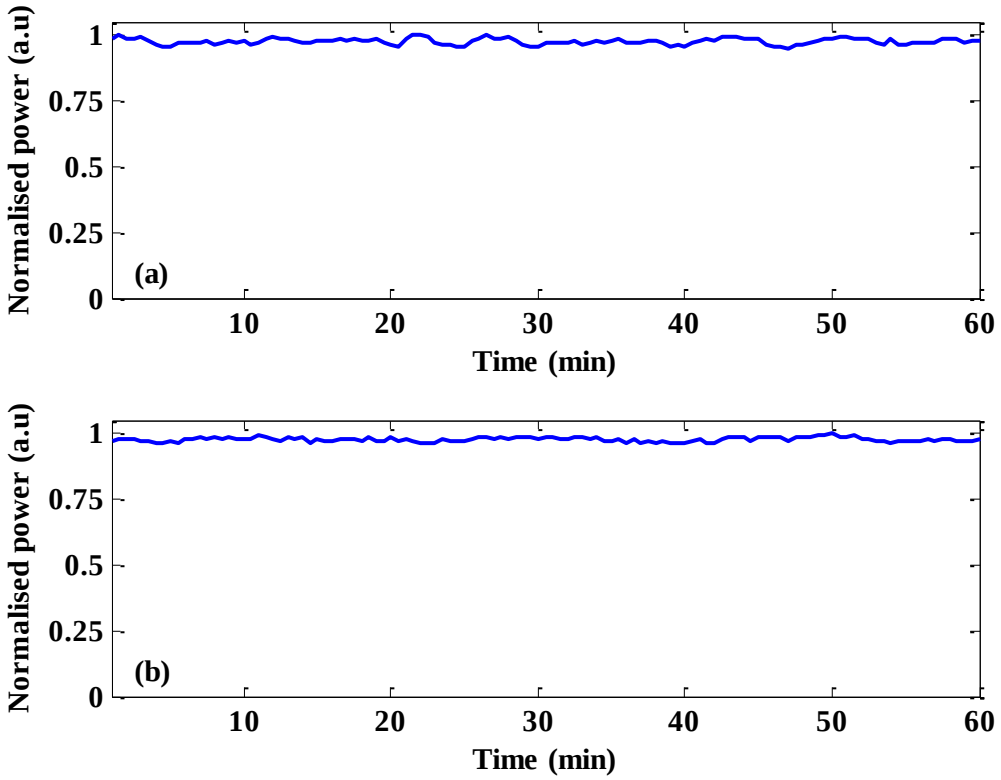

Fig. 7.4: Evolution of the spin-VECSEL output power with time LCP (a) and RCP (b), after one minute of turning the 980 nm pump on.

Therefore, the evolution of the output power with time was required to ensure that the setup alignment is optimal. In order to evaluate the output CW power stability and characteristics of the spin-VECSEL, the output power of the spin-VECSEL was measured for one hour after one minute of switching the laser pump on. Fig. 7.4 presents measurements of the evolution of the spin-VCSEL normalised output power under LCP (a) and RCP (b) pumping within the hour following the first minute since

the pump laser was switched on. It can be seen that the output power collected from the spin-VECSEL remained stable with no significant drop during the first hour of operation. These results also imply that the 980 nm pump laser was very stable in terms of optical power and wavelength with very good quality and reliability.

7.4.3 Evolution of the spin-VECSEL Polarisation

7.4.3.1 Evolution of the spin-VECSEL output ellipticity (ε) with time

While the output power of the spin-VECSEL was measured for the first hour from switching the pump laser on as described in the previous section, the output ellipticity of the spin-VECSEL (defined as the ratio of the *DOCP* to the total *DOP* of the emission of the spin-VECSEL as defined in Eq. 4.15), was also measured at the same time to ensure its stability and to investigate any possible dynamics such as PS that may emerge with time due to factors such as thermal effects. This was conducted by detecting and analysing the RCP or LCP output components of the spin-VECSEL (I_+) and (I_-), using the free space and in-line polarimeters as a function of time. Experimentally, Stokes vector elements {S0, S1, S2, S3} can be measured by the polarimeter and the value of the output polarisation ellipticity (ε) is calculated from these elements as defined in Eq.4.15. The evolution of the output polarisation ellipticity measurement is justified if the fact that our VECSEL emits in the orthogonal polarisation mode as shown in the previous chapter is taken into consideration. Hence, the laser may show similar or different behaviour under polarised optical pumping as will be discussed below.

The evolution of the output ellipticity of the spin-VECSEL corresponding to Fig. 7.4(a) and Fig. 7.4(b) when the laser was subject to RCP and LCP, respectively, shows that the output ellipticity of the spin-VECSEL was almost stable with degrees of

circular polarisation DOCP of ~84%. However, the output ellipticity of the spin-VECSEL has an inverted sign to that of the pump and this will be studied in detail in the following subsection.

7.4.3.2 Evolution of the spin-VECSEL ellipticity as a function of the polarisation of the pump

To evaluate the output polarisation ellipticity (ε), the output components of the spin-VECSEL (I_+) and (I_-), were measured and analysed as a function of the corresponding RCP or LCP input components of pump (η_+) or (η_-), respectively, using the free space and in-line polarimeters.

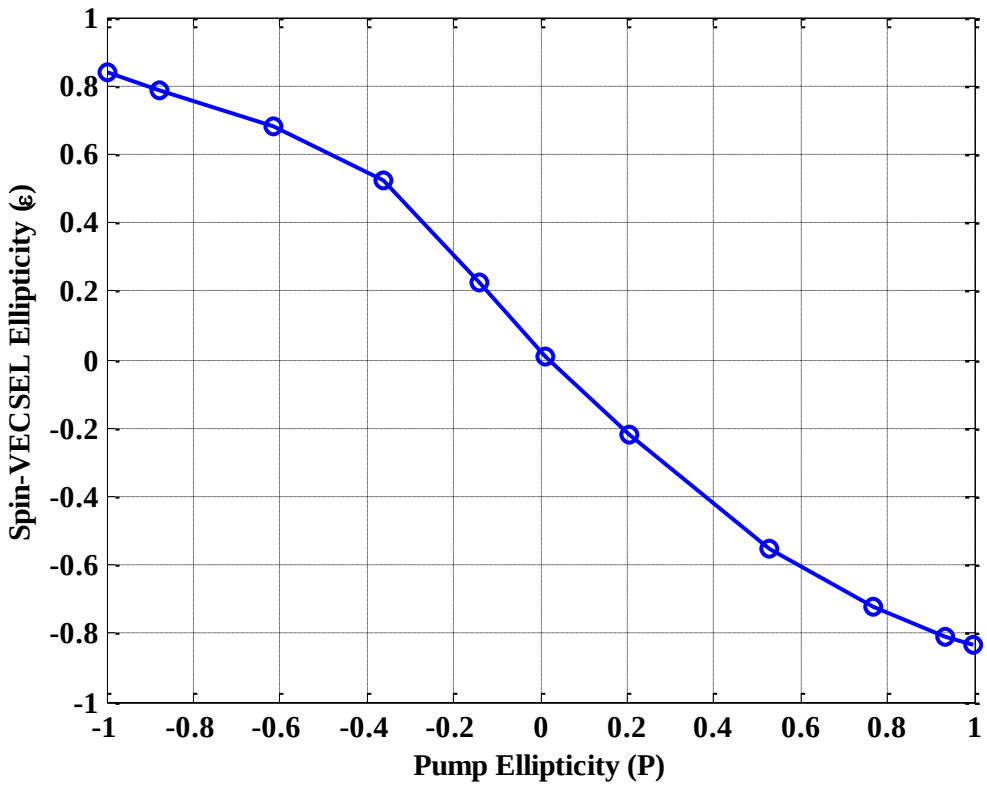

Fig. 7.5: Inverted spin-VECSEL output polarisation ellipticity (ε) as a function of the polarisation ellipticity of the CW pump (P).

Fig. 7.5 depicts the output polarisation ellipticity (ε) as a function of the pump polarisation (P), defined in Eq. 4.7, at a pump of 60 mW and estimated external cavity

length of 5~6 μm. It shows that the polarisation ellipticity (ε) of the VECSEL follows that of the pump (P) but with inverted sign. When manually changing the pump polarisation from right to left circular polarisation or vice-versa, a corresponding switch from left to right circular polarisation of the VECSEL occurred. This confirms spin polarised injection into the active region of the device. Similar behaviour has been reported by Hovel et al [72] and it has been attributed to the reflection geometry. In contrast, since our VECSEL emits in the orthogonal mode under LP pumping (equivalent to electrical current biasing), by analogy it should emit in the orthogonal circularly polarised mode with respect to the polarisation of the pump. It is attributed to the stability of the in-phase mode (with negative slope in the plot of η versus P) rather than the out-of-phase mode (with positive slope) [208].

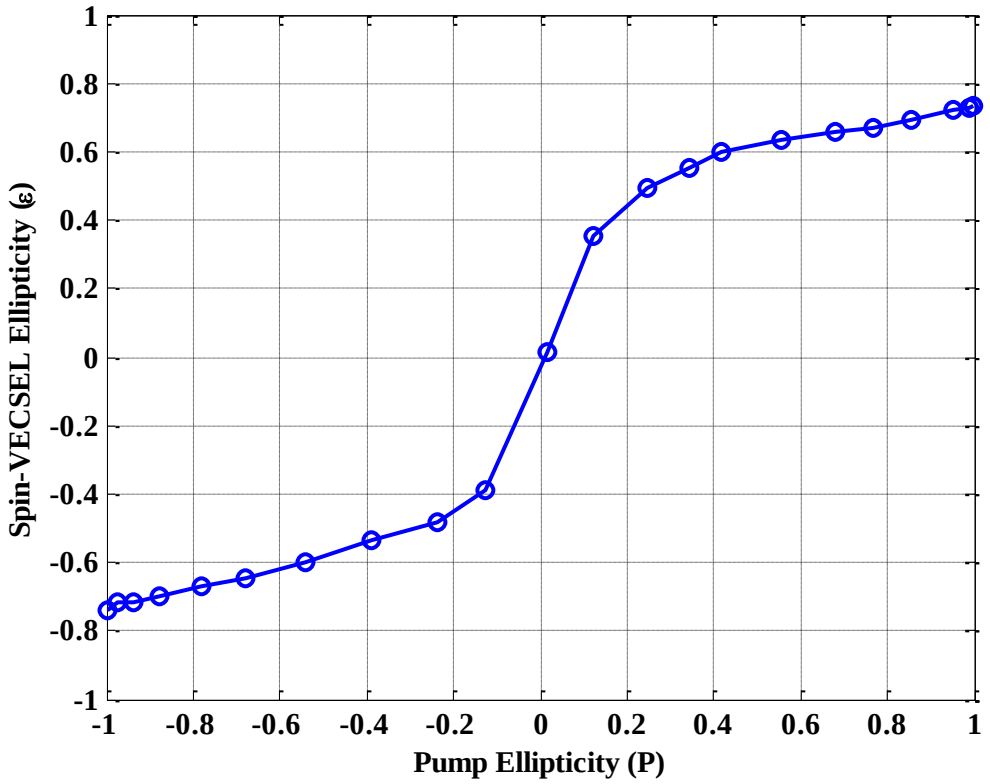

Fig. 7.6: Normal spin-VECSEL output polarisation ellipticity (ε) as a function of the polarisation ellipticity of the CW pump (P).

However, it should be mentioned that there are some regions of the sample where, when the HR fibre is nearer the sample, the output polarisation ellipticity (ε) of the spin-VECSEL switches gradually to the same sign as that of the pump. Such a positional change leads to variations in the spatial profile of the optical pump beam at the wafer surface as well as a change in the cavity. While we see greater sensitivity as the spot is moved away from the heatsink, suggestive of local thermally induced changes in birefringence, further work would be needed to confirm the root cause factors. In these regions, the output polarisation ellipticity (ε) follows that of the pump with the same sign as shown in Fig. 7.6 which was measured at the same pump power but with shorter external cavity length of 1~2 μm. This figure also reveals that the degree of output polarisation (between 0.1-0.6) is higher than the polarisation degree of the pump which demonstrates spin amplification. Our results show that, when pumped CW well above threshold, ellipticities up to 0.84 and 0.73 could be achieved with inverted and normal sign, respectively, with respect to that of the pump. The difference between the degrees of ellipticity in the two cases is suggestive of gradual PS caused by the effects mentioned earlier. However, understanding the differences between different trends in Fig. 7.5 and Fig. 7.6 will be the subject of future work by conducting further spectroscopic studies of the spin-VECSEL.

7.4.4 Ellipticity-resolved input-output curves

In order to understand the differences between different trends in Fig. 7.5 and Fig. 7.6, the output polarisation ellipticity was measured while the pump was increased from zero to higher values above threshold. This measurement was performed to investigate the output polarisation ellipticity as a function of the pump, which may exhibit PS or instability.

Fig. 7.7 presents the input-output characteristics of the spin-VECSEL (in blue) and the output polarisation ellipticity as a function of the pump (in red) under RCP (a) and LCP (b) pumping. The measurements were taken while the spin-VECSEL exhibited output ellipticity with inverted sign with respect to that of the pump as illustrated in Fig. 7.5. It was found that initially the spin-VECSEL exhibited inverted polarisation ellipticity with instability in the output polarisation ellipticity around the pumping threshold which is referenced by the vertical dashed line. As the pump was increased above threshold, the output ellipticity stabilised with ellipticity above 75%. For a further increase in the pumping power, the output ellipticity slightly increased to ellipticities of 84%. It should be mentioned that before the vertical dashed line the spin-VECSEL exhibits fluctuations in the output polarisation ellipticity due to the spontaneous emission noise.

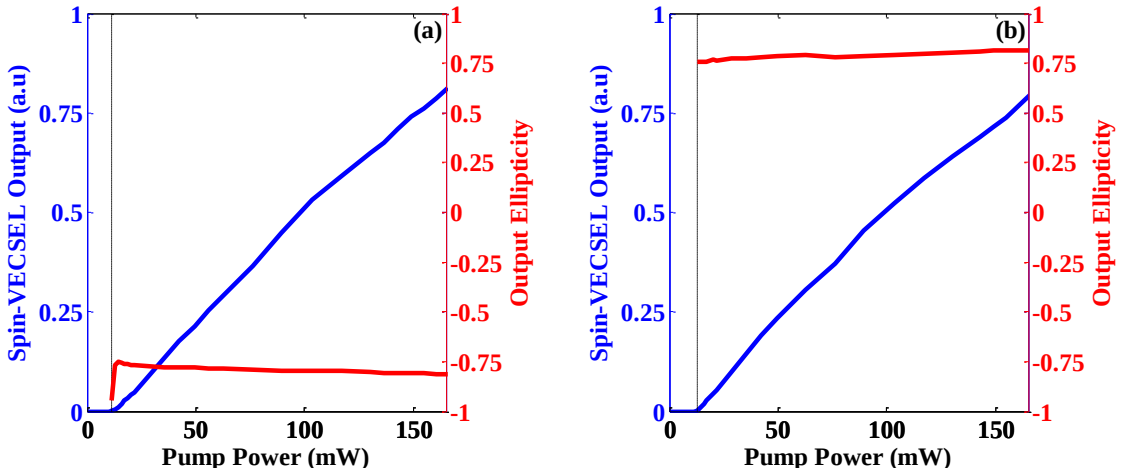

Fig. 7.7: Ellipticity resolved input-output curve for the case of inverted sign as in Fig. 7.5

Now we will study the effect of the pump power on the output polarisation ellipticity for the other case where the spin-VECSEL showed normal sign with respect to that of the pump as illustrated in Fig. 7.6. Fig. 7.8 presents two measurements of the input-output characteristics of the spin-VECSEL (in blue) and the output polarisation ellipticity as a function of the pump (in red) under RCP (a) and LCP (b) pumping. It

can be seen be seen that the spin-VECSEL at threshold exhibited output ellipticity with inverted sign with respect to that of the pump. However, as the pump was increased gradually above threshold, the output ellipticity started switching rapidly to the opposite state from almost LCP (a) {RCP, b} ($|\varepsilon| = 0.83$) to RCP (a) {LCP, b} ($|\varepsilon| = 0.70$). For a further pumping power increase, the output polarisation of the spin-VECSEL showed normal sign as that one of the polarisation of the pump. For a further increase in the pumping power, the output ellipticity slightly increased to ellipticities of 75%. When the output polarisation ellipticity reached to similar polarisation state to that of the pump, no PS or polarisation instability were observed for increasing pumping power.

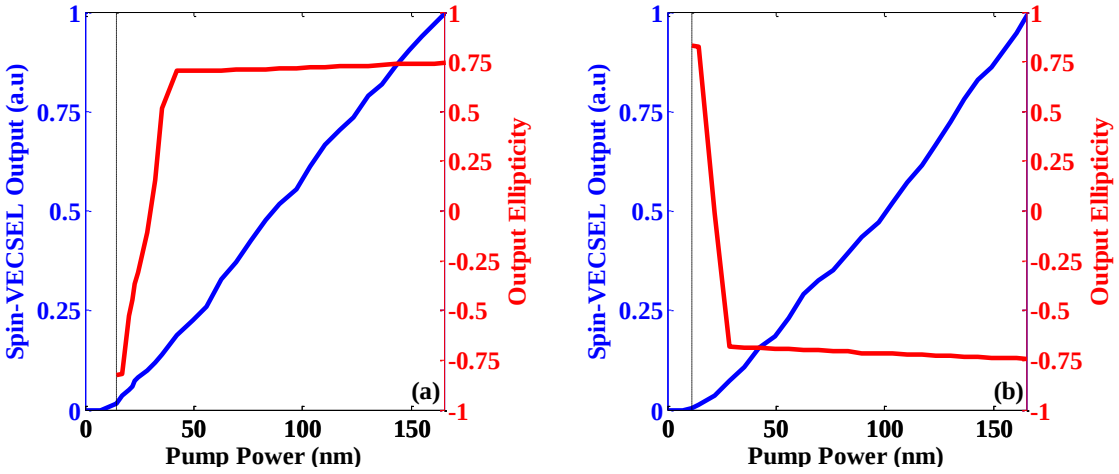

Fig. 7.8: Ellipticity resolved input-output curve for the case of normal sign as in Fig. 7.6

7.4.5 Polarisation switching

PS was found at some position on the surface of the sample when the spot of the pump beam was moved across the sample during the alignment stage after achieving the lasing action. There were regions where when the polarisation of the pump was varied from LCP to RCP or vice-versa the output ellipticity of the spin-VCSEL switched to the opposite state revealing PS. We believe that our experimental system

was not experiencing any significant optical feedback that may have led to the existence of PS resulting from back reflections due to misalignment. Nevertheless, this behaviour was related to the variation of the laser cavity and non-uniformity of the surface of the wafer, leading to different spot sizes and pumping conditions. Fig. 7.9 presents the evolution of the output polarisation ellipticity of the spin-VECSEL with PS for the case of normal (a) and inverted (b) output polarisation ellipticity cases corresponding to Fig. 7.6and Fig. 7.5 , respectively.

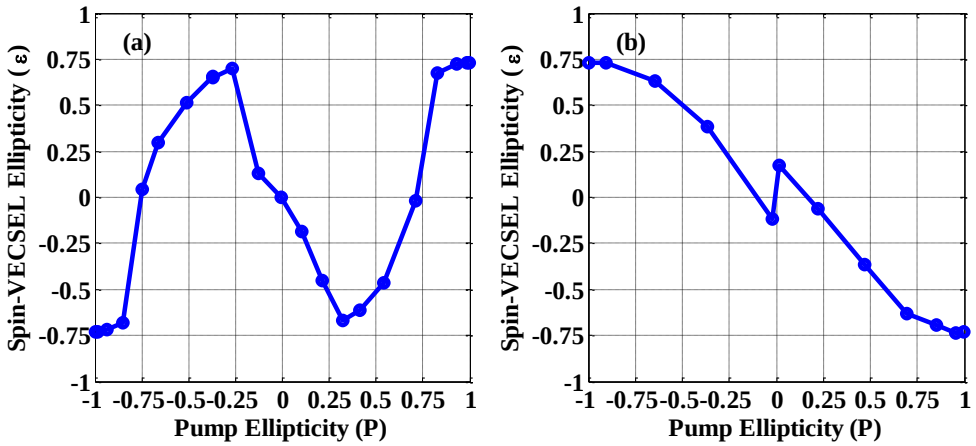

Fig. 7.9: Evolution of the spin-VECSEL output polarisation ellipticity with that of the pump in a case where polarisation switching was observed.

In Fig. 7.9(a) it can be seen that the spin-VECSL output polarisation ellipticity (ε) followed that of the pump at the beginning and then at $|P|$=0.80 it switched to the reversed sign. Furthermore, for pump ellipticities of (0 < $|P|$< 0.25), the output ellipticity of the spin-VECSEL started gradually switching back towards the first polarisation state until reaching linear polarisation state at $|P|$=0. In other words, the spin-VECSEL output polarisation ellipticity experienced polarisation transition from one polarisation state to the other as the absolute value of the pump ellipticity was decreased between 0.80 and 0.25. This results in a spin-VCSEL ellipticity of opposite sign to that of the pump for pump ellipticities between -0.75 and 0.75. Similar

behaviour was already found in our optically pumped dilute nitride spin-VCSEL [315]. Fig. 7.9(b) shows that that the polarisation ellipticity (ε) of the VECSEL follows that of the pump (P) but with inverted sign as shown in Fig. 7.5. However, for pump ellipticities of ($0 < |P| < 0.12$), the output polarisation ellipticity of the spin-VECSEL switched back to the normal distraction where it had the same polarisation state and sign as that of the pump. It is interesting to note that measurements performed on a piece from the edge of the wafer showed similar PS behaviour of the spin-VECSEL output polarisation ellipticity but with instability and oscillations for some pump ellipticities as will be discussed in the next section. No unstable behaviour was found in the results presented in this section.

7.4.6 Dynamics of solitary spin-VECSEL

Fig. 7.10 presents the experimental setup used for measurements of the RF spectrum of the spin-VECSEL sample from the edge of the wafer. It is almost identical to the setup presented in Fig. 7.2 but with the addition of few extra components.

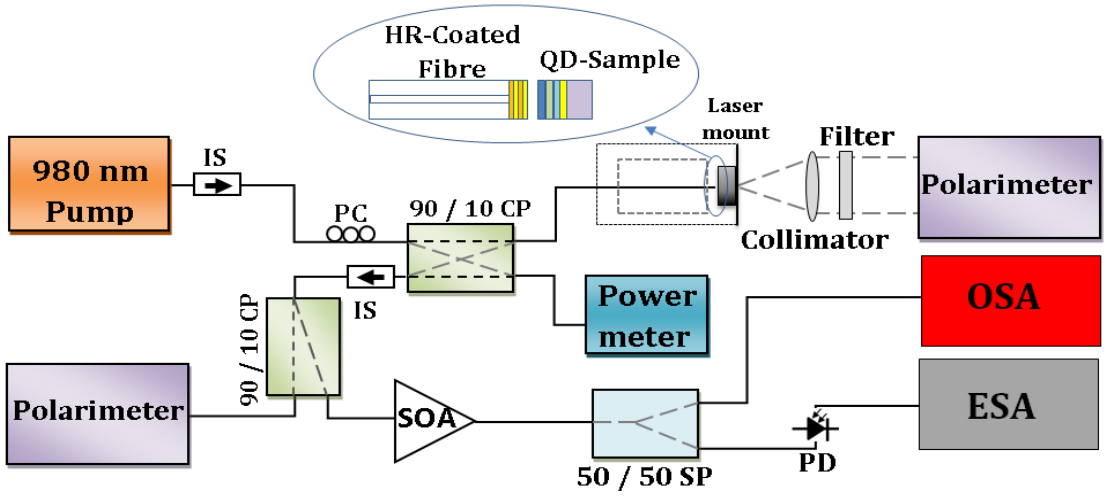

Fig. 7.10: Schematic diagram of the experimental setup for the analysis of the RF spectrum of the oscillatory behaviour of the spin-VECSEL.

The SOA was included due to insufficient power available for the ESA while the 50/50 SP was added to split the spin-VECSEL output power between the OSA and ESA to keep the laser under full monitoring. The SOA was biased to 115 mA while the spin-VECSEL was pumped to 60 mW.

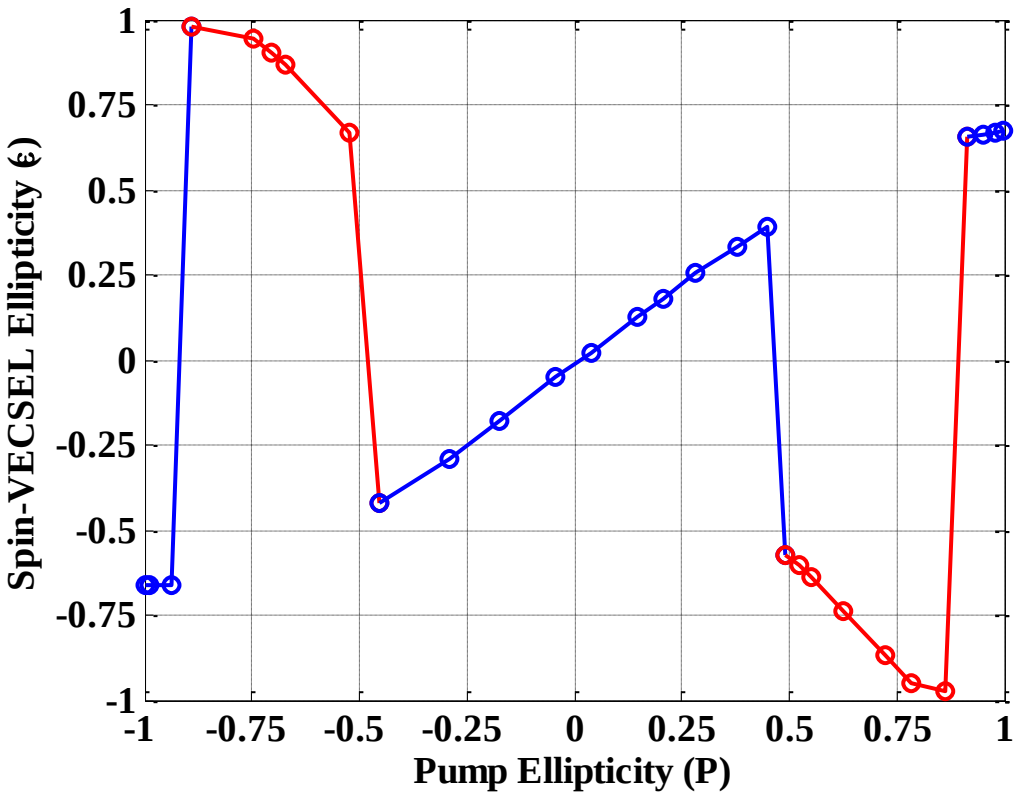

Fig. 7.11: Spin-VECSEL ellipticity as a function of the pump ellipticity from a sample from the edge of the wafer.

Fig. 7.11 presents the output polarisation ellipticity (ε) as a function of that of the pump (P) for a sample from the edge of the wafer. This figure illustrates that the output polarisation ellipticity (ε) followed that of the pump at the beginning and then at $|P|$=0.9 it switched abruptly to the reversed sign. Then as the absolute value of the polarisation of the pump was decreased between $|P|$= 0.90 and $|P|$= 0.50, the absolute value of the output polarisation ellipticity of the spin-VECSEL also decreased from ε= 0.97 to ε= 0.60. For a further decrease in absolute value of the polarisation of the pump, the output polarisation ellipticity abruptly switched back to the normal

direction at 0.45 with the same sign as that of the pump. Unlike the gradual PS presented in Fig. 7.9, in this case the output polarisation ellipticity experienced abrupt double PS in which type I ,in blue, (type II, in red) from one circular polarisation state with the mode of higher (lower) frequency to the opposite polarisation state with the mode of lower (higher) frequency. It should be mentioned that the spin-VECSEL under pump polarisation of ($0.45 < |P| < 0.90$) went into an unstable region where polarisation oscillations were observed in the RF spectrum as shown in Fig. 7.12.

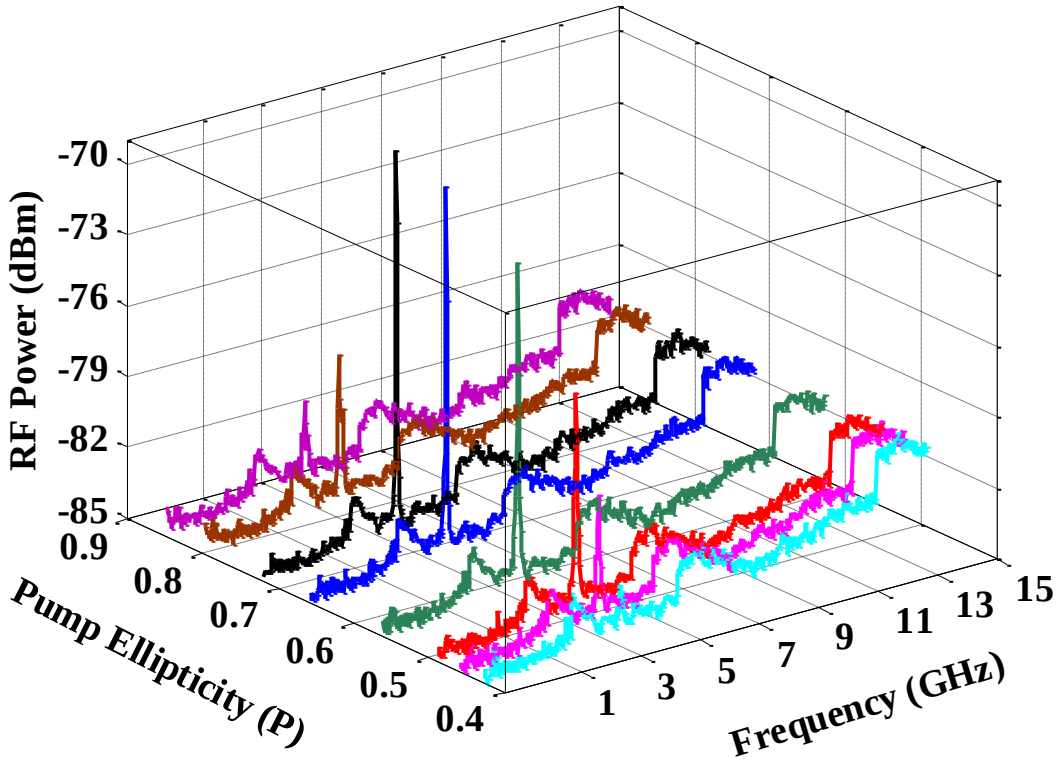

Fig. 7.12: RF spectrum of the output of the spin-VECSEL as a function of pump polarisation.

Fig. 7.12 presents different measurements of the RF spectrum of the solitary spin-VECSEL for different positive pump polarisation values at a constant pump power of 50 mW. These spectra show peaks with frequency of oscillation f_{osc} corresponds to the ROF of the device at 4.6 GHz as the absolute value of the polarisation of the pump was

decreased from 0.90 to 0.45. However, the measured RF power was varied as pump ellipticity changed and this will be shown in the next figure. These spectra reveal periodic oscillations in the output of the spin-VECSEL under polarised pumping.

Fig. 7.13 shows the measured peak RF power as a function of the pumping ellipticity for the oscillations reported in Fig. 7.12 at constant pumping power. It reveals that RF power increased until reached its maximum, which was found approximately around $|P| = 0.6$, and then decreased as the pump ellipticity was decreased from 0.90 to 0.45.

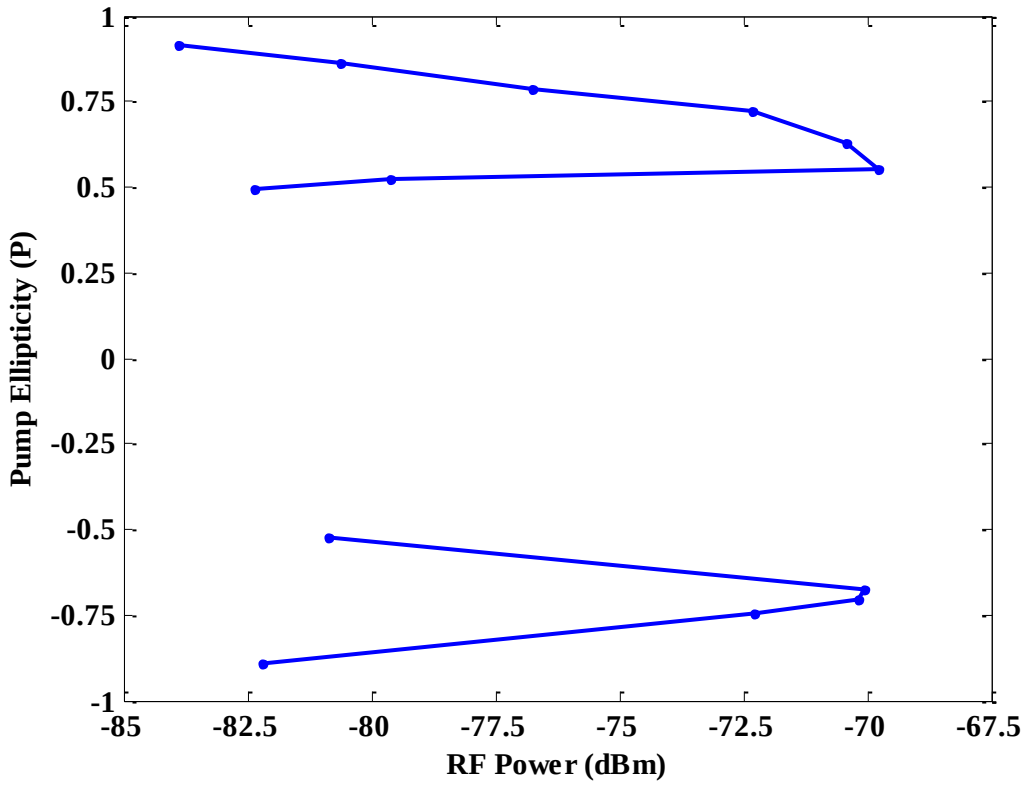

Fig. 7.13: Experimentally measured evolution of the peak RF power as a function of the pump ellipticity.

Finally, to study the effect of the pump power on the polarisation oscillations, the pumping power was reduced several times and the RF spectrum was measured accordingly while the polarisation of the pump was kept constant at $|P| = 0.6$ to ensure full RF power at each measurement. Fig. 7.14 presents the RF spectrum of the

output of the spin-VECSEL for 5 decreasing pumping power values under constant pump polarisation of 0.6. It can be seen that the frequency of oscillation f_{osc} decreased from 4.6 GHz to 1.5 GHz as the pump power was decreased from 60 mW downward to four estimated values of 51, 40, 31and 22 mW, respectively. However, the RF power of these oscillations increased and then decreased as the pump power was reduced to lower values as shown in Fig. 7.14.

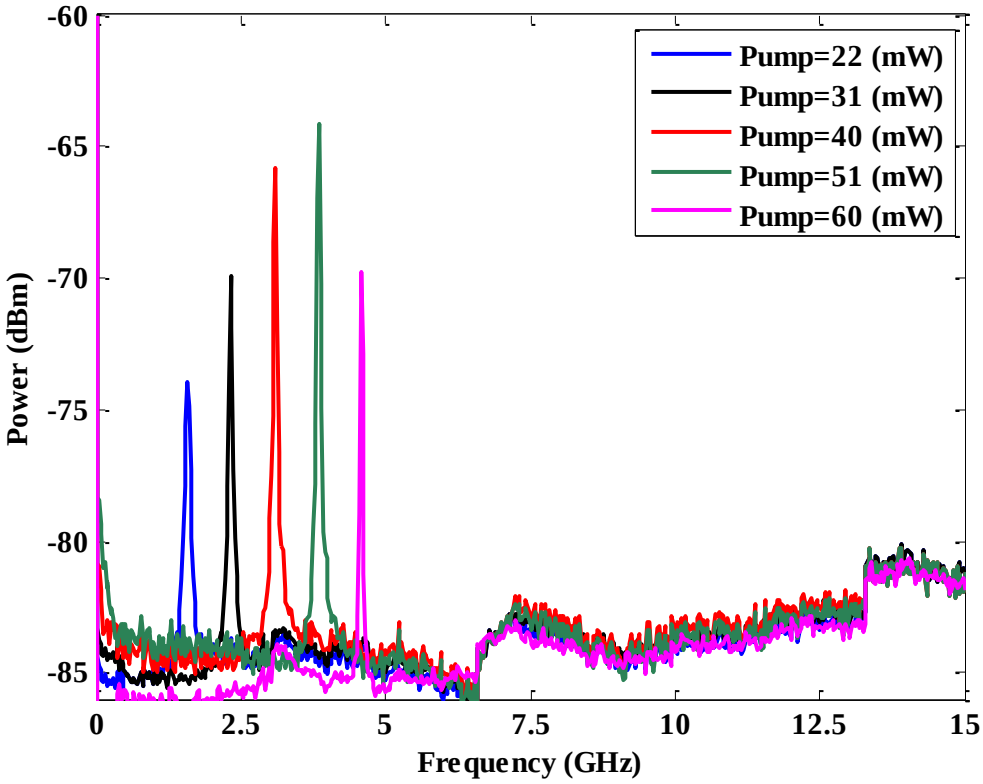

Fig. 7.14: RF spectrum of the output of the spin-VECSEL with pump ellipticity of 0.6 for arbitrary decreasing pumping power.

7.5 Discussion

This chapter is devoted to investigate the spin injection into the active region of a Vertical External-Cavity Surface-Emitting Laser (VECSEL) via an optical pumping scheme. The external cavity of the VECSEL was formed by employing an HR-coated

fibre as the top mirror, as reported in [196] and described in detail in the previous chapter. Various behaviours were observed during the spin injection measurements as already shown and they will be discussed below.

Firstly, our results reveal a slight threshold reduction of 8% and intensity enhancement of 4% at the maximum power under circularly polarised pumping compared to its LP counterpart. Threshold reduction was already predicted and observed in spin-VCSELs [67, 73, 75, 76, 82, 92, 94, 164, 316, 317] as well as enhanced emission intensities [73, 74].

The results also show that the polarisation ellipticity (ε) of the VECSEL follows that of the pump (P) but with inverted sign [90]. The controllability of the output polarisation ellipticity by that of the pump is a well-known feature of spin-polarised lasers. It has been previously reported for pulsed operation [89] with degrees of circular polarisation close to unity and for continuous excitation at short [63, 77] and long wavelengths [22]. The DOCP under CW operation is usually lower than under pulsed excitation due to sample heating caused by the continuous pumping. Results presented in this chapter show that, when pumped CW well above threshold, ellipticities up to 0.84 and 0.73 could be achieved with inverted and normal sign, respectively, with respect to that of the pump.

The inverted sign behaviour of the output polarisation ellipticity with respect to that of the pump has been reported by Hovel et al [72] and it has been attributed to the reflection geometry. However, this is attributed to the stability of the in-phase mode (with negative slope in the plot of η versus P) rather than the out-of-phase mode (with positive slope) [208] since our VECSEL emits in the orthogonal mode under LP pumping as shown in chapter 6; hence, by analogy it should emit in the orthogonal circularly polarised mode with respect to the polarisation of the pump.

It was also found that there were some regions of the sample where, when the external cavity length was reduced by bringing the HR fibre nearer the sample, the output polarisation ellipticity (ε) of the spin-VECSEL switches gradually to the same sign as that of the pump where also in these regions, the output polarisation ellipticity (ε) follows that of the pump with the same sign. Such a positional change leads to variations in the spatial profile of the optical pump beam at the wafer surface as well as a change in the cavity. While we see greater sensitivity as the spot is moved away from the heatsink, suggestive of local thermally induced changes in birefringence. Tightly focusing a small hot spot at the surface of the sample could induce some birefringence in the device as reported by van Doorn eta al [29] where an intentional birefringence was introduced by creating a small hot spot at the surface of the VCSEL [29]. This was done by tightly focusing a Ti-sapphire beam on the surface of the VCSEL with the aid of a lens. Thermal expansion around this hot spot produces strain in the VCSEL leading to birefringence in the VCSEL [29]. Another factor that might have contributed to the different trends of the output polarisation ellipticity is that the different cavity lengths result in a change of the lasing wavelength. The change in lasing wavelength will give a change in the gain anisotropy (dichroism). As the cavity resonance energy changes, the gain anisotropy will also change. As already known, very small changes of the dichroism can give relatively large changes in the behaviour of spin-VCSELs [62]. As the external cavity gets very small (~1 μm) the tip of the fibre might come into contact with the ½-VCSEL sample, which might induce local stress in the semiconductor and it is already known that stress leads to a change of birefringence.

To further understand the differences between different trends in Fig. 7.5 and Fig. 7.6, the input-output characteristics for the two trends were resolved with the output polarisation ellipticity to see if this difference was due to increasing pumping

power leading to PS or other dynamics. The results show the existence of gradual PS as the spin-VECSEL was pumped above threshold. This means that the pumping power is another factor that can affect the difference in the output polarisation ellipticity trends.

The competition between thermal effects, stress and nonlinear dynamics in explaining PS in conventional VCSELs (when the current changes) has been discussed extensively in the literature. Full analysis of these effects was reported in [318]. So there might be a similar competition in spin-VECSELs but with more complications and complexity. Thus, to gain full understanding of the behaviour of the two trends, further work by conducting further spectroscopic studies of the spin-VECSEL is required.

In addition, the output polarisation ellipticity of the spin-VECSEL slightly increased when the pumping power was increased. However, no significant improvement of the spin-VECSEL ellipticity could be achieved by pumping the device higher above threshold. This behaviour was already theoretically predicted where the theoretical results revealed that the output ellipticity will either remain constant or increase with an increasing pump power under a constant circular pump polarisation [62, 162, 319].

Output polarisation ellipticity amplification and amplification of spin information are considered as great advantages of spin-VCSELs [14, 69, 72, 77]. Output polarisation ellipticity amplification was experimentally observed where results show that the degree of output polarisation (between 0.1-0.6) is relatively higher than the polarisation degree of the pump.

Another interesting result is the observation of oscillatory behaviour. It was found that measurements performed on a sample from the edge of the wafer exhibit polarisation oscillation at the ROF of the device under absolute values of pump

ellipticity of ($0.45 < |P| < 0.90$) since the frequency of these oscillations is pump polarisation-independent. Interestingly, these self-sustained oscillations resemble the ones found in our 1300 nm dilute nitride spin-VCSEL reported for the first time in [61] and investigated in further details in chapter 3 of this thesis. However, the self-sustained oscillations reported here are pump polarisation-independent with lower frequency of oscillation f_{osc} than in [61] depending on the ROF of the device

Apart from the aforementioned reports, no similar oscillatory dynamics have been reported in the literature since most of the studies were devoted to investigate the output power and polarisation ellipticity of the spin-VCSEL. However, transient and damped oscillations of the output ellipticity in the vicinity of the PS point in response to pulsed optically spin-polarised pumping were predicted and observed in [95, 209, 210] and were reported for conventional electrical pumping in [211-213].

The PS and polarisation oscillations observed and illustrated in Fig. 7.9 and Fig. 7.12 are caused by the competition between fundamental physical processes at work in the device, namely the spin-flip processes that tend to equalise the gain for right- and left-circularly polarised fields, dichroism which tries to equalise the field amplitudes, and birefringence which couples power back and forth between the polarised fields [163]. These polarisation oscillations are related to PS and the development of the ellipticity in the case of $P = 0$ [41, 211, 214].

Increase of the birefringence, the frequency splitting between the two orthogonally polarised modes, by structurally engineering the VCSEL or by applying additional strain to the VCSEL was already investigated and reported. This was reported for the first time in 1998 where Hendriks et al managed to change the birefringence value from 19 ns^{-1} to 6.6 ns^{-1} in a conventional VCSEL by applying strain to the VCSEL (see Figs. 2 and 5, respectively, in [81]). Moreover, external mechanical strain along first

the [1,-1,0] axis and then the [1,1,0] axis of a conventional VCSEL was experimentally used to induce a high-birefringence rate of $\gamma p/\pi$~80 GHz [215]. The frequency splitting between the two polarisation modes was tuned from 1.3 GHz up to 79 GHz for increasing tensile strain along [1,1,0] direction [215]. Recently, theoretical predictions reveal the possibility of attaining high-frequency birefringence by applying a uniaxial strain to the VCSEL. This could enable fast polarisation oscillations of the emitted light with oscillation frequency of >200 GHz in spin lasers [216]. Later this year, these predictions for large birefringence were experimentally demonstrated in 850 nm QW VCSELs revealing birefringence values of > 250 GHz via mechanically induced stress along [0,1,-1] and [0,-1,-1] crystal directions [217, 218]. Therefore special care should be taken when engineering a device for high frequency applications.

The attributes of spin-VCSELs offer the potential for new applications such as reconfigurable optical interconnects, spin-dependent switches for optical telecommunications, quantum information processing and data storage, quantum computing, bandwidth enhancement, high speed modulators, cryptography of optical communication, circular dichroism spectroscopy, biological structure studies, biomedical sensing and advanced optical devices [14, 15]. Effective control of the polarisation of the spin-VCSEL via the pump offers prospects for applications such as optical networks and spintronics for data encoding or for other applications where stabilised VCSEL polarisation is required. In addition, polarisation oscillations could be exploited for optical communication and high performance interconnects such as optical oscillators for radio-over-fibre applications. PS spin-VECSELs could be employed in devices for applications such as coherent detection systems and all-optical helicity-dependent magnetic switches [320].

7.6 Summary

Using an external cavity formed by employing an HR-coated fibre as the top mirror, we presented the first demonstration of an optically pumped InAs/InGaAs QD-based spin-VECSEL operating at the important wavelength of 1300 nm. Circularly polarised lasing under CW optical spin injection is shown at RT with pump threshold of 11 mW.

The dependence of the output polarisation ellipticity (ε) of the spin-VECSEL on that of the pump (P) has been studied and analysed Our results reveal that the output polarisation ellipticity of the spin-VECSEL emission can exhibit either the same handedness as that of the pump polarisation or the opposite, depending on the experimental operating conditions. The difference between the two output polarisation ellipticity trends was discussed. However, further spectroscopic studies of the spin-VECSEL in necessary to obtain full understanding of the root cause factors.

Furthermore, PS and periodic oscillations in the range of the ROF of the device were observed and studied. The highest RF oscillation power was found with elliptically-polarised pumping with $P = \pm 0.6$. These oscillations can be tuned by varying the pumping power of the device.

CHAPTER 8: OPTICAL INJECTION OF 1300 NM SPIN-VECSEL[i]

Abstract:

This chapter investigates the control of the light polarisation emitted by a 1310 nm Quantum Dot spin-VCSEL at room temperature. The behaviour of the output polarisation ellipticity of the spin-VECSEL under circularly polarised optical injection is studied. In addition, rich nonlinear dynamics including limit cycle, period doubling, and chaotic oscillations are presented. These dynamics resemble the ones presented in the fourth and fifth chapters.

[i] This chapter is based on the papers:

1- S.S. Alharthi, E. Clarke, I.D. Henning and M.J. Adams, "Dynamics of optically injected 1300 nm Dot Spin Vertical External-Cavity Surface-Emitting Laser'', in preparation.

8.1 Introduction

Optical injection in semiconductor laser is a common technique used to obtain a rich variety of nonlinear dynamical behaviours suitable for numerous applications [321]. Nonlinear dynamics of EELs and VCSELs with optical injection have been extensively investigated over the last three decades [219, 321, 322]. However, injection-locking of VECSELs, or SDLs, has not received much attention. To the best of our knowledge, optical injection in VECSELs was only employed to achieve a single-frequency, CW and high output power optically pumped semiconductor laser [64]. Whilst most work has concentrated on the characteristics and dynamics of optically injected conventional VCSELs, apart from [64] the dynamics and behaviour of VECSELs under optical injection has not been explored. Therefore, in this work we will present the first, to the best of our knowledge, investigation of the output polarisation ellipticity characteristics and nonlinear dynamics of 1300 nm optically injected QD spin-VECSEL.

In this chapter experimental investigations of the dynamics behaviour and circular polarisation properties of a 1300 nm QD spin-VECSEL operating at RT and subject to circularly polarised optical injection are presented. At first the experimental setup used in this work is described. Then, control of the emitted polarisation by the optically injected signal is experimentally demonstrated. The polarisation state of the optical pump and that of the external signal is interchanged and results are presented accordingly. This includes the presentation of the experimental observation of circular PS induced by circularly polarised optical injection. This is followed by an experimental study of the nonlinear dynamics induced by circularly polarised optical injection. One case is investigated showing the situation when the pump and the ML have opposite circular polarisation states, viz. when the pump is RCP while the ML is

LCP. For the first time to the best of our knowledge we present experimentally measured evolution of optical spectra maps of that system identifying nonlinear dynamics via scanning the ML wavelength across the IL region of the spin-VECSEL under constant injection strength. A variety of nonlinear behaviours, including periodic (P1, P2), IL and chaotic dynamics are experimentally shown. The results presented in this chapter will be compared to the results presented in chapter 4 and 5.

8.2 Experimental Setup

Optical injection from an external tunable laser was applied on the 1300 nm QD spin-VECSEL sample described in chapter 6 and exposed to spin injection in chapter 7. Fig. 8.1 presents the experimental setup used in this work to investigate the effects of optical injection on the behaviour of the spin-VECSEL. This setup basically is the same as described in the previous chapter in Fig. 7.2. However, at the forth port of the 90/10 coupler; an external optical signal, generated by a 1300 nm external cavity tunable laser ML and amplified using an SOA, was injected into the spin-VECSEL sample via an optical circulator. The ML was set at 2 mW and amplified using a SOA whose gain was varied as required. The ML's polarisation was controlled by a PC. Through the third port of the circulator, all the outputs were sent via another 90/10 optical coupler to an OSA and an in-line polarimeter for analysis. The pump emission was blocked from travelling further in the setup by a 1300 nm IS placed before the 90/10 coupler. Furthermore, for studying the nonlinear dynamics of the optically injected spin-VECSEL the setup was adjusted by checking that the absolute output polarisation ellipticity of the spin-VECSEL measured by the head of a free-space polarimeter is similar to its relative counterpart measured by the in-line polarimeter. In

addition to the OSA, assessment of the dynamics was made using a PD and an ESA to measure any oscillatory behaviour.

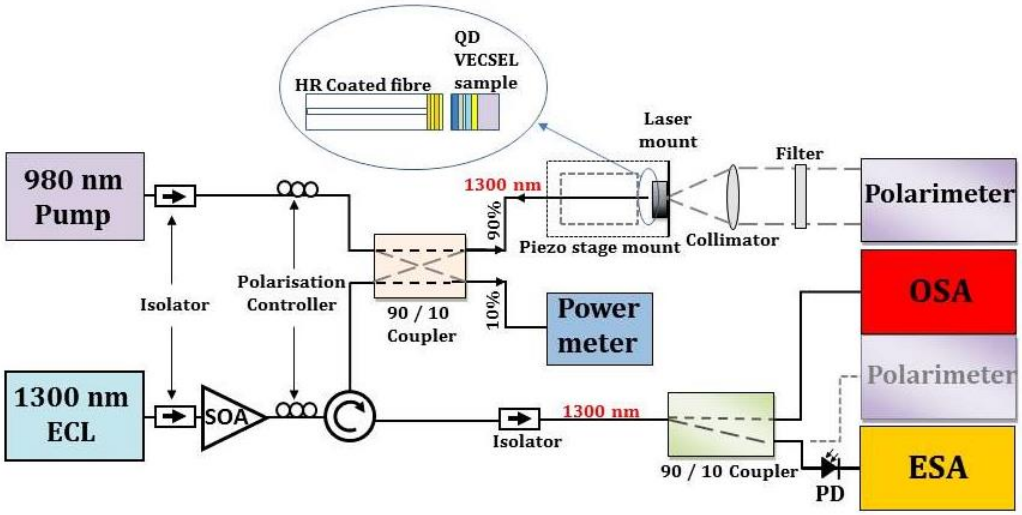

Fig. 8.1: Schematic diagram of the setup used in this work to study the effect of polarised optical injection in an optically-pumped 1300 nm spin-VECSEL sample. OSA: Optical Spectrum Analyser, SOA: Semiconductor Optical Amplifier; ECL: External Cavity Laser; PD: Photodiode; ESA: Electrical spectrum Analyser.

8.3 Results

The experimental setup above was used to perform all the measurements and results presented in this section. All of these were obtained from the sample when it emits circular polarisation with inverted sign with respect to that of the pump as shown in chapter 7. Moreover, no polarisation oscillations were found in the solitary spin-VECSEL when measurements were made.

8.3.1 Control of polarisation in a Spin-VECSEL subject to circularly polarised optical injection

In this subsection we have investigated the effects of the polarisation and initial detuning of the externally injected optical signal on the ellipticity (ε) of the

spin-VECSEL's emission. In chapter 7 it was experimentally demonstrated that the solitary spin-VECSEL's polarisation follows that of the optical pump but with inverted sign [90]. When optically injecting with either RCP or LCP, the spin-VECSEL shows a different behaviour as will be discussed below. The experimentally measured polarisation ellipticity of the spin-VECSEL's light emission was studied as a function of the initial frequency detuning, defined as $\Delta f = f_{SL} - f_{ML}$, where f_{ML} is the frequency of the ML and f_{SL} is the free-running frequency of the solitary spin-VECSEL SL, with the device subject simultaneously to circularly polarised optical pumping and optical injection. The polarisation state of the optical pump and that of the external optical injection signal were interchanged and results are presented accordingly.

8.3.1.1 Output polarisation ellipticity behaviour of spin-VECSEL under LCP pumping and different CP injections

In the first case, the spin-VECSEL was subject to LCP pumping and RCP optical injection. Fig. 8.2 shows that initially the spin-VECSEL's output polarisation ellipticity followed that of the pump but with inverted sign; then as the ML's frequency approached the locking bandwidth of the solitary SL, the output ellipticity of the spin-VECSEL moved slightly towards the polarisation of the pump. These results are centred at about 25 GHz due to the asymmetry of the IL region around zero detuning which is due to the change in the refractive index of the active region when the system is locked [111, 117, 323]. This consequently leads to a shift in the resonant wavelength of the laser towards higher values. For a further increase of the frequency detuning inside the locking range, the ML increasingly controlled the polarisation of the spin-VECSEL, changing the direction of the latter first and then driving it towards a higher degree of RCP ($\varepsilon \approx 0.98$) similar to that of the ML. As the detuning was

increased to higher values, the polarisation of the spin-VECSEL returned gradually to RCP (ε = 0.75) being again controlled by that of the pump.

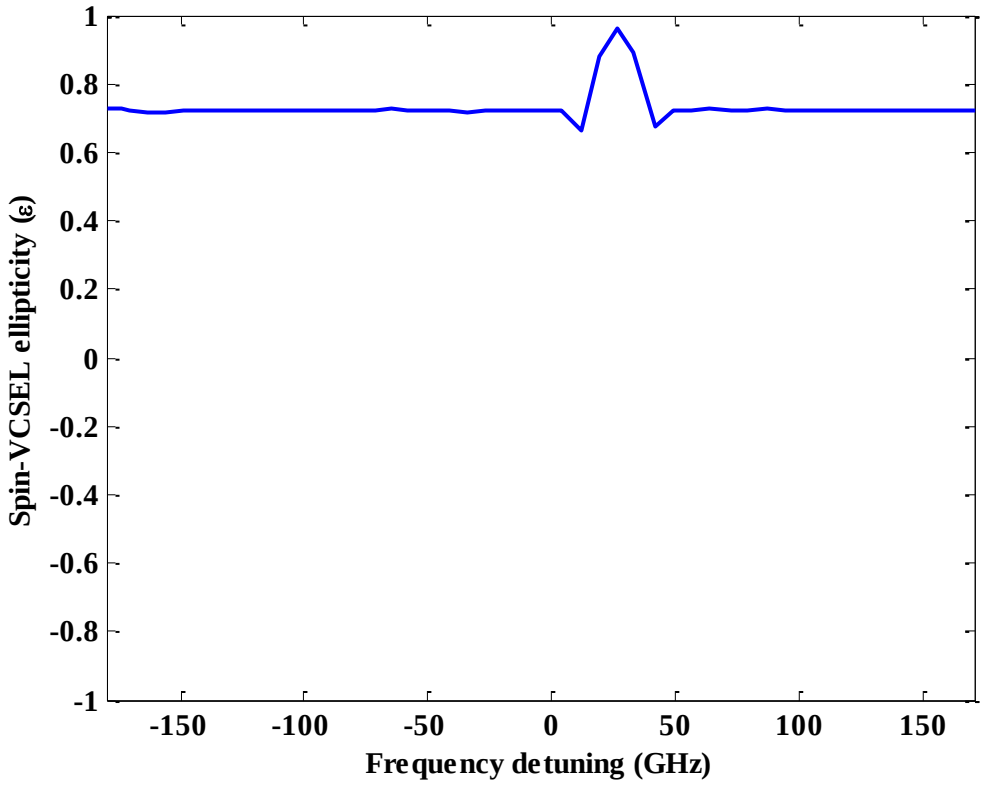

Fig. 8.2: Measured output polarisation ellipticity of the spin-VECSEL versus frequency detuning. The spin-VECSEL was optically-pumped with LCP light. The optically-injected signal from the ML had RCP.

Fig. 8.3 presents the case where the polarisations of the pump and the ML's injected signal are both set to LCP. It can be seen here again that initially the spin-VECSEL's output polarisation followed that of the pump; then as the ML's frequency approached the locking bandwidth of the solitary spin-VECSEL, the ML increasingly controlled the polarisation of the spin-VECSEL, switching it gradually from almost RCP (ε = 0.78) to LCP (ε = -0.99). As the detuning was increased to higher values, the polarisation of the spin-VECSEL returned abruptly to RCP (ε = -0.78) being again controlled by that of the pump. This behaviour is not independent of the direction of

change of frequency detuning which is indicative of PB and hysteresis. This will need to be verified in future works.

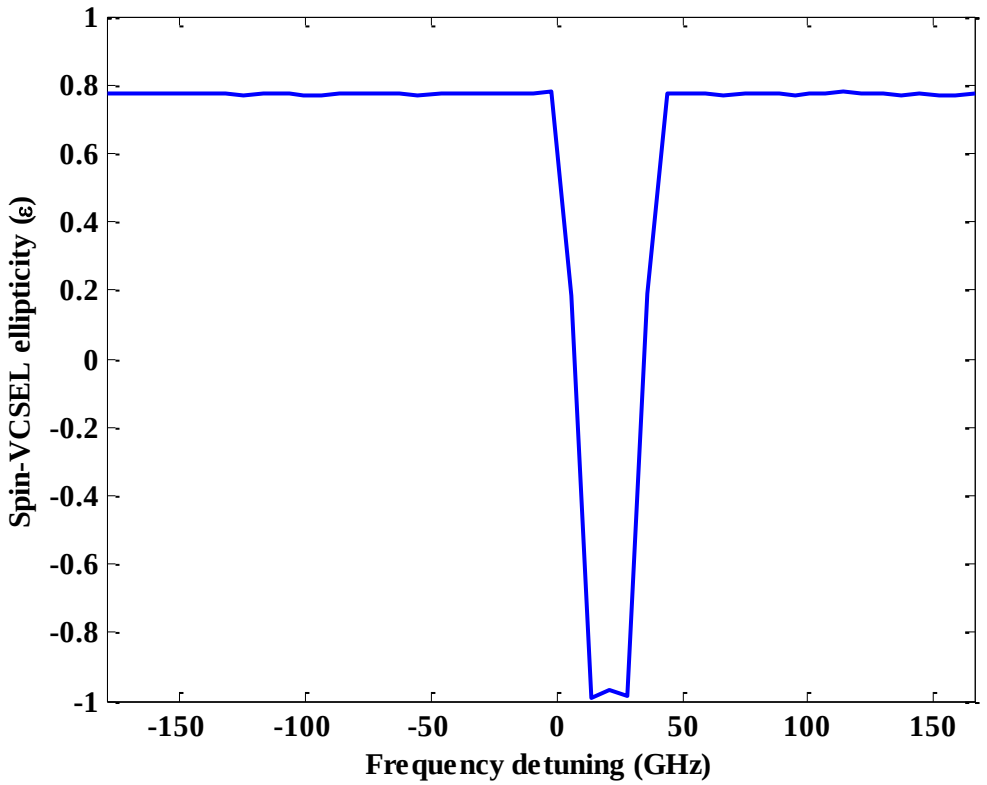

Fig. 8.3: Measured output polarisation of the spin-VECSEL versus frequency detuning. The spin-VECSEL is optically-pumped with LCP light. The optically-injected signal from the ML had LCP.

8.3.1.2 Output polarisation ellipticity behaviour of spin VECSEL under RCP pumping and different CP injections

We have also investigated the effects of polarisation and frequency detuning of the external signal on the ellipticity (ε) of the spin-VECSEL's emission when the SL was pumped with RCP with different polarisation states of the ML. As already demonstrated, when the spin-VCSEL is pumped with RCP (LCP), it produces RCP (LCP) emission [22]. However, our spin-VECSEL differs in that when it is pumped RCP (LCP), it can produce LCP (RCP) emission, an inverted sign with respect to that of the pump [90].Nevertheless, for RCP pumping with LCP and RCP optical injection,

the spin-VECSEL shows different behaviours as shown in Fig. 8.4 and Fig. 8.5, respectively.

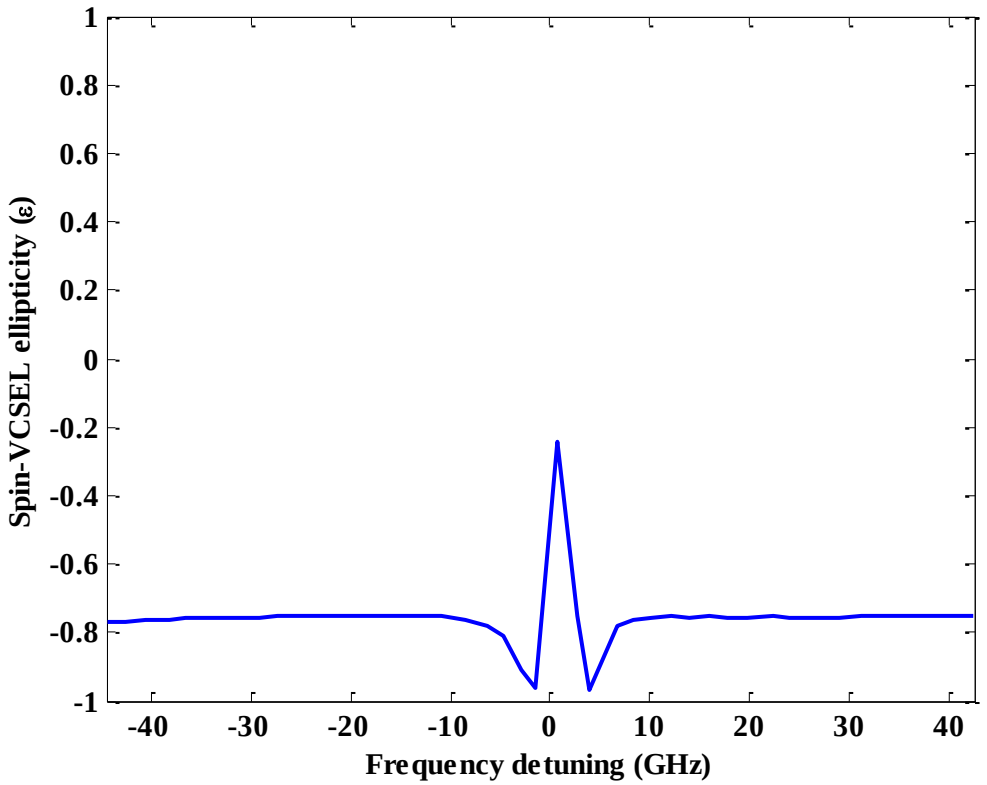

Fig. 8.4: Measured output polarisation of the spin-VECSEL versus frequency detuning. The spin-VECSEL is optically-pumped with RCP light. The optically-injected signal from the ML had LCP.

Specifically, Fig. 8.4 presents the output polarisation ellipticity of the spin-VECSEL under RCP pumping versus the detuning of the LCP ML's injection. This figure shows that the spin-VECSEL polarisation followed that of the pump at first; then as the ML's frequency approached the solitary spin-VECSEL's locking bandwidth, the ML controlled the polarisation of the spin-VCSEL and helped it to achieve a high degree of LCP (ε = -1). However, as the frequency detuning was increased, the output polarisation ellipticity first jumped to a lower degree of LCP (ε = -0.2) then returned back to a higher LCP degree of (ε = -0.97). This was due to the existence of polarisation oscillations with frequency above 10 GHz at these detuning values. As the

ML's wavelength approached higher detunings, the polarisation of the spin-VECSEL returned gradually to LCP (ε = -0.75) where it is now controlled again by that of the pump.

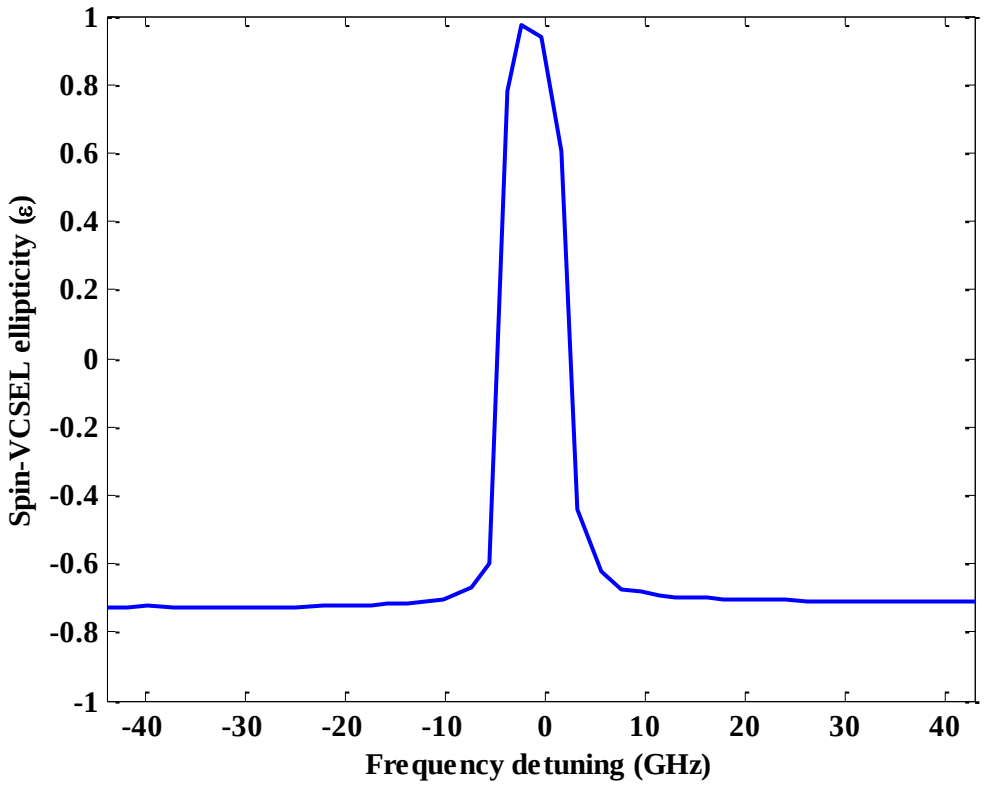

Fig. 8.5: Measured output polarisation of the spin-VECSEL versus frequency detuning. The spin-VECSEL is optically-pumped with RCP light. The optically-injected signal from the ML had RCP.

Fig. 8.5 presents the case where the polarisations of the pump and the ML are both set to RCP. It can be seen here that the SL output polarisation ellipticity for lower detuning values was following that of the pump but, as earlier mentioned, with opposite state to that of the pump. In addition, within the locking region of the SL, the ML controlled the polarisation of the spin-VECSEL, switching it gradually from almost LCP (ε = -0.78) to RCP (ε = 0.98). As the ML's wavelength approached higher detunings, the polarisation of the spin-VECSEL returned to LCP (ε = -0.72) where it is now controlled again by that of the pump.

8.3.2 Nonlinear dynamics of optically injected spin-VECSEL

This subsection is devoted to study the dynamic behaviour of the spin-VECSEL subject to polarised optical injection. The evolution of the optical spectra of the optically injected spin-VECSEL will be presented in the form of an evolution map in the plane of spin-VECSEL wavelength and the frequency detuning (Δf) between the ML and SL. The results presented in this case were obtained at a constant optical injection (K), while the frequency detuning was scanned, (decreased from positive, short wavelength, to negative, long wavelength, values), across the IL (IL) region of the solitary spin-VECSEL. It is worth pointing out that, due to the optical alignment power coupling losses, not all the optical injection power actually couples into the SL. While it is difficult to directly measure the actual K herein is defined as the ratio of the ML power over the solitary SL power as it appears on the optical spectrum of the OSA. In addition, the frequency detuning is defined as $\Delta f = f_{ML} - f_{SL}$, where f_{ML} is the frequency of the ML and f_{SL} is the free-running frequency of the solitary spin-VECSEL (SL). In this subsection one case will be presented in which the spin-VECSEL was subject to RCP pumping and simultaneously injected with LCP from the ML.

Fig. 8.6 presents the evolution of the optical spectrum of the SL subject to RCP pumping and LCP injection. The injection ratio (K) in this case was K= 98 and the wavelength of the solitary spin-VCSEL is 1302.3 nm bearing in mind that the pump power was set to 75 mW. The colour map is graded from black, representing the noise level of the measurement, to white, corresponding to the maximum peak power, through red and yellow. It can be seen that there was no effect from the ML on the SL before reaching the locking region of the SL. However, as the ML entered the SL's locking bandwidth, it locked the SL to its frequency. The locking characteristics are not very clear on this map alone due to the very narrow optical spectra compared with

the resolution of the OSA. Hence, the RF spectrum was used as an additional means to reveal the transitions and dynamics as will be shown below.

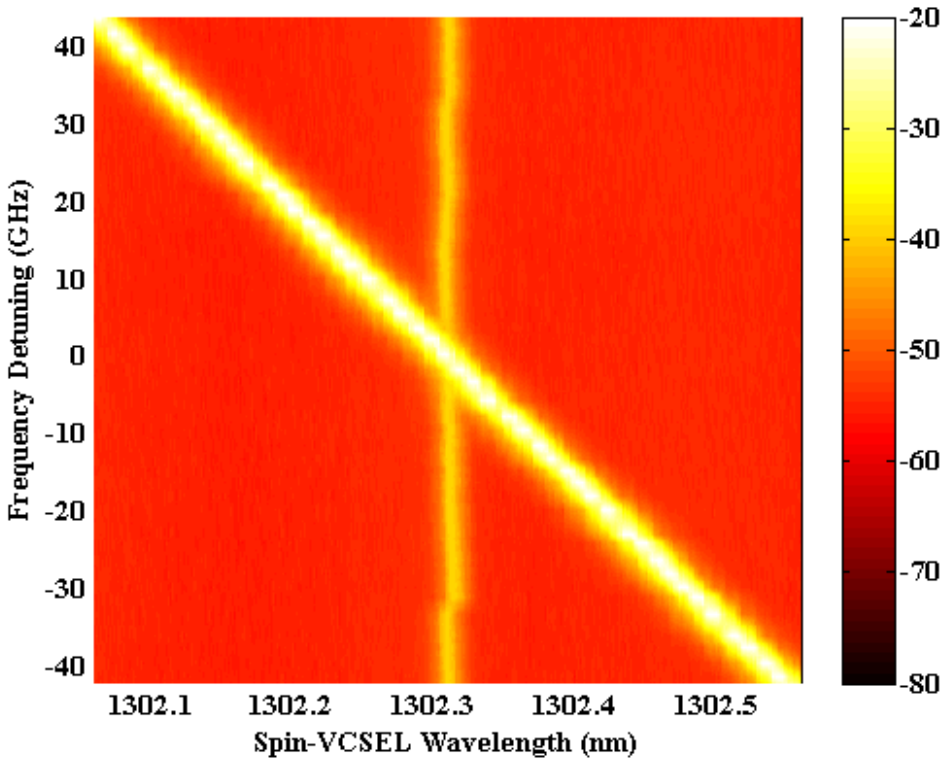

Fig. 8.6: Evolution of the optical spectrum of spin-VECSEL under RCP pumping and LCP optical injection.

The nonlinear dynamics of the optically injected spin-VECSEL are presented in Fig. 8.7. This figure shows the optical (left) and RF (right) spectra of the spin-VECSEL under LCP optical injection corresponding to the results shown in Fig. 8.6. When the frequency detuning between the ML and SL lay in the range of 3 to -1 GHz, one peak appeared in the RF spectrum of the SL revealing P1 oscillations as shown in the RF spectrum of Fig. 8.7(a-b). It should be mentioned that as the frequency detuning was decreased from 3 to -1 GHz, the frequency of oscillation was also reduced from ~15 to 8 GHz. We believe there might have been some dynamics with higher frequency of oscillations before this detuning range but due to the capability of our PD (it can only measure up to 15 GHz), they cannot be resolved or identified.

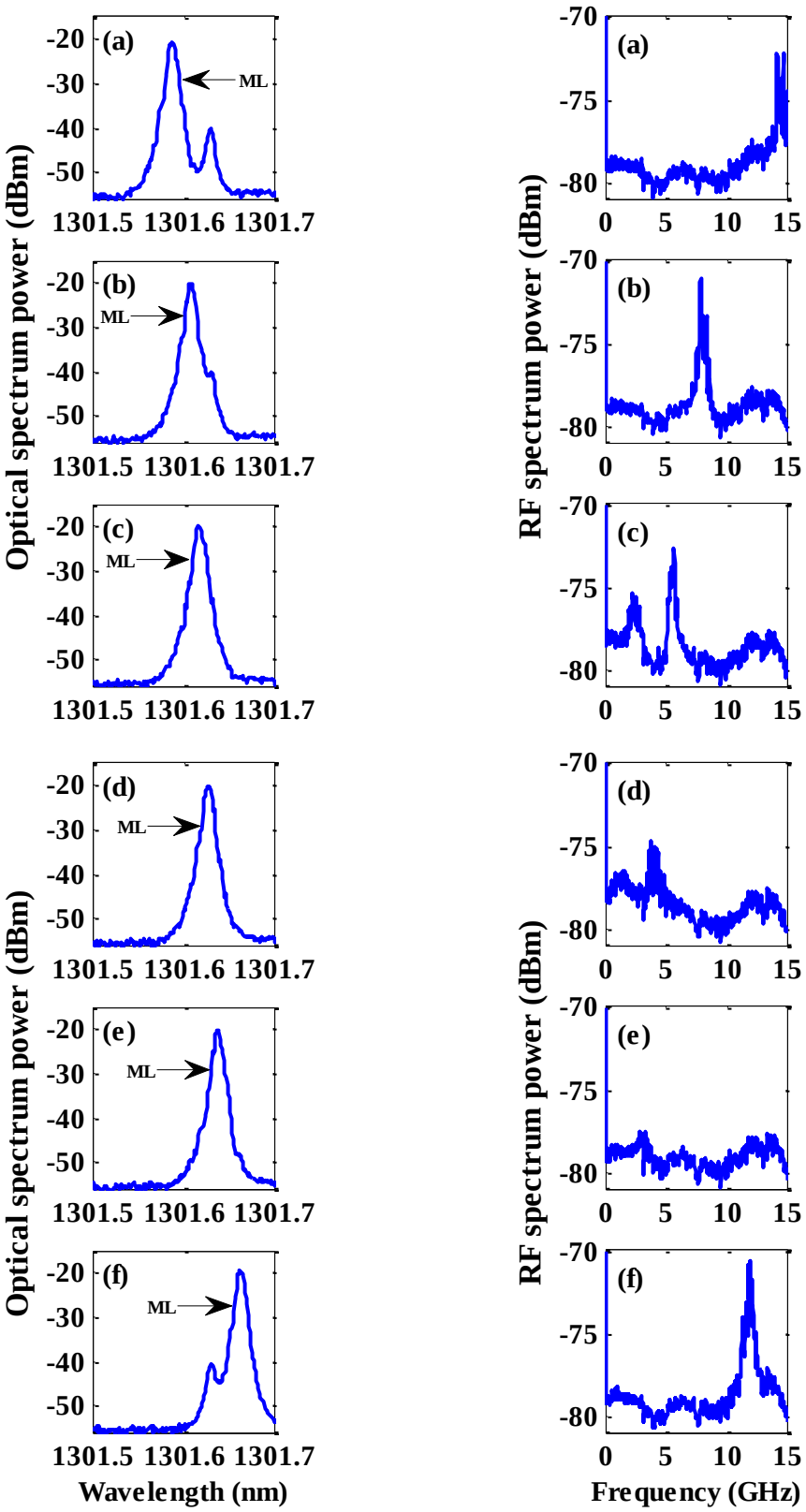

Fig. 8.7: Experimental optical (Right) and RF (Left) spectra of the spin-VECSEL; pumped with RCP and subject to optical injection with LCP.

For a further frequency detuning decrease, another weak peak appeared at half the oscillation frequency of P1 on the RF spectrum as shown in Fig. 8.7(c) forming period P2 dynamics for frequency detunings between -2 and -4 GHz. Next the spectrum became dominated by a broad pedestal as in Fig. 8.7(d), indicative of chaotic dynamics for detunings between -5 and -6 GHz. Decreasing the frequency detuning between -7 and -9 GHz, the RF spectrum showed a flatter and lower noise spectrum as presented in Fig. 8.7(e). This indicates that the SL was locked to the injected frequency of the ML. For a further decrease of the frequency detuning between -10 and -13 GHz, one peak appeared on the RF spectrum of the spin-VECSEL again revealing P1 oscillations. In contrast to P1 oscillation observed before the locking, it was found that as the frequency detuning was decreased, the frequency of oscillations of P1 increased from 7 to 14 GHz. For a further decrease of frequency detuning below -14 GHz, no peaks were observed on the RF spectrum whereas the ML optical spectrum moved away gradually from the SL leaving it at its solitary wavelength. However, there might have been more dynamics in this detuning range but as mentioned earlier, resolving such oscillations is beyond the capabilities of our lab.

8.3.3 Characteristics of the ML's reflected output power

The behaviour of the output of the ML reflected from the sample of the SL and measured by the OSA is studied in this subsection. Fig. 8.8 shows the ML's reflected output power as a function of the frequency detuning for injection ratio of 98 corresponding to the case in the previous subsection. The line in Fig. 8.8 was smoothed by 5% for clarity. It is worth mentioning that the SL was pumped to 75 mW with RCP and injected with LCP. The Y-axis of Fig. 8.8 shows the magnitude of the output power of the ML measured from the ML's peak of the optical spectrum when the SL is

subject to injection at constant injection strength and decreasing frequency detuning. It can be seen that as the detuning decreased, the reflected ML output increased until it got closer to the IL region of the SL. This increase of the magnitude of the ML peaks corresponds to the occurrence of amplification in the ML signal. Then as the detuning further decreased, the ML's output power started decreasing until it reached a minimum after which it recovered again.

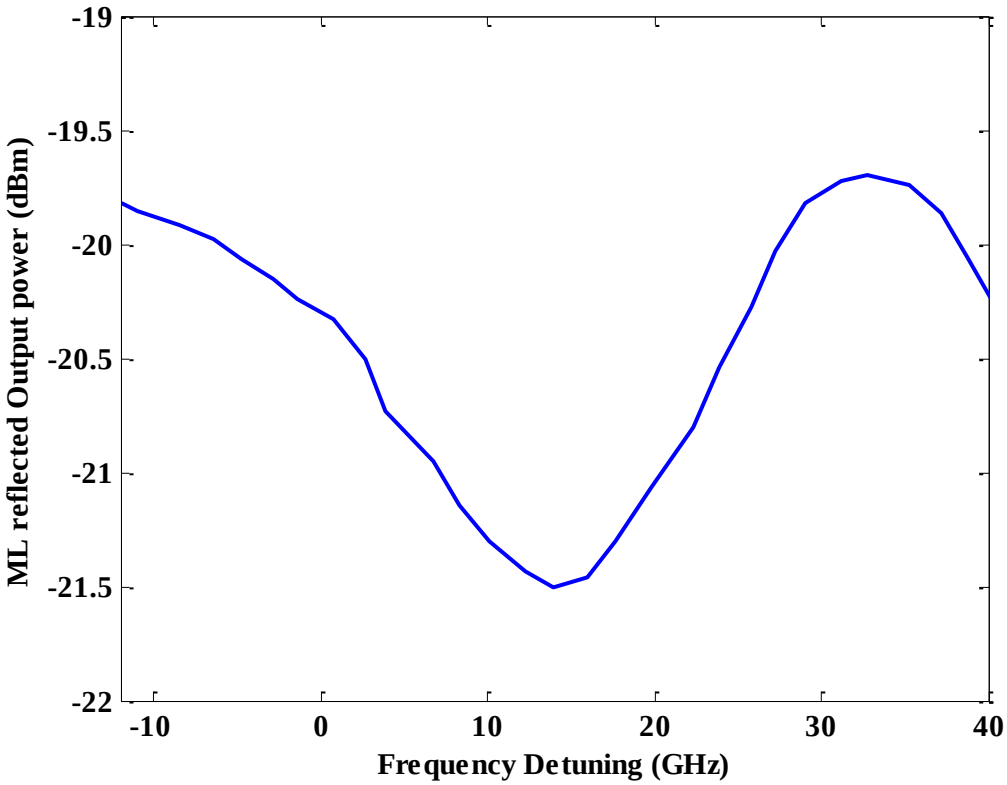

Fig. 8.8: ML's reflected output power as a function of the frequency detuning (Smoothed by 5%) for injection ratio of 98.

8.4 Discussion

The results presented in this chapter show that the optically pumped spin-VECSEL subject to polarised optical injection exhibits rich polarisation dynamics ranging from polarisation control [90, 132] to circular PS [133]. Moreover, nonlinear dynamics

similar to those found in spin-VCSELs and conventional VCSELs including P1, P2 and C are also presented [251-253].

The results started by presenting the effects of the polarisation and initial detuning of the externally injected optical signal on the ellipticity (ε) of the spin-VECSEL's emission. It has already been experimentally and theoretically demonstrated that the solitary 1300 nm spin-VCSEL polarisation follows that of the optical pump [22]. Furthermore, the spin-VECSEL device used for optical injection in this work shows that the polarisation of the pump controls that of the spin-VECSEL with inverted sign relative to its own polarisation state. However, when the spin-VECSEL is optically injected with either RCP or LCP from an external ML, the spin-VECSEL shows a different behaviour. It has been found that the polarisation of the spin-VECSEL follows that of the optical pump outside the locking region of the SL whereas inside the locking region the polarisation of the spin-VECSEL was effectively controlled by the polarisation of the ML's optically injected signal. Moreover, optical injection with circularly polarised light (RCP or LCP) produced a high degree of ellipticity in the spin-VECSEL. These results are consistent in terms of polarisation controllability with our results reported in [132, 230] and discussed in more detail in chapter 4. However, the detunings in the QD spin-VECSEL case, where the SL was effectively controlled by the ML, are much smaller than those in the case of the dilute nitride QW spin-VCSEL. This is attributed to the very narrow optical spectrum of the QD spin-VECSEL compared to the QW spin-VCSEL. Moreover, the polarisation ellipticity fluctuations when the ML approaches the locking range of the SL might be caused by the oscillatory behaviour within this region which cannot be seen in the QW spin-VCSEL due to its lower output power. PS induced by optical injection in conventional VCSELs has been extensively investigated in the literature since its first observation

by Pan et al [33]. Since then, parallel [37] and orthogonal [151, 155] optical injection has become a common method to obtain PS in short or long wavelength conventional VCSELs [126, 152, 156-158]. Optical injection of arbitrary polarisation was also reported theoretically by Al-Seyab et al. [130] and experimentally by Hurtado [155] to produce PS in a 1550-nm VCSEL. Nevertheless, there has only been one experimental report of PS induced by circularly-polarised injection into two 850 nm VCSELs [131]. Recently, we have reported the first observation of circular PS induced by circular polarisation optical injection in 1300 nm spin-VCSEL [133, 324]. These results were also discussed further in chapter 4. The PS results presented in this work are similar and consistent with those reported in [133]. However, in [133] the PS took place when the polarisation of the ML was in an opposite state to that of the pump laser whereas results presented here revealed that PS occurred when the polarisation of the pump and that of the ML were similar (e.g. had the same state). This is due to the fact that the QD spin-VECSEL emits circular polarisation with a state opposite to that of the pump as reported in [90] and discussed in the previous chapter.

A variety of nonlinear responses and dynamics of optically injected spin-VCSEL was presented. These included P1 oscillation, P2, chaotic oscillation (C). Similar nonlinear dynamics, including P1, P2, quasi-periodicity, IL and C, in conventional VCSELs under orthogonal optical injection has been experimentally and theoretically found and analysed for short wavelength (850 nm) [119, 120, 123, 148-153] and for long wavelength (1550 nm) [125-127, 154, 254] devices. These nonlinear dynamics were also theoretically predicted for QW spin-VCSEL under different forms of polarised optical injection (linear, circular, and elliptical) [62]. In addition, similar dynamics were observed and presented in chapter 5 for our 1300 nm dilute nitride spin-VCSEL subject to circular polarisation optical injection.

Four types of nonlinear dynamics were studied in this work. Limit cycle dynamics correspond to the beating between the ML and injected SL frequencies and appear as a periodic oscillation of the laser output at a single frequency and its harmonics. P2 dynamics appear as additional peaks on the RF spectrum of the SL at half the frequency of the P1 oscillation. IL appears as one peak on the OSA at the ML frequency with flat RF spectrum. Finally, chaotic oscillations (C) correspond to a complex behaviour and a strong aperiodic oscillation of the SL output. These dynamics were identified based on the RF spectra of the optically injected SL (measured by the ESA) since the very narrow optical spectrum of our QD spin-VECSEL cannot be resolved to identify such dynamics with our OSA (spectral resolution of 15 pm).

The last subsection of the results presented a study of the ML's reflected power; it was found that as the detuning decreases, the ML's power was amplified until reaching a range close to the free-running SL frequency. Then as the detuning further decreases the ML's output power started decreasing until it reached a minimum. Any further detuning decrease after this point led to the recovery of the ML output. The mechanism of this behaviour was explained in more detail in chapter 5. This behaviour indicates that the spin-VECSEL under optical injection might work as an amplifier.

8.5 Summary

In summary, this chapter presented the first experimental demonstration of optical injection into the QD 1300 nm spin-VECSEL. It was found that the polarisation of the spin-VECSEL follows that of the optical pump but with inverted sign outside the locking region of the SL whereas inside the locking region the polarisation of the spin-VECSEL was effectively controlled by the polarisation of the ML's optically-injected signal. Moreover optical injection with circularly polarised light (RCP or

LCP) produced a high degree of ellipticity in the spin-VECSEL. Additionally, the experimental observations of optical power circular PS in a QD 1300 nm spin-VECSEL subject to circularly polarised external optical injection were presented. These results are consistent with the results presented in chapter 4.

The investigation of the dynamics of the spin-VECSEL under circularly polarised injection revealed the evolution of the nonlinear dynamics as the frequency detuning changed. Various types of instabilities and nonlinear dynamics were found including P1, P2, C and IL. These nonlinear dynamics were analysed based on the RF spectra of the spin-VECSEL subject to optical injection and they also show consistency with results reported in the literature for conventional VCSELs and presented in chapter 5 for our QW spin-VCSEL.

CHAPTER 9: CONCLUSION AND FUTURE WORK

Abstract:

This concludes this thesis. The work that has been undertaken is summarised and notable results are restated. The direction of future research is also discussed.

9.1 Main achievements

This section highlights the main conclusions and restates the most significant results of work presented throughout this thesis.

9.1.1 Dynamics of solitary 1300 nm QW spin-VCSELs

We investigated experimentally and theoretically the nonlinear dynamics of solitary 1300 nm dilute nitride QW spin-VCSELs as a function of pump polarisation and power. Two VCSEL samples with different Nitrogen contents were investigated. Our results for both samples demonstrated the dependence of the output polarisation ellipticity on that of the pump and that a large DOCP can be achieved for the circular pump polarisation. In the experimental results sample 1 showed stable behaviour under pump power and polarisation variations whereas sample 2 showed instabilities. For the second sample we demonstrated self-sustained oscillations at the output of the spin-VCSEL, at frequencies of the order of 15 GHz. These oscillations can be finely tuned by varying the pump polarisation and power. Very good agreement was found with theoretical results for both samples based on the SFM in different aspects such as the output polarisation ellipticity, the shape of the instable region, the frequency of oscillation and RF oscillation power. The difference between the behaviour of the two samples is attributed to the nitrogen concentrations. In fact this is an interesting engineering parameter that could be controlled to improve the behaviour of the dilute nitride spin device and also to generate oscillation and dynamics. These oscillations would be of interest from a practical point of view and so this would be an area for future study.

9.1.2 Nonlinear dynamics of optically injected 1300 nm QW spin-VCSEL

We studied experimentally for the first time to the best of our knowledge the output polarisation ellipticity-resolved dynamics of optically injected spin-VCSELs. We found that the polarisation of the spin-VCSEL follows that of the optical pump under low injection power whereas under high injection power the polarisation of the spin-VCSEL was effectively controlled by the polarisation of the ML's optically-injected signal. These results are in very good agreement with our SFM theoretical simulations and also with theoretical predictions reported in [62] which were also generated by SFM. In addition, we experimentally studied the PS and PB dynamics of the spin-VCSELs under circularly polarised optical injection. We reported the experimental observation of optical power and wavelength induced circular PS and PB in a 1300 nm spin-VCSEL subject to circularly polarised external optical injection. The relationship between output polarisation ellipticity and optical injection power and wavelength were experimentally analysed under different polarisation states for pump and injection. Different forms of circular PS, gradual and abrupt, in addition to different forms of PB, anticlockwise and clockwise, were experimentally observed.

We reported an experimental study of the nonlinear dynamics in a 1300 nm spin-VCSEL subject to linear and circular polarised optical injection. A rich variety of nonlinear behaviours, including periodic (P1, P2), four-wave mixing and chaotic dynamics were observed. In addition features such as power amplification, frequency-pulling and pushing effects, wavelength conversion and power transfer were also reported.

9.1.3 Demonstration of 1300 nm QD Semiconductor Disk Laser

We demonstrated, for the first time to our knowledge, CW lasing at RT of an optically pumped QD-SDL operating at 1300 nm within an external cavity which was formed using an HR-coated fibre as the top mirror. A pumping threshold of 11 mW was reported in addition to an output power greater than 0.9 mW. Wavelength tuning over 14 nm was also reported.

9.1.4 Spin injection in 1300 nm QD VECSEL

We demonstrated the first CW-operation optically pumped InAs/InGaAs QD-based spin-VECSEL operating at the important wavelength of 1300 nm. Circularly polarised lasing under CW optical spin injection is shown at RT. We have analysed the dependence of the output polarisation ellipticity (ε) of the spin-VECSEL on that of the pump (P). Our results reveal that the ellipticity of the emission can exhibit either the same handedness as that of the pump polarisation or the opposite with ellipticities up to 0.73 and 0.84, respectively, depending on the experimental operating conditions. Furthermore, PS, and periodic oscillations at frequencies consistent with the ROF of the device were observed and studied. The highest RF oscillation power was found with elliptically-polarised pumping with P = ±0.6. These oscillations can be tuned by varying the pumping power of the device.

9.1.5 Nonlinear dynamics of optically injected 1300 nm QD spin-VECSEL

An experimental study of the optical injection of the dynamics of 1300 nm QD spin-VECSELs under circularly polarised optical injection was presented. The output

polarisation ellipticity of the spin-VECSEL was studied under interchanged cases of right and LCP optical pumping and optical injection. The results demonstrated that the polarisation of the spin-VECSEL follows that of the optical pump but with inverted sign outside the locking region of the SL whereas inside the locking region the polarisation of the spin VECSEL was effectively controlled by the polarisation of the ML's optically-injected signal. Moreover optical injection with circularly polarised light (RCP or LCP) produced a high degree of ellipticity in the spin VECSEL. Moreover, as the frequency detuning of the polarised optical injection changed the spin-VECSEL exhibited various types of instabilities and nonlinear dynamics including P1, P2, C and IL. These nonlinear dynamics show consistency with results reported in the literature for conventional VCSELs and presented in chapter 5 for our QW spin-VCSEL.

9.2 Recommendations for future work

The work presented in this thesis poses new questions which require further work and some of them suggest new research routes.

9.2.1 Solitary spin-V(E)CSELs

We believe that the self-sustained oscillations of the solitary 1300 nm QW spin-VCSEL have oscillation frequencies above 15 GHz; this was also predicted by the SFM, but due to the limitations of our measurement system these oscillations cannot be resolved. The existence of very high frequency oscillations would be of interest for use in a number of applications and so this presents an area for further investigation.

The difference between the degrees of ellipticity reported in the 1300 nm QD spin-VECSELs needs further work to understand the variation in trends in Fig. 7.5 and

Fig. 7.6. This could be helped by conducting further spectroscopic studies of the spin-VECSEL using polarisation-resolved PL. Furthermore, the differences in the degrees of ellipticity across the sample when the HR-coated fibre moved across it needs to be investigated both by measuring the output ellipticity at different positions, and checking for different samples as well.

Another route for future work is theoretically studying the behaviour and the nonlinear dynamics of our 1300 nm QD spin-VECSEL via the QD SFM as reported in [166]. There is great opportunity to understand the effect of different parameters such as the spin relaxation, dichroism and the birefringence rates on the behaviour of the output ellipticity of the solitary QD spin-VECSEL, and hence reveal more about the system dynamics.

9.2.2 Optical injection in 1300 nm spin-V(E)CSELs

In chapter 4 we studied the PB and switching properties of the output polarisation ellipticity of the 1300 nm VCSELs subject to circularly polarised optical injection and we found different types of power and wavelength-induced PS and PB. Further theoretical work is needed in order to extend the SFM to enable it to explain the different forms of PS and PB. Additionally, the injected optical power required for PS as a function of the wavelength detuning needs to be studied theoretically and experimentally. Similar work has been done on conventional 1550 nm VCSELs [156]. The same study could be performed on the 1300 nm QD spin-VECSELs since there was an indication of PB around the abrupt PS reported in chapter 8, which would be worth investigating.

The results showing the nonlinear dynamics of optically injected 1300 nm spin-V(E)CSELs in chapters 5 and 8 need to be extended to see the effects of the

wavelength detuning and injection strength on the these dynamics. This can be experimentally and theoretically done by creating stability maps of the spin-V(E)CSELs under a given pump power and polarisation. With the aid of a faster PD and another SOA to amplify the weak signal of our QW spin-VCSEL in order to split it between the OSA and the ESA, the nonlinear dynamics can be identified from both the OSA and ESA, and hence this work can be experimentally easily achieved. The stability map is a good tool to clearly show the boundaries amongst different dynamical regimes and its variation with change of wavelength detuning and injection strength. Although the dynamic behaviour and circular polarisation properties of QW spin-VCSELs subject to different forms of polarised optical injection (linear, circular, and elliptical) have been theoretically investigated in [62], the SFM parameters used in that work are different from the parameters that fit our QW spin-VCSELs presented in this thesis. Hence, it would be very interesting to simulate the nonlinear dynamics reported in chapter 5 and compare theoretical with experimental results. The whole issue of finding appropriate device and material parameters in order to model device behaviour remains an important aspect for further work.

Moreover, for the optical injection into 1300 nm spin QD VECSELs, the QD SFM [166] would be combined with the optical injection terms as in [130] to simulate the nonlinear dynamics of the optically injected spin-VECSEL that were experimentally reported in chapter 8.

One more route that could open a new research line is the possibility of realising spin-Vertical-Cavity Semiconductor Optical Amplifier (spin-VCSOA) with our spin-V(E)CSELs by optically driving these devices below threshold and then inserting an external signal to study the behaviour of the intensity and output ellipticity.

All the previously mentioned experimental works can be conducted on the existing setups in our lab without the need for new laser samples. However there are a few proposals on the topic of spin injection that might be worth studying such as the hybrid spin injection scheme.

9.2.3 Hybrid optical and electrical spin injection

An approach to achieving spin-VCSEL operation using conventional VCSELs under hybrid optical and electrical pumping has been reported by Hovel et al [72]. In early work at the beginning of this PhD a similar approach was tried using a commercial 1550 nm VCSEL with a combination of electrical and CW circularly polarised optical pumping. Unfortunately, we were unable to generate a sufficient population of spin polarised carriers compared with the unpolarised carriers produced by the electrical current. However, the same concept can be applied to our QD half-VCSEL to realise hybrid optically and electrically pumped spin-VECSEL. Perhaps electrical contacts could be incorporated with the half-VCSEL structure in order to electrically inject it with unpolarised carriers.

If the electrical contacts were incorporated into the QD half-VCSEL structure they also could be incorporated into arrays and driven by a hybrid electrical and optical pumping technique which would lead to the realisation of a QD spin-VECSEL array or at least to a QD conventional VECSEL array if the spin injection was not successful. This at least benefits from the low thresholds of these devices since our QD VECSEL has a threshold of 11 mW under pure optical pumping: thus this threshold will be reduced if combined with electrical pumping.

APPENDICES

Appendix A: Polarisation of Light

From the Maxwell equations, a monochromatic plane electromagnetic wave of light in a vacuum propagating in the z-direction with an angular frequency ω and a wave-number k can be described by two orthogonal field components E_x and E_y given by [325]:

$$E_x(z,t) = a_1 \cos(\omega t - kz + \delta_x) \quad \text{A. 1}$$

$$E_y(z,t) = a_2 \cos(\omega t - kz + \delta_y) \quad \text{A. 2}$$

where a_1, a_2 are the amplitude of the field components and δ_x, δ_y are their phases. Both E_x and E_y components are perpendicular to the propagation direction. Eliminating (ωt –kz) from equations (A1) and (A2) yields [325]:

$$\left(\frac{E_x}{a_1}\right)^2 + \left(\frac{E_y}{a_2}\right)^2 - 2\frac{E_x}{a_1}\frac{E_y}{a_2}\cos\delta = \sin^2\delta \quad \text{A. 3}$$

This is an ellipse equation, known as the polarisation ellipse, and often used to express the polarisation direction and state. The polarisation is presented by the amplitudes of the field a_1, a_2 and the phase difference $\delta = \delta_y - \delta_x$ between the two components E_x and E_y.

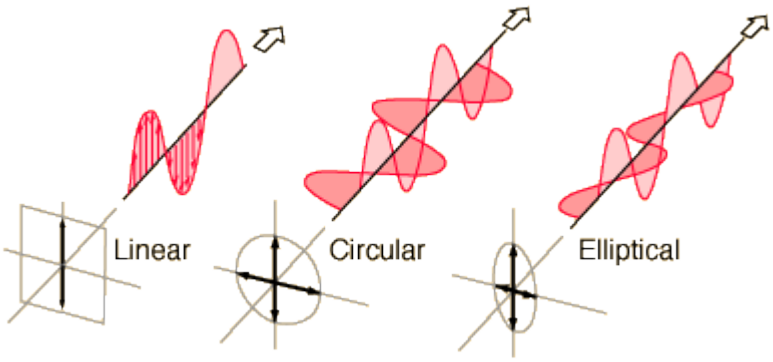

Fig. A.1: Types of polarisation in light, reprinted from Hyperphysics website [326].

By definition, the light is LP when E_x and E_y are in phase with each other $\Delta\delta = m\pi$ with m as an integer. In this case, the electric field oscillates in a two-dimensional

plane, which is parallel to the XY plane. The projection of the field vector on the XY plane is a straight line. When the amplitude of E_x (E_y) component is zero a_1=0 (a_2=0), there will be only one component oscillating along y(x) axis, thus this is referred as a vertical (horizontal) LP light (as illustrated on the left of Fig. A.1). If the two amplitudes are equal $a_1 = a_2$ and there is no phase difference ($\Delta\delta$= 0), and, then $E_x = E_y$ and this is referred as LP light rotated by 45°. If Ex = E_y and $\Delta\delta = (m + ½)\pi$ applies, the light is circularly polarised (as illustrated in the centre panel of Fig. A.1). In this case the propagation direction and the trajectory of the field vector will be either clockwise or anticlockwise; this is referred to as the wave's handedness, depending on the parity of m. If m is an odd (even) number, the trajectory will be in the clockwise (anticlockwise) direction resulting in right (left) circularly light polarisation. In all other cases, the light is elliptically polarised (as on the right of Fig. A.1). This includes the case when the amplitudes of the two components are different ($a_1 \neq a_2$) or the case when the phase difference is neither $\Delta\delta = m\pi$ nor $\Delta\delta = (m + ½)\pi$ [325].

Measurement of the polarisation state

The polarisation characteristics, of spin-V(E)CSELs and also of the tunable laser (ECL) used in this thesis, including polarisation direction and state are described via the use of the Stokes parameters. These parameters are a set of values {S_0, S_1, S_2, S_3} that provide information about the degree of linear, elliptical and circular polarisations. The first Stokes parameter {S_0} measures the total intensity (I_0) of the optical beam; while the second parameter {S_1} describes the amount of optical intensity transmitted over the linear (I_x) horizontal (0° or Ex) or linear (I_y) vertical (90° or Ey) polarisation axes. The third parameter {S_2} describes the amount of intensity transmitted over the two orthogonal linear polarisation axes (E_x and E_y) rotated by 45° and 135° (I_{+45}, I_{135}),

respectively, with respect to the horizontal axis. The fourth Stokes parameter {S_3} provides information about the amount intensity of right (I_R) and left (I_L) circular polarisation. Fig. A.2 (a) shows the most important components for measuring Stoke parameters.

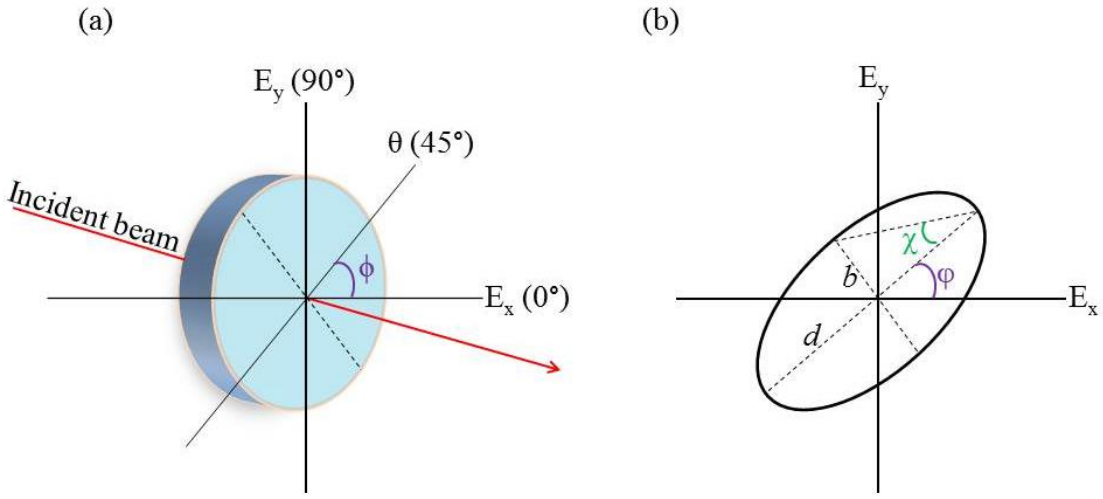

Fig. A.2: Schematic for (a) the important intensity components to measure Stokes parameters, (b) the Polarisation Ellipse.

The Stokes parameters {S_0, S_1, S_2, S_3} are defined from the intensity of the incident beam along the axes shown Fig. A.2 (a) as follows:

$$S_0 = I_0 = {a_1}^2 + {a_2}^2 \quad \text{A. 4}$$

$$S_1 = I_x - I_y = {a_1}^2 - {a_2}^2 \quad \text{A. 5}$$

$$S_2 = I_{45} - I_{135} = 2a_1.a_2 \cos\phi \quad \text{A. 6}$$

$$S_3 = I_R - I_L = 2a_1.a_2 \sin\phi \quad \text{A. 7}$$

where I_0, I_x, I_y, I_{45}, I_{135}, I_R and I_L are the optical intensities as defined above. Theoretically, the Stokes parameters for a perfect polarised light are derived from the RCP and LCP electric fields E_+ and E_-, thus the ellipticity is defined as [41]:

$$\varepsilon = \frac{\langle S_3 \rangle}{\langle S_0 \rangle} \quad \text{A. 8}$$

The Stokes parameters can be also characterised using the azimuthal orientation φ and ellipticity χ polarisation angles as shown the polarisation ellipse in Fig. A.2(b). The azimuth angle φ denotes the angle that the major axis of the ellipse makes with the x-axis, while χ is obtained from the ratio of the semi-minor to the semi-major axes of the ellipse (*tan(χ) = b/d*). Therefore, the Stoke parameters can be defined from these polarisation angles as follows [327, 328]:

$$\begin{gathered} S_0 = I_0 \\ S_1 = I_0 * \cos(2\varphi) * \cos(2\chi) \\ S_2 = I_0 * \sin(2\varphi) * \cos(2\chi) \\ S_3 = I_0 * \sin(2\chi) \end{gathered} \quad \text{A. 9}$$

The Stokes parameters for completely polarised light given in Equation (A.9) satisfy the identity.

$$S_0^2 = S_1^2 + S_2^2 + S_3^2 \quad \text{A. 10}$$

The fractional polarisation (FP) or ''(*DOP*)'' is defined by the four Stokes parameters as [41]:

$$FP = DOP = \frac{\langle S_1^2 \rangle + \langle S_2^2 \rangle + \langle S_3^2 \rangle}{\langle S_0^2 \rangle} \quad \text{A. 11}$$

where $\langle \bullet \rangle$ represents averaging over time scales in which the measurements are made. The value of the FP ranges from 0 (natural unpolarised light) to 1 (polarised light). The *DOCP* is defined from the Stokes parameters as:

$$DOCP = \frac{\langle S_3 \rangle}{\langle S_0 \rangle} \quad \text{A. 12}$$

The ellipticity ε of the polarisation is defined as the ratio of circular to total polarisation.

$$\varepsilon = \frac{DOCP}{DOP} \qquad \text{A. 13}$$

The ratio *DOCP*/*DOP* is the quantity studied in the experimental investigation of spin-injection.

Appendix B: Instrument Listing

❖ Laser Driver and Temperature Controllers

A variety of manually operated Thorlabs laser diode controller and temperature controller units have been used to control the bias and temperature of the 1300 nm SOA and 980 nm pump laser. The temperature controller Thorlabs TED200 is a precision temperature controller designed to drive thermoelectric cooler (TEC) elements with currents up to ± 2 A. The temperature is displayed with a resolution of 0.01 ºC. The temperature stability is less than 0.002 ºC. The operating temperature is from 0 to 40 ºC. The Thorlabs LDC220C laser diode controller has a current range from 0 to 2 A with a precision of 2 mA.

❖ Photodiodes

A Newport 818-BB-35F InGaAs photodiode was used to detect the oscillatory signal and send it to the RF spectrum. It was packaged in a mount and powered using embedded batteries. Its bandwidth was found to be in excess of 14 GHz.

❖ Tunable lasers

The 1300 nm tunable laser used in optical injection experiments was an external cavity semiconductor laser (ECL) module for the OSICS mainframe, now available from Yenista. The maximum output power of the ECL is 2 mW over a tuning range between 1270 and 1340 nm.

❖ Power Meters

The ILX OMM 6810B optical meter was used manually and in automated measurements. It has an automated detection of the wavelength and the power range. It covers wavelength measurements between 350 and 1650 nm with an accuracy of 0.1 nm. Powers were measured between -90 and 10 dBm with an accuracy of 1%.

The Thorlabs PM20 fiber-optic power meter is a fibre-optic power measurement system with built-in optical sensor with FC-PC fibre connector. This power meter can measure powers between -60 to 13 dBm with a width range of wavelengths from 800 to 1700 nm. The desired wavelength must to be selected manually. Both power meters offer measurements in dBm or in W.

❖ Optical Spectrum Analyser

An Ando AQ6317B was used for our measurements. Optical spectrum measurements could be performed between 600 and 1750 nm with power of -90 to 10 dBm, and a spectral resolution of 15 pm.

❖ Electrical Spectrum Analyser

This is also known as the RF spectrum analyser. The Agilent E4440A was used to measure RF spectra and to detect the oscillations of the solitary or optically injected spin-V(E)CSELs. The signal is received first by a fast photo-detector (13GHz) before being sent to the RF analyser. The RF analyser has a bandwidth of 26.5 GHz, however it was only used to perform measurements up to 15 GHz to respect the photodiode bandwidth.

❖ Isolators

In optical pumping and optical injection experiments, it is essential to eliminate any back reflection to ensure a stable operation and proper results. Therefore, an isolator, IO-J-980 from Thorlabs (with >30 dB isolation, <1.4 dB insertion loss at 980 nm and maximum power of 3 W) was inserted in front of the 980 pump laser while a second isolator IO-H-1310APC from Thorlabs (with >29 dB isolation, >0.5 dB insertion loss and maximum power of 300 mW) was placed in front of the ML and in the way of the collected spin-V(E)CSELs signal before being sent to the analysis tools.

❖ Fibre coupler (FC)

Thorlabs FC980-90B single mode 2x2 fibre coupler has a centre wavelength of 90 nm and a coupling ratio of 90:10. It was used to send the 980 pump to the sample and collect the 1300 nm signal from the spin-device and send it to the analysis tools. It has an insertion loss of 0.7 dB and 10.5 dB for the cross and bar port, respectively, and directivity of more than 55 dB.

Two FOCI C-NS (1x2 and 2x2) fibre couplers with operating wavelength of 1310 nm were used to split the 1300 nm signal from the spin-devices between the inline polarimeter and the OSA or the ESA. They have a 50:50 and 90/10 coupling ratios, with directivity of > 50 and > 60 dB and insertion loss of 3.4 and 0.7/ 10.8 dB, respectively.

❖ Circulators

A fibre optic circulator is a three-port device that allows light to travel in only one direction. It was used to inject light from ML on port 1 into the SL by port 2 and the output of the spin-V(E)CSELs was collected at port 3. This avoids back reflections. Two Thorlabs CIR1310-APC fibre optic circulators with a wavelength range of 1280-1340 nm, max insertion loss of 0.8 dB, isolation of > 40 dB and directivity of more than 50 dB were used in our optical injection experiments.

❖ Polarimeters

An Agilent 8509B in-line polarisation analyser was used to measure the relative polarisation of the spin devices. It has a wavelength operating range between 1200 nm and1600 nm and power operating range of -55 dBm to +10 dBm.

A PAX5710IR2-T free space polarimeter was used to measure the absolute polarisation of the pump laser and the spin devices. It has a wavelength operating range between 1000 nm and1350 nm and power operating range of -60 dBm to +10 dBm.

❖ Pump lasers

Two fibre-coupled JDSU Fibre Bragg Grating Stabilised 980 nm pump lasers were used to pump the spin-devices. They have a maximum operating power of 460 mW and threshold of 42 mA. They were driven at a constant RT of 293K.

Appendix C: Laser Safety

In the spin injection experiments used in this work the spin-V(E)CSEL samples were optically pumped by class 3B 980 nm pump lasers as described. Hence, these experiments were expected to possess possible beam hazards. Therefore, a risk assessment to identify the major possible hazards and the necessary precautions was a must.

Our setups were based on a semi-all-in-optical fibre beam-delivery-system. The possible exposure to open beam was confined to the free space section of the setup where the pump beam was either focused onto the sample or collimated behind the sample towards the head of the free space polarimeter. Initially, the pump beam travelled through spliced fibres from the pump laser to the end of either the lensed or the HR-coated fibres where it was focused onto the samples. This reduced the risk of accidents and possible hazards due to disconnection between fibres. In the free space section of the setup the hazard can be in the pumped beam in between the sample and the tip fibre and the spin-laser collimated beam behind the sample and on its way to the head of the free space polarimeter. Between the sample and the tip of the fibre, the maximum optical power was estimated to be about 250 mW. Behind the samples the pump and sample beams were collimated towards the head of the free-space polarimeter. The pump collimated beam diameter was identified by simple measurement using an IR card to be 2 mm. However, this part of the setup was partially covered, so it was not possible to reach the collimated beam without removing the panels placed around the setup.

To assess the risk of the possible hazards in the free space section, we had to calculate the minimum “eye-safe” distance where the beam is considered as safe for the human eyes. This was done by calculating the so-called nominal ocular hazard

distance (NOHD) where at this distance the intensity of the beam is lower than the maximum permissible radiation (MPR) on the eye.

$$\mathrm{NOHD} = \frac{\sqrt{\frac{4 \times S_{max}}{\pi \times \mathrm{MPE}}} - d}{\theta} \qquad \text{B. 1}$$

where $S_{\max}$ is the maximum power in W, d is the beam diameter in m, MPE is the maximum permissible radiation in W/m^2 and θ is the divergence of the beam in rad given by [329]:

$$\boldsymbol{\theta} = \frac{\boldsymbol{\lambda}}{\boldsymbol{\pi}\, \boldsymbol{d}} \qquad \text{B. 14}$$

The beam diameter was estimated to be 9 μm based on the core diameter of a standard single-mode fibre. By using equations B.1 and B.2, we calculated the NOHD to be 91 cm. To further minimise this hazards, safety goggles were worn all the time during the experiment. The goggles were rated with an optical density (OD) of 3 in the range 820-1720 nm, thus reducing the ocular safety distance three times.

Appendix D: Pattern design and processing

Due to the broad optical spectrum of our 1300 nm QW spin-VCSEL, patterns have been made on top of the spin-VCSEL samples as shown in Fig. A.3 in order to reduce the width of optical spectrum of the device.

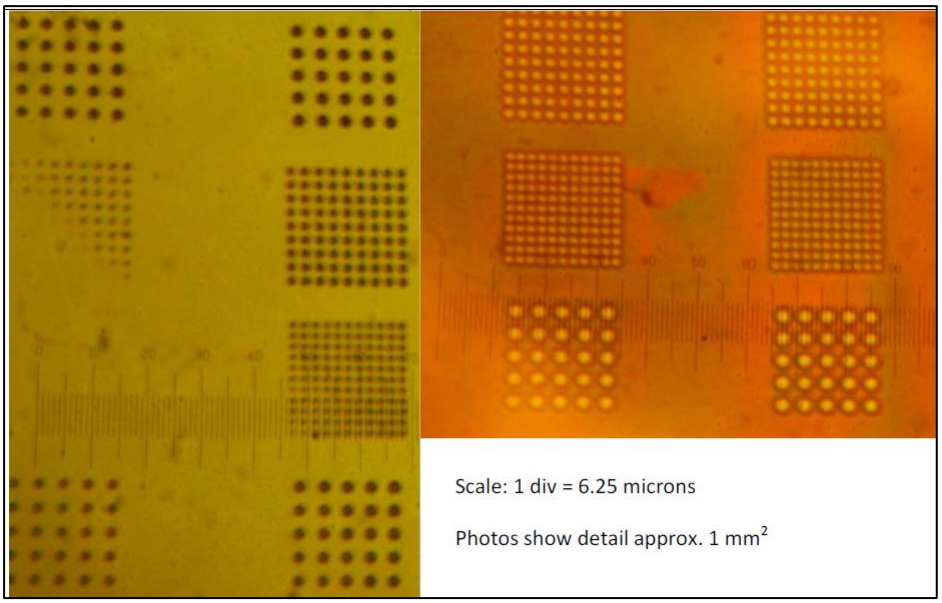

Fig. A.3: Different patterned masks on VCSEL sample (Courtesy of Adrian Boland-Thoms).

The samples were first spin coated with photoresist to form an even layer on top of the wafer. Samples were then soft-baked to thin the resist and exposed under a UV contact mask aligner to transfer the pattern shown in the photo. The exposed sample was then developed, washed in distilled water and dried. The resist pattern on the sample serves to alter the refractive index between exposed and unexposed areas so providing a degree of lateral variation in optical feedback to help define lasing area.

NOMENCLATURE

❖ Symbols

E_{sol}	The output of the solitary laser
Δf	Frequency Detuning
$f$osc	Main Frequency of Oscillation
f_d	Longitudinal-mode spacing
$\hbar$	Reduced Blank's constant
I	Intensity of the Electromagnetic Field
K	Injection Strength
n	Carrier Density
n_+	Spin-up carrier density
n_-	Spin-down carrier density
N	Total carrier density
m	Spin magnetization carrier density
P	Pumping ellipticity
P_{inj}	Injection power
$S_{0,1,\ 2,3}$	Stokes Parameters
T	Time

❖ Greek Symbols

α	Linewidth Enhancement Factor
β_s	Spontaneous emission noise term
δ	Ellipticity angle of the injection light
ε	Ellipticity

ε_n	Carrier density polarisation
ξ	Gaussian white noise term
η	Normalised pumping power
θ_p	Polarisation auxiliary angle
λ	Wavelength
ζ	Efficiency of the optical injection
κ	Photon Decay Rate
$\Delta\lambda$	Wavelength Detuning
γ	Carrier Decay Rate
γ_a	Dichroism
γ_p	Birefringence
γ_s	Spin Relaxation Rate
τ_n	Carrier Lifetime
τp	Photon Lifetime
φ	Azimuth Angle
$\phi_{x,y}$	Phase of the x,y-LP electrical field
χ	Ellipticity Angle
ω	Angular frequency

❖ Subscripts

ML	Master Laser
SL	Slave Laser
x	Orthogonal Polarisation
y	Parallel Polarisation suppressed
R	Right circularly polarised
L	Left circularly polarised

Inj	Injection
osc	Oscillation

❖ Acronyms

BAP	Bir-Arhonov-Pikus
C	Chaos
CBE	Chemical Beam Epitaxy
CW	Continuous-Wave
DBR	Distributed Bragg Reflector
DOCP	Degree of Circular Polarisation
DOP	Degree of Polarisation
DP	D'yakonov-Perel
DWELL	Dot-in-a-Well
ECL	External Cavity Laser
EEL	Edge emitting laser
EY	Elliot-Yafet
ESA	Electrical Spectrum Analyser
FBG	Fibre Bragg Grating
FFT	Fast Fourier Transform
FWM	Four Wave Mixing
GMR	Giant Magneto Resistive
hh	Heavy hole
HR	High reflection
IF	Interchangeable filter
IL	Injection Locking
IS	Isolator

I_+	Left-circular polarised intensity
I_-	Right-circular polarised intensity
I_x	Intensity of x- linearly-polarised mode
I_y	Intensity of y- linearly-polarised mode
K	Injection power ratio
K_{inj}	Injection coupling coefficient
lh	Light Hole
LAN	Local Area Network
LCP	Left Circularly Polarised
LED	Light-Emitting Diode
LHP	Linear Horizontal Polarised
LVP	Linear Vertical Polarised
LP	Linearly Polarised
LSB	Lower Side Band
MBE	Molecular Beam Epitaxy
ML	Master Laser
MOCVD	Metal Organic Chemical Vapour Deposition
MWM	Multi Wave Mixing
NDFWM	Nearly Degenerate Four Wave Mixing
NOHD	Nominal Ocular Hazard Distance
OD	Optical Density
ODE	Ordinary Differential Equations
OSA	Optical Spectrum Analyser
P1	Limit Cycle (Period 1)
P2	Period Doubling

PB	Polarisation bistability
PC	Polarisation Controller
PD	Photodetector
PL	Photoluminescence
PLE	Photoluminescence Excitation
PS	Polarisation Switching
PW	Pulsed Wave
QD	Quantum Dot
QW	Quantum Well
QWR	Quantum Wire
RCP	Right Circularly Polarised
RF	Radio Frequency
RIN	Relative Intensity Noise
ROF	Relaxation Oscillation Frequency
RT	Room Temperature
SESAM	Semiconductor Saturable Absorber Mirror
SDL	Semiconductor Disk Laser
SFM	Spin Flip Model
SL	Slave Laser
SML	Strain Mediating Layers
SP	Splitter
SOA	Semiconductor Optical Amplifier
USB	Upper Side Band
VCSEL	Vertical-Cavity Surface-Emitting Laser
VCSOA	Vertical-Cavity Semiconductor Optical Amplifier

VECSEL	Vertical-External-Cavity Surface-Emitting Laser
WAN	Wide-Area Network
WDM	Wavelength Division Multiplexer
0D	Zero dimension
1D	One dimension
2D	Two dimensions
3D	Three dimensions

LIST OF FIGURES

LIST OF TABLES

LIST OF PUBLICATIONS

➢ Journal Publications:

1- **Sami S. Alharthi**, Rihab K. Al Seyab, Ian D. Henning and Michael J. Adams, ‘’Simulated dynamics of optically pumped dilute nitride 1300nm spin-VCSELs’’, IET Optoelectronics, vol. 8, no. 2, pp. 117–121 (2014).

2- **S.S. Alharthi**, A. Hurtado, R.K. Al Seyab, V.-M. Korpijarvi, M. Guina, I.D. Henning and M.J. Adams, "Control of emitted light polarization in a 1310nm dilute nitride spin-vertical cavity surface emitting laser subject to circularly polarized optical injection", Applied Physics Letters, vol. 105, no. 18, p. 181106 (2014).

3- **S.S. Alharthi**, A. Hurtado, V.-M. Korpijarvi, M. Guina, I.D. Henning and M.J. Adams, "Circular polarization switching and bistability in an optically injected 1300 nm spin-VCSEL", Applied Physics Letters, vol. 106, no. 2, p. 021117 (2015).

4- **S.S. Alharthi**, E. Clarke, I.D. Henning and M.J. Adams, “1305 nm quantum dot vertical external cavity surface emitting laser”, IEEE Photonics Technology Letters, vol. 27, no. 14 (2015).

5- **S.S. Alharthi**, J. Orchard, E. Clarke, I.D. Henning and M.J. Adams, “1300 nm optically pumped quantum dot spin vertical external-cavity surface-emitting laser”, Applied Physics Letter, vol. 107, no.15 (2015).

➢ Conference Presentations:

1- **S.S. Alharthi**, I.D. Henning and M.J. Adams, ‘’Simulated dynamics of dilute nitride1300nm spin Vertical Cavity Surface Emitting Laser (VCSEL)’’, SIOE, Semiconductor and Integrated Optoelectronics, Cardiff, UK, April 2013.

2- **S.S. Alharthi**, A. Hurtado, V.-M. Korpijarvi, M. Guina, I.D. Henning and M.J. Adams, " Control of the Emitted Polarisation in a 1310 nm spin-VCSEL

Subject to Circularly Polarised Optical Injection", CLEO 2014, San Jose, USA, 8-13 June 2014.

3- **S.S. Alharthi**, A. Hurtado, V.-M. Korpijarvi, M. Guina, I.D. Henning and M.J. Adams, " Polarization switching and bistability in a 1300 nm spin-VCSEL Subject to Circularly Polarized Optical Injection", IPC 2014, IEEE Photonics Conference, San Diego, California, USA, from 12-16 October 2014.

4- **S.S. Alharthi**, E. Clarke, I.D. Henning and M.J. Adams, " 1300 nm Quantum Dot Semiconductor Disk Laser (QD-SDL)", ISLC 2014, IEEE International Semiconductor Laser Conference , Mallorca, Spain, from 7 - 10 September 2014.

REFERENCES

[1] J. Bardeen and W. Brattain, "Physical Principles Involved in Transistor Action," *Bell System Technical Journal*, vol. 28, no. 2, pp. 239–277, 1949.

[2] G. E. Moore, "Cramming More Components onto Integrated Circuits," *Electronics*, vol. 38, no. 8, pp. 114–117, 1965.

[3] M. Lundstrom, "Moore's Law Forever?" *Science*, vol. 299, no. 5604, pp. 210–211, 2003.

[4] G. E. Moore, "Lithography and the future of Moore's law," in *Proc. SPIE. 2438, Advances in Resist Technology and Processing XII*, 1995, p. 2.

[5] G. Binasch, P. Grünberg, F. Saurenbach, and W. Zinn, "Enhanced magnetoresistance in layered magnetic structures with antiferromagnetic interlayer exchange," *Physical Review B*, vol. 39, no. 7, pp. 4828–4830, 1989.

[6] M. N. Baibich, J. M. Broto, A. Fert, F. N. Van Dau, F. Petroff, P. Etienne, G. Creuzet, A. Friederich, and J. Chazelas, "Giant magnetoresistance of (001) Fe/(001) Cr magnetic superlattices," *Physical Review Letters*, vol. 61, no. 21, pp. 2472–2475, 1988.

[7] I. Žutic, J. Fabian, and S. D. Sarma, "Spintronics: Fundamentals and applications," *Reviews of Modern Physics*, vol. 76, no. 2, pp. 323–410, 2004.

[8] D. D. Awschalom, D. Loss, and N. Samarth, *Semiconductor Spintronics and Quantum Computation*. Springer Science & Business Media, 2013.

[9] W. Chen and I. Buyonova, *Handbook of Spintronic Semiconductors*. Pan Stanford Publishing, 2010.

[10] M. Oestreich, J. Hübner, D. Hägele, P. Klar, W. Heimbrodt, W. Rühle, D. Ashenford, and B. Lunn, "Spin injection into semiconductors," *Applied Physics Letters*, vol. 74, no. 9, pp. 1251–1253, 1999.

[11] M. Johnson, "Spin injection: a survey and review," *Journal of Superconductivity*, vol. 14, no. 2, pp. 273–281, 2001.

[12] D. Hägele, M. Oestreich, W. Rühle, N. Nestle, and K. Eberl, "Spin transport in GaAs," *Applied Physics Letters*, vol. 73, no. 11, pp. 1580–1582, 1998.

[13] J. Kikkawa and D. Awschalom, "Lateral drag of spin coherence in gallium arsenide," *Nature*, vol. 397, no. 6715, pp. 139–141, 1999.

[14] N. C. Gerhardt and M. R. Hofmann, "Spin-controlled vertical-cavity surface-emitting lasers," *Advances in Optical Technologies*, vol. 2012, p. 268949, 2012, 15 pages.

[15] M. Holub and P. Bhattacharya, "Spin-polarized light-emitting diodes and lasers," *Journal of Physics D: Applied Physics*, vol. 40, no. 11, pp. R179–R203, 2007.

[16] S. Datta and B. Das, "Electronic analog of the electro-optic modulator," *Applied Physics Letters*, vol. 56, no. 7, pp. 665–667, 1990.

[17] R. Parsons, "Band-to-band optical pumping in solids and polarized photoluminescence," *Physical Review Letters*, vol. 23, no. 20, p. 1152, 1969.

[18] N. Gerhardt, S. Hövel, C. Brenner, M. Hofmann, F.-Y. Lo, D. Reuter, A. Wieck, E. Schuster, W. Keune, S. Halm *et al.*, "Spin injection light-emitting diode with vertically

magnetized ferromagnetic metal contacts," *Journal of Applied Physics*, vol. 99, no. 7, p. 073907, 2006.

[19] H. Soldat, M. Li, N. C. Gerhardt, M. R. Hofmann, A. Ludwig, A. Ebbing, D. Reuter, A. D. Wieck, F. Stromberg, W. Keune *et al.*, "Room temperature spin relaxation length in spin light-emitting diodes," *Applied Physics Letters*, vol. 99, no. 5, p. 051102, 2011.

[20] S. Hövel, N. Gerhardt, M. Hofmann, F.-Y. Lo, D. Reuter, A. Wieck, E. Schuster, W. Keune, H. Wende, O. Petracic, and K. Westerholt, "Electrical detection of photoinduced spins both at room temperature and in remanence," *Applied Physics Letters*, vol. 92, no. 24, p. 242102, 2008.

[21] M. Holub, J. Shin, S. Chakrabarti, and P. Bhattacharya, "Electrically injected spin-polarized vertical-cavity surface-emitting lasers," *Applied Physics Letters*, vol. 87, no. 9, p. 091108, 2005.

[22] K. Schires, R. Al Seyab, A. Hurtado, V.-M. Korpijärvi, M. Guina, I. D. Henning, and M. J. Adams, "Optically-pumped dilute nitride spin-VCSEL," *Optics Express*, vol. 20, no. 4, pp. 3550–3555, 2012.

[23] K. Iga, F. Koyama, and S. Kinoshita, "Surface emitting semiconductor lasers," *IEEE Journal of Quantum Electronics*, vol. 24, no. 9, pp. 1845–1855, 1988.

[24] K. Iga, "Surface-emitting laser-its birth and generation of new optoelectronics field," *IEEE Journal of Selected Topics in Quantum Electronics*, vol. 6, no. 6, pp. 1201–1215, 2000.

[25] H. Soda, K.-I. Iga, C. Kitahara, and Y. Suematsu, "GaInAsP/InP surface emitting injection lasers," *Japanese Journal of Applied Physics*, vol. 18, no. 12, pp. 2329–2330, 1979.

[26] M. Grabherr, R. Jager, M. Miller, C. Thalmaier, J. Herlein, R. Michalzik, and K. Ebeling, "Bottom-emitting VCSEL's for high-CW optical output power," *IEEE Photonics Technology Letters*, vol. 10, no. 8, pp. 1061–1063, 1998.

[27] K. Iga, "Surface emitting laser," *The Institute of Electronics Information and Communication Engineering (IEICE) Transaction on Electronics*, vol. JBl-C-1, no. 9, pp. 483–493, 1998.

[28] K. Iga, "Vertical-cavity surface-emitting laser: its conception and evolution," *Japanese Journal of Applied Physics*, vol. 47, no. 1R, pp. 1–10, 2008.

[29] A. J. Van Doorn, M. Van Exter, and J. Woerdman, "Elasto-optic anisotropy and polarization orientation of vertical-cavity surface-emitting semiconductor lasers," *Applied Physics Letters*, vol. 69, no. 8, pp. 1041–1043, 1996.

[30] A. Jansen van Doom, M. Van Exter, and J. Woerdman, "Strain-induced birefringence in vertical-cavity semiconductor lasers," *IEEE Journal of Quantum Electronics*, vol. 34, no. 4, pp. 700–706, 1998.

[31] M. Van Exter, A. J. van Doorn, and J. Woerdman, "Electro-optic effect and birefringence in semiconductor vertical-cavity lasers," *Physical Review A*, vol. 56, no. 1, pp. 845–853, 1997.

[32] J. Danckaert, B. Nagler, J. Albert, K. Panajotov, I. Veretennicoff, and T. Erneux, "Minimal rate equations describing polarization switching in vertical-cavity surface-emitting lasers," *Optics Communications*, vol. 201, no. 1, pp. 129–137, 2002.

[33] Z. G. Pan, S. Jiang, M. Dagenais, R. A. Morgan, K. Kojima, M. T. Asom, R. E. Leibenguth, G. D. Guth, and M. W. Focht, "Optical injection induced polarization bistability in

vertical-cavity surface-emitting lasers," *Applied Physics Letters*, vol. 63, no. 22, pp. 2999–3001, 1993.

[34] A. Valle, I. Gatare, K. Panajotov, and M. Sciamanna, "Transverse mode switching and locking in vertical-cavity surface-emitting lasers subject to orthogonal optical injection," *IEEE Journal of Quantum Electronics*, vol. 43, no. 4, pp. 322–333, 2007.

[35] K. H. Jeong, K. H. Kim, S. H. Lee, M. H. Lee, B.-S. Yoo, and K. A. Shore, "Optical Injection-Induced Polarization Switching Dynamics in 1.5-m Wavelength Single-Mode Vertical-Cavity Surface-Emitting Lasers," *IEEE Photonics Technology Letters*, vol. 20, no. 10, pp. 779–781, 2008.

[36] A. Hurtado, I. D. Henning, and M. J. Adams, "Different forms of wavelength polarization switching and bistability in a 1.55 μm vertical-cavity surface-emitting laser under orthogonally polarized optical injection," *Optics Letters*, vol. 34, no. 3, pp. 365–367, 2009.

[37] A. Quirce, P. Perez, A. Valle, L. Pesquera, Y. Hong, H. Thienpont, and K. Panajotov, "Polarization switching in 1550nm VCSELs subject to parallel optical injection," in *2015 IEEE Photonics Conference (IPC)*, no. ME3.5, Reston, VA, USA, 4-8 October 2015, pp. 549–550.

[38] A. Valle, L. Pesquera, and K. Shore, "Polarization selection and sensitivity of external cavity vertical-cavity surface-emitting laser diodes," *IEEE Photonics Technology Letters*, vol. 10, no. 5, pp. 639–641, 1998.

[39] M. San Miguel, Q. Feng, and J. Moloney, "Light-polarization dynamics in surface-emitting semiconductor lasers," *Physical Review A*, vol. 52, no. 2, p. 1728, 1995.

[40] J. Martin-Regalado, F. Prati, M. S. Miguel, and N. Abraham, "Polarization switching in quantum-well vertical-cavity surface-emitting lasers," *Optics Letters*, vol. 21, no. 5, pp. 351–353, 1996.

[41] J. Martin-Regalado, M. S. Miguel, N. Abraham, and F. Prati, "Polarization properties of vertical-cavity surface-emitting lasers," *IEEE Journal of Quantum Electronics*, vol. 33, no. 5, pp. 765–783, 1997.

[42] K.-H. Ha, Y.-H. Lee, H. Shin, K. Lee, and S. Whang, "Polarisation anisotropy in asymmetric oxide aperture VCSELs," *Electronics Letters*, vol. 34, no. 14, pp. 1401–1402, 1998.

[43] B. Weigl, M. Grabherr, C. Jung, R. Jäger, G. Reiner, R. Michalzik, D. Sowada, and K. J. Ebeling, "High-performance oxide-confined GaAs VCSELs," *IEEE Journal of Selected Topics in Quantum Electronics*, vol. 3, no. 2, pp. 409–415, 1997.

[44] C. J. Chang-Hasnain, Y. Zhou, M. C. Huang, and C. Chase, "High-contrast grating VCSELs," *IEEE Journal of Selected Topics in Quantum Electronics*, vol. 15, no. 3, pp. 869–878, 2009.

[45] M. San Miguel, "Polarization properties of vertical cavity surface emitting lasers," in *Semiconductor quantum optoelectronics: From quantum physics to smart devices*, A. Miller, M. Ebrahimzadeh, and D. Finlayson, Eds. Bristol: Institute of Physics, 1999, pp. 339–366.

[46] R. Michalzik, *VCSELs: Fundamentals, Technology and Applications of Vertical-Cavity-Surface-Emitting Lasers*. Springer, 2012, vol. 166.

[47] J.-F. Seurin, A. L. D'Asaro, C. Ghosh , "A New Application for VCSELs: High-Power Pump Lasers," *Photonics Spectra*, vol. 41, no. 7, pp. 66–68, 2007.

[48] L. Mino, G. Agostini, E. Borfecchia, D. Gianolio, A. Piovano, E. Gallo, and C. Lamberti, "Low-dimensional systems investigated by x-ray absorption spectroscopy: a selection of 2D, 1D and 0D cases," *Journal of Physics D: Applied Physics*, vol. 46, no. 42, p. 423001, 2013.

[49] J. Beyer, I. A. Buyanova, S. Suraprapapich, C. Tu, and W. Chen, "Strong room-temperature optical and spin polarization in InAs/GaAs quantum dot structures," *Applied Physics Letters*, vol. 98, no. 20, p. 203110, 2011.

[50] A. Tackeuchi, R. Ohtsubo, K. Yamaguchi, M. Murayama, T. Kitamura, T. Kuroda, and T. Takagahara, "Spin relaxation dynamics in highly uniform InAs quantum dots," *Applied Physics Letters*, vol. 84, no. 18, pp. 3576–3578, 2004.

[51] J. Fabian, A. Matos-Abiague, C. Ertler, P. Stano, and I. Žutic, "Semiconductor spintronics," *Ácta Physica Slovaca. Reviews and Tutorials*, vol. 57, no. 4, pp. 565–907, 2007.

[52] M. I. Dyakonov, *Spin Physics in Semiconductors*. Springer Science & Business Media, 2008, vol. 157.

[53] A. Sobiesierski and P. M. Smowton, "Quantum-dot lasers: physics and applications," in *Comprehensive Semiconductor Science and Technology*, F. R. Bhattacharya, P. and H. Kamimura, Eds. Amsterdam: Elsevier, 2011, vol. 6, pp. 353–384.

[54] M. Kondow, K. Uomi, A. Niwa, T. Kitatani, S. Watahiki, and Y. Yazawa, "GaInNAs: a novel material for long-wavelength-range laser diodes with excellent high-temperature performance," *Japanese Journal of Applied Physics*, vol. 35, no. 2S, pp. 1273–1275, 1996.

[55] M. Fischer, M. Reinhardt, and A. Forchel, "A monolithic GaInAsN vertical-cavity surface-emitting laser for the 1.3-μm regime," *IEEE Photonics Technology Letters*, vol. 12, no. 10, pp. 1313–1315, 2000.

[56] T. Jouhti, O. Okhotnikov, J. Konttinen, L. Gomes, C. Peng, S. Karirinne, E. Pavelescu, and M. Pessa, "Dilute nitride vertical-cavity surface-emitting lasers," *New Journal of Physics*, vol. 5, no. 1, pp. 84.1–84.6, 2003.

[57] L. Lombez, P.-F. Braun, H. Carrere, B. Urbaszek, P. Renucci, T. Amand, X. Marie, J. Harmand, and V. Kalevich, "Spin dynamics in dilute nitride semiconductors at room temperature," *Applied Physics Letters*, vol. 87, no. 25, p. 252115, 2005.

[58] C. Reith, "Spin relaxation and carrier recombination in GaInNAs multiple quantum wells," Ph.D. dissertation, University of St Andrews, 2007.

[59] B. E. Saleh, M. C. Teich, and B. E. Saleh, *Fundamentals of photonics*. Wiley New York, 1991, vol. 22.

[60] M.-C. Amann and W. Hofmann, "InP-based long-wavelength VCSELs and VCSEL arrays," *IEEE Journal of Selected Topics in Quantum Electronics*, vol. 15, no. 3, pp. 861–868, 2009.

[61] K. Schires, R. Al Seyab, A. Hurtado, V.-M. Korpijärvi, M. Guina, I. D. Henning, and M. J. Adams, "Instabilities in optically-pumped 1300nm dilute nitride spin-VCSELs: Experiment and theory," in *2012 IEEE Photonics Conference (IPC)*, no. ThT4, Burlingame, CA, USA, 23-27 September 2012, pp. 870–871.

[62] R. K. S. Al-Seyab, "Dynamic behaviour of spin vertical cavity surface emitting lasers," Ph.D. dissertation, University of Essex, 2013.

[63] J. Frougier, G. Baili, M. Alouini, I. Sagnes, H. Jaffrès, A. Garnache, C. Deranlot, D. Dolfi, and J.-M. George, "Control of light polarization using optically spin-injected vertical

external cavity surface emitting lasers," *Applied Physics Letters*, vol. 103, no. 25, p. 252402, 2013.

[64] Y.-Y. Lai, K. Winn, J. Yarborough, Y. Merzlyak, and Y. Kaneda, "Injection-locked optically-pumped vertically external cavity surface emitting laser (VECSEL)," in *Proc. SPIE. 8966, Vertical External Cavity Surface Emitting Lasers (VECSELs) IV*, 2014, p. 89660Z.

[65] M. WU, J. JIANG, and M. WENG, "Spin dynamics in semiconductors," *Physics reports*, vol. 493, no. 2, pp. 61–236, 2010.

[66] M. I. Dyakonov and V. I. Perel, *Optical orientation*, F. Meier and B. P. Zakharchenya, Eds. Amsterdam: Elsevier, 1984, vol. 8.

[67] J. Rudolph, D. Hägele, H. Gibbs, G. Khitrova, and M. Oestreich, "Laser threshold reduction in a spintronic device," *Applied Physics Letters*, vol. 82, no. 25, pp. 4516–4518, 2003.

[68] J. Xia, W. Ge, and K. Chang, *Semiconductor Spintronics*. World Scientific, 2012.

[69] S. Hövel, N. Gerhardt, C. Brenner, M. Hofmann, F.-Y. Lo, D. Reuter, A. Wieck, E. Schuster, and W. Keune, "Spin-controlled LEDs and VCSELs," *Physica Status Solidi (a)*, vol. 204, no. 2, pp. 500–507, 2007.

[70] R. Fiederling, M. Keim, G. a. Reuscher, W. Ossau, G. Schmidt, A. Waag, and L. Molenkamp, "Injection and detection of a spin-polarized current in a light-emitting diode," *Nature*, vol. 402, no. 6763, pp. 787–790, 1999.

[71] P. Bhattacharya, D. Basu, A. Das, and D. Saha, "Quantum dot polarized light sources," *Semiconductor Science and Technology*, vol. 26, no. 1, p. 014002, 2011.

[72] S. Hövel, A. Bischoff, N. Gerhardt, M. Hofmann, T. Ackemann, A. Kroner, and R. Michalzik, "Optical spin manipulation of electrically pumped vertical-cavity surface-emitting lasers," *Applied Physics Letters*, vol. 92, no. 4, p. 041118, 2008.

[73] M. Holub, J. Shin, D. Saha, and P. Bhattacharya, "Electrical spin injection and threshold reduction in a semiconductor laser," *Physical Review Letters*, vol. 98, no. 14, p. 146603, 2007.

[74] D. Basu, D. Saha, C. Wu, M. Holub, Z. Mi, and P. Bhattacharya, "Electrically injected InAs/GaAs quantum dot spin laser operating at 200 K," *Applied Physics Letters*, vol. 92, no. 9, p. 1119, 2008.

[75] D. Saha, D. Basu, and P. Bhattacharya, "High-frequency dynamics of spin-polarized carriers and photons in a laser," *Physical Review B*, vol. 82, no. 20, p. 205309, 2010.

[76] D. Basu, D. Saha, and P. Bhattacharya, "Optical polarization modulation and gain anisotropy in an electrically injected spin laser," *Physical Review Letters*, vol. 102, no. 9, p. 093904, 2009.

[77] N. Gerhardt, S. Hövel, M. Hofmann, J. Yang, D. Reuter, and A. Wieck, "Enhancement of spin information with vertical cavity surface emitting lasers," *Electronics Letters*, vol. 42, no. 2, pp. 88–89, 2006.

[78] S. Hövel, N. Gerhardt, M. Hofmann, J. Yang, D. Reuter, and A. Wieck, "Spin controlled optically pumped vertical cavity surface emitting laser," *Electronics Letters*, vol. 41, no. 5, pp. 251–253, 2005.

[79] S. Hallstein, J. Berger, M. Hilpert, H. Schneider, W. Rühle, F. Jahnke, S. Koch, H. Gibbs, G. Khitrova, and M. Oestreich, "Manifestation of coherent spin precession in

stimulated semiconductor emission dynamics," *Physical Review B*, vol. 56, no. 12, p. R7076, 1997.

[80] H. Ando, T. Sogawa, and H. Gotoh, "Photon-spin controlled lasing oscillation in surface-emitting lasers," *Applied Physics Letters*, vol. 73, no. 5, pp. 566–568, 1998.

[81] R. Hendriks, M. Van Exter, J. Woerdman, K. Gulden, and M. Moser, "Memory effect for polarization of pump light in optically pumped vertical-cavity semiconductor lasers," *IEEE Journal of Quantum Electronics*, vol. 34, no. 8, pp. 1455–1460, 1998.

[82] J. Rudolph, S. Döhrmann, D. Hägele, M. Oestreich, and W. Stolz, "Room-temperature threshold reduction in vertical-cavity surface-emitting lasers by injection of spin-polarized electrons," *Applied Physics Letters*, vol. 87, no. 24, p. 1117, 2005.

[83] D. Sun, E. Towe, P. H. Ostdiek, J. W. Grantham, and G. J. Vansuch, "Polarization control of vertical-cavity surface-emitting lasers through use of an anisotropic gain distribution in [110]-oriented strained quantum-well structures," *IEEE Journal of Selected Topics in Quantum Electronics*, vol. 1, no. 2, pp. 674–680, 1995.

[84] H. Kawaguchi, "Spin-photonic semiconductor devices based on (110) quantum wells: Spin-VCSELs and spin-switches," in *2011 International Conference on Transparent Optical Networks (ICTON)*, no. We.B5.1, Stockholm, Sweden, 26-30 June 2011, pp. 1–4.

[85] H. Fujino, S. Iba, T. Fujimoto, S. Koh, and H. Kawaguchi, "Optically-pumped circularly-polarized lasing in a (110)-oriented VCSEL based on InGaAs/GaAs QWs," in *2009 Conference on Lasers and Electro-Optics and Conference on Quantum electronics and Laser Science (CLEO/QELS)*, no. CMRR5, Baltimore, MD, USA, 2-4 June 2009, pp. 1 – 2.

[86] H. Kawaguchi, "Circularly polarized lasing in a (110)-oriented VCSEL with InGaAs/GaAs QWs," in *2009 International Conference on Transparent Optical Networks (ICTON)*, no. We.D5.2, Azores, Portugal, 28 June- 2 July 2009, pp. 1–4.

[87] H. Fujino, S. Koh, S. Iba, T. Fujimoto, and H. Kawaguchi, "Circularly polarized lasing in a (110)-oriented quantum well vertical-cavity surface-emitting laser under optical spin injection," *Applied Physics Letters*, vol. 94, no. 13, p. 131108, 2009.

[88] S. Iba, S. Koh, K. Ikeda, and H. Kawaguchi, "Optically-pumped circularly polarized lasing in a (110) VCSEL with GaAs/AlGaAs QWs at room temperature," in *2011 Conference on Lasers and Electro-Optics (CLEO): Science and Innovations*, Baltimore, MD, USA, 1-6 May 2011, p. JTuI92.

[89] S. Iba, S. Koh, K. Ikeda, and H. Kawaguchi, "Room temperature circularly polarized lasing in an optically spin injected vertical-cavity surface-emitting laser with (110) GaAs quantum wells," *Applied Physics Letters*, vol. 98, no. 8, p. 081113, 2011.

[90] S. Alharthi, J. Orchard, E. Clarke, I. Henning, and M. Adams, "1300 nm optically pumped quantum dot spin vertical external-cavity surface-emitting laser," *Applied Physics Letters*, vol. 107, no. 15, p. 151109, 2015.

[91] H. Höpfner, M. Lindemann, N. C. Gerhardt, and M. R. Hofmann, "Controlled switching of ultrafast circular polarization oscillations in spin-polarized vertical-cavity surface-emitting lasers," *Applied Physics Letters*, vol. 104, no. 2, p. 022409, 2014.

[92] M. Holub and B. T. Jonker, "Threshold current reduction in spin-polarized lasers: Role of strain and valence-band mixing," *Physical Review B*, vol. 83, no. 12, p. 125309, 2011.

[93] S. Hosseinimotlagh, H. Ghavidelfard, and A. Shakeri, "Analytical investigation of electrons capture time effect on the threshold current density reduction in QD spin-lasers," *Physical Science International Journal*, vol. 4, no. 8, pp. 1050–1064, 2014.

[94] J. Lee, S. Bearden, E. Wasner, and I. Žutic, "Spin-lasers: From threshold reduction to large-signal analysis," *Ápplied Physics Letters*, vol. 105, no. 4, p. 042411, 2014.

[95] M. Li, H. Jähme, H. Soldat, N. Gerhardt, M. Hofmann, and T. Ackemann, "Birefringence controlled room-temperature picosecond spin dynamics close to the threshold of vertical-cavity surface-emitting laser devices," *Applied Physics Letters*, vol. 97, no. 19, p. 191114, 2010.

[96] M. J. Adams, K. Yasin, and A. Dyson, "Modelling spin-polarised VCSELs," in *Proc. SPIE. 5840, Photonic Materials, Devices, and Applications*, 2005, pp. 64–71.

[97] S. Yu, "Nonlinear dynamics of vertical-cavity surface-emitting lasers," *IEEE Journal of Quantum Electronics*, vol. 35, no. 3, pp. 332–341, 1999.

[98] R. J. Elliott, "Theory of the effect of spin-orbit coupling on magnetic resonance in some semiconductors," *Physical Review*, vol. 96, no. 2, pp. 266–279, 1954.

[99] M. Dyakonov and V. Perel, "Spin relaxation of conduction electrons in noncentrosymmetric semiconductors," *Soviet Physics Solid State*, vol. 13, no. 12, pp. 3023–3026, 1972.

[100] B. Murdin, K. Litvinenko, J. Allam, C. Pidgeon, M. Bird, K. Morrison, T. Zhang, S. Clowes, W. Branford, J. Harris *et al.*, "Temperature and doping dependence of spin relaxation in n-InAs," *Physical Review B*, vol. 72, no. 8, p. 085346, 2005.

[101] G. Bir, A. Aronov, and G. Pikus, "Spin relaxation of electrons due to scattering by holes," *Soviet Journal of Experimental and Theoretical Physics*, vol. 42, no. 4, pp. 705–712, 1976.

[102] A. W. Overhauser, "Paramagnetic relaxation in metals," *Physical Review*, vol. 89, no. 4, p. 689, 1953.

[103] X. Lou, C. Adelmann, M. Furis, S. Crooker, C. Palmstrøm, and P. Crowell, "Electrical detection of spin accumulation at a ferromagnet-semiconductor interface," *Physical Review Letters*, vol. 96, no. 17, p. 176603, 2006.

[104] R. Epstein, J. Stephens, M. Hanson, Y. Chye, A. Gossard, P. Petroff, and D. Awschalom, "Voltage control of nuclear spin in ferromagnetic Schottky diodes," *Physical Review B*, vol. 68, no. 4, p. 041305, 2003.

[105] R. Kawakami, Y. Kato, M. Hanson, I. Malajovich, J. Stephens, E. Johnston-Halperin, G. Salis, A. Gossard, and D. Awschalom, "Ferromagnetic imprinting of nuclear spins in semiconductors," *Science*, vol. 294, no. 5540, pp. 131–134, 2001.

[106] B. V. der Pol, "Forced oscillations in a circuit with nonlinear resistance," *Philosophical Magazine*, vol. 3, no. 13, pp. 65–80, 1927.

[107] R. Adler, "A study of locking phenomena in oscillators," *Proceedings of IRE*, vol. 61, no. 10, pp. 1380–1385, 1973.

[108] H. L. Stover and W. H. Steier, "Locking of laser oscillators by light injection," *Applied Physics Letters*, vol. 8, no. 4, pp. 91–93, 1966.

[109] L. Erickson and A. Szabo, "Spectral narrowing of dye laser output by injection of monochromatic radiation into the laser cavity," *Applied Physics Letters*, vol. 18, no. 10, pp. 433–435, 1971.

[110] S. Kobayashi and T. Kimura, "Injection locking characteristics of an AlGaAs semiconductor laser," *IEEE Journal of Quantum Electronics*, vol. 16, no. 9, pp. 915–917, 1980.

[111] F. Mogensen, H. Olesen, and G. Jacobsen, "Locking conditions and stability properties for a semiconductor laser with external light injection," *IEEE Journal of Quantum Electronics*, vol. 21, no. 7, pp. 784–793, 1985.

[112] Y. Yamamoto and T. Kimura, "Coherent optical fiber transmission systems," *IEEE Journal of Quantum Electronics*, vol. 17, no. 6, pp. 919–935, 1981.

[113] A. E. Siegman, *Lasers*. University Science Books Mill Valley, California, 1986, vol. 37.

[114] S. Eriksson, "Dependence of the experimental stability diagram of an optically injected semiconductor laser on the laser current," *Optics Communications*, vol. 210, no. 3, pp. 343–353, 2002.

[115] R. Lang, "Injection locking properties of a semiconductor laser," *IEEE Journal of Quantum Electronics*, vol. 18, no. 6, pp. 976–983, 1982.

[116] A. Gavrielides, V. Kovanis, and T. Erneux, "Analytical stability boundaries for a semiconductor laser subject to optical injection," *Optics Communications*, vol. 136, no. 3, pp. 253–256, 1997.

[117] S. Eriksson and Å. M. Lindberg, "Observations on the dynamics of semiconductor lasers subjected to external optical injection," *Journal of Optics B: Quantum and Semiclassical Optics*, vol. 4, no. 2, pp. 149–154, 2002.

[118] H. Li, T. L. Lucas, J. G. McInerney, M. W. Wright, R. Morgan *et al.*, "Injection locking dynamics of vertical cavity semiconductor lasers under conventional and phase conjugate injection," *IEEE Journal of Quantum Electronics*, vol. 32, no. 2, pp. 227–235, 1996.

[119] K. Panajotov, I. Gatare, A. Valle, H. Thienpont, and M. Sciamanna, "Polarization-and transverse-mode dynamics in optically injected and gain-switched vertical-cavity surface-emitting lasers," *IEEE Journal of Quantum Electronics*, vol. 45, no. 11, pp. 1473–1481, 2009.

[120] J. B. Altés, I. Gatare, K. Panajotov, H. Thienpont, and M. Sciamanna, "Mapping of the dynamics induced by orthogonal optical injection in vertical-cavity surface-emitting lasers," *IEEE Journal of Quantum Electronics*, vol. 42, no. 2, pp. 198–207, 2006.

[121] Y. Hong, P. S. Spencer, P. Rees, and K. A. Shore, "Optical injection dynamics of two-mode vertical cavity surface-emitting semiconductor lasers," *IEEE Journal of Quantum Electronics*, vol. 38, no. 3, pp. 274–278, 2002.

[122] B. Ryvkin, K. Panajotov, E. Avrutin, I. Veretennicoff, and H. Thienpont, "Optical-injection-induced polarization switching in polarization-bistable vertical-cavity surface-emitting lasers," *Journal of Applied physics*, vol. 96, no. 11, pp. 6002–6007, 2004.

[123] I. Gatare, M. Sciamanna, J. Buesa, H. Thienpont, and K. Panajotov, "Nonlinear dynamics accompanying polarization switching in vertical-cavity surface-emitting lasers with orthogonal optical injection," *Applied Physics Letters*, vol. 88, no. 10, p. 101106, 2006.

[124] A. Hurtado, I. D. Henning, and M. J. Adams, "Two-wavelength switching with a 1550 nm VCSEL under single orthogonal optical injection," *IEEE Journal of Selected Topics in Quantum Electronics*, vol. 14, no. 3, pp. 911–917, 2008.

[125] K. Schires, A. Hurtado, I. D. Henning, and M. J. Adams, "Comprehensive experimental analysis of nonlinear dynamics in an optically-injected semiconductor laser," *AIP Advances*, vol. 1, no. 3, p. 032131, 2011.

[126] R. Al-Seyab, K. Schires, N. A. Khan, A. Hurtado, I. D. Henning, and M. J. Adams, "Dynamics of polarized optical injection in 1550-nm VCSELs: theory and experiments," *IEEE Journal of Selected Topics in Quantum Electronics*, vol. 17, no. 5, pp. 1242–1249, 2011.

[127] A. Hurtado, A. Quirce, A. Valle, L. Pesquera, and M. J. Adams, "Nonlinear dynamics induced by parallel and orthogonal optical injection in 1550 nm vertical-cavity surface-emitting lasers (VCSELs)," *Optics Express*, vol. 18, no. 9, pp. 9423–9428, 2010.

[128] A. Valle, M. Sciamanna, and K. Panajotov, "Irregular pulsating polarization dynamics in gain-switched vertical-cavity surface-emitting lasers," *IEEE Journal of Quantum Electronics*, vol. 44, no. 2, pp. 136–143, 2008.

[129] R. Al-Seyab, K. Schires, A. Hurtado, I. Henning, and M. Adams, "Elliptical injection of a 1550 nm VCSEL: Theory and experiment," in *2012 IEEE International Semiconductor Laser Conference (ISLC)*, no. TuP9, San Diego, CA, USA, 7-10 October 2012, pp. 90–91.

[130] R. Al-Seyab, K. Schires, A. Hurtado, I. D. Henning, and M. J. Adams, "Dynamics of VCSELs subject to optical injection of arbitrary polarization," *IEEE Journal of Selected Topics in Quantum Electronics*, vol. 19, no. 4, p. 1700512, 2013.

[131] A. Qader, Y. Hong, K. A. Shore *et al.*, "Lasing characteristics of VCSELs subject to circularly polarized optical injection," *Journal of Lightwave Technology*, vol. 29, no. 24, pp. 3804–3809, 2011.

[132] S. Alharthi, A. Hurtado, R. Al Seyab, V.-M. Korpijarvi, M. Guina, I. Henning, and M. Adams, "Control of emitted light polarization in a 1310 nm dilute nitride spin-vertical cavity surface emitting laser subject to circularly polarized optical injection," *Applied Physics Letters*, vol. 105, no. 18, p. 181106, 2014.

[133] S. S. Alharthi, A. Hurtado, V.-M. Korpijarvi, M. Guina, I. D. Henning, and M. Adams, "Circular polarization switching and bistability in an optically injected 1300 nm spin-vertical cavity surface emitting laser," *Applied Physics Letters*, vol. 106, no. 2, p. 021117, 2015.

[134] X. J. Meng, T. Chau, and M. C. Wu, "Improved intrinsic dynamic distortions in directly modulated semiconductor lasers by optical injection locking," *IEEE Transactions on Microwave Theory and Techniques*, vol. 47, no. 7, pp. 1172–1176, 1999.

[135] L. Chrostowski, X. Zhao, and C. J. Chang-Hasnain, "Microwave performance of optically injection-locked VCSELs," *IEEE Transactions on Microwave Theory and Techniques*, vol. 54, no. 2, pp. 788–796, 2006.

[136] L. Chrostowski, B. Faraji, W. Hofmann, R. Shau, M. Ortsiefer, and M.-C. Amann, "40 GHz Bandwidth and 64 GHz Resonance Frequency in Injection-Locked 1.55 um VCSELs," in *2006 IEEE International Semiconductor Laser Conference (ISLC)*, no. WC2, Kohala Coast, HI, USA, 18-21 September 2006, pp. 117–118.

[137] E. K. Lau, L. J. Wong, X. Zhao, Y.-K. Chen, C. J. Chang-Hasnain, and M. C. Wu, "Bandwidth enhancement by master modulation of optical injection-locked lasers," *Journal of Lightwave Technology*, vol. 26, no. 15, pp. 2584–2593, 2008.

[138] Y. Hong, P. S. Spencer, and K. A. Shore, "Flat broadband chaos in vertical-cavity surface-emitting lasers subject to chaotic optical injection," *IEEE Journal of Quantum Electronics*, vol. 48, no. 12, pp. 1536–1541, 2012.

[139] P. Perez and A. Valle, "Enhancement of chaotic signal bandwidth in VCSELs induced by polarized optical injection," *IEEE Journal of Quantum Electronics*, vol. 51, no. 6, pp. 1–7, 2015.

[140] C.-H. Chang, L. Chrostowski, and C. J. Chang-Hasnain, "Injection locking of VCSELs," *IEEE Journal of Selected Topics in Quantum Electronics*, vol. 9, no. 5, pp. 1386–1393, 2003.

[141] E. K. Lau, X. Zhao, H.-K. Sung, D. Parekh, C. Chang-Hasnain, and M. C. Wu, "Strong optical injection-locked semiconductor lasers demonstrating> 100-GHz resonance frequencies and 80-GHz intrinsic bandwidths," *Optics Express*, vol. 16, no. 9, pp. 6609–6618, 2008.

[142] S. Wieczorek, W. W. Chow, L. Chrostowski, and C. J. Chang-Hasnain, "Improved semiconductor-laser dynamics from induced population pulsation," *IEEE Journal of Quantum Electronics*, vol. 42, no. 6, pp. 552–562, 2006.

[143] X. Zhao, M. Moewe, L. Chrostowski, C.-H. Chang, R. Shau, M. Ortsiefer, M.-C. Amann, and C. Chang-Hasnain, "28 GHz optical injection-locked 1.55 μm VCSELs," *Electronics Letters*, vol. 40, no. 8, pp. 476–478, 2004.

[144] L. Chrostowski, "Optical injection locking of vertical cavity surface emitting lasers," Ph.D. dissertation, UNIVERSITY of CALIFORNIA at BERKELEY, 2004.

[145] W. L. Zhang, W. Pan, B. Luo, M. Y. Wang, and X. H. Zou, "Polarization switching and hysteresis of VCSELs with time-varying optical injection," *IEEE Journal of Selected Topics in Quantum Electronics*, vol. 14, no. 3, pp. 889–894, 2008.

[146] S. Mazzucato, K. Schires, A. Hurtado, M. J. Adams, I. D. Henning, and N. Balkan, "1.3 to 1.55 All-Optical Wavelength Conversion for VCSEL-to-VCSEL Inversion and Logic," *IEEE Photonics Journal*, vol. 4, no. 3, pp. 817–824, 2012.

[147] S.-C. Chan, S.-K. Hwang, and J.-M. Liu, "Radio-over-fiber AM-to-FM up conversion using an optically injected semiconductor laser," *Optics Letters*, vol. 31, no. 15, pp. 2254–2256, 2006.

[148] I. Gatare, M. Sciamanna, M. Nizette, and K. Panajotov, "Bifurcation to polarization switching and locking in vertical-cavity surface-emitting lasers with optical injection," *Physical Review A*, vol. 76, no. 3, p. 031803, 2007.

[149] D. Boiko, G. Stephan, and P. Besnard, "Fast polarization switching with memory effect in a vertical cavity surface emitting laser subject to modulated optical injection," *Journal of Applied Physics*, vol. 86, no. 8, pp. 4096–4099, 1999.

[150] Y. Hong, P. Spencer, S. Bandyopadhyay, P. Rees, and K. A. Shore, "Polarisation-resolved chaos and instabilities in a vertical cavity surface emitting laser subject to optical injection," *Optics Communications*, vol. 216, no. 1, pp. 185–189, 2003.

[151] Y. Hong, K. Shore, A. Larsson, M. Ghisoni, and J. Halonen, "Polarisation switching in a vertical cavity surface emitting semiconductor laser by frequency detuning," *IEE Proceedings-Optoelectronics*, vol. 148, no. 1, pp. 31–34, 2001.

[152] I. Gatare, J. Buesa, H. Thienpont, K. Panajotov, and M. Sciamanna, "Polarization switching bistability and dynamics in vertical-cavity surface-emitting laser under orthogonal optical injection," *Optical and Quantum Electronics*, vol. 38, no. 4, pp. 429–443, 2006.

[153] Z. Wu, G. Xia, and H. Kong, "Nonlinear dynamics of an optical injection VCSEL," *Journal of Optoelectronics and Advanced Materials*, vol. 10, no. 6, pp. 1511–1514, 2008.

[154] P. Pérez, A. Quirce, L. Pesquera, and A. Valle, "Polarization-resolved nonlinear dynamics induced by orthogonal optical injection in long-wavelength VCSELs," *IEEE Journal of Selected Topics in Quantum Electronics*, vol. 17, no. 5, pp. 1228–1235, 2011.

[155] A. Hurtado, I. Henning, and M. Adams, "Dynamics of polarization switching in 1550nm-VCSELs under single and double optical injection," in *Proc. SPIE. 8255,Physics and Simulation of Optoelectronic Devices XX*, 2012, p. 82550A.

[156] M. Torre, A. Hurtado, A. Quirce, A. Valle, L. Pesquera, and M. Adams, "Polarization switching in long-wavelength VCSELs subject to orthogonal optical injection," *IEEE Journal of Quantum Electronics*, vol. 47, no. 1, pp. 92–99, 2011.

[157] A. Quirce, P. Perez, H. Lin, A. Valle, L. Pesquera, K. Panajotov, and H. Thienpont, "Polarization switching regions of optically injected long-wavelength VCSELs," *IEEE Journal of Quantum Electronics*, vol. 50, no. 11, pp. 921–928, 2014.

[158] I. Gatare, K. Panajotov, and M. Sciamanna, "Frequency-induced polarization bistability in vertical-cavity surface-emitting lasers with orthogonal optical injection," *Physical Review A*, vol. 75, no. 2, p. 023804, 2007.

[159] A. Homayounfar and M. Adams, "Polarisation effects in optically-injected VCSELs," *Electronics Letters*, vol. 42, no. 9, pp. 537–538, 2006.

[160] A. Homayounfar and M. J. Adams, "Locking bandwidth and birefringence effects for polarized optical injection in vertical-cavity surface-emitting lasers," *Optics Communications*, vol. 269, no. 1, pp. 119–127, 2007.

[161] A. Quirce and A. Valle, "High-frequency microwave signal generation using multi-transverse mode VCSELs subject to two-frequency optical injection," *Optics Express*, vol. 20, no. 12, pp. 13390–13401, 2012.

[162] D. Alexandropoulos and M. J. Adams, "Parametric analysis of spin-polarized VCSELs," *IEEE Journal of Quantum Electronics*, vol. 45, no. 6, pp. 744–749, 2009.

[163] A. Gahl, S. Balle, and M. S. Miguel, "Polarization dynamics of optically pumped VCSELs," *IEEE Journal of Quantum Electronics*, vol. 35, no. 3, pp. 342–351, 1999.

[164] C. Gøthgen, R. Oszwadowski, A. Petrou, and I. Žutic, "Ánalytical model of spin-polarized semiconductor lasers," *Applied Physics Letters*, vol. 93, no. 4, p. 042513, 2008.

[165] D. O'Brien, S. Hegarty, G. Huyet, and A. Uskov, "Sensitivity of quantum-dot semiconductor lasers to optical feedback," *Optics Letters*, vol. 29, no. 10, pp. 1072–1074, 2004.

[166] M. J. Adams and D. Alexandropoulos, "Analysis of quantum-dot spin-VCSELs," *IEEE Photonics Journal*, vol. 4, no. 4, pp. 1124–1132, 2012.

[167] D. Alexandropoulos, R. Al-Seyab, I. Henning, and M. Adams, "Instabilities in quantum-dot spin-VCSELs," *Optics Letters*, vol. 37, no. 10, pp. 1700–1702, 2012.

[168] J. Lee, W. Falls, R. Oszwadowski, and I. Žutic, "Spin modulation in semiconductor lasers," *Ápplied Physics Letters*, vol. 97, no. 4, p. 041116, 2010.

[169] M. Sciamanna and K. Panajotov, "Route to polarization switching induced by optical injection in vertical-cavity surface-emitting lasers," *Physical Review A*, vol. 73, no. 2, p. 023811, 2006.

[170] R. Al-Seyab, D. Alexandropoulos, I. D. Henning, and M. J. Adams, "Instabilities in spin-polarized vertical-cavity surface-emitting lasers," *IEEE Photonics Journal*, vol. 3, no. 5, pp. 799–809, 2011.

[171] T. Manago and H. Akinaga, "Spin-polarized light-emitting diode using metal/insulator/semiconductor structures," *Applied Physics Letters*, vol. 81, no. 4, pp. 694–696, 2002.

[172] N. Basov, O. Bogdankevich *et al.*, "Semiconductor lasers with radiating mirrors," *IEEE Journal of Quantum Electronics*, vol. 2, no. 9, pp. 594–597, 1966.

[173] O. Bogdankevich, S. Darznek, B. Vasiliev, M. Zverev *et al.*, "Semiconductor electron-beam-pumped lasers of the radiating mirror type," *IEEE Journal of Quantum Electronics*, vol. 9, no. 2, pp. 342–347, 1973.

[174] H. Le, S. Di Cecca, and A. Mooradian, "Scalable high-power optically pumped GaAs laser," *Applied Physics Letters*, vol. 58, no. 18, pp. 1967–1969, 1991.

[175] M. Kuznetsov, F. Hakimi, R. Sprague, and A. Mooradian, "High-power (> 0.5-W CW) diode-pumped vertical-external-cavity surface-emitting semiconductor lasers with circular TEM/sub 00/beams," *IEEE Photonics Technology Letters*, vol. 9, no. 8, pp. 1063–1065, 1997.

[176] J. Lott, A. Kovsh, N. Ledentsov, and D. Bimberg, "GaAs-based InAs/InGaAs quantum dot vertical cavity and vertical external cavity surface emitting lasers emitting near 1300 nm," in *2005 Pacific Rim Conference on Lasers and Electro-Optics (CLEO/Pacific Rim).*, no. CTuJ2-2, Tokyo, Japan, 30 July-02 Aug 2005, pp. 160–161.

[177] T. Germann, A. Strittmatter, U. Pohl, D. Bimberg, J. Rautiainen, M. Guina, and O. Okhotnikov, "Quantum-dot semiconductor disk lasers," *Journal of Crystal Growth*, vol. 310, no. 23, pp. 5182–5186, 2008.

[178] T. Germann, A. Strittmatter, J. Pohl, U. Pohl, D. Bimberg, J. Rautiainen, M. Guina, and O. Okhotnikov, "Temperature-stable operation of a quantum dot semiconductor disk laser," *Applied Physics Letters*, vol. 93, no. 5, p. 051104, 2008.

[179] P. J. Schlosser, J. E. Hastie, S. Calvez, A. B. Krysa, and M. D. Dawson, "InP/AlGaInP quantum dot semiconductor disk lasers for CW TEM 00 emission at 716–755 nm," *Optics Express*, vol. 17, no. 24, pp. 21782–21787, 2009.

[180] T. Schwarzbäck, R. Bek, F. Hargart, C. Kessler, H. Kahle, E. Koroknay, M. Jetter, and P. Michler, "High-power InP quantum dot based semiconductor disk laser exceeding 1.3 W," *Applied Physics Letters*, vol. 102, no. 9, p. 092101, 2013.

[181] A. R. Albrecht, A. Stintz, F. T. Jaeckel, T. J. Rotter, P. Ahirwar, V. J. Patel, C. P. Hains, L. F. Lester, K. J. Malloy, and G. Balakrishnan, "1220–1280-nm Optically Pumped InAs Quantum Dot-Based Vertical External-Cavity Surface-Emitting Laser," *IEEE Journal of Selected Topics in Quantum Electronics*, vol. 17, no. 6, pp. 1787–1793, 2011.

[182] M. Butkus, J. Rautiainen, O. G. Okhotnikov, C. J. Hamilton, G. Malcolm, S. Mikhrin, I. L. Krestnikov, D. Livshits, and E. U. Rafailov, "Quantum dot based semiconductor disk lasers for 1–1.3 μm," *IEEE Journal of Selected Topics in Quantum Electronics*, vol. 17, no. 6, pp. 1763–1771, 2011.

[183] A. Khiar, M. Rahim, M. Fill, F. Felder, F. Hobrecker, and H. Zogg, "Continuously tunable monomode mid-infrared vertical external cavity surface emitting laser on Si," *Applied Physics Letters*, vol. 97, no. 15, p. 151104, 2010.

[184] A. Khiar, M. Eibelhuber, V. Volobuev, M. Witzan, A. Hochreiner, H. Groiss, and G. Springholz, "Vertical external cavity surface emitting PbTe/CdTe quantum dot lasers for the mid-infrared spectral region," *Optics Letters*, vol. 39, no. 23, pp. 6577–6580, 2014.

[185] A. Ishida, Y. Sugiyama, Y. Isaji, K. Kodama, Y. Takano, H. Sakata, M. Rahim, A. Khiar, M. Fill, F. Felder *et al.*, "2 W high efficiency PbS mid-infrared surface emitting laser," *Applied Physics Letters*, vol. 99, no. 12, p. 121109, 2011.

[186] R. Bek, G. Kersteen, H. Kahle, T. Schwarzbäck, M. Jetter, and P. Michler, "All quantum dot mode-locked semiconductor disk laser emitting at 655 nm," *Applied Physics Letters*, vol. 105, no. 8, p. 082107, 2014.

[187] M. Hoffmann, O. D. Sieber, V. J. Wittwer, I. L. Krestnikov, D. A. Livshits, Y. Barbarin, T. Südmeyer, and U. Keller, "Femtosecond high-power quantum dot vertical external cavity surface emitting laser," *Optics Express*, vol. 19, no. 9, pp. 8108–8116, 2011.

[188] M. Hoffmann, O. Sieber, W. Pallmann, V. Wittwer, I. Krestnikov, S. Mikhrin, D. Livshits, G. Malcolm, C. Hamilton, Y. Barbarin *et al.*, "All quantum dot based femtosecond VECSEL," in *Proc. SPIE. 7919, Vertical External Cavity Surface Emitting Lasers (VECSELs)*, 2011, p. 79190X.

[189] A. Strittmatter, T. Germann, J. Pohl, U. Pohl, D. Bimberg, J. Rautiainen, M. Guina, and O. Okhotnikov, "1040 nm vertical external cavity surface emitting laser based on InGaAs quantum dots grown in Stranski-Krastanow regime," *Electronics Letters*, vol. 44, no. 4, pp. 290–291, 2008.

[190] D. Al Nakdali, M. K. Shakfa, M. Gaafar, M. Butkus, K. A. Fedorova, M. Zulonas, M. Wichmann, F. Zhang, B. Heinen, A. Rahimi-Iman *et al.*, "High-power quantum-dot vertical-external-cavity surface-emitting laser exceeding 8 W," *IEEE Photonics Technology Letters*, vol. 26, no. 15, pp. 1561–1564, 2014.

[191] M. Hoffmann, Y. Barbarin, D. Maas, M. Golling, I. Krestnikov, S. Mikhrin, A. Kovsh, T. Südmeyer, and U. Keller, "Modelocked quantum dot vertical external cavity surface emitting laser," *Applied Physics B*, vol. 93, no. 4, pp. 733–736, 2008.

[192] D. Al Nakdali, M. Gaafar, M. K. Shakfa, F. Zhang, M. Vaupel, K. Fedorova, A. Rahimi-Iman, E. Rafailov, and M. Koch, "High-Power Operation of Quantum-Dot Semiconductor Disk Laser at 1180 nm," *IEEE Photonics Technology Letters*, vol. 27, no. 10, pp. 1128–1131, 2015.

[193] A. Rantamaki, J. Rautiainen, L. Toikkanen, I. Krestnikov, M. Butkus, E. U. Rafailov, and O. Okhotnikov, "Flip chip quantum-dot semiconductor disk laser at 1200 nm," *IEEE Photonics Technology Letters*, vol. 15, no. 24, pp. 1292–1294, 2012.

[194] A. R. Albrecht, T. J. Rotter, C. P. Hains, A. Stintz, G. Xin, T.-L. Wang, Y. Kaneda, J. V. Moloney, K. J. Malloy, and G. Balakrishnan, "High-power 1.25 Âμm InAs QD VECSEL based on resonant periodic gain structure," in *Proc. SPIE.7919, Vertical External Cavity Surface Emitting Lasers (VECSELs)*, 2011, p. 791904.

[195] A. R. Albrecht, T. J. Rotter, C. P. Hains, A. Stintz, J. V. Moloney, K. Malloy, and G. Balakrishnan, "Multi-watt 1.25 μm quantum dot VECSEL," *Electronics Letters*, vol. 46, no. 12, pp. 856–857, 2010.

[196] S. Alharthi, E. Clarke, I. Henning, and M. Adams, "1305 nm Quantum Dot Vertical External Cavity Surface Emitting Laser," *IEEE Photonics Technology Letters*, vol. 27, no. 14, pp. 1489 – 1491, 2015.

[197] A. Rantamäki, G. S. Sokolovskii, S. A. Blokhin, V. V. Dudelev, K. K. Soboleva, M. A. Bobrov, A. G. Kuzmenkov, A. P. Vasil'ev, A. G. Gladyshev, N. A. Maleev *et al.*,

"Quantum dot semiconductor disk laser at 1.3 μm," *Optics Letters*, vol. 40, no. 14, pp. 3400–3403, 2015.

[198] S. Alharthi, E. Clarke, I. Henning, and M. Adams, "1300 Nm Quantum Dot Semiconductor Disk Laser (QD-SDL)," in *2014 International Semiconductor Laser Conference (ISLC)*, Palma de Mallorca, Spain, 7-10 September 2014, pp. 153–154.

[199] K. Hsu, C. M. Miller, D. Babic, D. Houng, and A. Taylor, "Continuously tunable photopumped 1.3-μm fiber Fabry-Perot surface-emitting lasers," *IEEE Photonics Technology Letters*, vol. 10, no. 9, pp. 1199–1201, 1998.

[200] N. Laurand, S. Calvez, M. Dawson, T. Jouhti, J. Konttinen, and M. Pessa, "Fiber-tunable dilute-nitride VCSEL," *Physica Status Solidi (c)*, vol. 2, no. 11, pp. 3895–3898, 2005.

[201] O. G. Okhotnikov, *Semiconductor disk lasers: physics and technology*. John Wiley & Sons, 2010.

[202] D. Maas, A. Bellancourt, M. Hoffmann, B. Rudin, Y. Barbarin, M. Golling, T. Südmeyer, and U. Keller, "Growth parameter optimization for fast quantum dot SESAMs," *Optics Express*, vol. 16, no. 23, pp. 18646–18656, 2008.

[203] A. Homayounfar and M. Adams, "Analysis of SFM dynamics in solitary and optically-injected VCSELs," *Optics Express*, vol. 15, no. 17, pp. 10504–10519, 2007.

[204] P. Pérez, A. Valle, and L. Pesquera, "Polarization-resolved characterization of long-wavelength vertical-cavity surface-emitting laser parameters," *Journal of the Optical Society of America B*, vol. 31, no. 11, pp. 2574–2580, 2014.

[205] W. Lau, V. Sih, N. Stern, R. Myers, D. Buell, A. Gossard, and D. Awschalom, "Room temperature electron spin coherence in telecom-wavelength quaternary quantum wells," *Applied Physics Letters*, vol. 89, no. 14, p. 142104, 2006.

[206] G. Knowles, R. Fehse, S. Tomic, S. J. Sweeney, T. Sale, A. R. Adams, E. P. O'Reilly, G. Steinle, and H. Riechert, "Investigation of 1.3-μm gainnas vertical-cavity surface-emitting lasers (vcsels) using temperature, high-pressure, and modeling techniques," *ÍEEE Journal of Selected Topics in Quantum Electronics*, vol. 9, no. 5, pp. 1202–1208, 2003.

[207] C. Reith, S. White, M. Mazilu, A. Miller, J. Konttinen, M. Guina, and M. Pessa, "Room temperature electron spin relaxation in gainnas multiple quantum wells at 1.3 mum," *Applied Physics Letters*, vol. 89, no. 21, pp. 211122–211122, 2006.

[208] H. Susanto, K. Schires, M. J. Adams, and I. D. Henning, "The spin-flip model of spin-polarized vertical-cavity surface-emitting lasers: asymptotic analysis, numerics, and experiments," *Physical Review A*, vol. 92, no. 6, p. 063838, 2015.

[209] N. Gerhardt, M. Li, H. Jähme, H. Höpfner, T. Ackemann, and M. Hofmann, "Ultrafast spin-induced polarization oscillations with tunable lifetime in vertical-cavity surface-emitting lasers," *Applied Physics Letters*, vol. 99, no. 15, p. 151107, 2011.

[210] N. Gerhardt, M. Li, H. Jaehme, H. Soldat, M. Hofmann, and T. Ackemann, "Ultrafast circular polarization oscillations in spin-polarized vertical-cavity surface-emitting laser devices," in *Proc. SPIE. 7597, Physics and Simulation of Optoelectronic Devices XVIII*, 2010, p. 75970Q.

[211] T. Ackemann and M. Sondermann, "Characteristics of polarization switching from the low to the high frequency mode in vertical-cavity surface-emitting lasers," *Applied Physics Letters*, vol. 78, no. 23, pp. 3574–3576, 2001.

[212] M. Sondermann, T. Ackemann, S. Balle, J. Mulet, and K. Panajotov, "Experimental and theoretical investigations on elliptically polarized dynamical transition states in the polarization switching of vertical-cavity surface-emitting lasers," *Optics Communications*, vol. 235, no. 4, pp. 421–434, 2004.

[213] M. Sciamanna, "Optical resonators: Chaos aids energy storage," *Nature Photonics*, vol. 7, no. 6, pp. 430–431, 2013.

[214] M. Willemsen, M. Van Exter, and J. Woerdman, "Anatomy of a polarization switch of a vertical-cavity semiconductor laser," *Physical Review Letters*, vol. 84, no. 19, p. 4337, 2000.

[215] K. Panajotov, B. Nagler, G. Verschaffelt, A. Georgievski, H. Thienpont, J. Danckaert, and I. Veretennicoff, "Impact of in-plane anisotropic strain on the polarization behavior of vertical-cavity surface-emitting lasers," *Applied Physics Letters*, vol. 77, no. 11, pp. 1590–1592, 2000.

[216] P. E. F. Junior, G. Xu, J. Lee, N. C. Gerhardt, G. M. Sipahi, and I. Žutic, "Toward high-frequency operation of spin lasers," *Physical Review B*, vol. 92, no. 7, p. 075311, 2015.

[217] T. Pusch, M. Lindemann, N. C. Gerhardt, M. R. Hofmann, and R. Michalzik, "Increasing the Birefringence of VCSELs Beyond 250 GHz," in *2015 European Conference on Lasers and Electro-Optics (CLEO/Europe)*, Munich, Germany, 21–25 June 2015, p. CB_2_2.

[218] T. Pusch, M. Lindemann, N. Gerhardt, M. Hofmann, and R. Michalzik, "Vertical-cavity surface-emitting lasers with birefringence splitting above 250 GHz," *Electronics Letters*, vol. 51, no. 20, pp. 1600–1602, 2015.

[219] S. Wieczorek, B. Krauskopf, T. Simpson, and D. Lenstra, "The dynamical complexity of optically injected semiconductor lasers," *Physics Reports*, vol. 416, no. 1, pp. 1–128, 2005.

[220] A. Hurtado, D. Labukhin, I. D. Henning, and M. J. Adams, "Injection locking bandwidth in 1550-nm VCSELs subject to parallel and orthogonal optical injection," *IEEE Journal of Selected Topics in Quantum Electronics*, vol. 15, no. 3, pp. 585–593, 2009.

[221] L. Chrostowski, B. Faraji, W. Hofmann, M.-C. Amann, S. Wieczorek, and W. W. Chow, "40 GHz bandwidth and 64 GHz resonance frequency in injection-locked 1.55 μm VCSELs," *IEEE Journal of Selected Topics in Quantum Electronics*, vol. 13, no. 5, pp. 1200–1208, 2007.

[222] J. Sakaguchi, T. Katayama, and H. Kawaguchi, "All-optical memory operation of 980-nm polarization bistable VCSEL for 20-Gb/s PRBS RZ and 40-Gb/s NRZ data signals," *Optics Express*, vol. 18, no. 12, pp. 12362–12370, 2010.

[223] T. Katayama, T. Ooi, and H. Kawaguchi, "Experimental Demonstration of Multi-Bit Optical Buffer Memory Using 1.55-Polarization Bistable Vertical-Cavity Surface-Emitting Lasers," *IEEE Journal of Quantum Electronics*, vol. 45, no. 11, pp. 1495–1504, 2009.

[224] J. Sakaguchi, T. Katayama, and H. Kawaguchi, "High switching-speed operation of optical memory based on polarization bistable vertical-cavity surface-emitting laser," *IEEE Journal of Quantum Electronics*, vol. 46, no. 11, pp. 1526–1534, 2010.

[225] S. H. Lee, H. W. Jung, K. H. Kim, M. H. Lee, B.-S. Yoo, J. Roh, and K. A. Shore, "1-GHz all-optical flip-flop operation of conventional cylindrical-shaped single-mode VCSELs under low-power optical injection," *IEEE Photonics Technology Letters*, vol. 22, no. 23, pp. 1759–1761, 2010.

[226] Y. Onishi, N. Nishiyama, C. Caneau, F. Koyama, and C.-e. Zah, "All-optical inverter based on long-wavelength vertical-cavity surface-emitting laser," *IEEE Journal of Selected Topics in Quantum Electronics*, vol. 11, no. 5, pp. 999–1005, 2005.

[227] K. Hasebe and F. Koyama, "Modeling of all-optical-signal processing devices based on two-mode injection-locked vertical-cavity surface-emitting laser," *Japanese Journal of Applied Physics*, vol. 45, no. 8S, pp. 6697–6703, 2006.

[228] C. Marki, S. Moro, D. Jorgesen, P. Wen, and S. Esener, "Cascadable optical inversion using 1550 nm VCSEL," *Electronics Letters*, vol. 44, no. 4, pp. 292–293, 2008.

[229] Y. Onishi and F. Koyama, "All-optical regeneration using a vertical-cavity surface-emitting laser with external light injection," *The Institute of Electronics Information and Communication Engineering (IEICE) Transaction on Electronics*, vol. 87, no. 3, pp. 409–415, 2004.

[230] S. Alharthi, A. Hurtado, V.-M. Korpijärvi, M. Guina, I. Hening, and M. Adams, "Control of the emitted polarization in a 1310 nm spin-VCSEL subject to circularly polarized optical injection," in *2014 Conference on Lasers and Electro-Optics (CLEO): Science and Innovations*, San Jose, CA, USA, 8-13 June 2014, pp. SF1G–7.

[231] K. Panajotov, B. Nagler, G. Verschaffelt, A. Georgievski, H. Thienpont, J. Danckaert, and I. Veretennicoff, "Impact of in-plane anisotropic strain on the polarization behavior of vertical-cavity surface-emitting lasers," *Applied Physics Letters*, vol. 77, no. 11, pp. 1590–1592, 2000.

[232] A. Quirce, A. Valle, and L. Pesquera, "Very wide hysteresis cycles in 1550-nm VCSELs subject to orthogonal optical injection," *IEEE Photonics Technology Letters*, vol. 21, no. 17, pp. 1193–1195, 2009.

[233] A. A. Qader, Y. Hong, and K. A. Shore, "Ultra-wide hysteresis frequency bistability in vertical cavity surface emitting lasers subject to orthogonal optical injection," *Applied Physics Letters*, vol. 103, no. 2, p. 021108, 2013.

[234] M. F. Salvide, C. Masoller, and M. S. Torre, "Polarization switching and hysteresis in vertical-cavity surface-emitting lasers subject to orthogonal optical injection," *IEEE Journal of Quantum Electronics*, vol. 50, no. 10, pp. 848–853, 2014.

[235] A. Hurtado, A. Quirce, A. Valle, L. Pesquera, and M. J. Adams, "Power and wavelength polarization bistability with very wide hysteresis cycles in a 1550nm-VCSEL subject to orthogonal optical injection," *Optics Express*, vol. 17, no. 26, pp. 23637–23642, 2009.

[236] Y. Nishikawa, A. Tackeuchi, S. Nakamura, S. Muto, and N. Yokoyama, "All-optical picosecond switching of a quantum well etalon using spin-polarization relaxation," *Applied Physics Letters*, vol. 66, no. 7, pp. 839–841, 1995.

[237] M. Grabherr, R. King, R. Jäger, D. Wiedenmann, P. Gerlach, D. Duckeck, and C. Wimmer, "Volume production of polarization controlled single-mode VCSELs," in *Proc. SPIE. 6908, Vertical-Cavity Surface-Emitting Lasers XII*, 2008, p. 690803.

[238] E. Kapon and A. Sirbu, "Long-wavelength VCSELs: Power-efficient answer," *Nature Photonics*, vol. 3, no. 1, pp. 27–29, 2009.

[239] A. Kaplan, G. P. Agrawal, and D. Maywar, "All-optical flip-flop operation of VCSOA," *Electronics Letters*, vol. 45, no. 2, pp. 127–129, 2009.

[240] S. Bandyopadhyay, Y. Hong, P. Spencer, and K. Shore, "VCSEL polarization control by optical injection," *Journal of Lightwave Technology*, vol. 21, no. 10, pp. 2395–2404, 2003.

[241] A. Quirce, J. R. Cuesta, A. Hurtado, K. Schires, A. Valle, L. Pesquera, I. D. Henning, and M. J. Adams, "Dynamic characteristics of an all-optical inverter based on polarization switching in long-wavelength VCSELs," *IEEE Journal of Quantum Electronics*, vol. 48, no. 5, pp. 588–595, 2012.

[242] S. Perrone, R. Vilaseca, and C. Masoller, "Stochastic logic gate that exploits noise and polarization bistability in an optically injected VCSEL," *Optics Express*, vol. 20, no. 20, pp. 22692–22699, 2012.

[243] M. F. Salvide, C. Masoller, and M. S. Torre, "All-optical stochastic logic gate based on a VCSEL with tunable optical injection," *IEEE Journal of Quantum Electronics*, vol. 49, no. 10, pp. 886–893, 2013.

[244] A. Hurtado, K. Schires, I. D. Henning, and M. Adams, "Investigation of vertical cavity surface emitting laser dynamics for neuromorphic photonic systems," *Applied Physics Letters*, vol. 100, no. 10, p. 103703, 2012.

[245] A. Hurtado, I. D. Henning, and M. J. Adams, "Optical neuron using polarisation switching in a 1550nm-VCSEL," *Optics Express*, vol. 18, no. 24, pp. 25170–25176, 2010.

[246] M. Nizette, M. Sciamanna, I. Gatare, H. Thienpont, and K. Panajotov, "Dynamics of vertical-cavity surface-emitting lasers with optical injection: a two-mode model approach," *Journal of the Optical Society of America B*, vol. 26, no. 8, pp. 1603–1613, 2009.

[247] D. Boggavarapu, W. Chow, R. Jin, J. Grantham, Y. Hu, F. B. de Colstoun, C. Lowry, G. Khitrova, S. Koch, M. Sargent *et al.*, "Instabilities of a microcavity laser with a weak injected signal," *Optics Letters*, vol. 18, no. 21, pp. 1846–1848, 1993.

[248] A. Quirce, P. Pérez, A. Valle, and L. Pesquera, "Correlation properties and time-resolved dynamics of linear polarizations emitted by single-mode vertical-cavity surface-emitting lasers subject to orthogonal optical injection," *Journal of the Optical Society of America B*, vol. 28, no. 11, pp. 2765–2776, 2011.

[249] A. Quirce, J. R. Cuesta, A. Valle, A. Hurtado, L. Pesquera, and M. J. Adams, "Polarization bistability induced by orthogonal optical injection in 1550-nm multimode VCSELs," *IEEE Journal of Selected Topics in Quantum Electronics*, vol. 18, no. 2, pp. 772–778, 2012.

[250] S. Osborne, A. Amann, K. Buckley, G. Ryan, S. Hegarty, G. Huyet, and S. O'Brien, "Antiphase dynamics in a multimode semiconductor laser with optical injection," *Physical Review A*, vol. 79, no. 2, p. 023834, 2009.

[251] S.-C. Chan, S.-K. Hwang, and J.-M. Liu, "Radio-over-fiber transmission from an optically injected semiconductor laser in period-one state," in *Proc. SPIE. 6468, Physics and Simulation of Optoelectronic Devices XV*, 2007, p. 646811.

[252] R. Al-Seyab, K. Schires, N. Khan, A. Hurtado, I. Henning, and M. Adams, "Novel theory and experiments on dynamics of polarised optical injection in long-wavelength VCSELs," in *2010 IEEE International Semiconductor Laser Conference (ISLC)*, no. P26, Kyoto, Japan, 26-30 September 2010, pp. 115–116.

[253] S.-C. Chan, S.-K. Hwang, and J.-M. Liu, "Period-one oscillation for photonic microwave transmission using an optically injected semiconductor laser," *Optics Express*, vol. 15, no. 22, pp. 14921–14935, 2007.

[254] J. P. Toomey, D. M. Kane, K. Schires, C. Nichkawde, A. Hurtado, I. D. Henning, and M. J. Adams, "Mapping transients in the nonlinear dynamics of an optically injected VCSEL," in *Proc. SPIE. 8432, Semiconductor Lasers and Laser Dynamics V*, 2012, p. 843219.

[255] P. Perez, A. Quirce, A. Valle, A. Consoli, I. Noriega, L. Pesquera, and I. Esquivias, "Photonic Generation of Microwave Signals Using a Single-Mode VCSEL Subject to Dual-Beam Orthogonal Optical Injection," *IEEE Photonics Journal*, vol. 7, no. 1, pp. 1–14, 2015.

[256] A. J. Seeds and K. J. Williams, "Microwave photonics," *Journal of Lightwave Technology*, vol. 24, no. 12, pp. 4628–4641, 2006.

[257] N. A. Olsson, H. Temkin, R. A. Logan, L. F. Johnson, G. Dolan, J. P. Van Der Ziel, and J. C. Campbell, "Chirp-free transmission over 82.5 km of single mode fibers at 2 Gbit/s with injection locked DFB semiconductor lasers," *Journal of Lightwave Technology*, vol. 3, no. 1, pp. 63–67, 1985.

[258] K. Iwashita and K. Nakagawa, "Suppression of mode partition noise by laser diode light injection," *IEEE Transactions on Microwave Theory and Techniques*, vol. 30, no. 10, pp. 1657–1662, 1982.

[259] Y. Hong, P. S. Spencer, and K. A. Shore, "Wideband chaos with time-delay concealment in vertical-cavity surface-emitting lasers with optical feedback and injection," *IEEE Journal of Quantum Electronics*, vol. 50, no. 4, pp. 236–242, 2014.

[260] A. Wang, Y. Wang, and H. He, "Enhancing the bandwidth of the optical chaotic signal generated by a semiconductor laser with optical feedback," *IEEE Journal of Photonics Technology Letters*, vol. 20, no. 19, pp. 1633–1635, 2008.

[261] G. Van Tartwijk and D. Lenstra, "Semiconductor lasers with optical injection and feedback," *Quantum and Semiclassical Optics: Journal of the European Optical Society Part B*, vol. 7, no. 2, pp. 87–143, 1995.

[262] M. Sciamanna, I. Gatare, A. Locquet, and K. Panajotov, "Polarization synchronization in unidirectionally coupled vertical-cavity surface-emitting lasers with orthogonal optical injection," *Physical Review E*, vol. 75, no. 5, p. 056213, 2007.

[263] Y. Hong, M. W. Lee, J. Paul, P. S. Spencer, and K. A. Shore, "GHz bandwidth message transmission using chaotic vertical-cavity surface-emitting lasers," *Journal of Lightwave Technology*, vol. 27, no. 22, pp. 5099–5105, 2009.

[264] A. Argyris, D. Syvridis, L. Larger, V. Annovazzi-Lodi, P. Colet, I. Fischer, J. Garcá-Ojalvo, C. R. Mirasso, L. Pesquera, and K. A. Shore, "Chaos-based communications at high bit rates using commercial fibre-optic links," *Nature*, vol. 438, no. 7066, pp. 343–346, 2005.

[265] H. Someya, I. Oowada, H. Okumura, T. Kida, and A. Uchida, "Synchronization of bandwidth-enhanced chaos in semiconductor lasers with optical feedback and injection," *Optics Express*, vol. 17, no. 22, pp. 19536–19543, 2009.

[266] M. Virte, E. Mercier, H. Thienpont, K. Panajotov, and M. Sciamanna, "Physical random bit generation from chaotic solitary laser diode," *Optics Express*, vol. 22, no. 14, pp. 17271–17280, 2014.

[267] X.-Z. Li and S.-C. Chan, "Heterodyne random bit generation using an optically injected semiconductor laser in chaos," *IEEE Journal of Quantum Electronics*, vol. 49, no. 10, pp. 829–838, 2013.

[268] I. Kanter, Y. Aviad, I. Reidler, E. Cohen, and M. Rosenbluh, "An optical ultrafast random bit generator," *Nature Photonics*, vol. 4, no. 1, pp. 58–61, 2010.

[269] F.-Y. Lin and J.-M. Liu, "Chaotic lidar," *IEEE Journal of Selected Topics in Quantum Electronics*, vol. 10, no. 5, pp. 991–997, 2004.

[270] P. Wen, M. Sanchez, M. Gross, and S. Esener, "Observation of bistability in a vertical-cavity semiconductor optical amplifier (VCSOA)," *Optics Express*, vol. 10, no. 22, pp. 1273–1278, 2002.

[271] W. Li, N. H. Zhu, L. X. Wang, J. H. Ke, S. F. Chen, X. Q. Qi, B. H. Zhang, and L. Xie, "Frequency-pushing effect in single-mode diode laser subject to external dual-beam injection," *IEEE Journal of Quantum Electronics*, vol. 46, no. 5, pp. 796–803, 2010.

[272] T. Simpson, J. Liu, K. Huang, and K. Tai, "Nonlinear dynamics induced by external optical injection in semiconductor lasers," *Quantum and Semiclassical Optics: Journal of the European Optical Society Part B*, vol. 9, no. 5, pp. 765–784, 1997.

[273] N. M. Al-Hosiny, I. D. Henning, and M. J. Adams, "Correlation of electron density changes with optical frequency shifts in optically injected semiconductor lasers," *IEEE journal of Quantum Electronics*, vol. 42, no. 6, pp. 570–580, 2006.

[274] L. Li and K. Petermann, "Small signal analysis of THz optical-frequency conversion in an injection-locked semiconductor laser," *IEEE Journal of Quantum Electronics*, vol. 29, no. 12, pp. 2988–2994, 1993.

[275] D. Marcenac, D. Nesset, A. Kelly, M. Brierley, A. Ellis, D. Moodie, and C. Ford, "40 Gbit/s transmission over 406 km of NDSF using mid-span spectral inversion by four-wave-mixing in a 2 mm long semiconductor optical amplifier," *Electronics Letters*, vol. 33, no. 10, pp. 879–880, 1997.

[276] S. Diez, C. Schmidt, R. Ludwig, H. G. Weber, K. Obermann, S. Kindt, I. Koltchanov, and K. Petermann, "Four-wave mixing in semiconductor optical amplifiers for frequency conversion and fast optical switching," *IEEE Journal of Selected Topics in Quantum Electronics*, vol. 3, no. 5, pp. 1131–1145, 1997.

[277] J. Renaudier, G. Duan, J. Provost, H. Debregeas-Sillard, and P. Gallion, "Phase correlation between longitudinal modes in semiconductor self-pulsating DBR lasers," *IEEE Photonics Technology Letters*, vol. 17, no. 4, pp. 741–743, 2005.

[278] B. Kögel, M. Maute, H. Halbritter, F. Riemenschneider, G. Böhm, M. Amann, and P. Meissner, "Long-wavelength MEMS tunable vertical-cavity surface-emitting lasers with high sidemode suppression," *Journal of Optics A: Pure and Applied Optics*, vol. 8, no. 7, pp. S370–S376, 2006.

[279] T. Schwarzbäck, H. Kahle, M. Eichfelder, R. Roßbach, M. Jetter, and P. Michler, "Wavelength tunable ultraviolet laser emission via intra-cavity frequency doubling of an AlGaInP vertical external-cavity surface-emitting laser down to 328 nm," *Applied Physics Letters*, vol. 99, no. 26, p. 261101, 2011.

[280] S. Calvez, J. E. Hastie, M. Guina, O. G. Okhotnikov, and M. D. Dawson, "Semiconductor disk lasers for the generation of visible and ultraviolet radiation," *Laser & Photonics Reviews*, vol. 3, no. 5, pp. 407–434, 2009.

[281] N. Schulz, J.-M. Hopkins, M. Rattunde, D. Burns, and J. Wagner, "High-brightness long-wavelength semiconductor disk lasers," *Laser & Photonics Reviews*, vol. 2, no. 3, pp. 160–181, 2008.

[282] U. Keller and A. C. Tropper, "Passively modelocked surface-emitting semiconductor lasers," *Physics Reports*, vol. 429, no. 2, pp. 67–120, 2006.

[283] K. G. Wilcox, Z. Mihoubi, G. Daniell, S. Elsmere, A. Quarterman, I. Farrer, D. A. Ritchie, and A. Tropper, "Ultrafast optical Stark mode-locked semiconductor laser," *Optics Letters*, vol. 33, no. 23, pp. 2797–2799, 2008.

[284] M. Lumb, E. Clarke, E. Harbord, P. Spencer, R. Murray, F. Masia, P. Borri, W. Langbein, C. Leburn, C. Jappy *et al.*, "Ultrafast absorption recovery dynamics of 1300 nm quantum dot saturable absorber mirrors," *Applied Physics Letters*, vol. 95, no. 4, p. 041101, 2009.

[285] M. Guina, A. Härkönen, V.-M. Korpijärvi, T. Leinonen, and S. Suomalainen, "Semiconductor Disk Lasers: Recent Advances in Generation of Yellow-Orange and Mid-IR Radiation," *Advances in Optical Technologies*, vol. 2012, p. 265010, 2012, 19 pages.

[286] M. Grundmann, O. Stier, S. Bognar, C. Ribbat, F. Heinrichsdorff, and D. Bimberg, "Optical Properties of Self-Organized Quantum Dots: Modeling and Experiments," *Physica Status Solidi (a)*, vol. 178, no. 1, pp. 255–262, 2000.

[287] L. U. Ltd, "Data sheet for HR-coated fibre," Tech. Rep. 1, 2012.

[288] K. A. Fedorova, M. A. Cataluna, I. Krestnikov, D. Livshits, and E. U. Rafailov, "Broadly tunable high-power InAs/GaAs quantum-dot external cavity diode lasers," *Optics Express*, vol. 18, no. 18, pp. 19438–19443, 2010.

[289] C. Borgentun, J. Bengtsson, A. Larsson, F. Demaria, A. Hein, and P. Unger, "Optically pumped high-power semiconductor disk laser with gain element engineered for wide tunability," in *Proc. SPIE. 7720, Semiconductor Lasers and Laser Dynamics IV*, 2010, p. 772014.

[290] D. Bimberg, N. Kirstaedter, N. Ledentsov, Z. I. Alferov, P. Kop'ev, and V. Ustinov, "InGaAs-GaAs quantum-dot lasers," *IEEE Journal of Selected Topics in Quantum Electronics*, vol. 3, no. 2, pp. 196–205, 1997.

[291] C. Hessenius, "Novel Cavities and Functionality in High-Power High-Brightness Semiconductor Vertical External Cavity Surface Emitting Lasers," Ph.D. dissertation, The University of Arizona, 2013.

[292] X. Lv, P. Jin, and Z. Wang, "Broadly tunable grating-coupled external cavity laser with quantum-dot active region," *IEEE Photonics Technology Letters*, vol. 22, no. 24, pp. 1799–1801, 2010.

[293] J. T. Olesberg, M. A. Arnold, C. Mermelstein, J. Schmitz, and J. Wagner, "Tunable laser diode system for noninvasive blood glucose measurements," *Applied Spectroscopy*, vol. 59, no. 12, pp. 1480–1484, 2005.

[294] B. Stevens, D. Childs, K. Groom, M. Hopkinson, and R. Hogg, "All semiconductor swept laser source utilizing quantum dots," *Applied Physics Letters*, vol. 91, no. 12, p. 1119, 2007.

[295] M. E. Brezinski and J. G. Fujimoto, "Optical coherence tomography: high-resolution imaging in nontransparent tissue," *IEEE Journal of Selected Topics in Quantum Electronics*, vol. 5, no. 4, pp. 1185–1192, 1999.

[296] Y. Mao, S. Chang, E. Murdock, and C. Flueraru, "Simultaneous dual-wavelength-band common-path swept-source optical coherence tomography with single polygon mirror scanner," *Optics Letters*, vol. 36, no. 11, pp. 1990–1992, 2011.

[297] A. Garnache, A. Kachanov, F. Stoeckel, and R. Houdre, "Diode-pumped broadband vertical-external-cavity surface-emitting semiconductor laser applied to high-sensitivity

intracavity absorption spectroscopy," *Journal of the Optical Society of America B-Optical Physics*, vol. 17, no. 9, pp. 1589–1598, 2000.

[298] S. C. Woodworth, D. T. Cassidy, and M. J. Hamp, "Sensitive absorption spectroscopy by use of an asymmetric multiple-quantum-well diode laser in an external cavity," *Applied Optics*, vol. 40, no. 36, pp. 6719–6724, 2001.

[299] T. Yanagawa, O. Tadanaga, K. Magari, Y. Nishida, H. Miyazawa, M. Asobe, and H. Suzuki, "CH4 monitoring in ambient air by communication band laser diode based difference frequency generation in a quasi-phase-matched LiNbO3 waveguide," *Applied Physics Letters*, vol. 89, no. 22, p. 1115, 2006.

[300] N. Kuramoto and K. Fujii, "Volume determination of a silicon sphere using an improved interferometer with optical frequency tuning," *IEEE Transactions on Instrumentation and Measurement*, vol. 54, no. 2, pp. 868–871, 2005.

[301] G. Galzerano, G. Mana, and E. Massa, "On the effect of broadband emission in external-cavity diode-laser interferometry," *Measurement Science and Technology*, vol. 18, no. 5, pp. 1338–1342, 2007.

[302] S. B. Yoo, "Wavelength conversion technologies for WDM network applications," *Journal of Lightwave Technology*, vol. 14, no. 6, pp. 955–966, 1996.

[303] U. Koren, T. Koch, B. Miller, G. Eisenstein, and R. Bosworth, "Wavelength division multiplexing light source with integrated quantum well tunable lasers and optical amplifiers," *Applied Physics Letters*, vol. 54, no. 21, pp. 2056–2058, 1989.

[304] M. Grundmann, "Feasibility of 5 Gbit/s wavelength division multiplexing using quantum dot lasers," *Applied Physics Letters*, vol. 77, no. 26, pp. 4265–4267, 2000.

[305] H. Ishii, K. Kasaya, and H. Oohashi, "Wavelength-tunable lasers for next-generation optical networks," *NTT Technical Review*, vol. 9, no. 3, pp. 1–6, 2011.

[306] L. Fan, M. Fallahi, J. Hader, A. Zakharian, M. Kolesik, J. Moloney, T. Qiu, A. Schülzgen, N. Peyghambarian, W. Stolz *et al.*, "Over 3 W high-efficiency vertical-external-cavity surface-emitting lasers and application as efficient fiber laser pump sources," *Applied Physics Letters*, vol. 86, no. 21, p. 1116, 2005.

[307] A. Garcá-Arellano, F. Granados-Agustn, M. Campos-Garcá, and A. Cornejo-Rodrguez, "Ronchi test with equivalent wavelength," *Ápplied Optics*, vol. 51, no. 15, pp. 3071–3080, 2012.

[308] C.-L. Wang, Y.-H. Chuang, and C.-L. Pan, "Two-wavelength interferometer based on a two-color laser-diode array and the second-order correlation technique," *Optics Letters*, vol. 20, no. 9, pp. 1071–1073, 1995.

[309] V. Ménoret, R. Geiger, G. Stern, N. Zahzam, B. Battelier, A. Bresson, A. Landragin, and P. Bouyer, "Dual-wavelength laser source for onboard atom interferometry," *OpticsLetters*, vol. 36, no. 21, pp. 4128–4130, 2011.

[310] S. Chang, Y. Mao, and C. Flueraru, "Dual-Source Swept-Source Optical Coherence Tomography Reconstructed on Integrated Spectrum," *International Journal of Optics*, vol. 2012, p. 565823, 2011, 6 pages.

[311] S. Shibata, "Dual-Wavelength Spectrophotometry," *Angewandte Chemie International Edition in English*, vol. 15, no. 11, pp. 673–679, 1976.

[312] A. S. Saad, "Novel spectrophotometric method for selective determination of compounds in ternary mixtures (dual wavelength in ratio spectra," *Spectrochimica Acta Part A: Molecular and Biomolecular Spectroscopy*, vol. 147, pp. 257–261, 2015.

[313] J. Jágerská, P. Jouy, B. Tuzson, H. Looser, M. Mangold, P. Soltic, A. Hugi, R. Brönnimann, J. Faist, and L. Emmenegger, "Simultaneous measurement of NO and NO 2 by dual-wavelength quantum cascade laser spectroscopy," *Optics Express*, vol. 23, no. 2, pp. 1512–1522, 2015.

[314] S. Buaprathoom, S. Pedley, and S. J. Sweeney, "Dual wavelength multiple-angle light scattering system for cryptosporidium detection," in *Proc. SPIE. 8427, Biophotonics: Photonic Solutions for Better Health Care III*, 2012, p. 84272K.

[315] K. Schires, "Dynamics of spin-VCSELs," Ph.D. dissertation, University of Essex, 2013.

[316] J. Lee, R. Oszwadowski, C. Gøthgen, and I. Žutic, "Mapping between quantum dot and quantum well lasers: From conventional to spin lasers," *Physical Review B*, vol. 85, no. 4, p. 045314, 2012.

[317] I. Vurgaftman, M. Holub, B. Jonker, and J. Meyer, "Estimating threshold reduction for spin-injected semiconductor lasers," *Applied Physics Letters*, vol. 93, no. 3, p. 031102, 2008.

[318] G. Van der Sande, M. Peeters, I. Veretennicoff, J. Danckaert, G. Verschaffelt, and S. Balle, "The effects of stress, temperature, and spin flips on polarization switching in vertical-cavity surface-emitting lasers," *IEEE Journal of Quantum Electronics*, vol. 42, no. 9, pp. 898–906, 2006.

[319] S. S. Alharthi, R. K. Al Seyab, I. D. Henning, and M. J. Adams, "Simulated dynamics of optically pumped dilute nitride 1300 nm spin vertical-cavity surface-emitting lasers," *IET Optoelectronics*, vol. 8, no. 2, pp. 117–121, 2014.

[320] S. Mangin, M. Gottwald, C. Lambert, D. Steil, V. Uhlr, L. Pang, M. Hehn, S. Alebrand, M. Cinchetti, G. Malinowski *et al.*, "Engineered materials for all-optical helicity-dependent magnetic switching," *Nature Materials*, vol. 13, no. 3, pp. 286–292, 2014.

[321] J. Ohtsubo, *Semiconductor lasers: stability, instability and chaos*, 3rd ed., W. T. Rhodes, Ed. Springer, 2012, vol. 111.

[322] E. K. Lau, L. J. Wong, and M. C. Wu, "Enhanced modulation characteristics of optical injection-locked lasers: A tutorial," *IEEE Journal of Selected Topics in Quantum Electronics*, vol. 15, no. 3, pp. 618–633, 2009.

[323] K. Kobayashi, H. Nishimoto, and R. Lang, "Experimental observation of asymmetric detuning characteristics in semiconductor laser injection locking," *Electronics Letters*, vol. 18, no. 2, pp. 54–56, 1982.

[324] S. Alharthi, A. Hurtado, V.-M. Korpijarvi, M. Guina, I. Henning, and M. Adams, "Polarization switching and bistability in a 1300 nm spin-VCSEL subject to circularly polarized optical injection," in *2014 IEEE Photonics Conference (IPC)*, no. ME1.5, San Diego, CA, USA, 12-16 October 2014, pp. 95–96.

[325] H. Tompkins and E. A. Irene, *Handbook of Ellipsometry*. William Andrew, 2005.

[326] Hyperphysics website. http://hyperphysics.phy-astr.gsu.edu/hbase/phyopt/polclas.html. Georgia Tech University, 2005. Accessed on 17 December 2015.

[327] S. Chandrasekhar, *Radiative Transfer*. Dover Publications Inc., 1960.

[328] C. Mätzler, *Thermal Microwave Radiation : Applications for Remote Sensing*. Institution of Engineering and Technology, 2006.

[329] H. Young, R. Freedman, A. Ford, F. Sears, and M. Zemansky, *Sears and Zemansky's University Physics: With Modern Physics*. Pearson Education, Limited, 2014, vol. 2.